UNIVERSITY OF LIVERPOOL

Institute of Integrative Biology

# Interactions of fibroblast growth factors with glycosaminoglycan brushes and the pericellular matrix.

Thesis submitted in accordance with the requirements of the University of Liverpool for the degree of doctor in Philosophy

BARADJI Aïseta

September 2017

## Author's declaration

I declare that the work in this dissertation was carried out in accordance with the regulations of the University of Liverpool and the CIC BiomaGUNE. The study described is original and have not been submitted for any other degree. All aspects of the experimental design and planning for the study were conducted by me under the guidance and agreement of my supervisors, Professor David G. Fernig, Dr. Ralf P. Richter and Dr. Edwin Yates. The experimental work in this study was undertaken by me, with specific contributions that are indicated in the core of the thesis when appropriate.

Any views and hypothesis presented in this thesis are from the author and to not represent those of the University of Liverpool. This thesis has not been presented to any other university for examination in the United Kingdom or overseas.

## Acknowledgments

I would like to express my gratitude to the people who contributed by their support, guidance and advice to this study and my training.

This work would not have been possible without the input of many people but first and foremost, I would like to express my thankfulness to my supervisors, Professor **David G. Fernig**, Dr. **Ralf P. Richter** and Dr. **Edwin Yates** for their guidance and support throughout this four years of training in conducting research and personal development.

I am grateful to my assessors who guided me throughout this journey: Pr. **Olga Mayans**, Dr. **David Adams** and Dr. **Igor Baruskov**. Special thanks to Pr. **Jeremy Turnbull** and Pr. **Catherine Picart**, my internal and external examiners respectively for giving their final review to this work.

I would like to thank the people who I have worked along and who advised me in multiple occasions in the biosurfaces laboratory at the CIC BiomaGUNE and the biochemistry laboratory at the Institute of Integrative Biology: **Yong Li**, **Elisa Migliorini**, the group members and supporting staff of both laboratories. Thanks to Thao Bui, Pawin Ngamlert, Dunhao Sun and Zaid Alghrair for their daily support and friendships.

Thanks to my friends and family for their continuous support on this journey. I could not possibly be thankful enough to my mother, **Dianessy Hawa**, for always being by my side and supporting my will of studying science.

*"Success is not an end in itself. It is a journey that is best judged by the number of times that the traveller has been able to stand up after he/she has fallen down."*

*H.E Ameenah Gurib-Fakim*

## Abstract

The components of the extracellular matrix (ECM) are produced *in situ* by cells and are either completely secreted from the cell into the ECM or remain associated with the cell membrane. Amongst them are polysaccharides of the glycosaminoglycans (GAG) family, which are either free or covalently bound to proteins to make proteoglycans (PGs). These form a highly-hydrated compartment in which the proteins are embedded. At the molecular level, all ECM components are structured to execute their function and have been implicated in regulating intercellular communication. The sulfated GAGs interact with a wide range of proteins and their structure and tissue localisation is related to their function. Thus, certain GAGs may be particularly enriched in specific tissues, *e.g.*, dermatan sulfate in skin, but they are found in all tissues; and heparan sulfate (HS) has the widest range of interacting protein partners. These partners include both the permanent ECM residents and the transients, such as the fibroblast growth factors (FGFs), which transmit signals from one cell to another in paracrine signalling involved in tissue development, differentiation and homeostasis. The aims of this thesis are (1) to use a simple biomimetic model of ECM in the form of a GAG brush to determine if FGF binding leads to different supramolecular structures. (2) To determine if these supramolecular arrangements allow FGF mobility as observed *in vivo*. The model GAG brush was assembled layer by layer by one-end grafting of biotinylated GAGs on a streptavidin monolayer, itself attached to a supported lipid bilayer. The structure of these brushes was probed using different recombinant human FGFs (FGF1, HaloFGF1, FGF2, HaloFGF2, FGF4, HaloFGF6, FGF9, FGF10, HaloFGF10, FGF17, FGF18 and HaloFGF20) with well characterised HS binding sites (HBSs) and where “Halo” refers to an N-terminal Halotag fused to the FGF for fluorescence labelling. Rigidification of soft and highly hydrated films was assessed by quartz crystal microbalance with dissipation monitoring (QCM-D), spectroscopic ellipsometry (SE) was used to quantify the biomolecules at the surface, and fluorescence recovery after photobleaching (FRAP) was employed to assess the lateral diffusion of the GAGs and the (Halo)FGFs. FGFs showed a preference in binding stoichiometry for specific disaccharide structures, and the ensuing interactions led to different supramolecular

organisations of the brush/FGF films. Upon binding to the brushes, FGFs possessing multiple HBSs ('multivalent' FGFs) with acidic borders delimiting their HBSs were able to immobilise the GAG chains; some of these FGFs, *e.g.* HaloFGF1, remained mobile, whereas others were trapped in the film, *e.g.* HaloFGF2. Monovalent FGFs, and multivalent FGFs with no acidic borders around their HBSs, were found to not cross-link the brushes and remained mobile.

To test the idea that acidic borders on the protein surface play an important role in determining the ability of an FGF to cross-link HS chains and thus regulate mobility of the FGF in the matrix, the behaviour of fluorescently labelled Halo-FGFs were measured in the native pericellular matrix of fixed human keratinocytes. HaloFGF2 was immobile in HS brushes and in the pericellular matrix of HaCaT cells. This indicates that although the other components of the pericellular matrix may also play roles in determining the diffusion dynamics of FGF2, HS would be the main director of it.

Interactions between growth factors such as FGFs with components of the ECM are specific to their molecular features and can be precisely monitored in biomimetic models. These interactions trigger supramolecular structures that can be characterised by their stiffness. It is also possible to assess the mobility of these growth factors using a fluorescent label. Interestingly, the mobility of at least HaloFGF1, HaloFGF2 and HaloFGF10 in HS brushes was reproduced in pericellular matrix of HaCaT cells. A key difference is that the local supramolecular arrangement of the pericellular matrix components will be heavily influenced by the interactions of the HS chains with endogenous HS binding proteins. This will form a network of binding sites for FGFs, which at least in the case of HaloFGF2, did not prevent the immobilisation of the growth factor. However, in the case of other FGFs, e.g. HaloFGF6 and HaloFGF20 we detected reduced mobility. Thus, bridging the gap between the analyses on the HS brush model and on pericellular matrix may require the elaboration of a more complex *in vitro* model, incorporating other molecules into the HS brush, such as collagens and fibronectin, which have multiple HBSs and would be expected to present to the FGF already cross-linked HS chains and a reduced number of available binding sites.

# Content

# List of figures

# List of tables

## List of supplementary figures

## List of abbreviations

BSA: Bovine serum albumin

CS: Chondroitin sulfate

CS-A : Chondroitin sulfate A

CS-C : Chondroitin sulfate C

CS-D : Chondroitin sulfate D

CS-E: Chondroitin sulfate E

DMEM: Dulbecco's modified Eagle medium

DMSO: Dimethylsulfoxide

DOPC: 1, 2-Dioleoyl-sn-Glycero-3-phosphocholine

DOPE-CAP-B: 1, 2-Dioleoyl-*sn*-Glycero-3-phosphoethanolamine-cap-biotin

DTT: Dithiothreitol

dp: degree of polymerization

DS : Dermatan sulfate

ECM : Extracellular matrix

EXT: exotosin

EXTL: exotosin-like

FCS: foetal calf serum

FGF: Fibroblast growth factor

FGFR: fibroblast growth factor receptor

FRAP: Fluorescence recovery after photobleaching

GAGs: glycosaminoglycans

Gal: Galactose

GalNAc: N-acetylgalactosamine

GlcA: Glucuronic acid

GlcNAc: N-acetyl glucosamine

GlcNS: N-sulfated glucosamine

HA: Hyaluronic acid

HaloTag: haloalkane dehalogenase tag

Halo-FGF: FGF fused to an N-terminal HaloTag

HB: HEPES buffer: 150 mM NaCl, 10 mM HEPES, pH 7.4

HBS: Heparin binding site

Hep: Heparin

HS: Heparan sulfate

HSPG: Heparan sulfate proteoglycans

IdoA: Iduronic acid

IPTG: isopropyl β-D-1-thiogalactopyranoside

LB: Lysogeny broth

MMPs: matrix metalloproteases

NDST: N-deacetylase/N-sulfotransferase

OD600: optical density at 600 nm

ON: overnight

OST: O-sulfotransferase

PAGE: polyacrylamide gel electrophoresis

PBS: phosphate-buffered saline

PDB: Protein data bank

PFA: paraformaldehyde

PGs: Proteoglycans

QCM-D: Quartz crystal microbalance with dissipation

ROI: region of interest

RT: room temperature

SAv: Streptavidin

SDS: Sodium dodecylsulfate

SE: Spectroscopic ellipsometry

SLB: Supported lipid bilayer

SUV: Small unilamellar vesicles

SPDBV: Swiss PDB viewer

TEMED: N, N, N', N'-Tetramethylethylenediamine

Tris: Tris (hydroxymethyl) methylamine

TPA: Time-resolved profile analysis

UDP: Uracil diphosphate

Xyl: Xylose

# 1 Introduction

## 1.1 Cell communication in multicellular organisms.

In multicellular organisms, intercellular communication processes are the foundation of their growth and expansion, development, function, integrity and regeneration. Intercellular communication happens via various modes, the cell can target itself, a process that is call “autocrine” signalling or a neighbouring cell by direct molecular contacts (juxtacrine signalling) or cytoplasm contacts through gap junctions (1). Paracrine signalling is the local communication between cells without a direct molecular physical contact. Chemokines, cytokines, growth factors and many morphogens are paracrine signalling agents. They are secreted into the pericellular matrix of the source cell, and travel throughout the interstitial matrix towards the target cells. On the target cell, the paracrine effector binds to a receptor that triggers downstream signalling within the cell (2). This is the case of fibroblast growth factors (FGFs) signalling via tyrosine kinase receptors (3) and transforming growth factors family members such as the bone morphogenetic proteins that bind to the bone morphogenetic protein receptor type II in development processes (4). Intercellular communication can happen over longer distances, in which case the secreted effector travels through the endothelial barrier and is transported in the vascular blood flow throughout the body, but only acts on cells expressing the cognate receptor. This is the endocrine system and concerns hormones (Figure 1.1). The extracellular matrix (ECM) is the extracellular environment in contact with the cell; it is implicated in controlling cell fate decisions. During development, morphogen gradients are shaped by ECM components, whereas in homeostasis the ECM takes part in tissue regeneration and immunity by controlling the activity and transport of proteins regulating cell growth, migration and differentiation. Besides the components, the physical characteristics of the ECM are also relevant. It was shown that the elasticity of the ECM controls the differentiation of stem cells (5) and the polarisation of fibroblasts has been related to the stiffness of ECM (6). Stiffness and elasticity are both determined by the supramolecular structure of ECM, which in turn

depends on its molecular composition and the interactions of the component molecules.

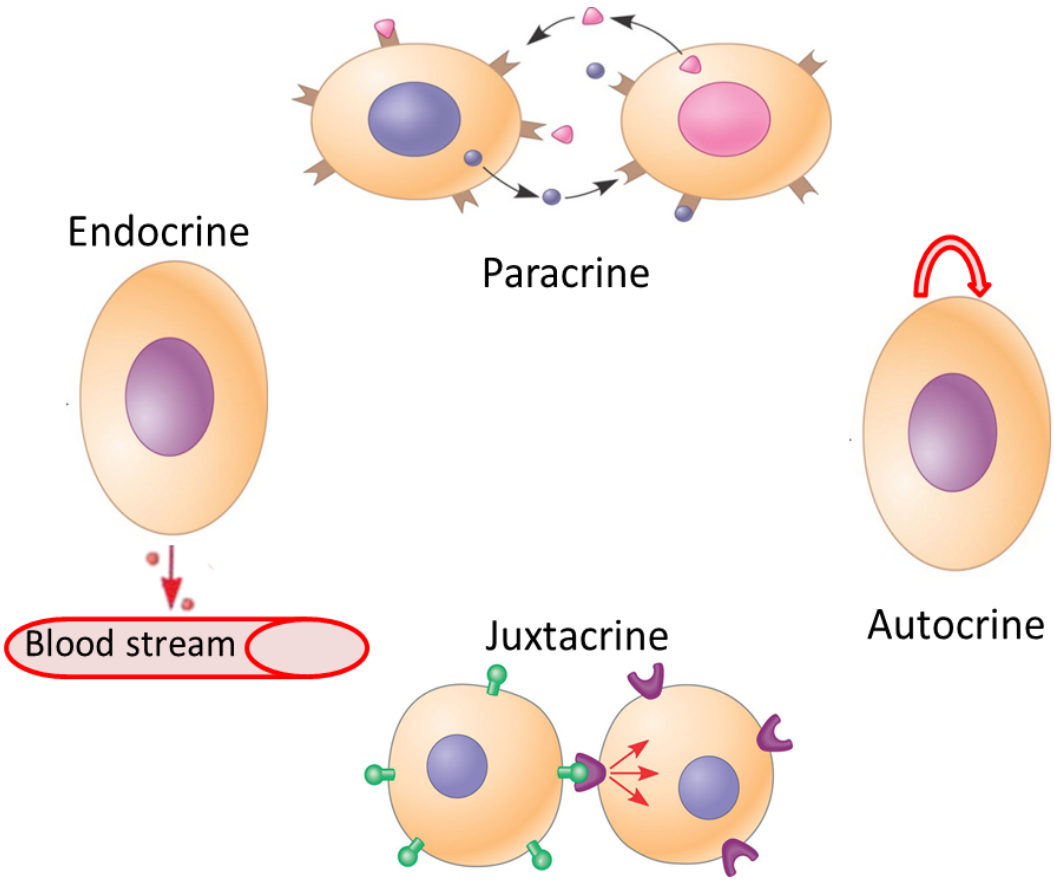


Figure 1.1: Forms of signalling in cellular communication.
Endocrine signalling corresponds to the intercellular communication that occurs via transport of the effector by the blood stream. Juxtacrine communication involves contact between the signalling and the targeted cell as described in the figure. Autocrine signalling depicts the signalling of a cell on itself and the paracrine signalling the one to a neighbouring cell. In paracrine and autocrine signalling, the effector molecule is transported in the immediate microenvironment of the cells that is the extracellular matrix.

## 1.2 Extracellular matrix

The ECM has distinct domains, the pericellular matrix is immediately adjacent to the cell surface, extending 1-5 µm in some tissues (7). Further away in mesenchymal tissues is the interstitial matrix. In epithelial tissues and the vasculature, a specialised ECM is found beyond the pericellular matrix, the basement membrane, so called due to its molecular density causing it to be heavily stained in a number of classic histological preparations. Basement membrane separates these compartments from

the underlying mesenchyme (8) (Figure 1.2). At the molecular level, all ECM have reasonably well-studied components and these are mainly fibrous proteins such as collagens, and the polysaccharides of the glycosaminoglycan (GAGs) family.

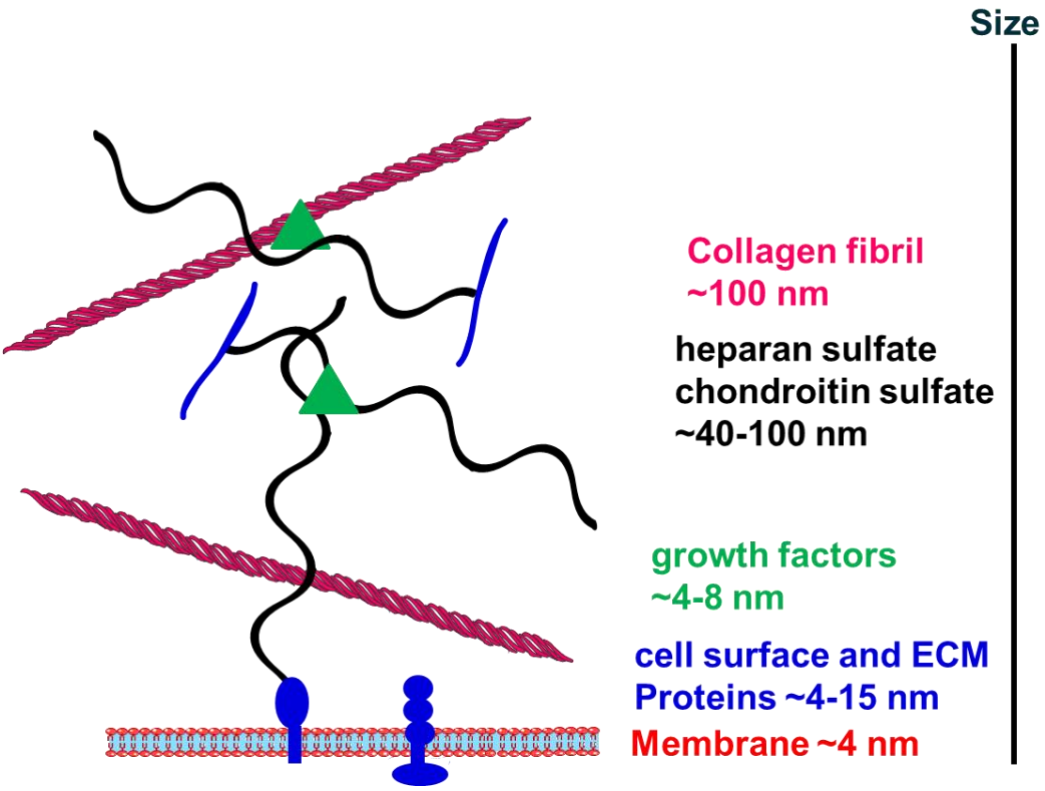


Figure 1.2: Schematic representation of the extracellular matrix proteoglycan organisation. Here schematized are the ECM with collagen fibrils and GAGs. HSPGs core proteins (blue) carrying HS chains (black) are sitting in the ECM or anchored in the cell membrane, with bound growth factor (green).

Collagens are the scaffold of extracellular matrices. They are tissue specific, organised in fibrils and provide resistance to shear and pressure (9). Type I and type III collagens sit in the interstitial matrices of soft tissues, *e.g.,* the dermis (10). In bones, collagen I fibrils can represent up to 90% of matrix protein components (11). Collagen type IV is the fibrous components of the basement membranes and is connected to the interstitial matrix via collagen VI, thus the fibrous scaffolds of basement membrane and the interstitial matrix form interconnected networks (12). Along with collagen type IV, fibronectins, laminins, nidogen and perlecan are the main constituents of the basement membrane. Laminins are connected to collagen IV and perlecans by nidogens (13). The ECM is a complex network where the main

components, HSPGs, collagens, polysaccharides and proteins are diverse and interconnected. However it is not a static environment but rather dynamic, constantly remodelled by matrix metalloproteases (MMPs) endoglycosidases such as heparanases, sulfatases and sialyltransferases (14). The first human MMPs were discovered as having a collagenolytic activity (15, 16), though this large family of proteases is now recognised to have many distinct substrates. Their activity is required in development (17), cell differentiation (18) and migration (19), homeostasis (20) and wound healing (21, 22). HS chains of perlecan in ECM of *in vitro* cultured endothelial cells (23) were shown to be storing FGF2 (24) and releasing it by the activity of MMPs such as collagenase and the endoglycosidase heparanase (25). Selective proteolysis of the ECM by these enzymes thus allows the release and activity of effectors that are stored by virtue of their binding to HS. This is one means of generating a gradient of the effector (26). Simple reversible binding of effectors to HS in the matrix will also result in a gradient, determined by the binding kinetics and the density of binding sites (27).

## 1.3 The glycosaminoglycans of the ECM

Of particular interest for this thesis are GAGs. GAGs in ECM are synthesized in the Golgi as post-translational modifications of core proteins, except for HA, which is synthesized in the cell membrane by hyaluronan synthases (28). GAGs are elongated as disaccharide repeats thus they are classified by those disaccharide repeats.

### 1.3.1 Heparan sulfate and heparin

Heparan sulfate (HS) and heparin are polysaccharides made of a modified repetitive disaccharide (50 to 100 repeats). Their biosynthesis is initiated on the serine of a SER-GLY sequence of the core protein in the Golgi (29). The initiating sequence of sugars for heparin and HS (and also for chondroitin sulfate (CS), see below) is a linker of 4 saccharides added to the serine residue, covalently built up by glycosyltransferases: [-4) GlcA β (1-3) Gal β (1-3) Gal β (1-4) Xyl β (1-$O_{SER}$] (GlcA: glucuronic acid; Gal: galactose; Xyl: xylose) (30). The exotosin-like (EXTL) enzymes have a αGlcNAc transferase activity and they proceed as a cascade in which EXTL2 catalyses the first reaction, the transfer of αGlcNAc (31) to the non-reducing end of the linker. This

directs the subsequent synthesis of a HS/heparin chain. The polysaccharide is elongated by the alternative transfer of GlcA and GlcNAc, thus [-4) GlcA β (1-4) GlcNAc β (1-] $_n$ is added to the first GlcNAc (32, 33). The elongation is catalysed by an enzymatic complex of exotosin (EXT), EXT1 and EXT2, possessing GlcA and GlcNAc transferase activities, respectively (34). The polysaccharide is then modified by N-deacetylation/N-sulfation on some GlcNAc, which become GlcNS (N-sulfated glucosamine) by one of four N-deacetylase/N-sulfotransferase (NDST) enzymes (35-37). However, the first sulfation may only occur 8-10 saccharide units after the linker. Then, the D-glucuronyl C5-epimerase (38) modifies some GlcA-GlcNS to IdoA-GlcNS (iduronic acid), thus the HS backbone varies in GlcA-GlcNAc, GlcA-GlcNS and IdoA-GlcNS (Figure 1.3). Finally, the saccharide units may be successively O-sulfated in positions C2 of GlcA and IdoA (the latter is far more common), C6 and/or C3 of GlcNAc or GlcNS by O-sulfotransferases (OST): 2OST, 6OST and 3OST and in this strict order of action (Figure 1.3). This is the most commonly depicted pathway for HS/heparin biosynthesis and leads to the production of the most commonly observed disaccharide units: GlcA-GlcNAc, GlcA-GlcNS, IdoA-GlcNS, IdoA,2S-GlcNS, IdoA-GlcNS,6S and IdoA,2S-GlcNS,6S (39).

There is also a minor pathway in which the epimerase reaction happens at an earlier stage of the biosynthesis, it converts GlcA-GlcNAc to IdoA-GlcNAc. This minor pathway leads to less represented sulfation patterns such as IdoA,2S-GlcNAc and IdoA-GlcNAc,6S (40). These modifications and their hierarchical dependence result in an organised structure of the polymer: it is an alternative succession of N-acetylated (NA), N-acetylated/N-sulfated (NA/NS) domains, and sulfated domains (S). NA domains are a sequence of [-4) D-GlcA α (1-4) D-GlcNAc β (1-] residues, so unmodified polymer, delimited by a GlcNS residue. The limiting GlcNS residue is usually part of a NA/NS domain, where GlcNS and GlcA alternate. The definition of these is resistance to scission by K5 lyase, which requires four successive GlcNAc residues (41). Thus, NA/NS can contain up to three successive GlcNAc disaccharides. S domains contain contiguous GlcNS disaccharides, which are respectively [-4) D-GlcNS β (1-4) D-GlcA β (1-, -4) D-GlcNS α (1-4) L-IdoA α (1-] and [-4) D-GlcNS (+/- 6S) α (1-4) L-IdoA (2S) α (1-] (Figure 1.4) (41). Sulfation on the 3-O position of the GlcNAc or GlcNS residue may

occur in NA/NS and NS domains, but is relatively rare, compared to the other sulfations. A single chain of HS may contain varying numbers of these domains of different lengths. Heparin (Hep) follows the same synthesis pathway as HS, but is excised from the parent HS chains by the action of heparanase, an endo beta D-glucuronidase. Hep is of the order of 15 to 20 disaccharides in length, has longer tracts of GlcNS and so a higher proportion of IdoA (42) and sulfate groups, averaging 2.5 sulfate groups per disaccharides, whereas HS has less than 2 (43). Thus, HS and hep share a common disaccharide backbone (Figure 1.3), but differ in the level of sulfation (44).

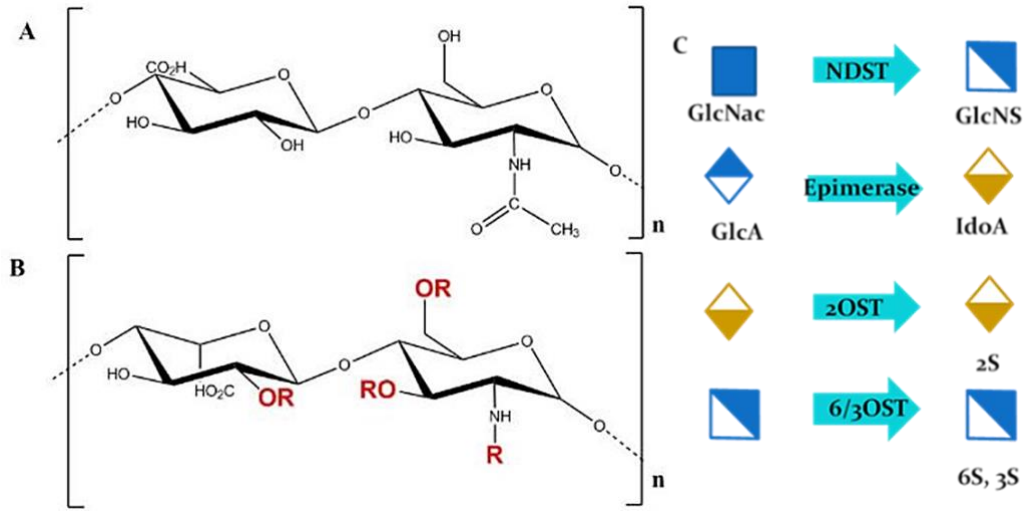


Figure 1.3: Heparan sulfate disaccharide repeat unit.
A: product of the initial polymerisation, [-4) D-GlcA β (1-4) D-GlcNAc β (1-]. B: possible final disaccharide with the C5 GlcA's epimer, L-IdoA. R is a possible sulfation position. C: The modifications of a disaccharide are hierarchical and ordered. Molecular structures drawn in ChemBioDraw.

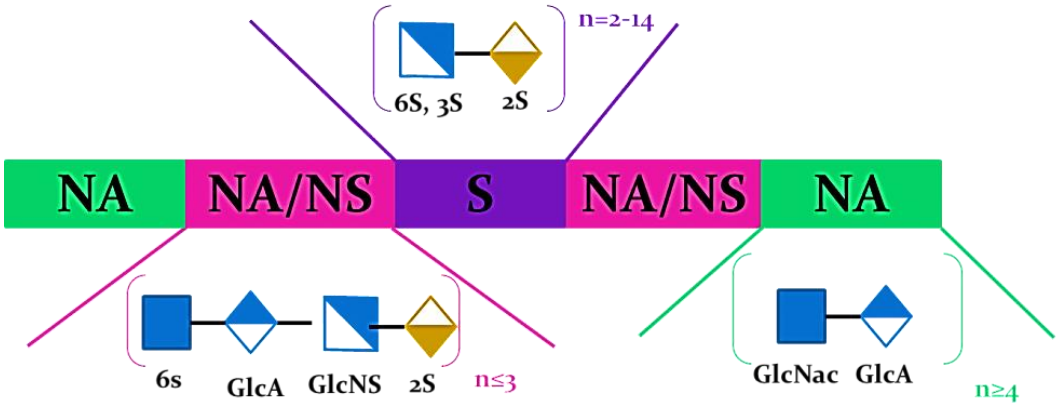


Figure 1.4: Model of alternating sulfation domains in HS proteoglycans.
Adapted from Murphy et al., 2004 (41).Proteins bind to sulfated motifs in S and NA/NS domains and many different patterns of sulfation are possible. Thus, HS/hep clearly has a large number of different potential binding sites for different protein partners including fibroblast growth factors (FGFs) (45).

### 1.3.2 Chondroitin sulfate and dermatan sulfate

Chondroitin sulfate (CS) chains are also elongated from core proteins and follow the same pathway as HS and Hep until the elongation step when the first GalNAc is added to the GlcA by GalNAc transferase I instead of a GlcNAc in the elongation of HS/heparin. The disaccharide repeat is then a [-4) GlcA β (1-3) GalNAc β (1-]$_n$ (see Figure 1.5), a repeat of glucuronic acid "β 1-3" linked to a galactosamine, respectively elongated by GlcA transferase II and GalNAc transferase II. The GlcA residues can be epimerised to IdoA to produce dermatan sulfate (DS, also called CS-B); with a single disaccharide repeat of IdoA and GalNAc: [-4) IdoA β (1-3) GalNAc β (1-] $_n$ in the chain sufficient for it to be called dermatan sulfate, though in general there are far more (46). O-sulfations occur on R positions of the GalNAc unit and of the GlcA/IdoA unit leading to different CS types: chondroitin-4-sulfate (CS-A), chondroitin-6-sulfate (CS-C), chondroitin-2,6-sulfate (CS-D) and chondroitin-4,6-sulfate (CS-E). In DS, the first sulfation occurs in position 4 of the GalNAc unit, it can also be further sulfated in position 6 of the GalNAc or position 2 of the IdoA.

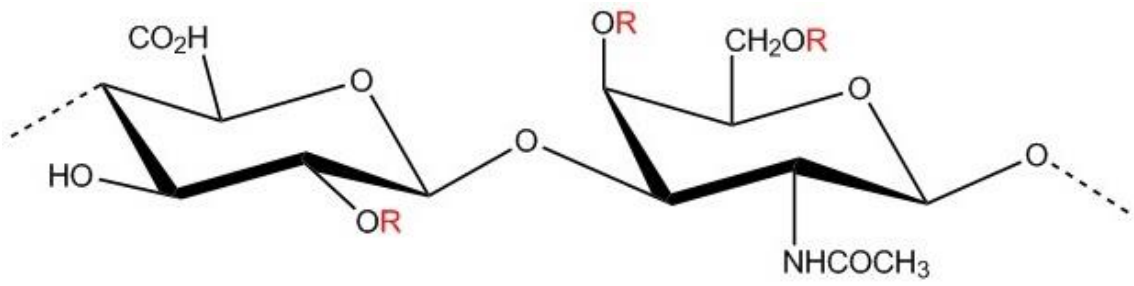


Figure 1.5: Chondroitin sulfate disaccharide repeat unit.
[-4) D-GlcA β (1-3) D-GalNAc β (1-]. R is a possible sulfation position. Molecular structures drawn in ChemBioDraw.

### 1.3.3 Molecular features, conformation and protein binding.

GAGs are linear elongated chains and offer a large range of structures for protein binding. Cataloguing the binding partners of hep and HS has identified, at least 480 proteins (47, 48), including the FGFs. The elucidation of the conformational structure of HS/hep oligosaccharides, which was done by NMR and computational calculations, showed that it involves multiple parameters. Intra- and inter-saccharide unit hydrogen bonds confer rigidity to the saccharide backbone. Sulfate groups in GlcNS units engage in hydrogen bounds with nearby C3 hydroxyl groups in IdoA2S and thus can maintain the conformation in one state. It also showed that inter- and intra-residue hydrogen bonds compete with each other, suggesting a locally dynamic structure rather than a fixed conformation (49-51). Weaker interactions, ionic interactions and dipole-dipole interactions between the residues and the solvent also play a role in the stabilisation of the GAG 3D structure (51). NMR studies have shown the in solution changes in conformational arrangements due to the hanging sulfate groups (52). The presence of cations in the vicinity of the chains modifies the conformation of the polysaccharide chain (53). The pyranose residues in the HS/hep and DS chains can adopt several conformations: boat or chair named after the shape formed by the sugar ring if the glycosidic bonds are in the same or opposite direction respectively. HS/hep and DS chains contain GlcA/IdoA residues that confer them higher flexibility because of its ability to adopt various stable ring conformations (54). In the $^{1}C_{4}$ and $^{2}S_{0}$ conformations, the C-2 and C-3 are in diaxial and diequatorial positions generating torsions/directional changes in the chain (Figure 1.6). The computational study suggested that in IdoA2S this equilibrium is displaced towards

the $^{2}S_{0}$ conformation by a ratio of 15:85 ($^{1}C_{4}$: $^{2}S_{0}$) and that it changes upon protein binding (51). (49-53, 55)

GAG chains were shown to stabilise FGFs in thermostability assays (56, 57) and for FGF1, but not FGF2 this was related to its ability to signal on cells (58). The molecular features required for a GAG chain to stabilise an FGF and the structural determinant that make an FGF sensitive to it are unknown.

The versatility of GAG chain with their multiple sulfation pattern combination possibilities and 3D conformational changes offers a variety of binding and thus stabilisation possibilities for proteins, including cytokines such as FGFs. Those lead to different requirements for FGF signalling even for FGFs from the same subfamily such as FGF1 and FGF2 (59).

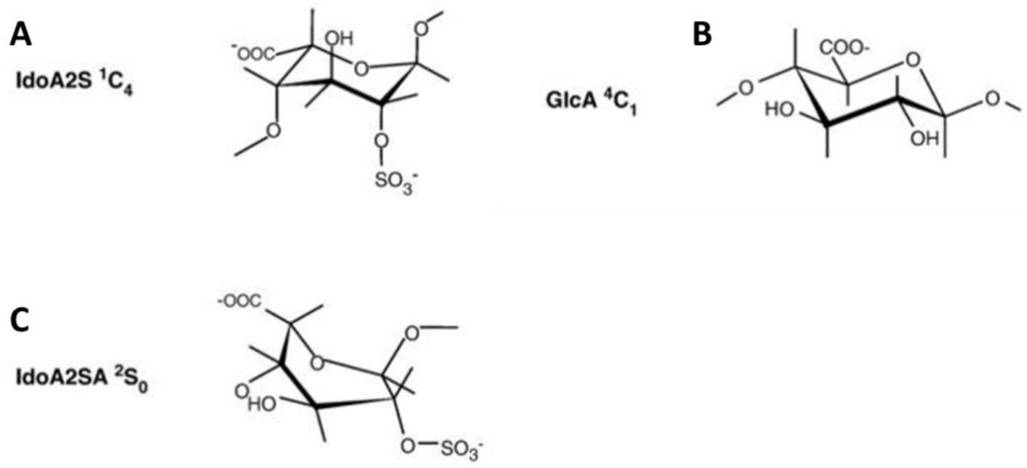


Figure 1.6: Conformational changes in saccharide rings.
Different conformation structure of L-IdoA2S and D-GlcA in GAG chains. The $^{1}C_{4}$ (A) conformation of L-IdoA2S presents the C-2 and C-3 diaxially oriented whereas the $^{4}C_{1}$ (B) in GlcA and $^{2}S_{0}$ (C) in IdoA present them diequatorially oriented and generate torsions in the chain. Adapted from Casu et al, 2010 (60).

## 1.4 Fibroblast growth factors: structures, functions and interactions with the ECM.

HSPGs have been shown to be involved in embryonic development in *Drosophila*. Mutants of genes encoding enzymes essential for HS biosynthesis (NDST and uracil-diphosphate-glucose, UDP-glucose dehydrogenase) have presented the same

characteristics as fibroblast growth factor receptor (*fgfr)* knock-out mutants (61). The UDP-glucose dehydrogenase mutation in mammals (mouse) prevented the complete mesodermal and endodermal migration during gastrulation, which stopped embryogenesis. Although the production of FGF was not altered, the transduction of its signal was not observed. Such experiments have contributed to the evidence that HS is indispensable for much of FGF signalling during embryogenesis (62). Further studies have suggested that HS is responsible for the formation of morphogen gradients, the movement of morphogens and, therefore, their activity (63). The mechanism under which HS operates to influence gradients, and to allow the transport of morphogens in the ECM is still debated. Free diffusion of morphogens in the extracellular matrix is limited by their interaction with their cognate receptor and extracellular matrix components (GAGs and fibrous proteins). Receptors have been found to control the formation of morphogen gradients by retaining them on the cell surface (64) and at times trigger their endocytosis for degradation (65). In Drosophila, HSPGs too have been shown to retain morphogens, thus enabling the formation of a reservoir of gradient formation (66). Although the role of HSPGs in the formation of gradients is relatively well documented in some vertebrates (67), there is a lack of information about the mechanisms under which they operate. In 2012, Duchesne *et al.* tracked the movements of FGF2 in the ECM of fibroblasts using gold nanoparticles (68). The study suggests that the diffusive movement of FGF2 in fibroblast pericellular matrix depends on the long-range order of FGF2 binding sites in the HS. The observed heterogeneous spatial organisation of these HS binding sites determined whether the motion of FGF2 was locally confined or was diffusive (in some instances clearly directional) over long distances, corresponding to the length of many extended HS chains (69).

### 1.4.1 Historical discovery

The members of the FGF family have a wide range of expression and localisation in the organism, from the pre-implantation embryo to adult tissues and they have very diverse activities in development, homeostasis and disease (70).

The first fibroblast growth factor (FGF) was discovered in 1973 as a pituitary and brain agent enhancing fibroblast proliferation (5, 6, 71). This was subsequently termed basic FGF (bFGF), as in 1975, Gospodarowicz et al. discovered the acidic FGF (aFGF), which also showed a cell proliferation enhancing activity in myoblasts (72). aFGF and bFGF were so called because of their isoelectric points, which are, respectively, acidic and basic. Today 22 genes encoding FGFs have been identified in humans named from *fgf1* (aFGF), *fgf2* (bFGF) to *fgf23*, but *fgf15* is "missing" since it has not been identified in the human genome, but is present in mice. However, human *fgf*19, which is not found in mice, has been suggested to be a homologous form of the murine *fgf*15 (73, 74).

The FGF family comprises cell signalling molecules implicated in diverse cellular processes such as cell differentiation in embryonic development. They can induce cell proliferation, but also delay cell differentiation as observed by Gospodarowicz *et al.* in 1975. The discovery of other FGF subfamily members is summarised below.

- FGF3 was discovered as the proto-oncogene *int-2* and then related to the FGF family because of its sequence homology to FGF1 and FGF2 (75) and to FGF4, FGF5 and FGF6 (45).
- FGF4 was first studied as an oncogene, but the analysis of its gene and protein coding sequence showed that it was closely related to FGFs 1 to 6; therefore it was included in the FGF family (76).
- FGF5 and FGF6 were discovered as oncogenes as well. FGF5 was found to be involved in embryogenesis (77, 78). FGF6 was identified as the product of the hst-2 gene and related to the FGF family for its similarities with hst-1 gene, FGF4 (69, 79).
- FGF7 was initially called keratinocyte growth factor (KGF), as a consequence of its apparent specificity for keratinocytes (80, 81).
- FGF8 was isolated as an FGF-like and androgen-induced growth factor in mouse. It was shown that it is actually a distinct FGF protein, now called FGF8 (82).
- FGF9 was identified as a glia activating factor (83).

- The cDNA of FGF10 was isolated from rat embryos and identified by homology as a new FGF protein, initially called KGF2, as it is most closely related to FGF7 (KGF) (84).
- Four proteins, homologous to FGFs and referred to as FGF homologous factors (FHF), are mainly expressed in nervous systems and have been named FGF11 to FGF14 (85). They are intracellular and do not bind FGF receptors or HS.
- FGF16 to FGF21 (except FGF19) have all been identified by using homology based polymerase chain reaction cloning strategies (86-90).
- FGF19 was identified as a homologue of mouse FGF15 (91).
- FGF22 was isolated from human placenta and identified as an FGF family member mainly expressed in hair follicles (92).
- FGF23 was first identified in 2000 (93), and further characterised as a hormone which regulates the metabolism of phosphate and vitamin D (94).

There are many similarities in amino acid sequence, protein structure and gene organisation between the FGFs. Indeed, these have served as a basis for the identification of many members of the FGF family. Figure 1.7 shows a phylogenetic tree of the mammalian FGF family and its subfamilies based on the alignment of their protein sequences. Some invertebrate FGFs are related to the vertebrate ones, but there are also other FGFs in invertebrates, which have been apparently lost in the vertebrate lineage in the course of evolution (74).

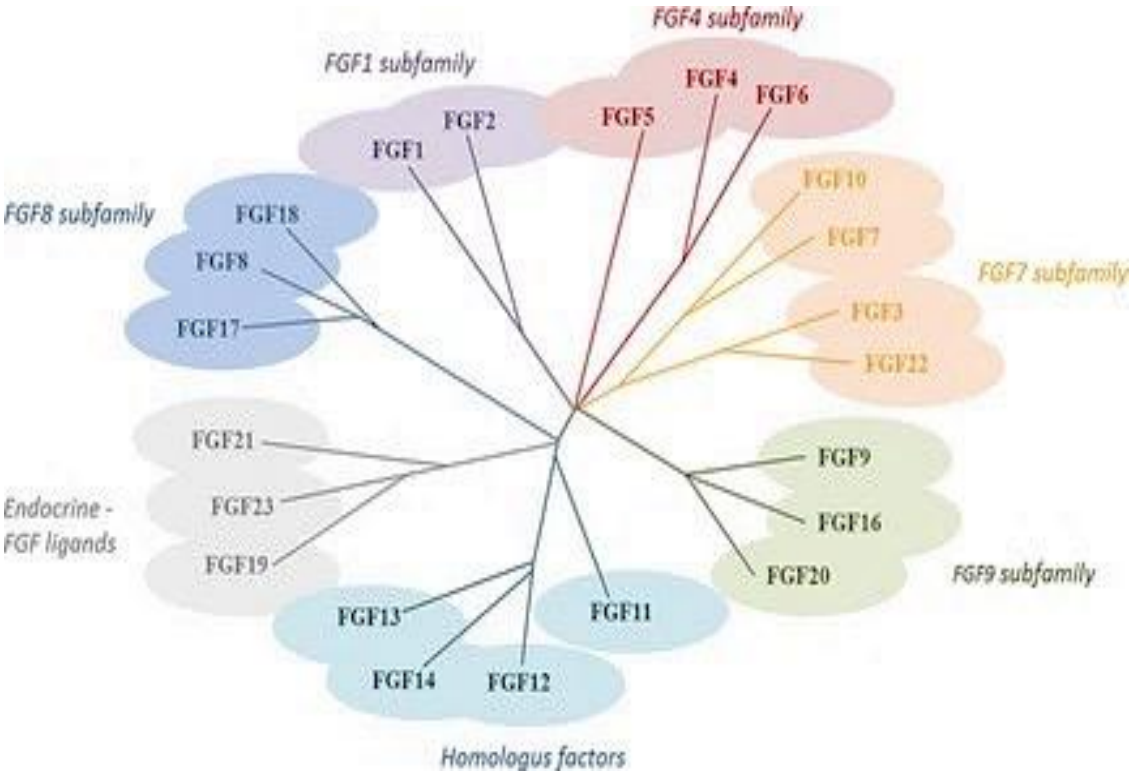


Figure 1.7: Radial phylogram of the FGF family.
Phylogenic tree based on protein sequence alignment extracted from Laestander and Engstorm (95).

### 1.4.2 Structure-function relationship in FGFs and consequences for HS binding.

In vertebrates, FGF proteins are between 17 and 34 kDa in size and share a conserved sequence containing 28 identical amino acids and 6 conserved residues (77). Crystallisation of FGF2 has shown that the protein folds in a succession of four stranded antiparallel β sheets to form a "β-trefoil" (Figure 1.8) (78, 96, 97). This core structure is present in all the other FGF proteins, with variations occurring in the length of loops and the N- and C-termini (Figure 1.8). Hep binding sites (HBS) are present on the surface of FGFs with growth factor/morphogen activity and they contain arginine and lysine residues. There is a canonical HBS required for receptor signalling, HBS1 (55, 98), and several secondary HBSs may also be present. This core structure may also contain the FGF receptor binding site as identified in FGF4 (99). The secondary HBSs in FGF1 and FGF2 were suggested in early studies (100-102) and recently confirmed in FGF2 by specific identification using selective labelling and mass spectrometry (103). The locations of HBS1, HBS2 and HBS3 on the surface of

FGF2 are shown in Figure 1.9 along with identified binding lysines. Lysines residues in FGFs that are engaged in binding with HS have been catalogued and characterised using the protect/label technique (56, 103, 104).

FGFs have preferences for sulfation patterns, and thus potentially specific localisations of the HS chains in tissues; the sulfation patterns and so the 'decision' as to whether a cell's HS can bind a particular FGF are made in the Golgi during HS biosynthesis (105). Thus 2-O and 6-O sulfation are the most common in NS domains (106) and it was shown that FGF2, but not FGF1 and FGF4 presented an increased affinity for an HS with low 6-O sulfation but high 2-O sulfation compared to standard HS(59). It suggested that the binding of FGF to hep showed that FGF1, FGF2 and FGF4 had different and specific requirements to enable their function (59). The presence of N- and 2-O sulfation was enough for FGF1 to bind HS and enable signalling (59), however the 6-O sulfation was shown to consequently increase the affinity of FGF1 for HS/hep(107) and thus its function. However, FGF4 responded to the sole presence of the 2-O or 6-O sulfation in heparin, both separately could bind FGF4 and enable signalling in cells. It is therefore suggested that the biological function of each FGF may reside in its ability to bind and be stabilised by well-defined structures in heparin/HS and that the discrimination is driven by the HBSs on the FGFs which also present variabilities. FGFs bind a range of different sulfation patterns in HS/hep but do present preferences of which some have been catalogued and reported (56).

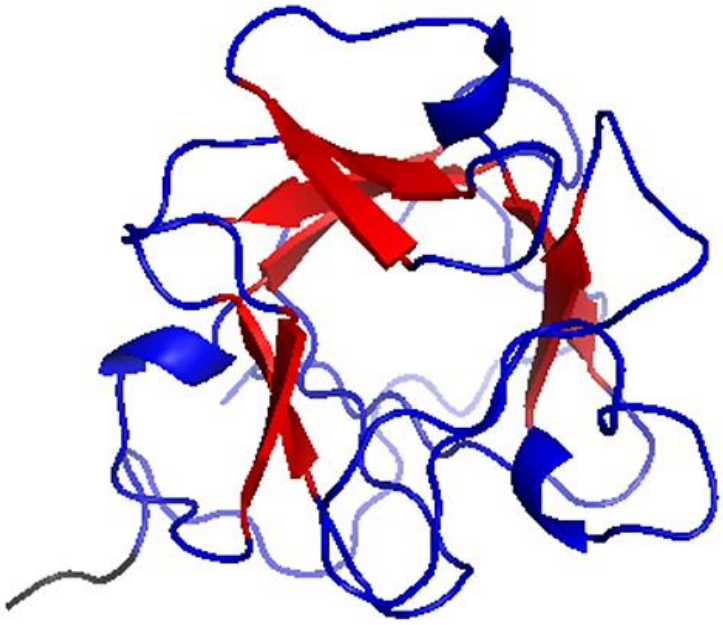

Figure 1.8: β-trefoil structure of FGFs.
The X-ray structure of FGF2 (P09038) amino acids 1-155. "β-trefoil" structure drawn in PyMol®: in red and the N-terminal in grey. PDB accession number: 1BLA.

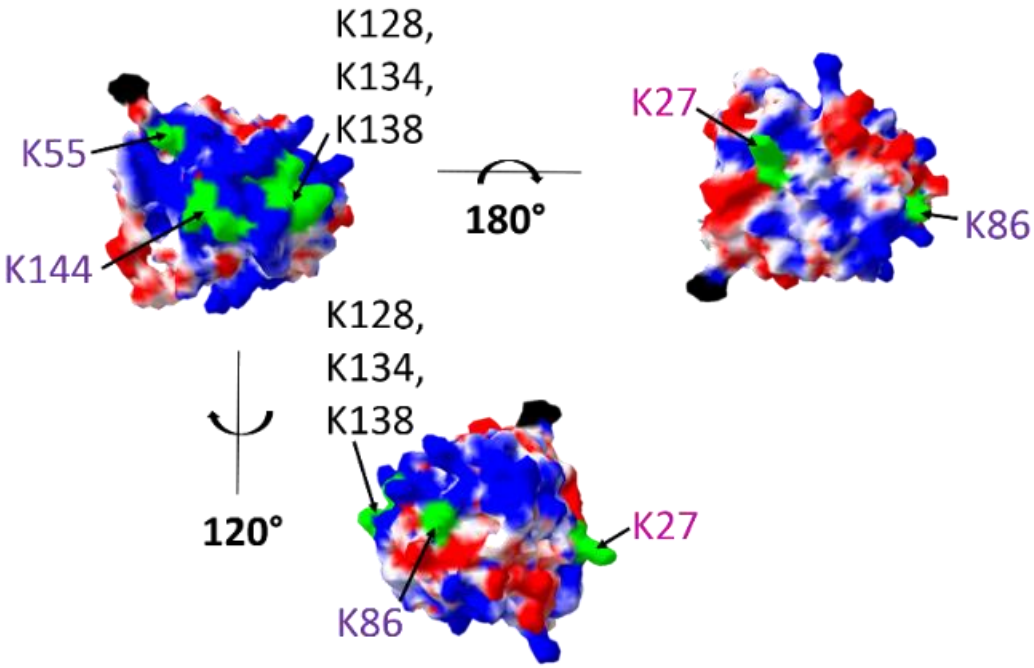


Figure 1.9: Surface electrostatic potential mapping and position of heparin binding lysines in FGF2.
Identified hep binding lysines in HBS1, HBS2 and HBS3 in FGF2 (1BLA) are labelled in green (103). The electrostatic mapping of partial charges [-1.8 (red), 0 (white) and +1.8 (blue)] was generated using the Poisson-Boltzmann algorithm in Swiss PDB viewer (SPDBV). The N-terminal residue is labelled in black.

However additional specificity is suggested at the level of the formation of a signalling complex of FGF with HS and FGF receptors (FGFRs). The organisation of the ternary complex by which the function of FGFs are transduced is still debated. Whilst multiple studies support a symmetric model of interaction between two HS chains, two FGFs and two FGFRs (98, 108), others have depicted the possible establishment of an asymmetric complex of a single HS chain engaging with 2 FGFs and two FGFRs (100). Deciphering the molecular features involved in the interactions of these three may bring an understanding of the actual structure of the complex. Evidence shows that additionally to the N- and 2-O sulfation necessary for FGF2 binding (109), 6-O sulfation was required for the signal transduction of FGF2, which is due to this sulfate engaging the FGFR in the ternary signalling complex (107, 110, 111). More recently, the presence of an NS domain at the reducing end of the HS chains, or within the HS chains, has been suggested to be preferred for FGF2 signalling via the FGF receptor (FGFR) 1c over other sulfation patterns (112, 113). This suggests that the binding preferences of FGFs for HS might also take in account their interaction with FGFRs in the ternary complex. Known and identified HBSs in FGFs were previously reported along with their binding preference for HS sulfation patterns and oligosaccharide sizes (Figure 1.10) (56, 103, 104). Together they suggest that there is a gap in our understanding of the relationship between the molecular details and the biological function of FGFs. One reason for this gap is that *in vivo* FGFs bind HS chains which may engage multiple HBS on a FGF and multiple partners in the ECM. In contrast, molecular studies use small and well-defined fragments of GAGs, and thus neglect the complexity of the multi-partner presentation in the ECM.

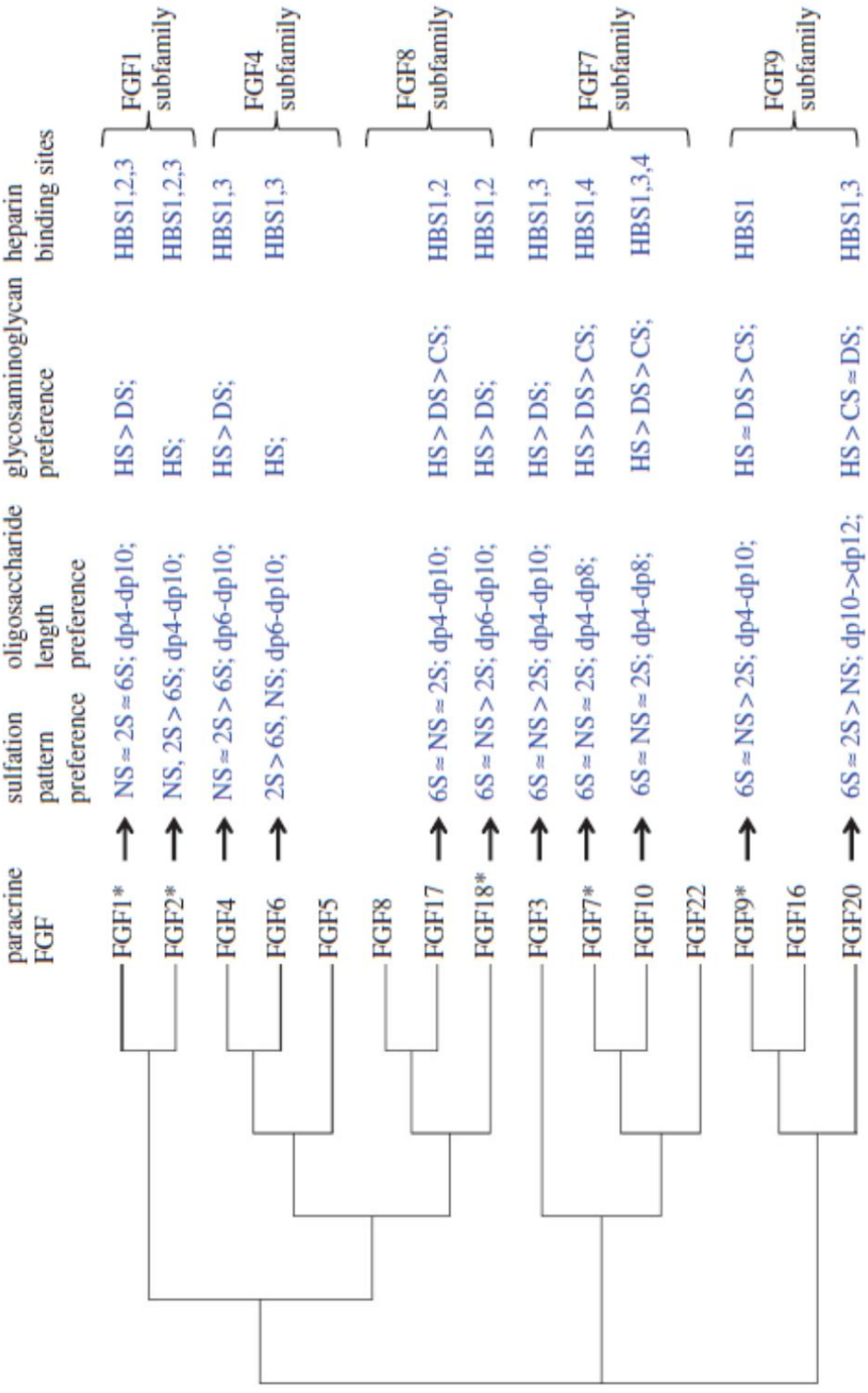


Figure 1.10: HBSs, sulfation pattern and oligosaccharide size preferences in FGF.
Asterisks represent data from (103, 104, 114), dp is “degree of polymerisation”. The FGF evolutionary tree is annotated with their sulfation pattern, oligosaccharide length and GAG preferences along with identified HBSs in the literature. NS: N-sulfated. 2S: 2-O sulfated. 6S: 6-O sulfated. HS: heparan sulfate. DS: dermatan sulfate. CS: chondroitin sulfate. Data summarized from (56, 103, 114, 115).

## 1.5 FGF and polysaccharide interactions.

FGFs are globular proteins, and engage with the solvent through weak atomic bonds in the same way as the polysaccharide chains. The weak interactions identified as contributors to FGF interaction with HS/hep have been mapped for FGF1 by computation (116). Hydrogen bonds occur when a hydrogen covalently bound to an electronegative element (C, N, O, F) is located in the vicinity of another electronegative element. (117) The two polar groups are electrostatically attracted to one another creating bonds. In polysaccharides, this can involve any hydroxyl and sulfated group. In proteins, it involves the polar aminoacid residues at the protein surface: asparagine, cysteine, glutamine, histidine, serine, threonine, tryptophan and tyrosine. (117, 118) Ionic interactions also play their part in FGF-GAG binding, and this feature is used in our methods (see Chapter 4.1) to purify FGFs by hep affinity. The ionic interactions are stronger than hydrogen bonds and involve charged aminoacids: arginine, lysine, aspartate, and glutamate. The strength of a hydrogen bond ranges between 0.2 to 7.4 $kcal.mol^{-1}$ for polar groups available in proteins (102, 117, 118), for reference that is 10 to 100 fold weaker than a covalent bond (119). FGFs and GAGs have relatively well defined and characterised molecular features, and as described here, their interactions are subject to multiple factors including internal dynamic structural organisations: secondary and ternary structure of globular proteins and intra-residue/chain interactions in GAGs. They are also influenced by their interaction with solvated components such as ions and environmental conditions. Heparin and FGF co-crystals have been studied to elucidate which sub-molecular features were involved in the interactions. Using FGF2 and heparin tetra- and hexasaccharides, the study showed the presence of both ionic and hydrogen bonds between sulfate and hydroxyl groups in the heparin oligosaccharides and the lysines, arginines, asparagine and glutamine residues in the protein (55).

## 1.6 Other methods for studying FGF and GAG interactions.

### 1.6.1 Quartz crystal microbalance with dissipation monitoring (QCM-D).

Quartz crystal microbalance with dissipation monitoring (QCM-D) allows real-time measurement of the changes in resonance frequency and dissipation of a quartz crystal sensor upon adsorption of material on the surface. This acoustic technique provides information on binding kinetics and rigidity of the adsorbed films. Viscoelastic modelling of the extracted data can give quantitative information on the thickness and viscoelastic properties of the adsorbed materials.

QCM-D originated from a method that first described the use of an ultrasonic wave to evaluate the viscoelastic properties of liquids. Mason used an oscillating piezoelectric crystal to apply a rapid shear motion to liquid and measured its response. The liquid presented a viscous effect, change in resonant frequency and a shear elastic effect as an increased resistance at resonance (126). The method was further explored and applied to polymer solutions (127) and developed to allow the simultaneous monitoring of the dissipation factor and the resonance frequency of the crystal : the "ring-down" method (128). Amongst others, Rodahl *et al.* successfully applied this method to adsorbed proteins, lipid, and cells (129).

#### Theoretical principle

QCM-D uses a piezoelectric quartz crystal placed between two gold electrodes (**Error! Reference source not found.**). When an alternating current is applied to the crystal, it oscillates (**Error! Reference source not found.**) and generates a standing shear wave at a frequency, $f_i$ (**Error! Reference source not found.**) close to the resonance frequency, $f_1$ (4.95 MHz for AT-cut quartz crystals from Biolin Scientific) or its odd overtones ($i$ = 3, 5, 7, 9, 11, 13, corresponding to resonance frequencies of $f_i \approx$ 15, 25, 35 … 65 MHz). When the alternating external current is turned off, the oscillation decays exponentially. From the decay curve, the resonance frequency ($f$) and the energy dissipation ($D$) can be extracted.

The resonance frequency, $f_i$ is related to the mass at the surface and the frequency change upon mass adsorption can be directly related to the absorbed areal mass density for rigid films, as the Sauerbrey equation states:

$$\Delta \boldsymbol{m} = - \boldsymbol{C} * \Delta \boldsymbol{f}/\boldsymbol{i} \qquad \text{Equation 1}$$

where the Sauerbrey constant, $C$, is 18 ng $Hz^{-1}$ $cm^{-2}$ for a crystal with a resonance frequency $f_1$ of 5 MHz. Rigidity or softness of the film can be measured by the dissipation of energy into the film, we are able to measure $D$:

$$\boldsymbol{D} = \boldsymbol{E_{lost}} / 2\,\boldsymbol{\pi}\, \boldsymbol{E_{stored}} \qquad \text{Equation 2}$$

Where $E_{lost}$ is the energy lost (dissipated) during one oscillation cycle and $E_{stored}$ is the total energy stored in the oscillator. $D$ is dependent of the ability of the surface to store/ dissipate energy and thus varies with the composition of the medium at the surface (Figure 1.11**Error! Reference source not found.**).

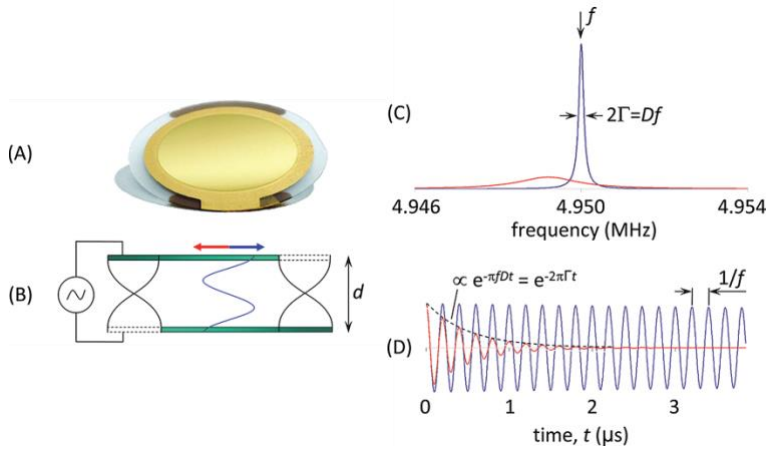


Figure 1.11: The working principle of QCM-D.
(A) Picture of a 4.95 MHz AT-cut quartz crystal sandwiched between 2 gold electrodes from Biolin Scientific. (B) Illustration of the opposite movement of the top and bottom parts of the crystal upon application of an alternating current. The fundamental frequency (black) and its 3rd overtone (blue) are represented. (C) Resonances, characterised by their frequency, *f* and their bandwidth, Γ, are observed for a crystal in air (blue) and liquid (red). The dissipation factor, D can be extracted from the equation: D= 2 Γ/*f*. (D) The "ring-down" method allows to record the frequency decay curve and extract the resonance frequency, *f*, and the dissipation, D. The blue curve represent the oscillation of the crystal in air and the red curve the dissipation of 1.6 * $10^{-1}$. Extracted from Reviakine et al., 2011 (130).

$\Delta f$, the change in frequency, and $\Delta D$, the change in dissipation, are related to the physical properties of the film at the surface (density, mass bound to the surface, ridigity). QCM-D measurements were performed with a Q-Sense E4 system (Q-Sense

AB, Västra Frölunda, Sweden). $\Delta f$ and $\Delta D$ were measured at 7 overtones. We chose to represent $\Delta f$ as $\Delta f_i$/i and the $\Delta D$ for the third overtone ($i$ = 3). Solutions were infused in passivated (see below) chambers using a syringe pump at 20 µL/min or as stated otherwise. The temperature was set and controlled at 23°C.

### 1.6.2 Spectroscopic ellipsometry.

Ellipsometry is an optical technique that is used to measure changes at interfaces. It can be applied to quantify the refractive index and the thickness of nanofilms made of biomolecules, but also the surface density of adsorbed molecules (132). We have applied SE to characterise our ECM models and probe the binding propensity of FGFs to the GAG brushes.

SE measures the changes in polarisation of light at a range of wavelengths upon reflection on a planar surface. In particular, it measures the changes in Δ and Ψ, ellipsometric angles which characterise the polarised light. The presence of films on the surface directs the changes in Δ and Ψ. Thus, from the changes in Δ and Ψ, the parameters of the film can be extracted: the refractive index and the thickness. By fitting the collected data to models, we quantified the areal molar density of biomolecules: proteins and GAGs.

#### Principle of spectroscopic ellipsometry.

Spectroscopic ellipsometry (SE) uses polarized light, light as an electromagnetic wave is propagated in a 3 dimensional vector field: $\vec{E}$, the amplitude of the electric field strength, $B$, the amplitude of the magnetic field and the directional vector of propagation, $z$. According to James Clerk Maxwell, $E$ and $B$ are perpendicular to each other and to $z$. The wave is characterised by its electric field, $E$ which is the superposition of two components, $E_x$ and $E_y$, orthogonal to z as presented in Figure 1.12.

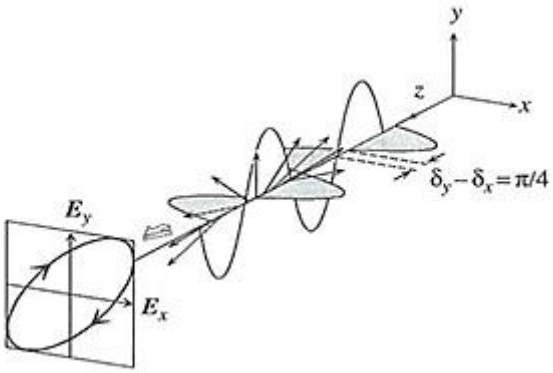


Figure 1.12: Polarization of light as an electromagnetic wave.
The electric wave E, is decomposed in its two orthogonal components $E_x$ and $E_y$. The superposition of $E_x$ and $E_y$ forms an elliptical pattern in the x-y plan (as illustrated in the figure) as the phase shift, $\delta_y - \delta_x$ is π/4. Extracted from (133).

*E*, the electric field wave is described by an amplitude and frequency by (133):

$$\boldsymbol{E = E_0 \cos(qz - \omega t + \delta}$$ Equation 3

Where $E_0$ is the amplitude of E, q = 2π/λ is the wave number, ω is the angular frequency, t is time and δ is the phase constant. The equation 3 can be decomposed into two as the superposition of $E_x$ and $E_y$, as follows (133):

$$\boldsymbol{E_x = E_{01} \cos(qz - \omega t + \delta x)}$$ Equation 4

$$\boldsymbol{E_y = E_{02} \cos(qz - \omega t + \delta_y)}$$ Equation 5

Where $E_{01}$ and $E_{02}$ are the amplitudes of the components $E_x$ and $E_y$, and $\delta_x$ and $\delta_y$ their phase constants. The phase shift between $E_x$ and $E_y$ determines the type of polarization, in linearly polarized light, $E_x$ and $E_y$ are in phase, $\delta_x - \delta_y$ is null. Circularly polarized light is characterised by a phase shift equal 90° (133). In elliptically polarized light, $\delta_x - \delta_y$ is between 0° and 90° and the vector *E* describes an ellipse when observed along *z*.

When linearly polarized light is reflected on a homogenous bulk substrate or biofilm as described in Figure 1.13, the reflected light becomes elliptically polarized.

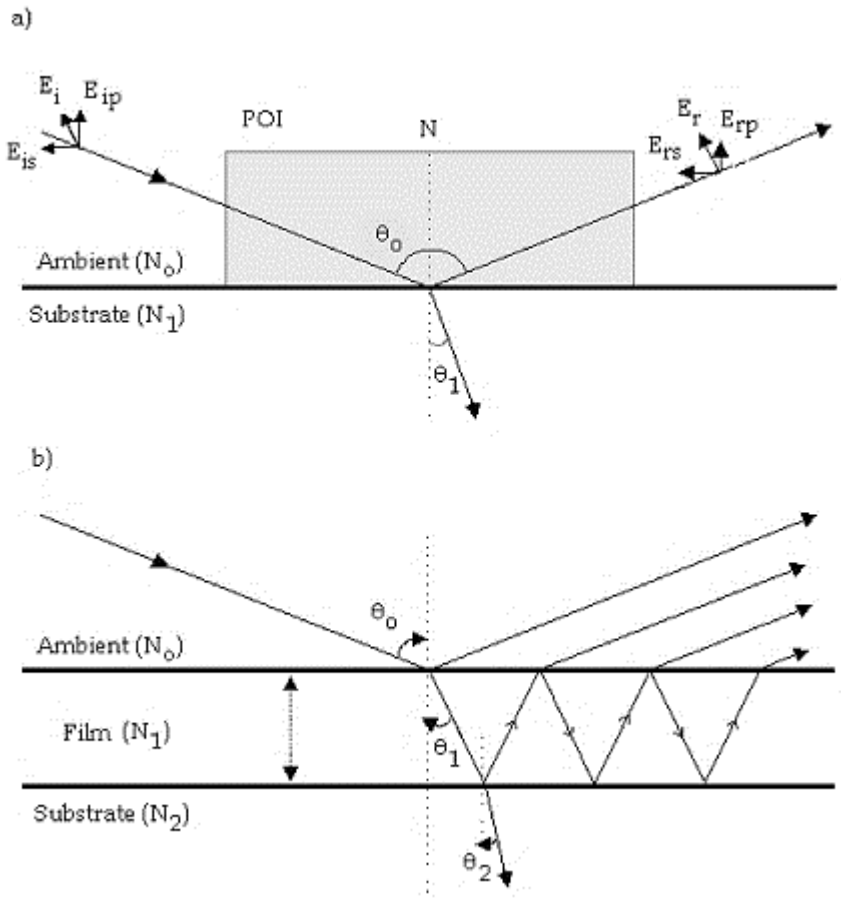


Figure 1.13: Reflection of polarized light.
The reflection of a linearly polarized light on a bare (a) or film-covered (b) surface. (a) When the incident beam, $E_i$ (a superposition of its components $E_{ip}$ and $E_{is}$, respectively parallel and perpendicular to the plane of incidence) reaches the plane of incidence (POI) with an angle of incidence 1- $\theta_0$, it is partially transmitted and reflected as $E_r$ (a superposition of its components $E_{rp}$ and $E_{rs}$). Upon reflection there is a change in phase shift and amplitude of the components of the light wave. The changes in polarization of the light are dependent of the surface composition and optical properties and can be measured by ellipsometry. (b) The effect of a thin film on the reflection of a polarized light beam. Extracted from (133)

The detected change in polarisation is represented by the complex reflectance ratio, ρ (104, 133, 134).

$$\boldsymbol{\rho = \tan(\psi)\exp(i\Delta) = -r_p/r_s} \qquad \text{Equation 6}$$

Where Δ is the phase shift $\delta_{rp} - \delta_{rs}$ and ψ the amplitude difference between $E_{rp} - E_{rs}$. The ratio "$r_p/r_s$" is the ratio of Fresnel amplitudes and is directly related to the angle of incidence and the wavelength of the light, the thickness of the biofilm and the refractive indexes of the substrate, the solvent and the biofilm (133-135).

Therefore, the measured Δ and Ψ are directly related to the refractive index and the thickness of the film. In the present study, Δ and Ψ were measured over a range of wavelengths from 380 to 1000 nm with an angle of incidence of 70 degrees. In 1978, De Freijter et al. (136) described the use of SE to relate the refractive index increment, $d_n/d_c$ with the areal mass density (Γ) of adsorbed BSA and other proteins and established the Equation 9, the De Freijter approximation of areal mass. Using SE, one can therefore quantify the amount of biomolecules on a given surface area.

### 1.6.3 Confocal microscopy

Confocal microscopy originated as a technique to overcome optical challenges in traditional fluorescence microscopy. In fluorescence microscopy, when the sample is illuminated, the resulting fluorescence that is detected by the photodetector comes from the whole sample, so areas both in and outside the focal plane. In confocal microscopy the fluorescence that is detected goes through a pinhole to reduce the out-of-focus fluorescence. The diameter of the pinhole can be adjusted to detect the fluorescence in an area of interest, though this may alter the amount of out-of-focus light that is eliminated (Figure 1.14**Error! Reference source not found.**).

Fluorescence occurs when a molecule absorbs a photon and then, following internal energy transfers, re-emits a photon at a longer wavelength. Fluorescent tags are often used in cell biology to track biomolecules and label cellular components. In this study, we used fluorescently labelled SAv as a marker of lateral mobility of GAG brushes and tracked halotagged FGFs in models of the ECM and on fixed cells.

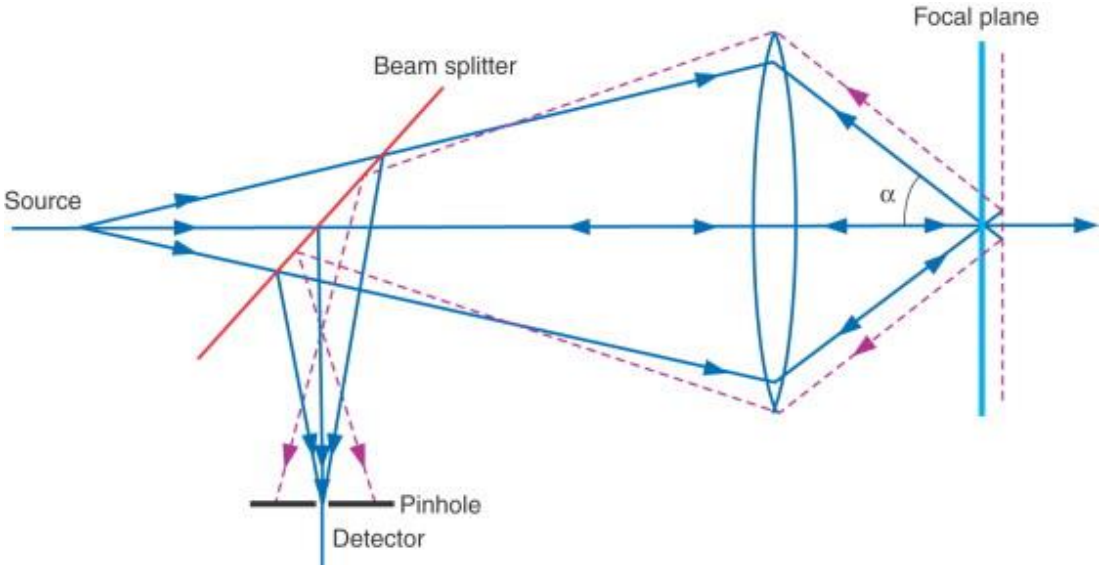


Figure 1.14: Diagram of the confocal microscopy working principle.
A simplified diagram of the confocal microscope and its optical components. A laser is beamed on a sample and the emitted fluorescence is focused at a pinhole placed before the detector (blue lines). Any emitted light that was out of the focal plane (pink lines) is not focused and thus will not be included in the images. Extracted from (146).

# 2 Aims and objectives

The aim of this thesis is to start to develop an understanding of how the structure of the ECM may regulate signalling by its transient protein residents that enable intercellular communication, such as growth factors, morphogens, cytokines and chemokines. This thesis focuses on FGFs, and the study will start by using biomimetic models of ECM, and probing these with FGFs. The biomimetic models consist of an HS brush formed by one-end anchoring HS chains via a streptavidin (SAv)-biotin bond on a lipid bilayer. The effect of FGF binding on the organisation of these ECM and HS chains can then be probed quantitatively and we can also observe and evaluate the mobility of FGFs in them. In parallel the binding and mobility of FGFs in native fixed pericellular matrix of keratinocytes will be measured to provide an insight into similarities and differences between the HS brush model and ECM. In this way, an understanding will be gained of:

1. the effect of FGF binding on the supramolecular organisation of glycosaminoglycans,
2. the effect of glycosaminoglycan (model) matrices on FGF retention and mobility, and
3. the comparability of the binding and diffusion of FGFs in ECM models and in the native pericellular matrix of keratinocytes

# 3 Experimental strategy

## 3.1 A well-defined biomimetic model of the ECM

The model was first established in previous studies (120) and consists of a soft and highly hydrated arrangement of GAG chains specifically anchored on a lipid bilayer through a SAv linkage (Figure 3.1). The 2-dimensional mobility of SAv, and thus of the GAG brush can be restrained by increasing the SAv coverage. The SAv coverage is determined by the percentage of biotinylated lipids in the SUV preparation (see Chapter 4.2.2). The model is a simple representation of the ECM that can be built layer-by-layer in different experimental setups and, therefore, various characterization techniques can be applied that are not accessible for the characterization of the ECM on cells. We used spectroscopic ellipsometry to quantify the surface density of molecular components, QCM-D to measure viscoelastic changes upon protein interaction with the GAG brushes and fluorescence microscopy after photobleaching (FRAP) to evaluate the molecular mobility of the SAv, as a proxy for the HS chains and of the FGFs.

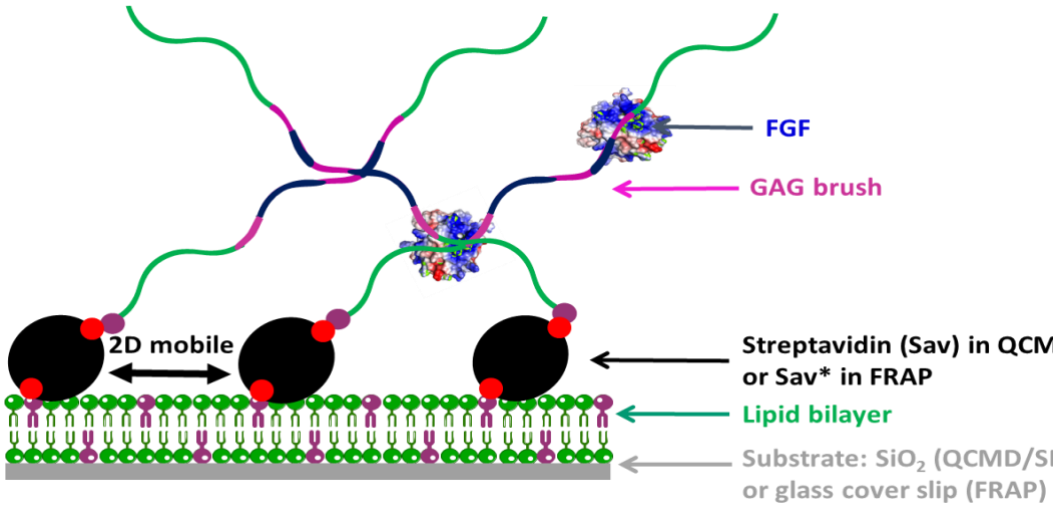


Figure 3.1: HS brush – a well-defined ECM model.
Experimental model supported by a $SiO_2$ sensor (in QCM-D and SE apparatus) or a glass cover slip (in FRAP assays). The supported lipid bilayer is formed by the adsorption and subsequent rupture of biotinylated small unilamellar vesicles (SUVs). The 2 dimensionally mobile SAv or Sav* (Atto488 labelled Sav) layer is specifically formed on the bilayer and further exposed to biotinylated GAGs. FGFS are presented to the model and changes upon binding are monitored by QCM-D, SE and FRAP imaging. Legend: purple dots: biotin, red dot: biotin binding pocket in Sav.

## 3.2 Production and purification of FGF proteins

A bank of plasmids containing FGF proteins is available in Liverpool along with protein expression *Escherichia coli* strains. The purification of FGF proteins is based on their affinity to heparin, their surface charge, and whether or not they contain a halotag or a 6-histidine tag. The purification principles that will be used are hep affinity, ion-exchange and Immobilized metal ion affinity chromatography (IMAC) on $Ni^{2+}$. Available proteins include FGF1, FGF2, FGF4, FGF6, FGF7, FGF9, FGF10, FGF17, FGF18 and FGF20, and mutants of FGF2 where the hep binding residues in the secondary sites were mutated to alanine.

## 3.3 Quartz crystal microbalance with dissipation monitoring and spectroscopic ellipsometry monitoring of the establishment of ECM models

The preparation of ECM models will be followed and assessed using the quartz crystal microbalance with dissipation monitoring (QCM-D) technology. The system allows the monitoring of the deposition of soft films on the sensors. The processed data gives information on the areal mass density deposited on the surface (including hydrodynamically coupled solvent) and the viscoelastic properties of the film. The two are related since the amount of substances on the surface might impact the structural organisation of the film, and thus the softness. The ECM models used are well-defined (Figure 3.1**Error! Reference source not found.**) and the QCM-D technology allows the assessment of the interactions of FGF proteins with the ECM models.

Spectroscopic ellipsometry (SE) allows the monitoring of the formation of the ECM models by measuring the changes in polarisation of light after reflection at a surface. The technique enables the quantification of the areal mass density of adsorbed material on the surface and, therefore, the determination of the absolute areal mass density of GAGs and FGFs.

## 3.4 FRAP assessment of FGF interaction with HS films.

Fluorescent labelling and imaging of the streptavidin monolayer allows the analysis of the lateral diffusion of HS in the brush (Figure 3.1). Cross-linking of HS by the binding of multivalent FGF proteins can restrain the mobility of HS, and as a consequence, the mobility of streptavidin (SAv). The relative cross-linking of HS brushes by FGF proteins can be observed by a decrease in the lateral mobility of the SAv monolayer. To do so, a biotinylated lipid bilayer is formed on a glass slide and labelled with a fluorescent partial monolayer of SAv. The HS film is formed on the SAv monolayer through the biotinylated reducing end of the polysaccharide. The formed HS film is then exposed to FGFs, and FRAP enables quantification of changes in the physical parameters that characterise the mobility of HS, i.e., the mobile fraction(s) and their associated diffusion constants. It will also be possible to evaluate the mobility of fluorescently labelled FGFs in the ECM models. For this purpose, HS will be grafted on a complete SAv monolayer, in which case SAv forms two-dimensional crystal on the supported lipid bilayer and therefore is largely immobile, and FGF proteins will be produced with an N-terminal Halo tag. The latter will then be labelled specifically with a fluorescent dye. The mobility of the complex in the ECM model and the pericellular matrix of fixed keratinocytes (HaCaT cells) will be assessed by FRAP.

# 4 Methods

## 4.1 FGF production, purification and molecular biology

### 4.1.1 Media, buffers and plate preparation

Lysogeny broth (LB) agar plates were prepared by solubilizing 27 g LB agar (Merck, Hertfordshire, UK) granules in 1 L of reverse osmosis (RO) water and pipetting 15 mL of the autoclaved solution into petri dishes. Antibiotic supplemented LB agar plates were prepared by adding the desired amount of antibiotic to the cooled LB agar solution before adding it to the petri dishes. LB media solution was prepared by solubilizing 20 g LB granules in 800 mL of RO water and autoclaving it. For 1 L of super optimal broth (SOB), 20 g of bactotryptone® (SLS, Nottingham, UK), 5 g of yeast extract (Merck), 0.5 g of sodium chloride (Sigma-Aldrich, Dorset, UK) were solubilized in 990 mL of RO water and autoclaved. The SOB media was completed by adding 10 mL of magnesium chloride (2 M) after autoclaving. For 500 mL of frozen storage buffer (FSB), 5 mL of potassium acetate (1 M, pH 7.5), 4.45 g of manganese (II) chloride tetrahydrate, 0.78 g of calcium chloride dihydrate, 3.37 g of KCl, 0.40 g of Hexamine cobolt chloride and 50 mL of glycerol (all chemicals were from Sigma-Aldrich) were solubilised in RO water, sterile filtered and stored at 4°C before usage. Phosphate buffer saline (PBS): 137 mM NaCl, 2.7 mM KCl and 10 mM disodium phosphate and 1.8 mM potassium phosphate monobasic pH 7.4 was prepared by dissolving PBS tablets (Sigma) in the suggested amount of RO water.

### 4.1.2 Expansion of competent cells (DH5α and C41 (DE3) pLysS)

*Escherichia coli* strains DH5α and C41 were expanded and made competent for plasmid intake using the Hanahan method. A 50 µL aliquot of cells from the in-house stock was spread on a LB agar plate and incubated overnight at 37°C. One colony was picked and inoculated in a round bottomed flask with 100 mL SOB medium. The culture was incubated at 37°C while shaking at 240 rpm until $OD_{600}$ reached 0.5 A.U. The cells were cooled on a wet ice bath for 20 min before being harvested by centrifugation (10 min, 1100 g at 4°C). The pellets were gently resuspended in 24 mL of ice cold FSB and incubated on wet ice for another 20 min. The cells were harvested

by centrifugation and gently resuspended in 8 mL of cold FSB. dimethylsulfoxide (DMSO) (Sigma-Aldrich) (280 µL) was added to the cells and they were incubated for 5 min on ice, this step was repeated and the cells were dispensed 100 µL in sterile Eppendorf tubes. The aliquots were flash frozen in a dry-ice-ethanol bath before being stored at -80°C.

### 4.1.3 Plasmid design, transformation and amplification

The DH5α strain was transformed for plasmid amplification. An aliquot of the frozen cells and of plasmid were thawed on ice for 5 min. 1-2 µL (200 ng) of plasmid were added to the cell aliquot and the mixture was placed on ice for 40 min. The mixture was then heat shocked in a 42°C water for 45 s and chilled on ice for 2 min before being plated on a LB agar plate supplemented with the appropriate antibiotic (50 µg/mL ampicillin or 100 µg/mL kanamycin sulfate) (Sigma-Aldrich); the plate was then incubated overnight at 37°. The expression plasmids based on the pET-14-b and pETM-11 vectors contain a gene encoding for resistance to ampicillin and kanamycin, respectively. Cells transformed with pET-14-b and pETM-11 plasmids were cultured in the presence of ampicillin and kanamycin, respectively, as a means of selection. On the next day, a single colony was inoculated into 50 mL LB medium supplemented with the appropriate antibiotic and incubated overnight (37°C, 250 rpm). The next day the bacteria were collected by centrifugation (15 min, 2800 g, 4°C). The supernatant was discarded, the plasmid was extracted using the QIAprep Spin Miniprep Kit (Qiagen, Manchester, UK) according to the manufacturer's instructions and stored at -20°C.

A cDNA encoding for a mutant of FGF2 with a silenced hep binding site 3 (160K/A, 163K/A and 164R/A) (FGF2 HBS3-) (Life Technologies, Paisley, UK) with restriction sites for BamHI (New England Biolabs, Ipswich, USA) and NcoI (New England Biolabs) was amplified by polymerase chain reaction and inserted in the plasmid vector pET-M11 using the T4 DNA ligase (New England Biolabs)

### 4.1.4 Protein expression and purification

One hundred ng pET-14b-FGF2 (Uniprot P09038-2; residues 1-155), pETM-11-FGF9 (Uniprot P31371; residues 1-208), pET-M11-HBS3, pET-M11-FGF18 (Uniprot O76093; residues 1-207), pET-14b-HaloFGF2, pET-14b-HaloFGF6 (Uniprot P10767; residues 38-208) or pET-14b-HaloFGF20 (Uniprot Q9NP95; residues 1–211) plasmids were transformed into CL41 (DE3) cells and plated on lysogeny broth, LB-agar plates supplemented with appropriate antibiotic (see 4.1.34.1.3). The plate was incubated for 16 h at 37°C. LB supplemented with the appropriated antibiotic (50 mL) was inoculated with 1 colony from the plate and incubated for 16 h at 37°C at a shaking rate of 240 rpm. Three flasks of 800 mL of LB supplemented with the appropriated antibiotic were inoculated with 800 µL of the previous culture and incubated at 37°C at a shaking rate of 240 rpm until the $OD_{600}$ reached 0.4-0.5 AU. The expression of protein was then induced by adding isopropyl β-D-1-thiogalactopyranoside (IPTG) to 1 mM at 16°C and shaking at 180 rpm for 16 h. The cells were collected by centrifugation at 11000 g and 4°C for 30 min. The supernatant was discarded and the cell pellet resuspended in 60 mL cell lysis buffer P1: 0.6 M NaCl (Sigma-Aldrich), 10 mM HEPES (Sigma-Aldrich), 1 mM dithiothreitol (DTT, Sigma-Aldrich), pH 7.4. Cell breakage was achieved by sonicating (40 % duty cycle) the suspension for 30 s and placing it on ice for 1 min. This cycle was repeated 6 times and the suspension was centrifuged at 38000 g, 4°C for 30 min to remove cell debris and insoluble protein aggregates/inclusion bodies. Recombinant protein was purified from the supernatant using procedures previously established in the research group (56, 104, 121). FGF1, HaloFGF1, FGF4, FGF10, HaloFGF10, FGF17, HaloFGF17 and HaloFGF18 were previously purified following these procedures by group members: Sun Changye, Li Yong, Bui Phuong Thao and Ngamlert Pawin.

#### 4.1.4.1 FGF2 purification

A 0.45 µm filter was used to clarify the supernatant containing FGF2 protein, which was then applied onto a 1 mL agarose hep (BioRad, Hercules, USA) column at 1 mL/min. Following a wash with 30 mL of P1, bound protein was eluted with 8 mL of (2 M NaCl, 10 mM HEPES, 1mM DTT, pH 7.4). The eluate was then diluted 3-fold with

P0 (10 mM HEPES, 1mM DTT, pH 7.4), applied to a 1 mL Hitrap Hep column and eluted with a NaCl gradient from 0.9 M NaCl to 1.5 M NaCl in 10 mM HEPES, pH 7.4 using an AKTA system. The collected fractions were analysed on a SDS-PAGE gel and the fractions containing a protein with a size around 17 kDa (the size of FGF2 is 17.2 kDa) were kept for further purification. The fractions containing FGF2 were pooled and diluted 10-fold with P0. The sample was applied to a cation-exchange column (1 mL CaptoS, GE Healthcare) and eluted with a NaCl gradient between 0.1 M and 2 M NaCl in 10 mM HEPES, pH 7.4 using the same AKTA system. The fractions were analysed by SDS PAGE and the ones containing a band around 17 kDa were kept for further purification. These fractions were pooled and diluted 4-fold with P0. The sample was loaded on a 1 mL Hitrap Hep column, washed with P1 (10 mM HEPES, 0.6 M NaCl, pH 7.4) and eluted with P4 (10 mM HEPES, 2 M NaCl, pH 7.4). The protein concentration was measured by reading the absorbance at 280 nm, and the sample stored at -80°C in aliquots before usage.

#### 4.1.4.2 Purification of halotagged FGFs

The samples containing Halo tagged FGF2 (HaloFGF2) protein were applied onto a 1 mL agarose hep (Bio-Rad, Hercules, USA) column at 1 mL/min, and then washed with 30 mL P1. The proteins were then eluted with 8 mL of P4, and the eluate was diluted 3-fold with P0. The diluted sample was applied onto a 1 mL Hitrap Hep column and eluted with a NaCl gradient between 0.9 M and 1.5 M NaCl in 10 mM HEPES, pH 7.4 using an AKTA system. The collected fractions were analysed on a SDS-PAGE gel and the fractions containing a protein with a size around 52 kDa (which corresponds to the size of HaloFGF2) were kept for further purification. The fractions were pooled and diluted 10-fold with P0. The sample was applied to an anion-exchange column (1 mL CaptoQ, GE Healthcare) and the halotagged FGF eluted with a 0.2 M NaCl, 10 mM HEPES, pH 7.4. The protein concentration was measured by measuring the absorbance at 280 nm and stored at -80°C in aliquots.

#### 4.1.4.3 Purification of his tagged FGFs FGF2 HBS3-, FGF18 and FGF9

His tagged FGF9 (FGF9) and FGF18 (FGF18) proteins have an N-terminal $his_6$ sequence. FGF2 HBS3- is an in-house engineered protein where the identified lysines

and arginine residues considered to be part of HBS3 (82) were mutated to alanine. The DNA was ordered and ligated into pET-M11. Thus the plasmid, pET-M11-HBS3 was designed to produce an N-terminally his tagged FGF2 with a non-functional HBS3.

For all three proteins, following cell breakage and purification on hep agarose (Section 4.1.4.1, the eluate was diluted 3-fold with 10 mM HEPES, 60 mM imidazole, 1 mM DTT, pH 7.4. The diluted sample was loaded on a 1 mL Histrap nickel (GE Healthcare) column and eluted with a competitor gradient between 50 mM and 500 mM imidazole in 10 mM HEPES, 0.5 M NaCl, pH 7.4 using an AKTA system. In each case, the collected fractions were analysed by SDS-PAGE and the fractions containing proteins with a size around 26 kDa (for *his*FGF9), 18 kDa (for FGF2 HBS3-) and 23 kDa (for FGF18) were kept for further purification. The fractions were pooled and loaded on a 1 mL Hitrap Hep column, washed with P1) and eluted with P4. The protein concentration was measured by reading the absorbance at 280 nm, the sample stored at -80°C in aliquots.

### 4.1.5 SDS-PAGE electrophoresis

For SDS-PAGE, samples were mixed with 5× sample buffer: 2% (w/v) bromophenol blue (Sigma-Aldrich), 50 % (v/v) glycerol, 10 % (w/v) SDS and 25 % (w/v) 2-mercaptoethanol (Sigma-Aldrich) in 315 mM Tris (hydroxymethyl) methylamine Cl (Tris-Cl, Sigma-Aldrich, pH 6.8) in a ratio of 4:1 (v/v). Five µL of this sample was mixed with 45 µL 1× sample buffer. The samples were then heated at 95°C for 10 min and centrifuged at 13000 rpm for 10 min to remove any insoluble material. The gels were loaded with 10 µL sample per well and electrophoresis was carried out at 200 volt (V) and 60 milliampere per gel for 45 min. The gels were either 4-15 % (acrylamide w/v) gradient SDS-PAGE gels purchased from Bio-Rad via Teknovas (San Sebastian, Spain) or prepared as follows: the gels were prepared in a 0.75 mm thick spacer glass plate apparatus, where 3.4 mL of the resolving gel was poured and polymerized *in situ*, covered by a layer of water. After polymerization, the water was discarded and replaced by the stacking gel solution. A 10-well forming comb was placed in the stacking gel solution and let to mould the well while the gel polymerized. The gels

were then soaked in a Coomasie blue solution, 1% (w/v) Coomasie blue (Sigma-Aldrich), 1.5% (v/v) glacial acetic acid and 25% (v/v) ethanol in water for 30 min, then de-stained in de-staining buffer, 10% (v/v) glacial acetic acid (Sigma-Aldrich) and 30 % (v/v) ethanol (Sigma-Aldrich) in water, until the background became clear.

For the preparation of 4 gels with a 15 % (w/v) acrylamide/bis-acrylamide (Sigma-Aldrich) resolving gel and a 6% (w/v) acrylamide/bis-acrylamide stacking gel, the two solutions were prepared as described in Table 1.

Table 1: SDS PAGE gel preparation recipe

| *Components* | *Resolving gel (volume)* | *Stacking gel (volume)* |
|---|---|---|
| *Acrylamide/bis-acrylamide stock (30%, w/v)* | 10 mL | 1.4 mL |
| *Tris-Cl (3 M, pH 8.8)* | 5.2 mL | x |
| *Tris-Cl (1.25 M, pH 6.8)* | x | 2.5 mL |
| *Water* | 4.4 mL | 3 mL |
| *10% (w/v) SDS* | 200 µL | 100 µL |
| *TEMED* | 20 µL | 10 µL |
| *Ammonium persulfate (50 g/l)* | 200 µL | 100 µL |

## 4.2 Supported extracellular matrix models.

The HEPES buffer (HB) was prepared in glass bottles that were cleaned by rinsing with acetone, ethanol (2 times) and water (10 times) and subsequent drying. HEPES and NaCl were dissolved in ultrapure water at 10 mM and 150 mM, respectively, the pH was adjusted to 7.4 with HCl. The solution was filtered through 2 µm pore filters.

### 4.2.1 Treatment of substrates for QCM-D, SE and FRAP measurements.

Silica coated QCM-D sensors (QSX303, Q-sense, Gothenburg, Sweden) were placed in 2% (w/v) sodium dodecyl sulfate for 30 min, rinsed with ultrapure water and dried under a nitrogen flow. The surfaces were further cleaned by treatment with

UV/ozone for 30 min using a Compact UV-Ozone Cleaner Chamber (BioForce Nanosciences, Ames, IA, USA). The surfaces were then placed in the QCM-D chamber for QCM-D measurements.

Silicon wafers with a native silicon oxide coating for spectroscopic ellipsometry were cleaned with acetone, rinsed with water and dried under nitrogen flow. The surfaces were further cleaned by treatment with UV/ozone for 30 min.

For FRAP, 1.5 mm glass cover slips were cleaned by dipping them in piranha solution, a 3:1 mixture of $H_2SO_4$ (99% pure, Sigma) and 30% $H_2O_2$ for 1 h, rinsed with ultrapure water and blow dried with nitrogen. Before use, the cover slips were rinsed with absolute ethanol, ultrapure water, blow dried under nitrogen and further cleaned by UV/ozone treatment for 30 min.

### 4.2.2 Preparation of small unilamellar vesicles (SUV) for supported lipid bilayers.

To form small unilamellar vesicles (SUV), a standardised sonication procedure was applied to the lipid components (122). A mixture of 1,2-dioleoyl-sn-glycero-3-phosphocholine (DOPC; Avanti, Alabaster, USA) and 1,2-dioleoyl-*sn*-glycero-3-phosphoethanolamine-cap-biotin (DOPE-CAP-B; Avanti) in chloroform was dried and re-solubilised in HB at the desired concentration and ratio. For a 95:5 ratio of DOPC: DOPE-CAP-B SUVs: 1.79 mg of DOPC (64.31 µL of the 27.87 g/L stock solution in chloroform) and 0.13 mg of DOPE-CAP-B (5.06 µL of the 26.2 g/L stock solution in chloroform) were mixed, dried and resuspended in 0.96 mL HB. The final concentration of DOPC: DOPE-CAP-B was 2 $mg.mL^{-1}$. For the preparation of 99.5:0.5 DOPC:DOPE-CAP-B SUVs, 1.88 mg DOPC and 0.01 mg DOPE-CAP-B were mixed, dried and resuspended in 0.95 mL of HB. The solution was frozen in liquid nitrogen and thawed repetitively 5 times and then sonicated twice on a wet-ice bath for 15 min using a 3 mm microtip sonicator (Branson 450 Cell disruptor, Branson, Connecticut, Danbury, USA) in pulse mode at 30 % duty cycle. The solution was centrifuged 10 min at 16000 *g* to remove any titanium particles coming from the tip sonicator. The SUV solutions were then stored in aliquots at 4°C under an argon atmosphere.

### 4.2.3 Biotinylated glycosaminoglycans

Biotinylated HS was kindly provided by Dhruv Thakar (Université Grenoble Alpes, France). Briefly, HS from porcine intestinal mucosa (Celsus Laboratories, Cincinnati, OH, USA) was conjugated with biotin via a 1 nm long oligoethylene glycol linker. Oxime ligation was used to specifically conjugate the HS at the reducing end with a hydrazide functionalised biotin (123). The HS was previously characterised as polydisperse with an average molecular weight of 12 kDa and a dispersity index, Đ of 1.59 (124). Biotinylated hep (Hep, 13 kDa), chondroitin sulfate A (CS-A, 30 kDa), chondroitin sulfate C (CS-C, 26 kDa), chondroitin sulfate E (CS-E, 26 kDa) and dermatan sulfate (DS, 6.5 kDa) were provided by Xu Wang (University of Illinois, Arizona). Their disaccharide composition and average molecular weight are presented in Table 2. Monodisperse DS (dp18) was purchased from Iduron (Alderley Edge, United Kingdom) and is characterised by 88% of IdoA – GalNAc,4S and 7% of IdoA,2S – GalNAc,4S (125). DS (dp18) was biotinylated by Pawin Ngamlert (University of Liverpool). In all these cases oxime ligation was used.

Table 2: Disaccharide repeat of glycosaminoglycans.
Table adapted from information provided by Xu Wang (University of Illinois, Arizona)

| GAG (average size) | Disaccharide unit |
|---|---|
| CS-A (30 kDa)<br><br>GlcA-GalNAc-4S | 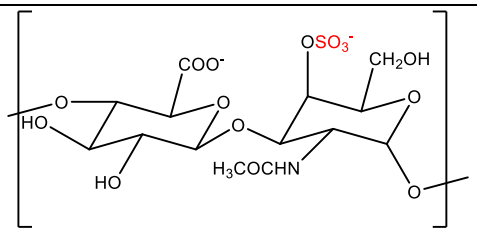 |
| CS-C (26 kDa)<br><br>GlcA-GalNAc-6S | 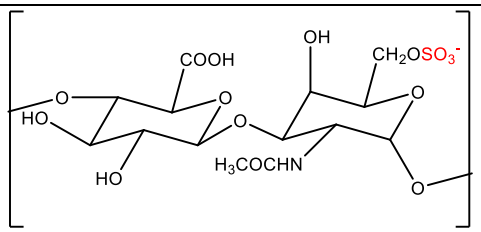 |
| CS-E (chemically sulfated CS-C, 26 kDa)<br><br>GlcA-GalNAc-4,6-diS | 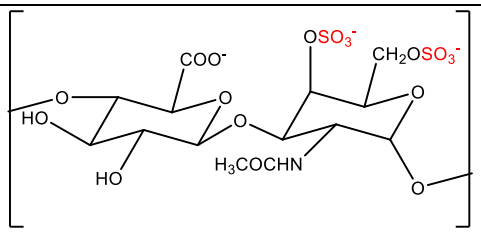 |
| DS (6.5 kDa)<br><br>IdoA-GalNAc-4S | 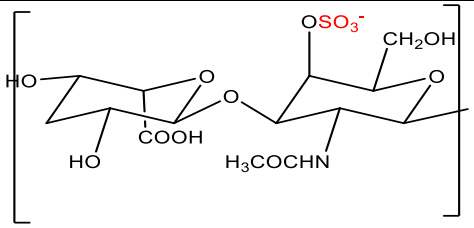 |

## 4.3 Quartz crystal microbalance with dissipation monitoring (QCM-D).

## 4.4 Quartz crystal microbalance with dissipation monitoring (QCM-D).

Prior to QCM-D measurement an old sensor was placed in the chamber as a template to help passivation of the chamber walls. The chamber was infused with an aqueous solution of 10 g/L of BSA then rinsed with water, both steps for 20 min at a 20 µL/min flow. The template sensor was then removed from the chamber, and the chamber

walls were dried under a flow of nitrogen. During QCM-D measurements, all substances were infused through passivated tubings at 20 µL/min or as stated otherwise.

To investigate the softness of the GAG brushes upon interaction with cytokines, -*ΔD*/*Δf* as a function of *Δf*, with *ΔD*/*Δf* being proportional to the elastic compliance (a physical measure of softness), and *Δf*, a measure of areal mass density of the film at the surface. Our models (see Chapter 3.1) fall under the condition of being films much thinner than the penetration depth of the shear wave in liquid which is 250 nm for the fundamental frequency in water (130, 131), and the following equation (130) can then be exploited:

$$\frac{\Delta \Gamma_i}{\Delta f_i} = -i\,\omega_F\,\eta\,L\,J' * (\rho_L/\rho) \qquad \text{Equation 7}$$

Thus,

$$\Delta D/\Delta f = (4\,\pi\,i\,\eta_L\,\rho_L/\rho) \times J' \qquad \text{Equation 8}$$

Where *J'* is the elastic compliance of the film, $\eta_L$ and $\rho_L$ are the viscosity and the density of the liquid bulk solution, ρ the density of the film and $\omega_F = 2\,\pi\,f_1$ is the angular fundamental resonance frequency. In our conditions, $\eta_L$ = 0.89 mPa·s, $\rho_L$ = 1.0 g cm$^{-3}$ and $\rho \approx$ 1.0 g cm$^{-3}$.

## 4.5 Spectroscopic ellipsometry applied to ECM models.

In-house designed 110 µL chambers for *in situ* SE measurements (137) were cleaned as follows: 2% SDS for 10 min, thoroughly rinsed with ultrapure water, ethanol and ultrapure water again. The chamber was dried under nitrogen flow before being passivated in 10 mg.mL$^{-1}$ bovine serum albumin (BSA) for 10 - 20 min. The chamber was rinsed with ultrapure wat er and dried under nitrogen flow before usage.

The data, Δ and Ψ as a function of λ was fitted with a multi-layer model using the software CompleteEASE. The model consisted of a planar silicon substrate, followed by a thin silicon oxide layer, the biomolecular film and the ambient solvent. The optical properties of the silicon substrate are tabulated in the software. The optical

properties of the silicon oxide layer, the biomolecular film and the ambient were approximated as Cauchy materials. In 1836, Cauchy described, for transparent materials, which do not absorbed light in the visible range, the relationship between their refractive index and the wavelength they are exposed to, and found the relation $n(\lambda) = A + B / \lambda^2$ to fit the data well.

The initial silicon oxide layer was modelled as a transparent Cauchy layer and its parameters $A_o$ and $B_o$ determined the refractive index, $n_o(\lambda) = A_o + (B_o / \lambda^2)$. The parameters $A_o$ and $B_o$, and the Thickness of the dry and in-solvent silicon oxide layer were characterised before each measurement to be used as a reference. To do so, the refractive index of the solvent $n_s$ was calculated from available tables in the literature as $n_s(\lambda) = 1.325 + (0.00322 / \lambda^2)$ (132, 138).

To calculate the molecular density of adsorbed layers of biomolecules on the silicon oxide layer, we treated the biomolecular film as a single transparent and homogenous layer. Their parameter $B_{layer}$ was fixed to 0.00322 (that is, identical to the solvent) and $A_{layer}$ and the thickness, $\theta_{layer}$ were used as adjustable fit parameters in the model. From the results, the refractive index of the biomolecular film is given by $n_{layer}(\lambda) = A_{layer} + B_{layer} / \lambda^2$. The molar surface density of biomolecules is then given by De Fejter's equation (139):

**Equation 9:**

$$\Gamma = \frac{1}{MW} \frac{\theta_{layer}(n_{layer} - n_s)}{d_n / d_c}$$

Here, $d_n/d_c$ is the refractive index increment of the biomolecule (132), and reflects how the refractive index n changes with the concentration c. We used refractive index increments, $d_n/d_c$, of 0.132 $cm^3/g$ for hep(140) (141), 0.180 $cm^3/g$ for all proteins (142) and 0.169 $cm^3/g$ for lipids (143-145).

## 4.6 FRAP of extracellular matrix models

A LSM700 confocal microscope (Zeiss, Jena, Germany) was used to acquire imaging data with a 561 nm excitation laser and a 590 nm emission filter for detection. For all FRAP measurements, a 63×/1.4 oil DIC oil immersion lens was used and images were 120 * 120 $\mu m^2$ (256*256 pixels). The laser intensities were 0.6 % for imaging and 100 % for bleaching. The pinhole size was 1 airy unit and the intensity resolution 12 bit.

### 4.6.1 FRAP assessment of the lateral mobility of GAG

To assess the mobility of HS brushes in the absence and presence of FGFs, we used a well-defined model of the ECM, as presented in Chapter 3.1. This model was established in a previous study (120). The cover slips were glued to a 4-well teflon holder using freshly mixed bi-component dental glue (Picodent) (Figure 4.1). After the glue had dried, the supported lipid bilayer (SLB) was formed by adding SUVs of DOPC: DOPE-CAP-B 99.5:0.5 (mole/mole) on the dry and clean surface to a final concentration of 50 µg/mL. The SUVs were incubated for 30 min in the well before rinsing. The SLB was labelled with fluorescent SAv by adding atto 565-SAv to a final concentration of 20 µg/mL and incubating for 30 min. After rinsing, the biotinylated GAGs were added to the wells at a final concentration of 5 µg/mL and incubated for 30 min. After rinsing, FGF proteins were added at the concentrations indicated in the figure legends and FRAP measurements were taken at each step.

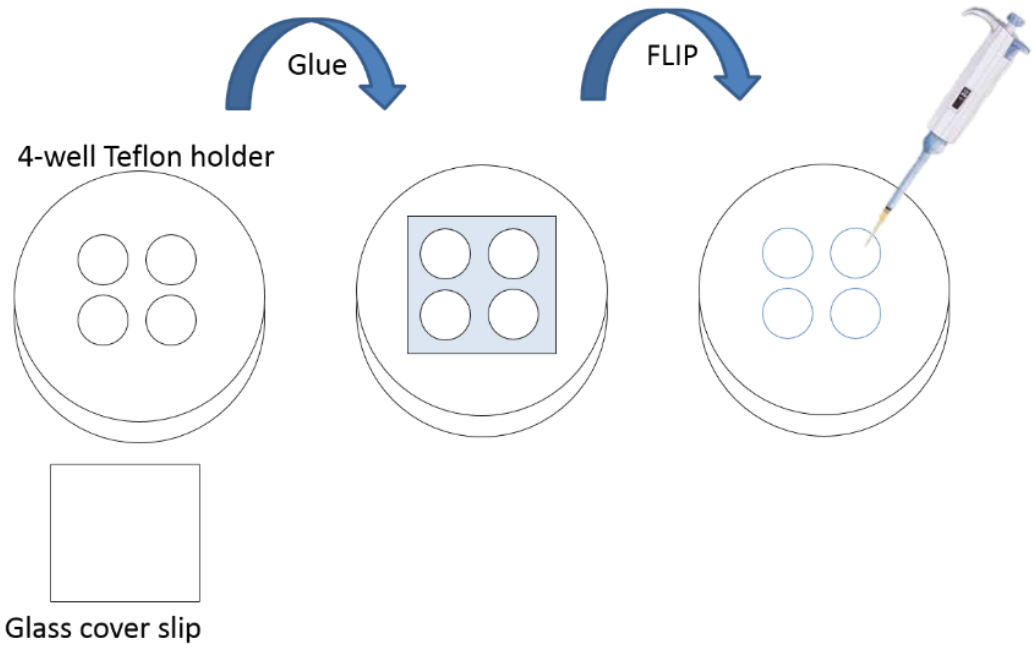


Figure 4.1: Schematic illustration of the custom-made sample holder for FRAP measurements.

FRAP measurement were set as follows: 3 images were taken before bleaching of a circular region of interest. The fluorescence recovery due to lateral mobility of lipids

was measured by a series of images, every second up to 1 minute, then every 5 seconds up to 2 minutes and finally every 15 seconds until the end of the experiment. The images were treated using a Matlab based program that fits the collected data with a lateral diffusion model (83). For each image taken after bleaching, the Time-resolved Profile Analysis (TPA) algorithm program corrects for the background fluorescence and generates an average radial profile (147). The profile is then compared to the solution of a diffusion equation. The diffusion model contains one mobile fraction and one immobile fraction. The mobile fraction is defined by its relative proportion and diffusion constant (147, 148). The fluorescent recovery curves were also plotted according to the data treatment process explained in 4.6.4.

### 4.6.2 FRAP assessment of growth factor mobility

To assess the mobility of FGFs in the GAG brushes, HS chains were immobilised via 2-D SAv crystals. 2-D SAv crystals were previously observed on lipid bilayers using atomic force microscopy and occur when a high concentration of SAv is used on a SLB with a high proportion of biotinylated lipid (149). Thus, by using these conditions the formation of virtually immobile fluorescent SAv crystals was observed (Figure 4.2). Immobilising the GAGs on the immobile SAv, therefore, allowed the mobility of fluorescently labelled Halo tagged FGFs in the brushes to be measured with no interference from the intrinsic mobility of the HS brush due to the lateral mobility of lipids.

The immobile GAG brushes were supported on a glass cover slip as described in 4.6. The SLB was formed by adding SUVs of DOPC:DOPE-CAP-B 95:5 (mole/mole) on the dry and clean surface to a final concentration of 50 $\mu g.mL^{-1}$. The SUVs were incubated for 30 min in the well before rinsing. The SLB was labelled with fluorescent SAv or functionalised with SAv by adding atto-SAv or SAv, respectively to a final concentration of 20 µg/mL and incubating for 30 min. After rinsing, the biotinylated GAGs were added to the wells at a final concentration of 5 µg/mL and incubated for 30 min. The 5% (mole/mole) biotinylated lipid fraction allows full coverage of the bilayer with atto-SAv. 2-D SAv crystallisation depends on the assay conditions

including pH and ionic strength (150), and the incubation buffer (50 mM HEPES, 150 mM NaCl, pH 7.4) allows the formation of immobile 2-D SAv crystals (Figure 4.2).

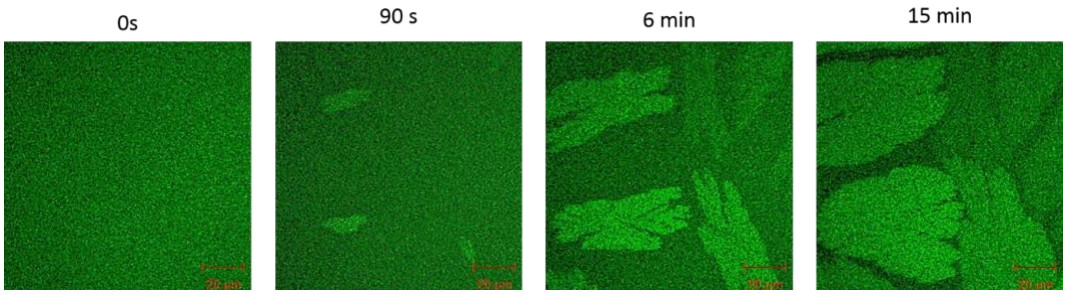

Figure 4.2: Time resolved formation of streptavidin crystals for GAG immobilisation on a supported lipid bilayer.
The SLB was made from 95:5 DOPC: DOPE-CAP-Biotin SUVs, and incubated with fluorescent SAv at a final concentration of 20 µg/mL. Fluorescent images were taken in series immediately after the injection of the fluorescent SAv at different times to follow the formation of SAv crystals. The expansion of crystals was observed over time. The variable intensities between crystallites are likely due to the different orientation of the fluorophores in the polarized laser light which affects fluorescence excitation.

After rinsing, halotagged FGF proteins were added at the concentrations indicated in the figure legends and FRAP measurements were taken as follows: 3 images were taken before bleaching of a circular region of interest. The fluorescence recovery due to mobility of halotagged FGFs was measured by a series of images (intervals: every second for 1 minute then every 5 seconds for 1 minute and finally every 15 seconds) for 300 or 600 seconds. Collection of the average fluorescence in the bleached area as a function of time gives information on the potential mobility of FGFs in ECM models. The fluorescence recovery curves were plotted according to the data treatment process explained in 4.6.4.

### 4.6.3 FRAP of labelled FGFs on HaCaT cells

The mobility of fluorescently labelled FGFs was assessed in the pericellular matrix of keratinocytes. To do so, the cells were fixed as described in 4.7 so innate cellular and cytoskeletal movement would not contribute to the movement of the labelled FGF. Halotagged FGFs were labelled by reacting the halotag with a fluorescent chloroalkane ligand, chloroalkane-Tetramethylrhodamine, chloroalkane-TMR (Promega, Southampton, UK). Halotagged FGFs were mixed with the chloroalkane TMR at a 1:5 molar ratio and incubated at room temperature for 30 minutes before usage directly on the fixed cells. The native matrix served as a mean of *in situ*

purification step, it retained the labelled HaloFGF while the free dye was removed by rinsing.

The fixed cells were incubated with 2 nM of TMR-Halo-FGF by adding the labelled protein to the dishes and placing them in the incubator for 30 min. Before the FRAP measurement, the cells were rinsed three times with PBS. A LSM780 confocal microscope (Zeiss, Jena, Germany) was used to acquire cell imaging data with a 561 nm excitation laser and a 590 to 765 nm emission filter for detection. For all FRAP measurements, a 63X/1.4 oil DIC oil immersion lens was used and images were 22.49 *22.49 $\mu m^2$ (256*256 pixels) in size. The laser intensities were 0.6% for imaging and 100% for bleaching. The pinhole size was 1 airy unit (0.47 µm) and the intensity resolution 8 bit. The fluorescence was recorded in three regions of interest (ROI) of 2.5 µm (radius), a reference, a background and a bleached area. Six images were taken before bleaching, images were taken every second for 300 seconds after bleaching. The bleaching step consisted in radiating the ROI.

### 4.6.4 Fluorescence recovery curves

For all measurements the absolute fluorescence intensities of each region was extracted using the ZEN 2012 software (Zeiss). The intensities in the different ROIs are defined as: $I_r$ in the reference area, $I_b$ in the background and I in the bleached area at each time point. The photobleaching was corrected by the intensities in the reference area and normalised by the intensities before bleaching. The mean of the three or six (X= 3 or 6) values of the reference, $I_r$ [1-X], was used to normalise the data. For the FRAP measurements on GAG brushes, the fluorescence recovery was monitored in the reference and the bleached areas only. However, an average background measurement was taken prior to the FRAP measurement (Figure 4.3).

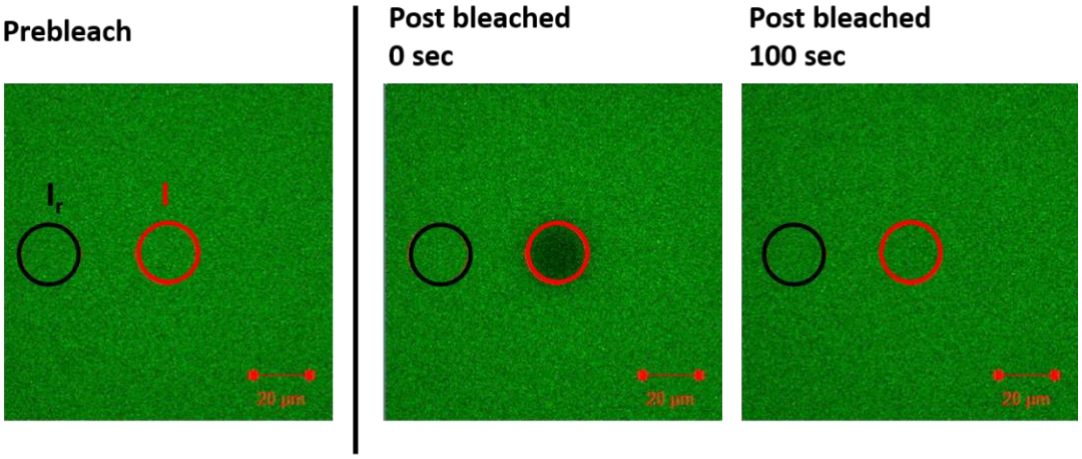


Figure 4.3: Lateral mobility of an HS brush.
An HS brush was established as described in 4.6.1 and the fluorescence in the $I_b$ and the $I_r$ was recorded. In this experiment, the HS brush recovered 100% of its fluorescence in the ROI within 100 seconds.

The background and bleach corrected recovery level, $I_{cn}$ at a given time point was calculated as follows:

$I_{cn} = I_c/I_c\ [1\text{-}X]$ Equation 10

Where $I_c\ [1\text{-}X]$ is the average intensity in the X prebleach images and $I_c$ is the corrected intensity as follow:

$I_c = (I - I_b) * (I_r\ [1\text{-}X] - I_b)/ (I_r - I_b)$ Equation 11

Where $I_b$ is the intensity in the background area recorded prior to or concomitantly to the FRAP measurement.

A graph of recovery level ($I_{cn}$) = f(time) starting after bleaching was presented as means of at least 3 experiments as shown for bare HS brushes in Figure 4.4.

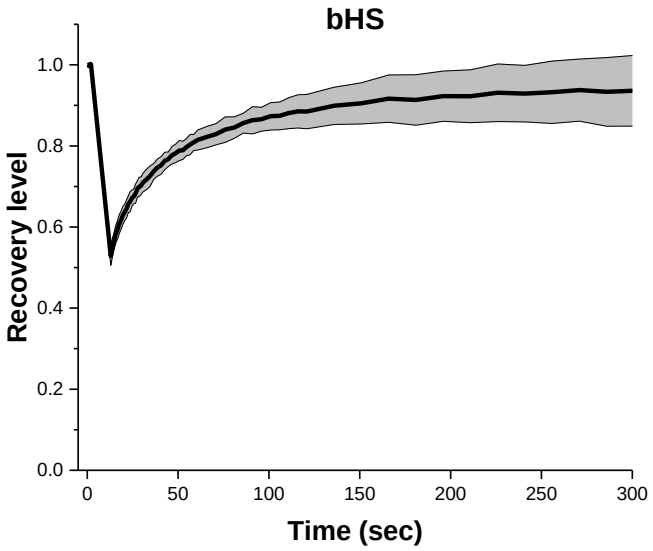


Figure 4.4: Fluorescence recovery curve of HS brushes.
Illustrative curve of the lateral mobility of a bare HS brush as followed by FRAP. The mean recovery level of 8 measurements (including the figure 18), highlighted in black, is a plotted as a function of time. The grey area around the curve represents the standard deviation.

## 4.7 Preparation of native extracellular matrix from eukaryotic cells.

### 4.7.1 Cell culture routine

The spontaneously immortalised human keratinocyte cell line (HaCaT) (151) was used. The HaCaT cells were grown in Dulbecco's modified Eagle's medium (DMEM, Life Technologies, Paisley, UK) supplemented with 10% (v/v) fetal calf serum (FCS, Labtech International Ltd, East Sussex, UK), 1% (v/v) antibiotics (10,000 µg/mL streptomycin and 10,000 units/mL penicillin) and 4 mM L-glutamine (Life Technologies) at 37°C with 10% (v/v) $CO_2$ in a 10 cm round culture dishes (Corning, Nottingham, UK). Cells were subcultured when they reached 90% confluence by two washes with 10 mL sterile PBS and then incubated with 3 mL versene (Life technologies) for 5 min at 37°C, 10% (v/v) $CO_2$. The versene was discarded and replaced by 1 mL versene/trypsine (versene containing 2.5% (v/v) of trypsin, Life technologies) and incubated for 5 more min at 37°C, 10% (v/v) $CO_2$ to detach the cells. The action of the versene/trypsine was stopped by resuspending the cells in 9

mL of culture medium and2 mL of the resuspended cells was added to a new dish along with 8 mL of culture medium.

### 4.7.2 Fixation of HaCaT cells

From imaging purposes, HaCaT cells were cultured on glass-bottomed imaging dishes (CELLview™ culture dish: 35mm non-treated glass bottom, Greiner Bio-one, Stonehouse, UK). To do so, 0.5 mL of resuspended cells (see Section 4.7.1) were added to the dishes and supplemented with 1.5 mL of culture media, the dishes were then placed in the incubator for 24-48 h until they reached 90% confluence. The medium was then removed and the cells were washed three times with 2 mL sterile PBS and then fixed by adding 2 mL 4% (w/v) paraformaldehyde (PFA) in PBS for 15 min at room temperature. The fixed cells were washed with PBS three times and incubated with 2 mL 10 mg/mL BSA in PBS for 15 min to block any remaining activity of the PFA. The BSA was discarded and the cells were incubated with the fluorescent probes or stored in 0.02% (v/v) sodium azide in PBS at 4°C before use.

# 5 Surface charges and heparin binding site distribution regulate dynamics of fibroblast growth factors in extracellular matrix models.

## 5.1 Introduction

In this chapter, the interaction of FGFs with HS brushes (section 5.2) and the subsequent supramolecular changes in the brush are measured. The amino acid sequence of the FGFs provides a clear phylogenetic relationship of this family of proteins (Figure. 5.1). This reflects also their functions, so that FGFs in the same subfamily (so most closely related and on the same branch) possess more conserved structure-function relationships (section 1.4).

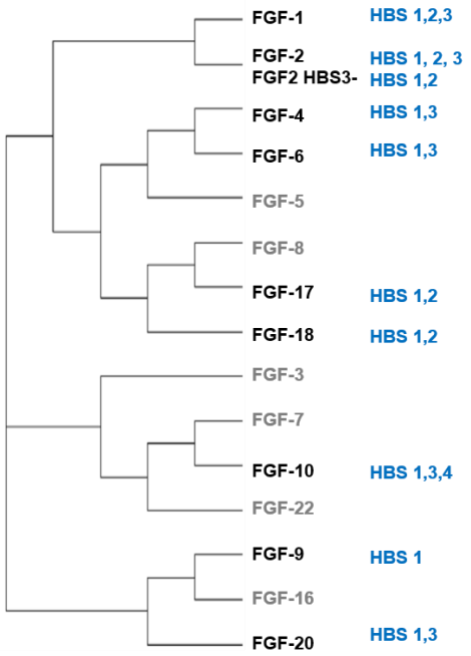


Figure 5.1: Phylogenetic tree of FGFs.
A phylogenetic tree of similarities was generated based on sequence multiple alignment with Clustal Omega online tool. The identified and reported HBSs are annotated (56, 104). The amino acid sequences of FGF 1 (P05230-1, residues 1-155), FGF2 (P09038-2, residues 1-155), FGF2 HBS3- (27 K/A, 30 K/A P09038-2, residues 1-155), FGF4 (P08620-1, residues 1-200), FGF6 (P10767-1, residues 1-208), FGF9 (P31371-1, residues 1- 208), FGF10 (O15520-1, residues 1-208), FGF17 (O60258-1, residues 1-216), FGF18 (O76093-1, residues 1-207), FGF20 (Q9NP95-1, residues 1-211) were submitted for similarity analysis on the Clustal Omega platform and a phylogenetic tree was generated from the results. Other FGFs used in this study were also included in the sequence alignment and are shown faded in grey.

HS brushes as a model of the ECM was used to quantify the binding of FGFs and assess the changes in mechanical properties of the brush when bound by different FGFs. FGFs of different subfamilies presenting a variety of HBSs combination were presented to the HS brush. Our study suggests that the presence of multiple HBSs and acidic borders isolating them regulates the cross-linking and the possible immobilization of HS chains in the brush. Here we suggest a hypothetical dichotomy based on surfaces charges to predict the entrapment of FGFs in HS brushes and their mobility.

## 5.2 Manuscript

Surface charges and heparin binding site distribution regulate dynamics of fibroblast growth factors in extracellular matrix models

BARADJI Aïseta,[1, 2] YATES Edwin A.,[1] FERNIG David G.[1]and RICHTER Ralf P.[2, 3, 4]

[1] Department of Biochemistry, Institute of Integrative Biology, University of Liverpool, Liverpool L69 7ZB, United Kingdom

[2] Biosurfaces Lab, CIC biomaGUNE, Paseo Miramon 182, 20014 San Sebastian, Spain

[3] School of Biomedical Sciences, and School of Physics and Astronomy, University of Leeds, LS2 9JT, Leeds, United Kingdom

[4] Laboratory of Interdisciplinary Physics, University Grenoble Alpes – CNRS, 140 Rue de la Physique, 38402 Saint Martin d'Hères, France

**BARADJI Aïseta**: Produced and purified FGF2, FGF2 HBS3-, FGF9 and FGF18. Performed all the QCD-D, SE and FRAP experiments and analysed the results. Wrote the paper

**YATES Edwin A**: Conceived the project and edited the manuscript.

**FERNIG David G**.: Conceived the project, supervised the production and purification of proteins, contributed to data analysis approaches, and edited the manuscript.

**RICHTER Ralf P**.: Conceived the project, supervised the QCM-D, SE and FRAP experiments, contributed to data analysis, and edited the manuscript.

# Abstract

Some fibroblasts growth factors (FGFs) have multiple heparin binding sites (HBS): a canonical (HBS1) and lower affinity secondary sites *e.g.* FGF2 and some are monovalent *e.g.* FGF9. The interaction of their HBS with heparan sulfate (HS) controls their interaction with FGF receptors (FGFRs) and their transport in the extracellular matrix (ECM). The native ECM is a complex compartment that contains many proteins and glycosaminoglycans that are interacting with each other in the manner of a bloc copolymer. To study its interactions with chemokines, we designed simple biomimetic models of the pericellular matrix heparan sulfate (HS). The models have been assembled layer by layer by graphting biotinylated HS oligosaccharides on a supported lipid bilayer via a streptavidin layer. These have been challenged with various FGFs and the interactions were followed by quartz crystal microbalance with dissipation (QCM-D), spectroscopic ellipsometry (SE) and fluorescence recovery after dissipation (FRAP). FGF2 has been shown to cross link HS chains, it is not known if this is a general property of FGFs with multiple HBS. If it is, then this raises some interesting possibilities, for example (i) FGFs may change the organization of extracellular matrix by cross linking HS chains; (ii) cross linking HS chains may result in FGFs becoming immobile, thus confined in the ECM. The data shows that FGF2 and mutants of its third heparin biding sites (HBS3): FGF2 HBS3$^-$, FGF9 and FGF18 bind effectively heparan sulfate (HS) brushes in our systems. Real-time monitoring by QCM-D of the HS film interaction with FGFs allowed us to appreciate the binding of the FGFs by looking at the changes in frequency shift. The analysis of the dissipation data upon binding of FGFs gave clues about the rigidification of the HS film thus the potential crosslinking of the brushes. FRAP imaging of the streptavidin layer confirmed he crosslinking of HS brushes for FGF2, FGF2 HBS3$^-$ and FGF18 when FGF9 was found to not crosslink the brushes. Data from spectroscopic ellipsometry allowed us to quantify number of FGFs per HS. It revealed that FGF2 and FGF2 HBS3$^-$ equally bind HS brushes; this suggests that the functionality of some HBS is not necessary to the binding and confinement of FGF2 in HS brushes. Understanding the relative implication of the HBS in the function of the FGFs may give an understanding of their conservation/deletion throughout the FGF subfamilies. Acido-basic mapping of residues at the surfaces of FGFs allowed us to understanding that the presence and repartition of acidic borders around the HBSs is implicated in the HS crosslinking properties of FGFs.

# Introduction

Many effectors, including morphogens, growth factors, cytokines and chemokines, such as fibroblast growth factors (FGFs) exert a local, paracrine activity to regulate cell communication in development and homeostasis (152-154). An important property in this respect is their interactions with glycosaminoglycans (GAGs) of the

extracellular matrix (ECM), particularly the sulfated GAGs, heparan sulfate (HS) and chondroitin sulfate (CS) (155), which regulate their transport between cells and often, their subsequent interactions with cognate signalling receptors on target cell surfaces (156-158). In the organism, the variability of structure and type of sulfated GAG depends on the tissue (159-161), which provide scope for tissue-specific regulation (162) of the activity of these paracrine effectors (163-165) and of tissue regeneration (166). These protein-polysaccharide interactions are modulated by the type, size and sulfation patterns of the GAG (55, 56, 167-171), and in the protein by its heparin binding sites (HBS), so called because heparin is often used as an experimental proxy for cell HS. The variability and diversity of HBSs lead to selective interaction with HS (103, 104, 172).

So far, 435 extracellular heparin binding proteins have been reported (47), and the identification of their HBS demonstrates them to consist of a surface cluster of basic amino acids arginine, lysine (165, 173, 174). Amongst the heparin binding proteins, the 15 paracrine fibroblast growth factors (FGFs) have a well conserved structure and possess a canonical HBS (HBS1) (55) and in many instances secondary HBS(s) of lower affinity (102, 175). The amino acids engaging in the interaction of FGFs with heparin/HS were initially identified using synthetic peptide (101) recently the lysines involved in binding were identified using the “protect and label” method (56, 104). The number and type of secondary HBSs has been found to follow the phylogeny of the FGF. That is, FGFs from the same subfamily have a more similar pattern of secondary HBSs than those from different subfamilies. This relationship holds for preference for binding particular sulfated structures in GAGs, FGF receptor binding and function (56, 104, 175, 176). Consequently, it would appear that the secondary HBSs have been subjected to the same natural selection pressures that drove the diversification of FGFs and they are likely to be of functional importance. However, the role secondary HBSs in FGF function remains enigmatic. A previous study demonstrated that the presence of secondary HBSs in FGF2 correlated with the cross-linking of HS chains, because cross-linking was not observed with FGF9, which possesses just an HBS1 and no secondary HBSs (148). Here, “cross-linking” of brushes is defined by the ability of a protein to stably restrain the mobility of the GAG chains.

However, this study is limited by the fact that only two FGFs from different subfamilies were examined. It is not a general phenomenon.

To address this question, we probed the dynamics of interaction of seven FGFs with a HS brush model of the ECM: biotinylated HS oligosaccharides grafted on a supported lipid bilayer via a streptavidin linker. These FGFs would encompass members of the same subfamily (FGF1, FGF2, and FGF17, FGF18), so two pairs of FGFs with very similar secondary HBSs and cover a total of five subfamilies, with characterised and distinct patterns of secondary HBSs. Three complementary techniques were used. Quartz crystal microbalance with dissipation (QCM-D) evaluated the changes in viscoelastic properties of the HS brush upon binding of the FGFs; spectroscopic ellipsometry (SE) determined the stoichiometry of binding and fluorescence recovery after photobleaching (FRAP) measured the changes in movement of the HS chains and of the FGF protein. The results demonstrate that some FGFs with multiple HBSs do not cross-link HS chains. Thus, the property of cross-linking HS chains is not dependent solely on the number of HBSs. Analysis of the surface electrostatic potential of the FGFs suggests that the presence of acidic borders around HBSs is also required for the FGF to cross-link HS chains. The importance of such cross-linking is that it may contribute to determine the mobility of FGFs in the ECM and may also change the supramolecular structure of ECM, which would in turn have pleiotropic effects.

# Methods

**Buffer, heparan sulfate and proteins**

The working buffer used for all experiments and for protein dilution was made of 150 mM NaCl (Sigma Aldrich, Madrid, Spain), 10 mM HEPES (Sigma Aldrich), pH 7.4 in ultrapure water. Bovine serum albumin (BSA, 66 kDa), streptavidin (SAv, 60 kDa) and streptavidin labelled with the atto 565 fluorophore (SAv-atto, 61 kDa) were purchased from Sigma Aldrich. Biotinylated heparan sulfate (HS) was prepared as described previously (123). Briefly, HS from porcine intestinal mucosa (Celsus Laboratories, Cincinnati, OH, USA) with an average molecular weight of 12 kDa was biotinylated at the reducing end by oxime ligation via an oligoethylene glycol linker.

Plasmid sequences encoding for FGF1, HaloFGF1, FGF2, FGF2 HBS3- (FGF2 160K/A, 163K/A and 164R/A), HaloFGF2, FGF4, HaloFGF6, FGF9, FGF10, HaloFGF10, FGF17, FGF18 and HaloFGF20, methods for their transformation in expressing cells, expression and purification protocol were described in previous studies (56, 57, 104, 121, 177). Briefly, plasmids encoding FGF2 (18 kDa), FGF2 HBS3- (18 kDa), FGFs with an N-terminal hexahistidine tag, [FGF1 (18 kDa), FGF4 (23 kDa), FGF9 (24 kDa), FGF10 (24 kDa), FGF17 (25 kDa) and FGF18 (25 kDa)], and FGFs with an N-terminal halo tag: HaloFGF1 (52 kDa), HaloFGF2 (52 kDa), HaloFGF6 (57 kDa), HaloFGF10 (57 kDa) and HaloFGF20 (57 kDa) were transformed in C41 (DE3) cells and cultured at 37 °C for 3 h until $OD_{600}$ reached 0.5. The proteins were expressed by induction of the *lac operon* with 1 mM isopropyl-1-thio-β-d-galactopyranoside (IPTG, Sigma Aldrich) at 16 °C for 16 h.

**Preparation of small unilamellar vesicles (SUVs) for supported lipid bilayers.**

SUVs were prepared as described previously (39). Briefly, mixtures of dioleoylphosphatidylcholine (DOPC) and dioleoylphospatidylethanolamine-CAP-Biotin (DOPE-CAP-B) (both Avanti Polar Lipids, Alabaster, AL, USA) in chloroform were dried and re-suspended in working buffer at a concentration of 2 $mg.mL^{-1}$. The suspensions were homogenized by five cycles of freezing in liquid nitrogen and thawing. SUVs were produced by sonication, for twice 15 min using a 3 mm microtip

sonicator (Branson 450 Cell disruptor, Branson, Connecticut, Danbury, USA) in pulse mode at 30% duty cycle on an iced water bath. The SUV solution was centrifuged for 10 min at 14000 *g* to remove titanium particles coming from the sonicator tip, and then stored at 4°C under argon atmosphere and used within a year.

**Treatment of substrates.**

Surfaces treatment have been described in detail in a previous study (120). Silica-coated sensors for QCM-D measurements (QSX303; Biolin Scientific, Västra Frölunda, Sweden) were cleaned in 2% (w/v) sodium dodecyl sulfate (Sigma Aldrich) in ultrapure water (30 min), rinsed with ultrapure water and blow-dried with nitrogen gas. Silicon wafers with a native $SiO_2$ coating (University Wafers, South Boston, MA, USA) for spectroscopic ellipsometry (SE) measurements were first rinsed with acetone and blow-dried with nitrogen gas, and then rinsed with water and blow-dried with nitrogen gas. Glass cover slips (0.15 mm thick, 24 × 24 $mm^2$; Menzel Gläser, Braunschweig, Germany) for fluorescence recovery after photobleaching (FRAP) measurements were cleaned by immersion in piranha solution (3:1 (v/v) mixture of concentrated $H_2SO_4$ and $H_2O_2$; both Sigma Aldrich) for 1 h, rinsed with ultrapure water and blow-dried with nitrogen gas. Before use, the cover slips were rinsed with ethanol (HPLC gradient grade, ≥99.8% pure; Sigma Aldrich), ultrapure water, and blow-dried with nitrogen gas. Before use, all substrates were further conditioned by UV/ozone (BioForce Nanosciences, Ames, IA, USA) treatment for 30 min.

**Quartz crystal microbalance with dissipation monitoring (QCM-D).**

QCM-D follows the evolution of the resonance frequency and the dissipation of quartz crystal sensors upon adsorption of material on their surface. The change in frequency, $\Delta f$, and the change in dissipation, $\Delta D$, are related to the physical properties of the film at the surface such as the areal mass density (including hydrodynamically coupled solvent) and mechanical properties. QCM-D measurements were performed with a Q-Sense E4 system equipped with Flow Modules (Biolin Scientific). $\Delta f$ and $\Delta D$ were measured at 6 overtones ($i$ = 3, 5, 7, 9, 11, 13, corresponding to resonance frequencies of $f_i \approx 15, 25, 35 \ldots 65$ MHz). We chose to represent $\Delta f = \Delta f_i/i$ and $\Delta D = \Delta D_i$ for the third overtone ($i$ = 3). All other overtones

provided equivalent data. Prior to each measurement, the walls of tubing and flow modules were passivated against non-specific binding of biomolecules. To this end, a sacrificial sensor was placed in the flow module, and the fluidic system was infused first with an aqueous solution of 10 mg/mL of bovine serum albumin (BSA; 10 min) and then ultrapure water (10 min). The sacrificial sensor was then removed and the fluidic system blow-dried with nitrogen gas. Solutions were infused in passivated modules using a syringe pump (KD Scientific Legato Syringe, Holliston, MA, U.S.A) at 20 µL/min or as stated otherwise. The working temperature was set and controlled at 23°C. For sufficiently rigid films, the analysis of QCM-D data allows to estimate the thickness (*d*) of the film using Sauerbrey's equation: $d = - C \Delta f / \rho$, where $C$ = 18.0 $ng.Hz^{-1}.cm^{-2}$ is the mass sensitivity constant for the sensors with a fundamental resonance frequency of 4.95 MHz. For the film density, we used $\rho$ = 1 $g.cm^{-3}$, which is a reasonable approximation for strongly hydrated biomolecular films (130).

**Quantification of biomolecular surface densities by spectroscopic ellipsometry (SE).**

SE measures the changes in polarisation of light upon reflection on the sample surface. Specifically, these changes are characterized by the ellipsometric angles Δ and Ψ which are measured for wavelengths ranging from λ = 380 nm to 1000 nm. The presence of biomolecular films on the surface directs the changes in Δ and Ψ and is caused by the change in refractive index upon film formation. SE was used to quantify the surface density of adsorbed biomolecules.

A M2000V spectroscopic ellipsometer (J. A. Woollam, Lincoln, NE, USA) was used to acquire changes in Δ and Ψ every 5 seconds at room temperature. In-house designed 110 µL open chambers for *in situ* SE measurements (137) were cleaned by immersion in 2% (w/v) SDS for 10 min, thoroughly rinsed with ultrapure water, ethanol and ultrapure water, and blow-dried with nitrogen gas. The chambers were passivated with 10 mg/mL BSA (10 min), rinsed with ultrapure water and blow-dried with nitrogen gas before use. Biomolecules were directly injected into the chamber containing buffer and kept homogenised by continuous agitation with a magnetic stirrer located at the bottom of the cuvette. Rinsing steps were operated by applying an upward buffer flow of 50 µl/min through tubing connected at the bottom (inlet)

and at the top (outlet) of the cuvette until apparent stabilisation of the SE signals. The HS brushes were formed by sequentially incubating 99.5:0.5 or 95:5 DOPC: DOPE-CAP-B SUV at 50 µg.mL$^{-1}$, SAv at 20 µg.mL$^{-1}$ and HS at 5 µg.mL$^{-1}$ and each step was followed by a rinsing step with the incubation buffer. The solutions were infused for a minimum of 15 minutes and apparent stabilisation of the SE signals.

The time-resolved ellipsometric data, Δ and Ψ as a function of λ, were fitted with a multi-layer model consisting of the opaque silicon substrate, a silicon oxide layer, a biomolecular layer and the ambient using the software CompleteEASE (Woollam), as previously described (178). The two discrete layers and the ambient were modelled as transparent Cauchy media with the dispersion of the refractive index $n$ being described by the Cauchy parameters $A$ and $B$ such that $n(\lambda) = A + B / (\lambda/\mu m)^2$. Tabulated values were used for the silicon substrate. The Cauchy parameters of the silicon oxide layer were determined prior to the formation of biomolecular films by simultaneous fitting of data sets from two measurements on the clean wafer surface, one in ambient air (for which $A$ = 1 and $B$ = 0) and the other in working buffer (for which $A_{buffer}$ = 1.325 and $B_{buffer}$ = 0.00322, calculated from available tables in the literature (132, 138)). The thickness of the silicon oxide layer was then determined from the measurement on the clean wafer surface in working buffer. For the biomolecular layer, the thickness $d_{bml}$ and the Cauchy parameter $A_{bml}$ are the sole fitting parameters. $B_{bml} = B_{buffer}$ =0.00322 was fixed.

To calculate molar surface densities, we used De Fejter's equation and the (average) molecular weight of the biomolecules (139):

$$\Gamma = \frac{1}{M_W} \frac{d_{bml}\,(n_{bml} - n_{buffer})}{dn/dc}$$

where $dn/dc$ is the refractive index increment (132). We used $dn/dc$ = 0.132 cm$^3$/g for HS (140), 0.180 cm$^3$/g for all proteins (142) and 0.169 cm$^3$/g for lipids (143-145).

**FRAP assessment of FGF interaction with HS films.**

FRAP measures the recovery by lateral mobility of fluorescently labelled biomolecules following photobleaching of a defined region of interest (ROI). To this end, fluorescently labelled SAv (SAv-atto) or HaloFGF were used, together with a LSM700 confocal microscope (Zeiss, Oberkochen, Germany). The lateral mobility of the components was followed by recording the fluorescence intensity as a function of time.

For FRAP measurements, a clean and dry glass cover slip was glued to a custom-made 4-well Teflon holder using freshly mixed bi-component dental glue (Picodent; Wipperfürth, Germany). All surface functionalization steps were performed in still solution. After the glue had dried, each well was filled with 50 µL of SUVs made of DOPC:DOPE-CAP-B 99.5:0.5 or 95:5 (mol/mol) to a final concentration of 50 µg/mL in working buffer. The SUVs were incubated for 30 min to form supported lipid bilayers (SLBs). Subsequent rinsing was achieved by diluting the well content with a two-fold excess volume of incubation buffer, mixing by repetitive liquid suction and dispensing with a pipette (avoiding bubbles and leaving the glass cover slip wet), and removal of the excess buffer; this process was repeated 10 times. The SLB was functionalized with SAv (non-labelled or fluorescent, as desired) to a final concentration of 20 µg/mL for 30 min. After rinsing, the SAv monolayer was functionalized with HS (5 µg/mL, 30 min). After rinsing, FGF (non-labelled or halotagged, as desired) was added at concentrations indicated in the figure legends. Halotagged FGF were labelled by reacting the halotag with a fluorescent chloroalkane ligand, chloroalkane-Tetramethylrhodamine (TMR) (Promega, Southampton, UK). Halotagged FGFs were mixed with the chloroalkane TMR at a 1:5 molar ratio and incubated at room temperature for 30 minutes before usage directly on the brushes. FRAP measurements were taken at the steps of interest.

FRAP measurements were performed on a square area (120 × 120 $\mu m^2$, 256 × 256 pixels) using a 63× oil immersion objective (63× 1.4 oil DIC) and a fully opened pinhole (1 mm diameter). Three images were taken before a circular ROI with a 20 µm diameter was bleached, and fluorescence recovery was subsequently monitored. The bleaching was effectuated with lasers at maximal intensity at 488, 565 and 633 nm

wavelengths for approximately 10 s. The fluorescence recovery was monitored by a series of images at intervals of 1 s and/or 5 s.

FRAP image series were analysed with a time-resolved profile analysis (TPA) routine implemented in Matlab, as described in detail elsewhere (148, 179). The routine corrects for background fluorescence, bleaching and heterogeneous illumination, and generates a radially averaged intensity profile from each image. The profiles are then fitted with predictions of diffusion equations using the first post-bleach image to define the boundary conditions. The diffusion model used here assumes two fractions of fluorescent species, one immobile and the other mobile with a given diffusion constant. The only adjustable fit parameters are the size and the diffusion constant of the mobile fraction, and both are reported here.

The mean intensity of the bleached ROI was also extracted for every time point to plot recovery curves illustrating the mobility of the HS brushes (i.e. attached to SAv-atto) or the labelled FGFs. In this case, the background fluorescence measured in the glass slide was measured before each measurement and it was used along with the fluorescence of a reference ROI to correct for bleaching during imaging.

To assess the lateral mobility of HS, an incomplete and mobile monolayer of SAv-atto (to which the HS was anchored) was used as a reporter. To this end, the 0.5% biotinylated SLB was employed. To evaluate the mobility of FGFs, HaloFGFs were used as fluorescent probes in HS brushes grafted to dense SAv monolayers on 5% biotinylated SLB. The dense SAv monolayers (but not the incomplete monolayers) were found to form two-dimensional crystals (150), and in our experimental conditions, we observed at least 90% of the surface to be covered by these crystals.

# Results

### Assembly of HS brushes on QCM-D sensor surfaces

HS brushes are molecular films of HS polymers grafted via their reducing end to a planar support. With their distinct molecular orientation and tuneable grafting density, they represent a well-defined model of HS-rich ECM that enables quantitative analysis (Figure 5.2). The QCM-D allows the monitoring of the formation

of the HS brush on a silicon oxide coated sensor (Figure 5.3). Small unilamellar vesicles (SUVs) containing 0.5 or 5 mole-% biotinylated lipids spontaneously adsorb on the surface of the sensor and rupture to form a supported lipid bilayer (SLB). The frequency shift ($\Delta f$) is a measure of wet (with trapped solvent) mass present at the surface of the sensor, and decreases upon binding of biomolecules. The dissipation ($\Delta D$) is a measure of the stiffness of the film. The resulting shifts in frequency, $\Delta f$ = -24 $\pm$ 1 Hz, and dissipation, $\Delta D \leq 0.4 \times 10^{-6}$, are similar to those measured previously (120) and demonstrate the formation of an SLB of good quality. Subsequent binding of SAv to a level commensurate with a mid-dense brush leads to a further decrease in $\Delta f$ (-21 $\pm$ 1 Hz) and a small increase in $\Delta D$ ($0.80 \times 10^{-6}$). For the dense brushes (5 mole-% biotinylated SUVs) the SAv monolayer leads to decrease in $\Delta f$ (-27 ± 1 Hz) and a transient small increase in $\Delta D$ that returns to the level of a rigid layer ($\leq 0.4 \times 10^{-6}$). When HS binds to SAv the decrease in frequency ($\Delta f$ = 12 $\pm$ 1 Hz) is accompanied by a large increase in dissipation ($\Delta D = 4.0 \pm 0.5 \times 10^{-6}$). For dense brushes (5 mole-% of biotinylated lipids in the SUV), the HS anchorage leads to a higher decrease in $\Delta f$ (-17 ± 1 Hz) and increase in dissipation ($\Delta D = 5.0 \pm 0.5 \times 10^{-6}$). This is indicative of a soft HS brush being formed, that is, HS chains bind selectively through the biotin tag at the reducing end, leaving the relatively flexible polysaccharide chains free (39).

The frequency change reports on the HS brush (HS chains and interacting solvent), therefore, to provide quantitative data on bound molecules only, spectroscopic ellipsometry (SE) was used to characterise each biomolecular layer with its areal mass density (Γ). The SLB possessed an areal mass density of 345 ± 12 ng.cm$^{-2}$. The surface densities of the SAv and HS layers were 1.7 ± 0. 1 pmol.cm$^{-2}$ and 1.1 ± 0.3 pmol.cm$^{-2}$, respectively. The average distances between SAv molecules and between HS chains were extracted and theses values were not significantly different: 12 ± 3 and 12 ±4 nm respectively, showing the specificity of the SAv-HS anchorage (Supplementary figure 5.1). The average molecular weight the HS used in this study is 12 kDa, and with the average disaccharide molecular weight being 0.5 kDa and its length 1 nm, the average contour length is estimated at 24 nm (180). However, the actual molecular weight and contour length at the surface may well be smaller. Indeed the smallest HS chains would anchor preferably than the longer ones (120). This well-

defined HS brush was used in our study as a simple representation of one element of extracellular matrix, HS, to determine the molecular features underpinning the specific interaction and dynamics of FGFs with HS.

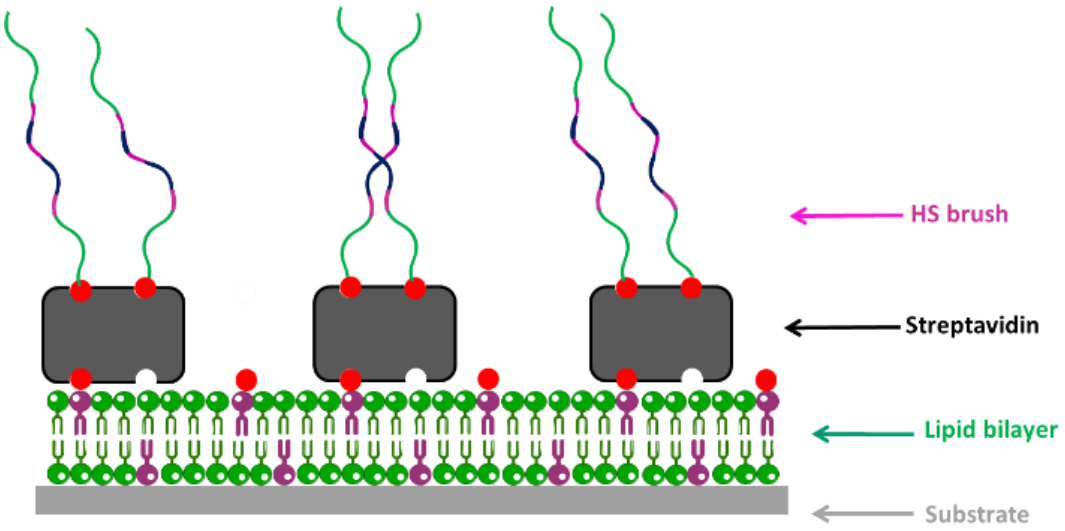


Figure 5.2: Representative sketch of HS brushes as a well-defined ECM model.
A biotinylated lipid bilayer is formed on a planar silica or glass substrate, and the HS chains are specifically anchored to it via a streptavidin. Here a mid-dense brush is represented as the streptavidin monolayer is partial. This allows the streptavidin, and the attached HS chains, to diffuse laterally on the fluid supported lipid bilayer.

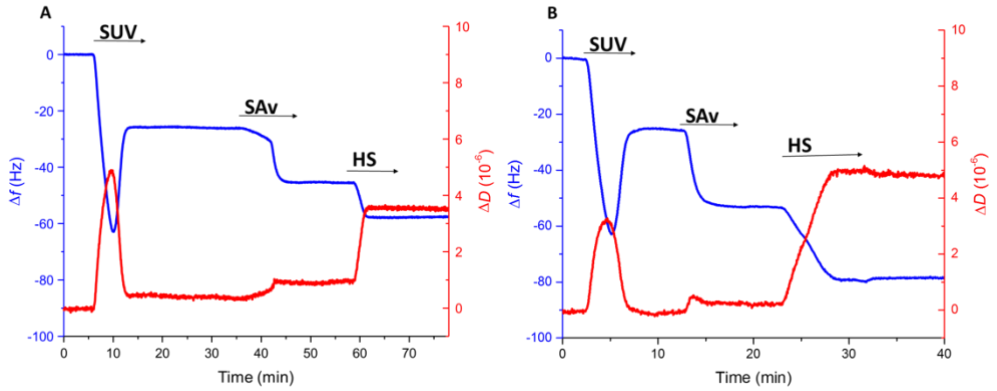


Figure 5.3: QCM-D monitoring of the formation of a mid-dense (A) and a dense (B) HS brush. The changes in Δf represent the evolution of mass adsorption at the surface of the sensor; ΔD provides information about the mechanical properties of the film with an increase being associated with a softer film. The black arrows represent the infusion step of the particular biomolecules, here at 20 µl.min-1. A supported lipid bilayer (SLB) was formed by infusing a 50 µg.mL-1 SUV solution (containing 99.5:0.5 (A) or 95:5 (B) (mol:mol) DOPC:DOPE-CAP-B) on a silica coated QCM-D sensor. The biphasic response upon SUV incubation is characteristic for the initial binding of SUVs and their subsequent rupture (green arrow) and formation of

a SLB. Δf = -24 ± 1 Hz and ΔD ≤ 0.4 × 10-6 indicate the formation of an SLB of good quality (120). The infusion of 1 µg.mL-1 SAv at 6 µl.min-1 (A) prior to infusing at 20 µg.mL-1 (44 min) generates as a slow decrease in Δf and increase ΔD, this feature illustrates the ability of QCM-D apparatus to detect small changes and highlights of the successful passivation of the tubing with BSA. The two SAv infusions were carried out for 5 minutes and the final relative Δf and ΔD were (A) -22 ± 1 Hz and 0.5 ± 0.2 × 10-6, respectively and (B) -27 ± 1 Hz and 0.2 ± 0.1 × 10-6. The infusion of HS at 5 µg.mL-1 triggered a further decrease in Δf (-12 ± 1 Hz) and a large increase in ΔD (4.0 ± 0.5 × 10-6), values characteristic of a mid-dense brush and -17 ± 1 Hz (Δf) and 4.0 ± 0.5 × 10-6 (ΔD) for the dense brush.

**Viscoelastic changes in HS brushes following binding of FGF1 and FGF2.**

The binding of FGF1 and FGF2 to HS brushes was followed by QCM-D. The specificity of FGF binding to the HS brushes was verified by infusing the FGFs in the same conditions on the SAv coated SLB. Upon infusion of FGF2 at 0.28 µM (Figure 5.4A), we observed a rapid drop in $\Delta f$ that stabilised at -28 Hz. This event illustrates the binding of FGF2 to the HS brush until it reached a maximum. Rinsing the surface caused desorption of some of the bound FGF2 from the HS brush, as $\Delta f$ increased to -17 Hz. These results are consistent with those published previously with FGF2 binding to HS brushes (148). The changes in softness of the film upon binding of FGF2 can be analysed by the parametric plot of $\Delta D/-\Delta f$ vs. $-\Delta f$. $\Delta D/-\Delta f$ is a measure for the elastic compliance (*i.e.*, softness) of the HS brush, and $-\Delta f$ is a measure for the surface coverage (130). The parametric plot thus shows the trend of HS brush rigidification as protein binds and is particularly useful for comparing the interactions of different proteins (130). The parametric plot for FGF2 (Figure 5.4A) shows that the bare HS brush has a softness corresponding to $0.20 \times 10^{-6}$ $Hz^{-1}$, and that the softness decreases by roughly 3-fold (to $0.06 \times 10^{-6}$ $Hz^{-1}$) upon FGF2 binding at 0.28 µM. The rigidified protein-loaded HS brush retains its rigidity even after rinsing and partial release of FGF2, as it did not recover its softness (Figure 5.4A). The specificity of FGF binding to the HS brushes and the inertness of the SAv layer to the FGFs was verified by infusing the FGFs in the same conditions on the SAv coated SLB (Supplementary figure 5.9).

The closely related FGF1, which is in the same FGF subfamily, has the same pattern of HBSs as FGF2 and similar, but not identical binding selectivity for structures in the polysaccharide (56, 104, 114). Upon infusion of FGF1 at 0.28 µM, we observed a

decrease in $\Delta f$ (Figure 5.4Figure 5.4) to a maximum of $\Delta f$ of -30 Hz, similar to that observed for FGF2. However, compared to FGF2, upon rising more FGF1 desorbed, as a final $\Delta f$ of -10 Hz was reached. Moreover, in contrast to FGF2, the dissipation response of FGF1 binding to HS (Figure 5.4Figure 5.4) was a rapid increase in $\Delta D$ that stabilised at $1.0 \times 10^{-6}$. Upon rinsing the $\Delta D$ was largely restored stabilised at $0.6 \times 10^{-6}$. Nonetheless, the parametric plot shows a gradual rigidification of the HS brush upon binding of FGF1 (Figure 5.4).Figure 5.4). The level of $\Delta D/-\Delta f = 0.07 \times 10^{-6}$ $Hz^{-1}$ at maximal coverage is comparable to FGF2 and FGF2 HBS3-, and a superposition of the parametric plots (Figure 5.4Figure 5.4) shows that the rigidification trends upon binding are the same for the two FGFs. However, the initial differences in dissipation changes discovered on FGF2 and FGF1 and the recovery of the HS-FGF1 film's softness upon rinsing and partial protein release, indicates that these films are not identical. Thus, FGF1-loaded HS brushes are softer than HS brushes loaded with FGF2 after the rinsing step.

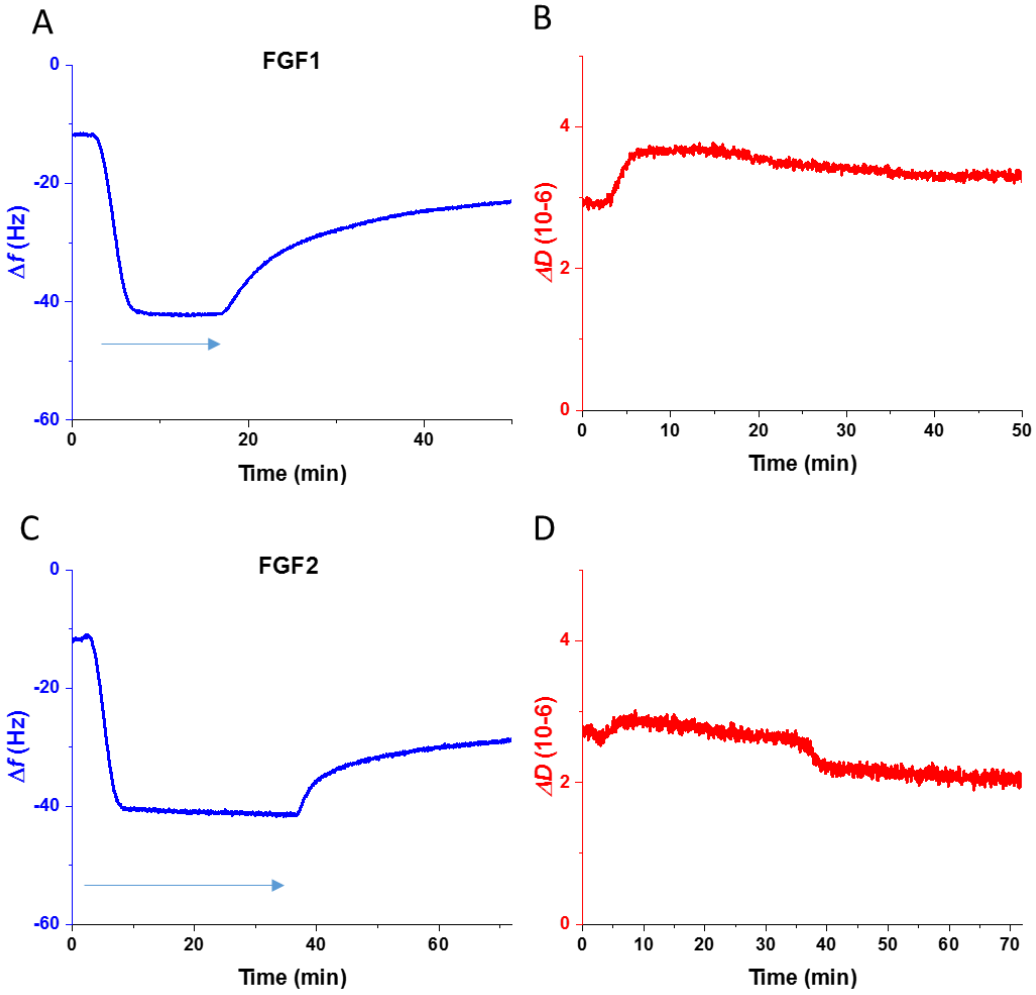


Figure 5.4: QCM-D monitoring of FGFs from the FGF1 subfamily binding to a mid-dense HS brush.

The frequency (panels A and C) and dissipation (panels B and D) were offset after the formation of the HS brush (cf. Figure 5.3). FGF1 (panels A and B) and FGF2 (panels C and D) were infused at 0.28 µM until equilibrium (blue arrows indicate the infusion time) before rinsing with working buffer.

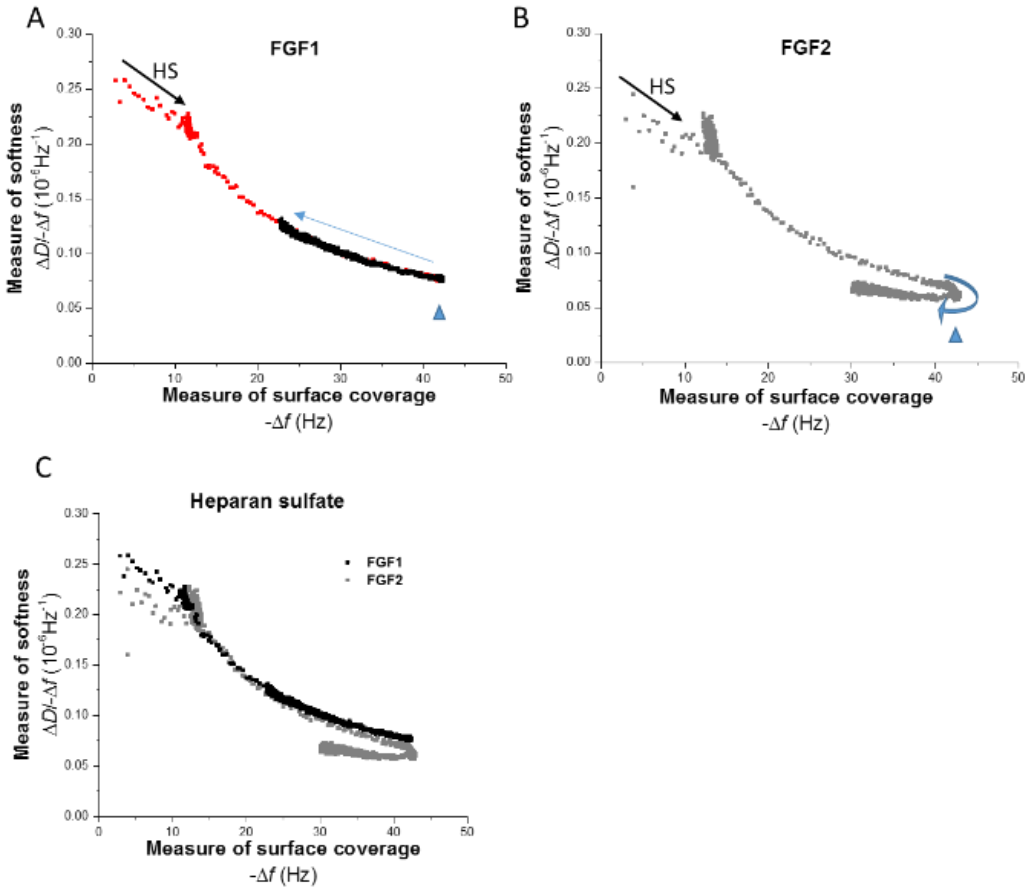


Figure 5.5: FGFs from the FGF1 subfamily bind and rigidify HS brushes.
Parametric plots of *ΔD/-Δf* (a measure of softness) vs. *-Δf* (a measure of surface coverage) for the HS film, first without (until *-Δf* ≈ 12 Hz, process of HS film formation indicated with black arrow) and then with FGFs bound (data extracted from Figure 5.4). HS brushes rigidify progressively upon FGF1 (A) and FGF2 (B) binding. Upon rinsing (the start of rinsing is indicated with a blue arrow head), the FGFs desorbed following protein specific trends (blue arrows). In A, we showed the binding (red) and unbinding (black) of FGF1 in different colours for clarity purposes. C. Overlay of the three plots shown in A and B. All binding curves fall on top of each other, indicating that the three proteins have very similar coverage-dependent effects on HS film morphology. Unbinding curves are distinct, however, with FGF1 but not FGF2 softening upon protein release.

**Quantification of bound HS, FGF1 and FGF2.**

QCM-D frequency changes provide a first estimate of protein binding, but they are also affected by solvent trapping, and by the viscoelastic properties of the GAG-protein film. To measure the amount of molecules actually bound SE was used, it measures the absolute molecular density of each layer of the film. First we characterised the HS brush, which has a density of 1.7 ± 0.1 pmol.cm$^{-2}$ (Figure 5.6). At maximum binding, the amounts of FGF1 and FGF2 bound to HS were equivalent with no significant difference. Assuming a molecular weight of 12 kDa for the HS chains (181), this yielded an average stoichiometry of 6 ± 3 FGF1 and 6 ± 1 FGF2 per

HS chain at maximal loading, hence 1 FGF every 4 disaccharides (Figure 5.6). However, after rinsing with the working buffer, FGF1 dissociated from the brush and stabilised to 2 ± 1 FGF1 per chain or 1 FGF1 every 12 disaccharide, whereas FGF2 stabilised at 4 ± 1 per HS or 1 FGF2 every 6 disaccharide (Figure 5.6).

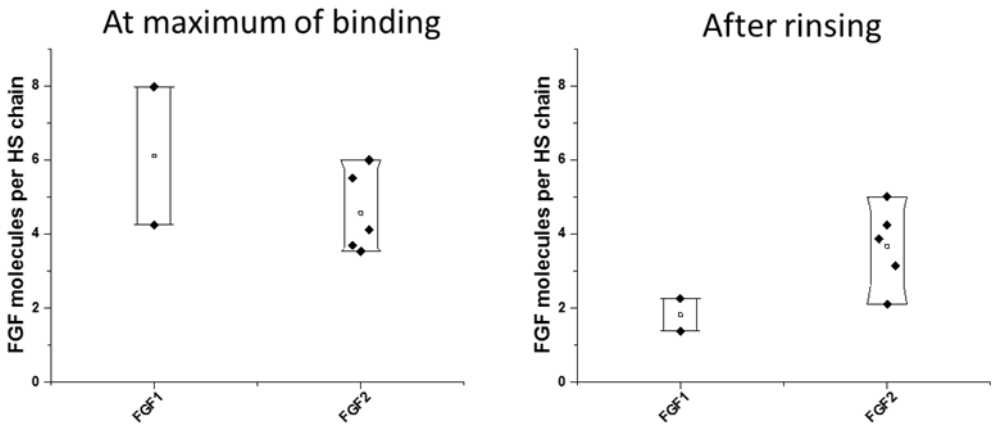


Figure 5.6: Stoichiometry of FGF binding to HS, for proteins of the FGF1 subfamily
Molar FGF surface densities were determined by SE at equilibrium after incubation at 0.28 µM (left), and after rinsing with working buffer for at least 60 minutes (right), and compared to molar HS surface densities obtained in the same measurements. The means comparison test was carried out with a Fisher test at a level of significance of 5 %. The data presented is the range for a minimum of 2 independent measurements.

**Cross-linking of HS brushes by FGF2 and FGF1**

Cross-linking of HS chains by the bound protein can account for the observed rigidification of HS brushes, but other processes, such as collapse of individual HS chains around the protein may also cause this effect. FRAP of fluorescently labelled SAv provides the means to determine whether cross-linking is occurring (148), since this will reduce the lateral diffusion of the fluorescent SAv proxy. FRAP on bare biotinylated HS brushes confirmed that the lateral mobility of the HS brushes is fast and allows full recovery of the fluorescence in the bleached area within 300 seconds (Figure 5.7A). The quantitative analysis of the FRAP data characterised an HS brush as 97 ± 1% mobile with a diffusion constant of 1.7 ± 0.5 $\mu m^2.s^{-1}$ (Supplementary figure 5.2).

Figure 5.7 shows how the mean intensity of the bleached spot recovers over time for a film of bare HS (Figure 5.7A) and for HS films that were incubated with FGFs at 0.28 µM for 30 min and then rinsed with incubation buffer (Figure 5.7B-C). These plots

provide a simple visual comparison of the recovery of fluorescence, and the mobility of the fluorescent SAv with bound HS chains. In addition, Supplementary Fig. 2 provides a quantitative analysis of the size and diffusion constant of the mobile fraction.

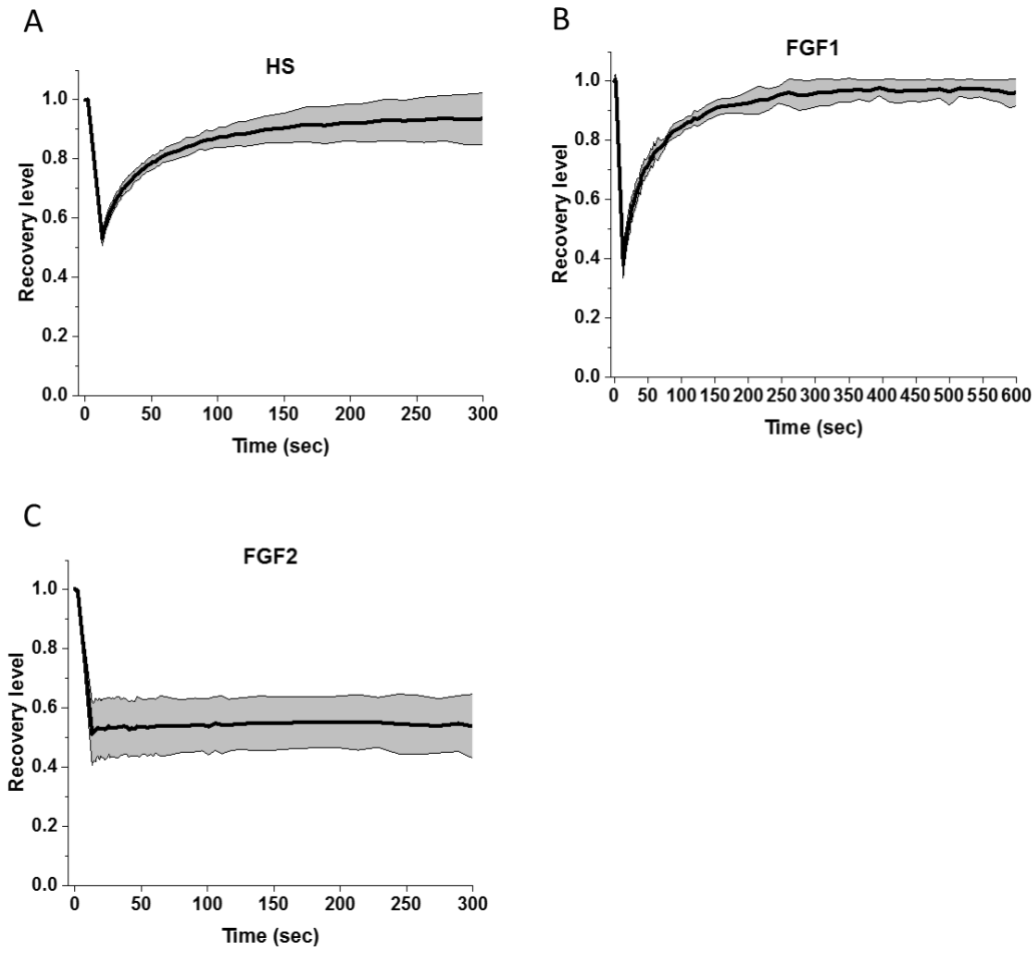


Figure 5.7: FGF2 reduces HS mobility but FGF1 does not.
FRAP curve of atto488-SAv supporting HS (A) HS-FGF1 (B) and HS-FGF2 (C) films. The black curve and the grey region around it are the mean and standard deviation, respectively, of 4 measurements obtained after rinsing with the working buffer.

FGF2 essentially immobilised the HS chains over 600 s (Figure 5.7), the corrected recovery level after bleaching was of 52 ± 1 % was constant during the time of the experiment. In contrast, HS brushes with bound FGF1 recovered up to 100% fluorescence after bleaching and the mobile fraction of the bHS-FGF1 brush remained constant. Comparisons of the mobile fraction and the diffusion constant with the Fisher test between HS and HS-FGF1 indicate that FGF1 does not significantly affect the mobility of HS brushes (Figure 5.7). Thus, the rigidification of

the HS brushes caused by FGF2 is representative of a supramolecular arrangement that restrains the mobility of the HS chains, whereas in the case of FGF1 the rigid state of the film allows the HS brush to be carried around by the lateral diffusion of the lipid. Therefore, these data surprisingly show that although FGF1 and FGF2, which are in the same FGF subfamily, possess a high level of amino acid sequence conservation and the same configuration of secondary HBSs, they differ markedly in their ability to immobilise HS chains. An important conclusion is that the presence of secondary HBSs cannot be the sole predictor of whether an FGF immobilise HS chains. To identify what other property of FGFs may contribute to determining whether the binding of HS chains would lead to cross-linking/immobilisation, measurements were undertaken on FGF4, FGF9, FGF10, FGF17 and FGF18, which are in other FGF subfamilies.

**Interactions of FGF4, FGF9, FGF10, FGF17 and FGF18 with midense HS brushes**

As observed previously (148), the binding of FGF9 bound to HS brushes increased continuously over 60 min, which was associated with an increasing *ΔD* (Figure 5.8). All other FGFs bound to equilibrium within 60 min. In contrast, the binding of FGF2, FGF10, FGF17 and FGF18, like that of FGF1 and FGF2 reached a maximum. The binding of FGF4 was rapid, whereas FGF10, FGF17 and FGF18 (Figure 5.8) bound more slowly. At equilibrium, the *Δf* values ranged from -13 Hz for FGF17 to -18 Hz for FGF10 and -21 Hz for FGF4 and FGF18. Upon rinsing, FGF4, FGF9 and FGF17 showed only small increases in frequency, indicating a low level of protein release, whereas FGF10 and FGF18 were not released, since there was no change in frequency at this point. The corresponding dissipation shifts were negative, and ranged between -0.5 and -2.0 × $10^{-6}$, providing a first indication for relatively strong stiffening of the HS film s. In the case of FGF4 and FGF18, after rinsing the dissipation increased towards its starting level. In contrast, the dissipation for FGF10 and FGF17 remained unchanged after rinsing.

The analysis of the parametric plots (Figure 5.9) provided more information on the morphologies of the FGF bound HS brushes. All these FGFs induced a rigidification of the HS brushes, as evident from the decreasing $\Delta D/-\Delta f$ upon protein binding. FGF9 was not desorbed from the brush upon rinsing, and thus the $\Delta D/-\Delta f$ remained stable at a value of 0.08 × $10^{-6}$.$Hz^{-1}$. FGF4 bound the HS brush until $\Delta D/-\Delta f$ = 0.05 × $10^{-6}$.$Hz^{-1}$. Upon rinsing, a small fraction of the FGF4 desorbed and there was a degree of softness recovery (Figure 5.9B, blue arrow) with the film stabilising at 0.08 × $10^{-6}$.$Hz^{-1}$. In the case of FGF10, $\Delta D/-\Delta f$ = 0.03 × $10^{-6}$.$Hz^{-1}$ at maximal binding and immediately after rinsing, though the film then became more rigid. FGF17 showed a more potent rigidifying effect on the HS brushes that increased considerably after rinsing and the release of some FGF17 from the brush, with a final $\Delta D/-\Delta f$ = 0.01 × $10^{-6}$.$Hz^{-1}$. The same trend was observed for FGF18, but less pronounced, with a final $\Delta D/-\Delta f$ = 0.04 × $10^{-6}$.$Hz^{-1}$. The rigidification of HS brushes depends on the FGF type. The parametric plots of FGF17 and FGF18, which belong to the FGF8 subfamily (Figure 1) are the most similar, whereas the parametric plots for the other FGFs, each of which represents a different subfamily differ more substantially.

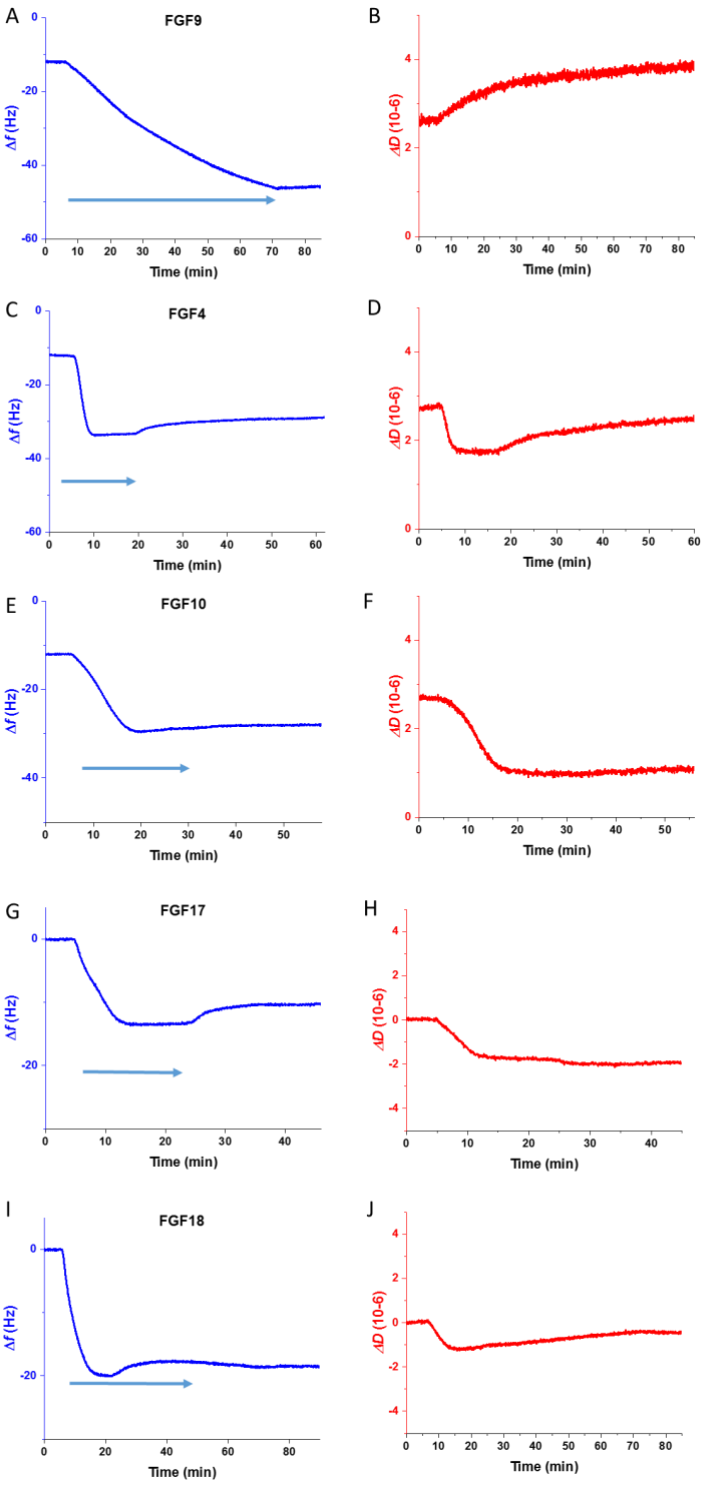


Figure 5.8: QCM-D monitoring of FGF binding to HS brushes.
The frequency (panels A, C, E, G and I) and dissipation (panels B, D, F, H and J) shifts presented are data acquired for the 3rd overtone and offset after the formation of the HS brush. FGF9 (panels A and B), FGF4 (panels C and D), FGF10 (panels E and F), FGF17 (panels G and H) and FGF18 (panels I and J) were infused at 0.28 µM until equilibrium or a maximum of 60 minutes (blue arrow) before rinsing with the working buffer. The rinsing step was carried out until the system reached another equilibrium or for 30 minutes.

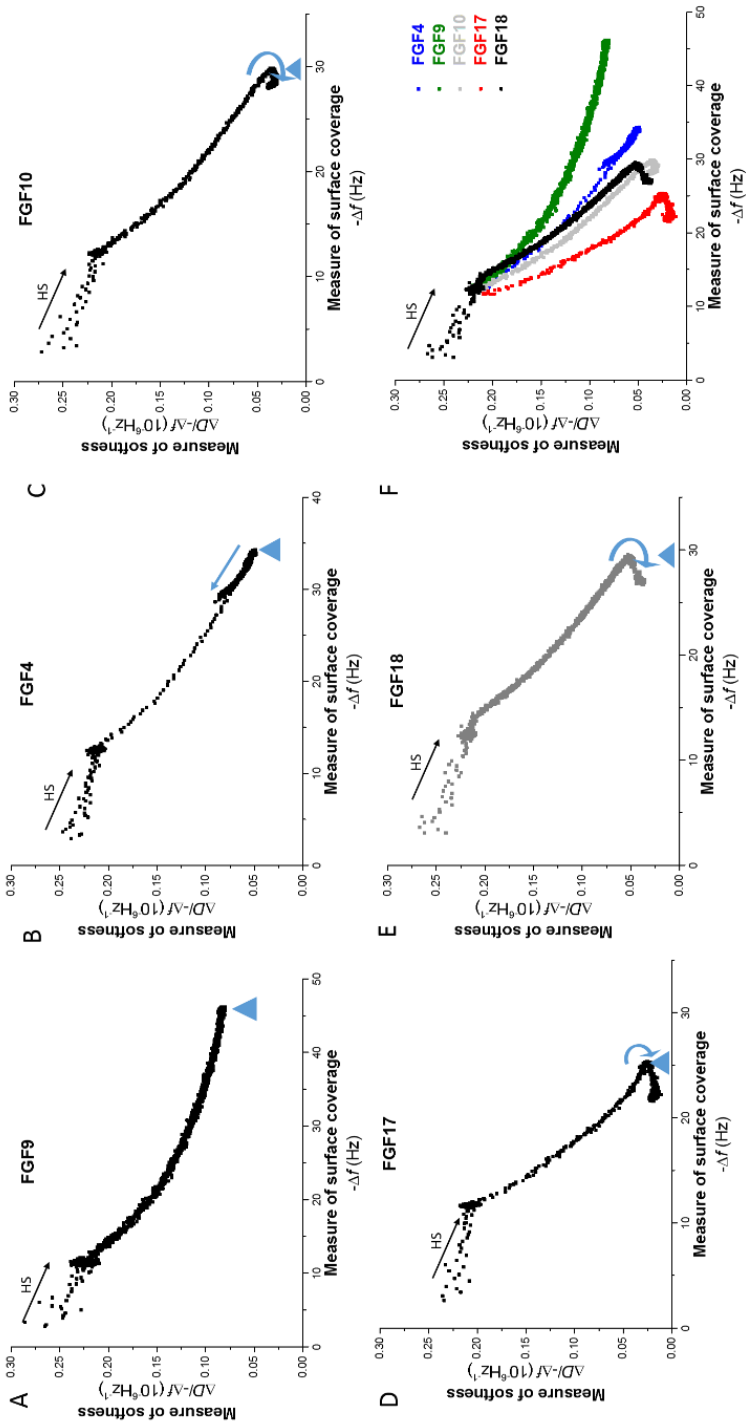


Figure 5.9: HS film rigidification by FGFs from subfamilies other than FGF1
Parametric plots of *ΔD/-Δf* (a measure of softness) vs. *-Δf* (a measure of surface coverage) for the HS film, first without (until *-Δf* ≈ 12 Hz, process of HS film formation indicated with black arrow) and then upon FGF9 (A), FGF4 (B), FGF10 (C), FGF17 (D) and FGF18 (E) binding. HS brushes rigidify progressively upon FGF binding for all FGFs. Upon rinsing (the start of rinsing is indicated with a blue arrow head), the HS films released FGFs and recovered some softness (FGF4 and FGF10) or became more rigid (FGF17 and FGF18). The blue arrows represent the trends upon rinsing. The overlap of the parametric plots (F) shows that each FGF follows its own rigidification trend unlike previously observed amongst proteins of the FGF1 sub-family (Figure 5.5).

SE was then used to quantify the amount of HS, and of FGF bound, to assess the binding stoichiometry (Figure 5.10). At maximal binding, the stoichiometries were in the range of 2 to 6 FGF molecules per HS chain. Specifically, there were 4 ± 1 FGF4, 2 ± 1 FGF9, 5 ± 1 FGF10, 6 ± 1 FGF17 and 2 ± 1 FGF18 per HS chain. After rinsing and stabilisation, the stoichiometries were 2 ± 1 FGF4, 1 ± 1 FGF9, 4 ± 1 FGF10, 5 ± 1 FGF17 and 2 ± 1 FGF18 per HS chain. The HS used in this study is polydisperse, and has an average molecular weight of 12 kDa, and so an average of 22 dissacharide units (assuming a disaccharide is 0.50-0.55 kDa (180) carrying 1.4 sulfate groups per disaccharide (124). Thus this translates to a number a dissacharide available for the FGFs to bind: 1 FGF4 every 5, 1 FGF9 every 10, 1 FGF10 every 4, 1 FGF17 every 3 and 1 FGF18 every10 disaccharides. The differences observed in maximum of binding and in final binding after rising will reflect the selectivity of the different FGFs for specific sulfated structures in the HS chains (56, 182-184). While the results demonstrate that the proteins bound and rigidified the HS brushes, they do not identify the cause of this rigidification.

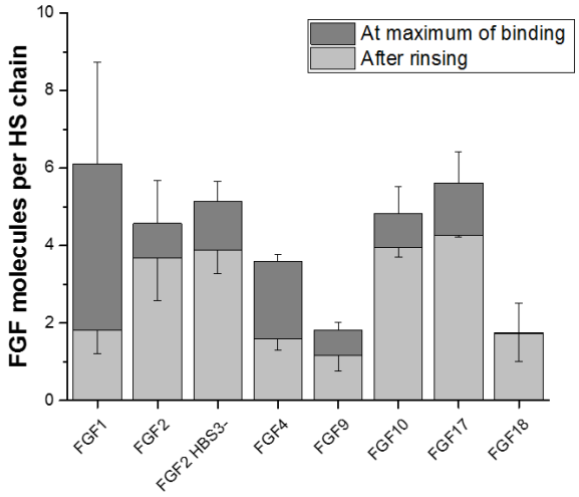


Figure 5.10: Stoichiometry of FGF binding to HS, for all tested FGFs.The molar FGF surface densities were determined by SE at equilibrium after incubation at 0.28 µM, and after rinsing with working buffer for a minimum of 60 minutes, and compared to molar HS surface densities obtained in the same measurements. The data presented is for two independent measurements, and the mean values and standard deviations are indicated.

Two possible mechanisms for rigidification are the collapse of HS chains around a protein or to the protein causing the cross-linking of the HS chains. These can be distinguished by measuring the mobility of the brushes in the presence of the FGF.

**Mobility of HS chains binding FGF4, FGF9, FGF10, FGF17 and FGF18**

FRAP of fluorescent SAv was used to determine whether the observed rigidification of the HS chains was due their cross-linking by the FGFs. When HS-FGF4 and HS-FGF9 bound to HS brushes a quick and complete recovery was observed, reaching 100% recovery within the measurement time (Figure 5.11). Thus, more than 95% of the HS-FGF4 and HS-FGF9 brushes remained mobile. Though HS-FGF9 recovered fluorescence slightly faster than HS-FGF4; their mobility parameters were not significantly different from one another nor different from the ones of HS-FGF1 (Supplementary figure 5.5). Therefore, the monovalent FGF9 (possessing just a HBS1) and the divalent FGF4 (possessing HBS1 and HBS3) interact with HS in the same manner as the trivalent FGF1 (HBS1, HBS2 and HBS3). These data support the conclusion drawn earlier from the comparison of FGF1 and FGF2 that the number of HBS does not account fully for the property of an FGF to immobilise HS brushes.

In contrast HS-FGF10, HS-FGF17 and HS-FGF18 showed slower and partial recoveries of the fluorescence (Figure 5.11). These three proteins induced a significant reduction in the mobile fractions of the SAv and this was accompanied by lower diffusion constants for the mobile fraction, compared to the bare HS brushes (Supplementary figure 5.5).

The mobility parameters of HS-FGF17 were significantly lower than those of the bare HS brush (Supplementary figure 5.5), as only 67 ± 1% of the HS-FGF17 brush was mobile with a diffusion constant of 0.82 ± 0.20 $\mu m^2.s^{-1}$ whereas 95 ± 2 % of the bare HS brush is mobile with a diffusion constant of 1.82 ± 0.30 $\mu m^2.s^{-1}$. HS-FGF10 and HS-FGF18, respectively, presented mobile fractions of 65 % and 53% and diffusion constants of 0.63 ± 0.30 $\mu m^2 s^{-1}$ and 1.64 ± 0.19 $\mu m^2 s^{-1}$. A comparison of the mobility parameters show that HS-FGF10 and HS-FGF17 are equivalent in diffusion and so immobilise HS brushes to the same extent (Supplementary figure 5.5). FGF18, which is in the same subfamily as FGF17 possessed different immobilisation parameters.

That FGF1 differs from FGF2 and FGF17 from FGF18 in this respect suggests that the property assessed by the measurement of mobility of the HS brush provides insight into how different members of the same subfamily may have diverged in function.

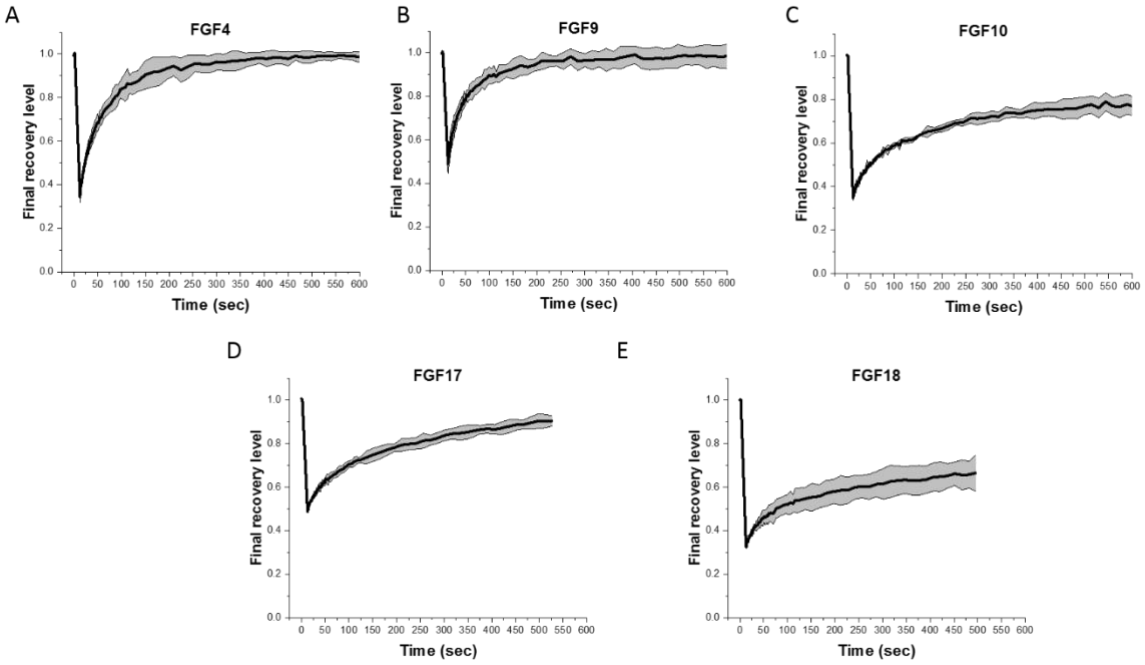


Figure 5.11: Mobility of FGF bound HS brushes as observed in FRAP.
FRAP curve of SAv-atto supporting HS-FGF4 (A), HS-FGF9 (B), HS-FGF10 (C), HS-FGF17 (D) and HS-FGF18 (E) films. The black curve and the grey region around it are the mean and standard deviation, respectively, of 4 measurements obtained after rinsing with the working buffer following or protein incubation.

### Mobility of FGFs in HS brushes

It has previously been postulated that the cross-linking of HS chains by FGFs may impact on the mobility of the FGFs (148). To evaluate the mobility of FGFs in HS brushes, FGF fusion proteins with an N-terminal halotag were used, as described previously (121, 185). Dense and immobile HS brushes were established by saturating the lipid with SAv as described in the methods. The SAv monolayer then served as an anchorage of the biotinylated HS. It was first important to determine whether the halotag had a major effect on the interaction of FGFs with the HS brush. This also provided the opportunity to measure the properties of FGF6 and FGF20, which only remain soluble as N-terminal fusions with HaloTag (121). However, the N-terminal fusions of FGF4, FGF9, FGF17 and FGF18 were not available.

**Halo-FGFs as a model for native FGFs mobility**

QCM-D responses for the binding of 0.28 μM HaloFGF1, HaloFGF2, HaloFGF6, HaloFGF10 and HaloFGF20 to HS brushes are shown in Supplementary figure 5.10. However, *ΔD* increased in all cases and this continued during the desorption of the protein (Supplementary figure 5.10). The HaloTag protein itself, which has a slightly acidic isoelectric point does not bind hep(121). Thus, the difference in the changes in dissipation between the native FGFs and their N-terminal HaloTag fusion counterparts is likely to be due to the presence of the halotag. The latter is attached to the FGF via a flexible linker. Previous work has shown that rigid globular proteins attached via a flexible linker to surfaces can give rise to significant dissipation due to the liquid motion associated with the rocking of proteins upon the small-amplitude MHz mechanical oscillation of the QCM-D sensor surface (186). Thus, the drag of the HaloTag on solvent, aided by the flexible linker is likely to cause the increase in dissipation of HaloFGF compared to native FGFs. The parametric plot of HaloFGF1, HaloFGF2, HaloFGF6, HaloFGF10 and HaloFGF20 binding to an HS brush (Figure 5.12) shows that the despite the increased *ΔD* (Supplementary figure 5.10), the binding of HaloFGF1, HaloFGF2, HaloFGF6, HaloFGF10 and HaloFGF20 to the HS brushes rendered them more rigid, since the softness of the brushes decreases upon binding of the proteins (Figure 5.12). After rinsing of the brushes and the partial desorption of the proteins, the HS-HaloFGF1, HS-HaloFGF6 and HS-HaloFGF10 films recovered some of their softness, but not HS-HaloFGF2 and HS-HaloFGF20. These data indicate that the interaction of the Halo-FGFs is similar to that of the native FGFs, with the difference in dissipation likely being due to the HaloTag protein interacting with solvent.

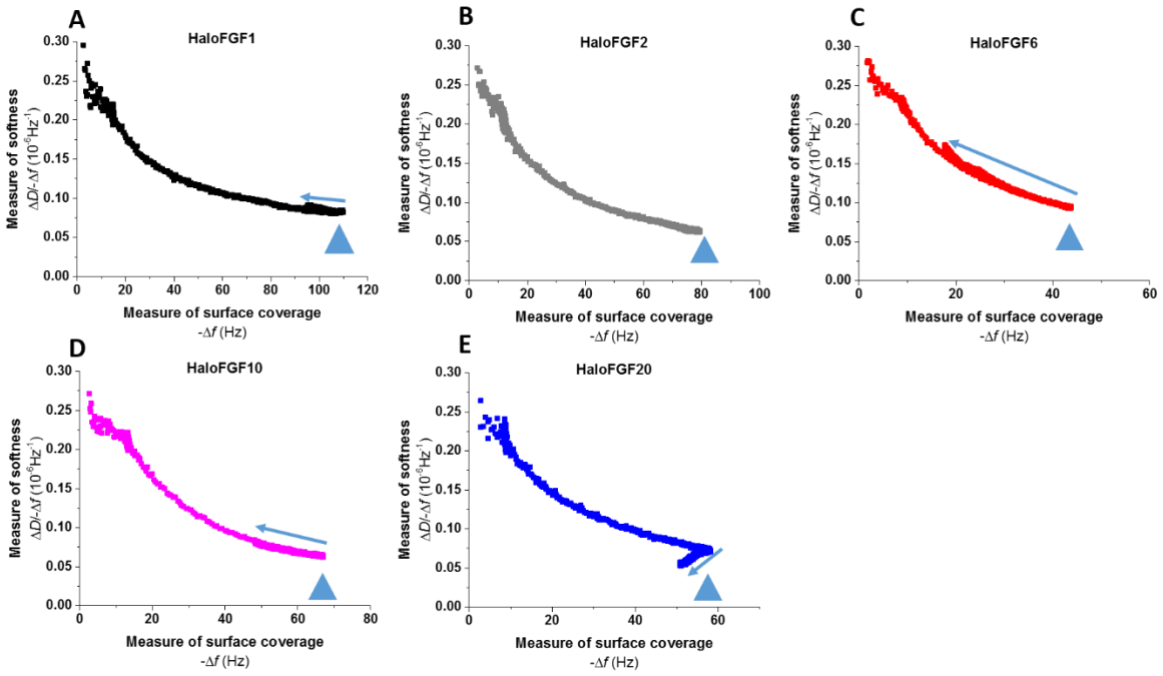


Figure 5.12: Mid-dense HS film rigidification by HaloFGFs.
Parametric plots of *ΔD/-Δf* (a measure of softness) vs. *-Δf* (a measure of surface coverage) for the HS film, first without (until *-Δf* ≈ 12 Hz, process of HS film formation indicated with black arrow) and then with HaloFGFs bound. HS brushes rigidify progressively upon HaloFGF binding for all HaloFGFs (original data presented in Supplementary figure 5.10). Upon rinsing (the start of rinsing is indicated with a blue arrow head), the HS films released FGFs and recovered some softness (HaloFGF6 and HaloFGF10), rigidified (HaloFGF20) or did not change (HaloFGF1 and HaloFGF2). The blue arrows represent the trends upon rinsing.

By SE, we quantified the stoichiometry of HaloFGFs bound per HS chain in mid-dense brushes as described above for native FGFs (Figure 5.13). When we compared the binding of halo-tagged FGFs with the native counterparts (Figure 5.6, Figure 5.10 and Figure 5.13), at the maximum of binding HaloFGF1 and FGF1 bound equivalent amounts, 6 ± 3 FGF1 per HS and 5 ± 2 HaloFGF1 per HS chain. After rinsing, the numbers of FGF1 and HaloFGF1 per HS chain were also not significantly different: 2 ± 1 FGF1 per HS and 4 ± 2 HaloFGF1 per HS chains. Compared to FGF2, the amount of HaloFGF2 protein bound was around half at the maximum of binding, and after rinsing HS brushes contained 3 ± 1 HaloFGF2 per HS, which again is less than observed for FGF2 (5 ± 1 FGF2 per chain). In addition, there was a difference in the level of binding of HaloFGF10 compared to FGF10. Thus, after rinsing the brushes retained 2 ± 1 HaloFGF10 per HS chain compared to 5 ± 1 FGF10 per HS chain (Figure 5.10 and Figure 5.13). The origins of these differences are not clear, but they may be due in

part to a crowding effect, whereby the HaloTag protein obstructs some of the binding sites on HS.

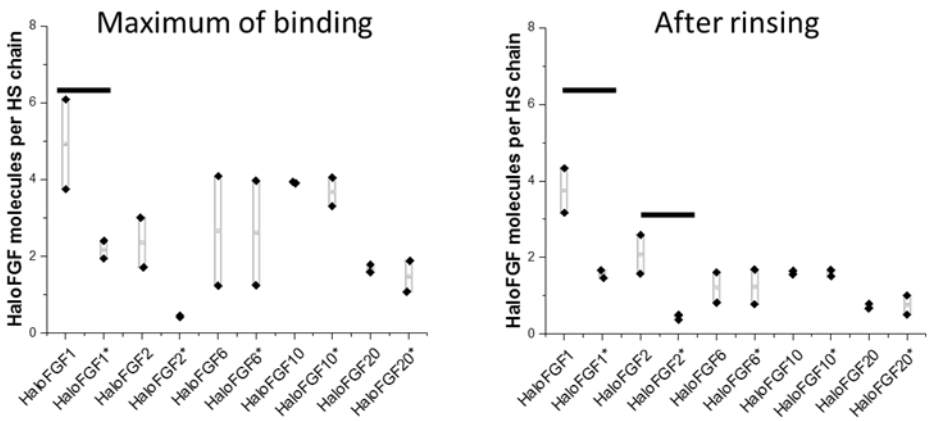


Figure 5.13: Quantification of HaloFGF binding to mid-dense and dense HS brushes.
The molar HaloFGF surface densities were determined by SE equilibrium after incubation at 0.28 µM (left), and after rinsing with working buffer until stabilisation (right), and compared to molar HS surface densities obtained in the same measurements. The data for the binding to dense brushes are marked with an asterisk and means with significant differences are marked with bars above them. The presented is the range of 2 independent measurements.

When we compared the binding of HaloFGFs to mid-dense and dense HS brushes. A difference was observed in HaloFGF1 binding before and after rinsing (Figure 5.13). HaloFGF1 showed a maximum binding of 5 ± 2 HaloFGF1 per HS chain in mid-dense brushes, but only 2 ±1 HaloFGF1 to dense brushes. However, after rinsing, the difference decreased, there was 4 ± 2 HaloFGF1 per HS chain in mid-dense brushes and 2 ± 1 HaloFGF1 per HS chain in dense brushes. The maximum level of binding of HaloFGF2 to mid-dense brushes was also higher than to dense brushes, however, this difference disappeared after rinsing (Figure 5.13). We did not observe any difference in binding stoichiometry of the other HaloFGFs between mid-dense and dense brushes. Thus, the differences in the amounts of Halo-FGFs bound, compared to their native counterparts were at a minimum after rinsing and may relate in part to obstruction of binding sites by the Halo protein. Since the properties of the brushes in terms of rigidity were very similar between Halo-FGFs and native FGFs, the halo-FGFs were considered to be suitable for the analysis of the mobility of the FGFs in the brushes.

**Mobility of HaloFGF in HS brushes**

HaloFGF1, HaloFGF2, HaloFGF6, HaloFGF10 and HaloFGF20 were incubated for 30 to 60 min with an immobile dense HS brush. The immobility of the HS brushes was ensured by using SUVs containing 5% DOPE-CAP-biotin to form SLBs. At this biotin content, dense SAv monolayers are formed and SAv forms two-dimensional crystals that render the SAv-bound HS immobile (Supplementary figure 5.11). Thus, after rinsing, the FRAP of a region of interest was monitored and only the mobility of the labelled proteins was measured. HaloFGFs labelled with fluorescent TMR were bleached in a region of interest and the fluorescence recovery in that area was recorded for 300 or 600 s.

The fluorescence recovery in a region of interest containing TMR labelled HaloFGF1 was followed, HaloFGF1 recovery was continuous and did not return to basal levels by the end of our assays (300 s, Figure 5.14A).Figure 5.14A). The quantitative analysis of HaloFGF1 mobility determined the mobile fraction as 15 ± 3% (Supplementary figure 5.12Supplementary figure 5.12) and a diffusion constant of 0.22 ± 0.08 $\mu m^2.s^{-1}$, represented by the slow fluorescence recovery in the recovery curve of HaloFGF1. In contrast, the fluorescence recovery curve of HaloFGF2 showed that the protein was immobile in the brushes, as no significant change in the recovery level was observed between 0 and 600 seconds (Figure 5.14B). The "mobile" fraction of HaloFGF2 was not detectable (Supplementary figure 5.12).

Labelled HaloFGF10 recovered in two phases, the curves show an initial short burst that was followed by a continuous recovery until stabilisation at 36 ± 7 % of the original level (Figure 5.14D). The mobile fraction of HaloFGF10 bound to the HS brush was 32 ± 5% and its diffusion constant 0.18 ± 0.08 $\mu m^2.s^{-1}$ (Supplementary figure 5.12). Compared to HaloFGF2 that was immobile, both HaloFGF1 and HaloFGF10 were somewhat mobile in the HS brushes, with low and slow mobile fractions. There was no significant difference between their diffusion constants, but the mobile fraction of HaloFGF1 was smaller than the one of HaloFGF10.

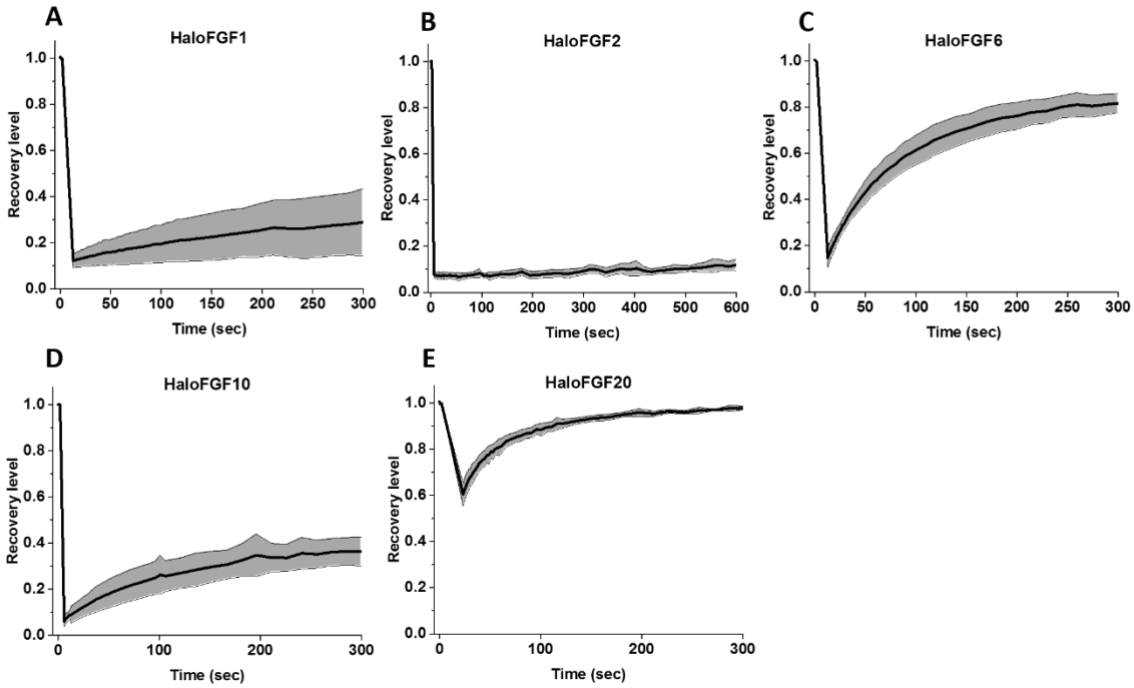


Figure 5.14: Mobility of HaloFGFs in HS films.
FRAP curve of TMR565 labelled HaloFGF1 (A), HaloFGF2 (B), HaloFGF6 (C), HaloFGF10 (D) and HaloFGF20 (E) in HS films. The black curve and the grey region around it are the mean and standard deviation, respectively, of 3 to 6 measurements obtained after rinsing with the working buffer.

In the case of HaloFGF6 the fluorescence recovery was rapid, and fluorescence reached 82 ± 4% of the original level (Figure 5.14C). HaloFGF6 was 90 ± 5% mobile with a diffusion constant of 0.51 ± 0.15 $\mu m^2.s^{-1}$ (Supplementary figure 5.12). The recovery of HaloFGF20 was rapid and gradual and virtually complete, at 98 ± 1% (Figure 5.14D). Almost all the Halo-FGF20 was mobile 91 ± 2%) and had a diffusion constant of 0.15 ± 0.10 $\mu m^2.s^{-1}$ (Supplementary figure 5.12). Thus, both HaloFGF6 and HaloFGF20 were mobile in HS brushes, with HaloFGF20 diffusing rather faster than HaloFGF6.

Taken together, we identified 3 distinct dynamics of diffusion for the HaloFGFs in HS brushes: (1) immobile, HaloFGF2 did not present any fluorescence recovery in the bleached region of interest, (2) slightly mobile, HaloFGF1 and HaloFGF10 with a mobile fraction well below 50% and (3) mobile, HaloFGF6 and HaloFGF20 with a mobile fraction close to 100% (Figure 5.17 and Supplementary figure 5.10).

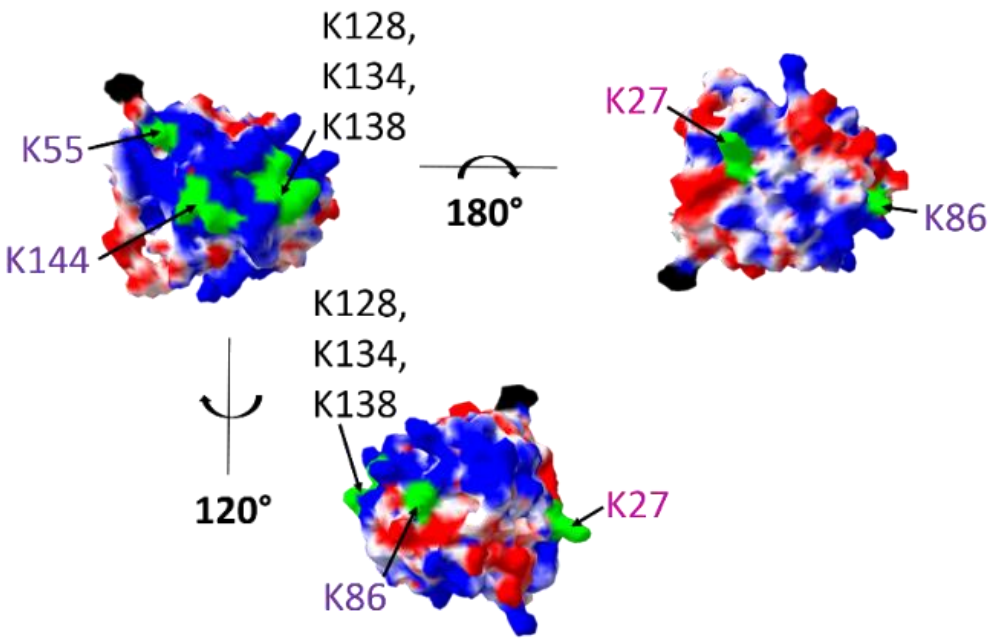


Figure 5.15: Surface electrostatic potential mapping and position of heparin binding lysines in FGF2.
Identified hep binding lysines in HBS1, HBS2 and HBS3 in FGF2 (1BLA) are labelled in green (103). The electrostatic mapping of partial charges [-1.8 (red), 0 (white) and +1.8 (blue)] was generated using the Poisson-Boltzmann algorithm in SPDBV. The N-terminal residue is labelled in black.

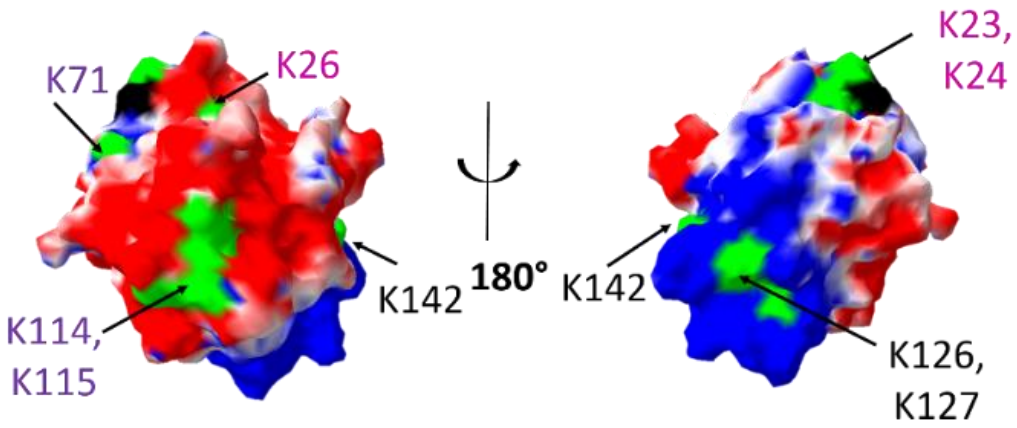


Figure 5.16: Surface electrostatic potential mapping and position of heparin binding lysines in FGF1.
Identified hep binding lysines in HBS1, HBS2 and HBS3 in FGF2 (1BLA) are labelled in green (104). The electrostatic mapping of partial charges [-1.8 (red), 0 (white) and +1.8 (blue)] was generated using the Poisson-Boltzmann algorithm in SPDBV. The N-terminal residue is labelled in black.

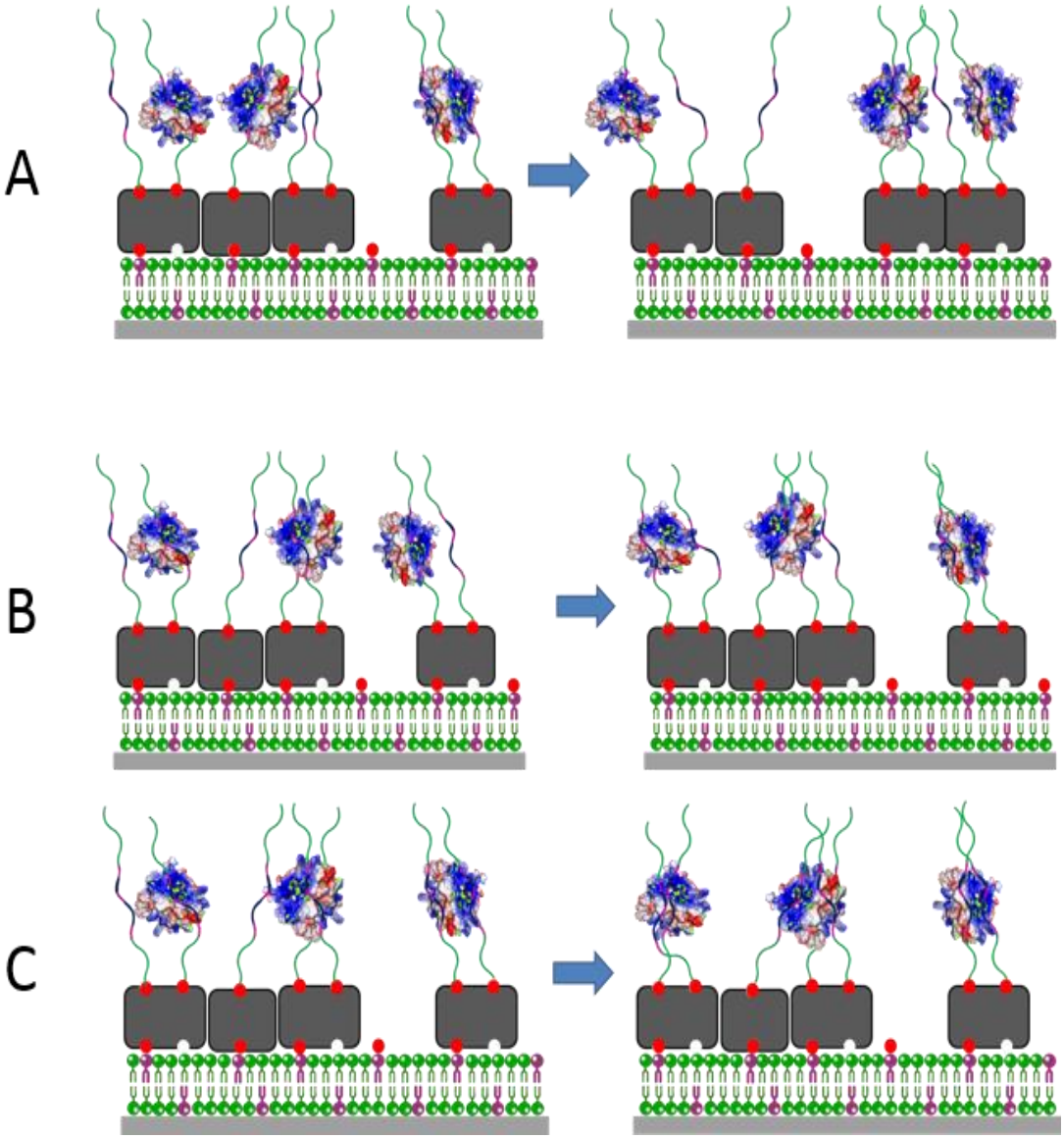


Figure 5.17: Representative sketch of supramolecular events in HS-FGF brushes.
A. The FGF protein is not permanently cross-linking HS chains which allows the chains to be mobile (carried by the SAv) and is mobile in the brushes. B. The FGF protein is transiently cross-linking HS chains, thus they are slightly mobile. The FGF is mobile in the brushes, it travels from chain to chain. C. The FGF protein is stably cross-linking HS chains, thus they are immobile. The FGF are tightly bound to the chains and do not diffuse in the brush.

**Discussion**

The FGFs represent a group of a group of evolutionary related proteins, with well characterised HBSs and binding preferences for particular structures in the polysaccharide (101-103). These properties of FGFs follow their phylogeny, established from their amino acid sequence. Thus, as for FGFR isoform preferences (115, 175, 176), the pattern of HBSs and the saccharide binding selectivity are more

similar for members of the same subfamily, than for members from different subfamilies (56, 104). This indicates that these properties which provide functional differences between FGFs have been under natural selection pressure (56, 104).

The HS brush provides a simple mimetic of one component of the extracellular matrix, HS, and a means to interrogate the interactions between proteins and the polysaccharide matrix quantitatively. In the first such measurements, using FGF2 and FGF9, it was found that the number of HBSs in FGFs correlated with their cross-linking of HS chains (148). Thus, FGF2, which has three HBSs (103) was found to cross-link and so immobilise HS chains in the brush, whereas FGF9, which has just a canonical HBS1 (104) did not (148). The present work aimed to test whether this might be a general principle, that is, proteins with multiple HBSs would possess the property of cross-linking HS chains. The importance of cross-linking HS chains is twofold. First, it would reduce the mobility of proteins in the ECM, and therefore steepen diffusion gradients. In the extreme, a protein would be immobile and require ECM degradation to diffuse. Second, crosslinking HS chains will change the stiffness of ECM, and so might have an effect on cellular mechanical signalling. Such cross-crosslinking can be proposed after observation of the stiffening of the brush accompanied by a decrease in dissipation in QCM-D. Relatively stable cross-linking is confirmed by a significant reduction of the mobile fraction and diffusion constant of an HS film in the presence of an FGF (FRAP). The current results demonstrate that the presence of multiple HBSs is necessary, but does not in itself bestow the property of stably cross-linking HS chains to an FGF. Thus, FGF1, which possesses the same pattern of three HBSs on its surface as FGF2 (56, 103, 104), does not cross-link HS chains stably. Thus, though it does cause a stiffening of the HS brush, the mobility of the SAv as reported by FRAP remains high (Figure 5.7 and Supplementary figure 5.2). FGF4, which has two HBSs, also does not cross-link HS chains stably (Figure 5.11 and Supplementary figure 5.5). Similarly, HaloFGF6, which is in the FGF4 subfamily and possesses two HBSs, fails to cross-link HS stably (Supplementary figure 5.13). However, other bivalent FGFs, FGF17 and FGF18 (with HBS1 and HBS2), and trivalent FGF10 and HaloFGF10 (HBS1, HBS3 and HBS4), cross-linked and partially immobilised the HS brushes (Figure 5.11

and Supplementary figure 5.13). The question arises as to what additional factor(s) may contribute to determining whether a protein may cross-link HS chains stably.

One property that might explain why an FGF with multiple HBSs does not cross-link HS chains stably is structural, based on the surface between the HBSs. If this was neutral or basic it would not repel the chains, hence these may be able to wrap around the protein. In contrast if HBSs were separated by an acidic border, this would repeal the highly anionic HS, and hence the multiple HBSs would be more likely to engage different HS chains. Alternatively, the kinetics of binding of the FGFs to the HS chain could allow transient crosslinking, through cycles of dissociation-association. This would not be detected as crosslinking on the time scale of the FRAP experiments. Rather than full dissociation, a mechanism analogous to sliding proposed to account for FGF diffusion in extracellular matrix (187) would allow the HBSs of an FGF to exchange HS chains without losing contact with a polysaccharide.

The surface electrostatic potential of FGF2 (Figure 5.15), historically called basic FGF, presents a rather globally basic (blue) surface with some acidic (red) clusters. Although FGF2 is a very basic protein, the distribution of the surface charges results in the isolation of HBSs from one another by these acidic clusters. Thus, HBS1 (K128 to K144), HBS2 (K86, K119), HBS3 (K27 to K30) in FGF2 are isolated by acidic borders. These borders comprise E87D88E89 and D99E100 that isolate HBS1 from HBS2 and D99E100 and E67E68 isolating HBS3 from HBS1 and HBS2. In the case of FGF1 (Figure 5.16), historically called acidic FGF, because it has an acidic isoelectric point, its surface presents a predominantly acidic surface. Despite this, the distribution of surface charge results in HBS1 (K126 to K142), HBS2 (K71, K114K115) and HBS3 (K23 to K26) forming an uninterrupted basic surface. Thus, HBS1 is connected to HBS2 by a basic/neutral surface contributed by the side chains and peptide bonds of Y29, S31, G33G34, F36, R49 and R51. HBS2 is connected to HBS3 by the basic surface of Y22 and T73. Therefore, the HBSs in FGF1 may bind a single HS chain rather than crosslinking different chains.

Examination of the surface electrostatic potential of the other FGFs supports the idea that isolation of HBSs by acidic borders is required for a protein with multiple HBSs to cross-link HS brushes. FGF4, has an HBS3 as a secondary HBS. However the hep

binding amino acids of HBS3 are not isolated from HBS1 (Supplementary figure 5.3), K142 (HBS1) and K158 (HBS3) are connected by Y172. The structure of FGF6 has not been resolved, however based on the structure of FGF4 (PDB: 4IJT), here again, the HBSs are likely not to be isolated. HBS1 and HBS3 are connected by P112Y113 and R132. Both FGF4 and HaloFGF6 did not cross-link HS chains. FGF9, contains HBS1 only and did not cross-link HS brushes as previously (148) described and verified here (Supplementary figure 5.4). FGF10, like other members of the FGF7 subfamily, has a canonical HBS1, an HBS4 perpendicular to the HBS1 and an HBS3 (56, 104). Whereas HBS4 and HBS1 are in contact on the surface and so offer a large binding surface to HS, with at least two different dispositions of the HS chain, there is an HBS3 N-terminal to the first beta strand (104). The electrostatic mapping of the FGF10 shows that HBS3 is isolated by an acidic/neutral border from HBS1 and HBS4 (Supplementary figure 5.6). This border is composed of Y130, V206 and H207. FGF17 and FGF18 were found to slightly immobilise HS brushes in FRAP measurements and so cross-link HS chains. FGF17 and FGF18 are from the same subfamily and share similar HBSs: HBS1 and HBS2. Their surface electrostatic potentials show acidic borders isolating their HBSs (Supplementary figure 5.7and Supplementary figure 5.8). In FGF17, K82 (HBS1) is isolated from K76 (HBS2) by an E78D79G80 acidic border. In FGF18, the constituents of this acidic border are: E103, E105 and E78D79. These isolate HBS1 (K113 to K119) from HBS2 (K82, K102). FGF20 may have a secondary HBS, consisting a single K205 close to the N-terminal, which is separated from the neighbouring HBS1 residues by an acidic border (56). However, the present results, which demonstrate no cross-linking of HS by FGF20 argue that this is not an independent binding site.

The above structural explanation, combining multiple HBSs and acidic borders would appear to be explain whether an FGF can crosslink HS chains. However, it does not explain why some FGF10, FGF17 and FGF18 only cause partial crosslinking. In FRAP experiments with these FGFs there is a significant mobile fraction of SAv, as well as the immobile fraction (Supplementary figure 5.5), which is a hallmark of stable crosslinking.

In terms of affinity and kinetics, there are no direct measurements on the secondary HBSs of FGFs. One study using synthetic peptide derived from the amino acid sequence of FGF2 indicates that its secondary HBSs are likely to be of low affinity and possess rapid off rates (102). However, when an FGF is bound to the polysaccharide *via* its HBS1, proximity effects would mitigate the lower affinity. Indeed, the selective identification of lysine side chains involved in hep binding in FGFs requires a stable interaction during the initial 5 min protection step (103). Data acquired by this approach (56, 103, 104) demonstrate that the majority of the lysine side chains remain bound over 5 min. There are instances where a single lysine is both biotinylated (so remains bound) and acetylated (has dissociated from the polysaccharide during the 5 min protection step). However, only some lysines in a given HBS are in such a dual state. Consequently, over 5 min, it would appear that neither primary nor secondary HBSs fully dissociate from the polysaccharide. This would seem to preclude cycles of dissociation-association explaining the partial cross-linking of HS chains by FGF10, FGF17 and FGF18 that have multiple HBS.

Polysaccharide binding site exchange, is compatible with the data on modification of lysine residues. This mechanism does not require exposure of the lysine side chains to solvent. While there are no data on heparin-binding proteins, biophysical analysis of DNA binding proteins indicates that these not only slide along an individual strand of DNA but can exchange between strands without dissociating from the nucleic acid polymer (188).Five of the FGFs were available as Halo-tagged proteins and so could be used to measure the mobility of the FGF itself. There was some correspondence between an FGF's ability to crosslink HS chains and its mobility in the HS brush. This holds for FGF2 (crosslinks and immobile), FGF10 (partly immobile and partly crosslinks), FGF6 and FGF20 (do not cross-link and highly mobile). However, FGF1 is a puzzle in this respect, since it does not cross-link HS chains, yet is only partly mobile.

FGF mobility has been measured in various cell systems, most recently in rat mammary fibroblasts. The present results have some differences with those acquired in these cells. The most striking include the lack of mobility of FGF2 (mobile in cells), the mobility of FGF10 (immobile in cells) and the binding and mobility of FGF20 (failed to bind fibroblast pericellular matrix). It is not known to what extent this

fibroblast pericellular matrix is representative. In any case these difference highlight that the HS brush is a model. Extracellular matrix is far more complex. The HS itself may be more complex in structure, endogenous HS binding proteins may affect HS chain structure and there are other sulfated GAGs present. Thus, the extent to which the physical basis of interaction of an FGF with HS determines the dynamics of that FGF in extracellular matrix must depend also on the properties of that extracellular matrix.

**Acknowledgments**

The authors would like to acknowledge Elisa Migliorini (University Grenoble Alpes) for assistance in setting up the fluorescence recovery after photobleaching (FRAP) assays, Dhruv Thakar (University Grenoble Alpes) for providing the biotinylated heparan sulfate, Phuong Thao Bui (University of Liverpool) for providing FGF1, FGF4 and FGF17, Pawin Ngamlert (University of Liverpool) for providing HaloFGF1 and Changye Sun (University of Liverpool) for providing HaloFGF10.

This work was supported by the joint PhD fellowship program of the University of Liverpool and CIC BiomaGUNE (to A.B.), the Spanish Ministry of Competitiveness and Innovation (project MAT2014-54867-R; to R.P.R.), the European Research Council (Starting Grant "JELLY" 306435; to R.P.R.) and the North West Cancer Research, the Cancer and Polio Research Fund (to D.G.F).

## Supplementary figures

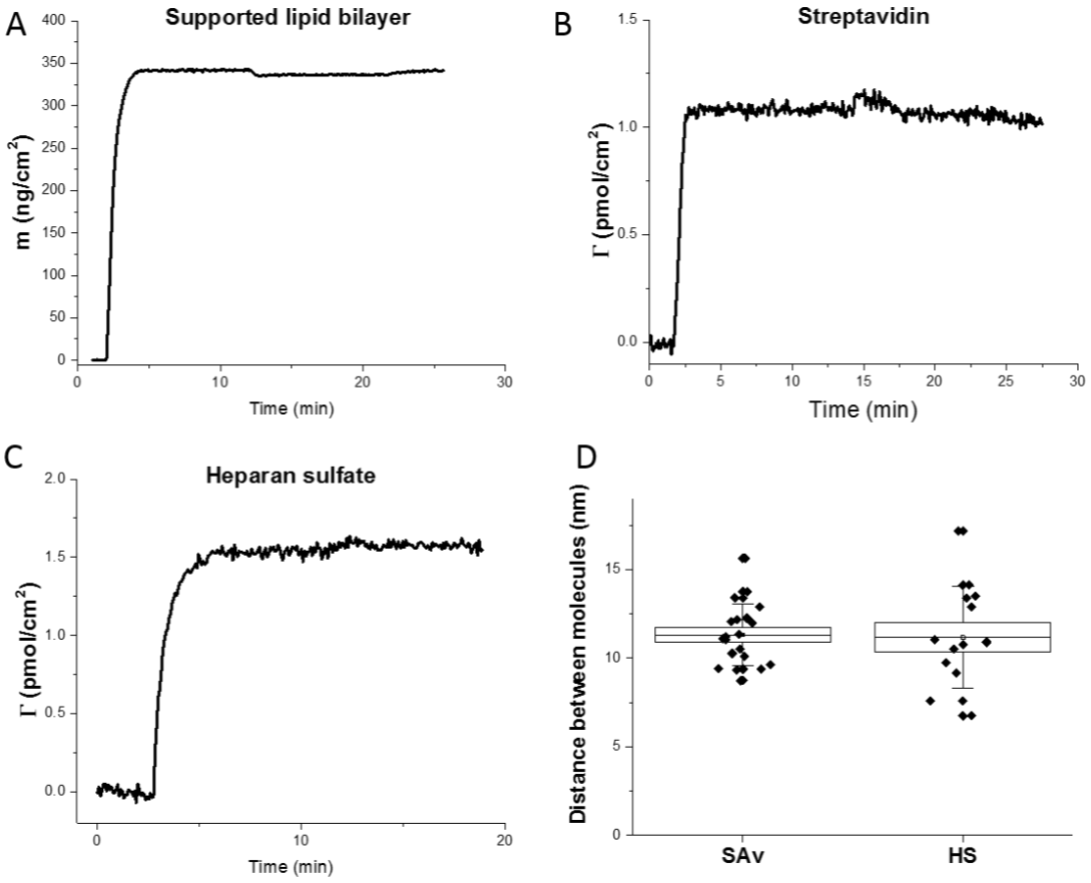


Supplementary figure 5.1: Quantitative characterisation of a mid-dense HS brush by SE.
A. Real time monitoring of SLB formation on a silicon oxide wafer. SUVs containing 99.5:0.5 mol:mol DOPC:DOPE-CAP-biotin were injected in the SE chamber to a final concentration of 50 µg.mL$^{-1}$ and the areal mass density (m) was extracted from the SE data, the SLB obtained was characterised by m= 345 ± 12 ng.cm$^{-2}$ (mean ± standard deviation of 23 experiments). B. Real time monitoring of the binding of SAv on the SLB. SAv was injected to a final concentration of 20 µg.mL$^{-1}$, and the surface coverage at saturation was, Γ= 1.7 ± 0.1 pmol.cm$^{-2}$ was extracted from the SE data. C. Real time monitoring of the anchoring of biotinylated HS (HS) to the SAv layer. HS was injected to a final concentration of 5 µg.mL$^{-1}$, and the areal mass density at saturation was Γ= 1.2 ± 0.3 pmol.cm$^{-2}$ (assuming $M_w$ = 12 kDa). D. Estimated root-mean-square distance between molecules of SAv and HS. A box plot of the standard error is presented with the mean of the values (black diamonds) marked by a line. The whiskers represent the standard deviations.

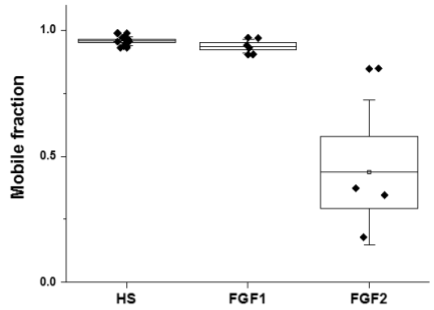


Mean difference

| Factor | bHS | FGF1 | FGF2 |
|---|---|---|---|
| bHS | | -0.02 | **-0.52** |
| FGF1 | | | **-0.50** |
| FGF2 | | | |

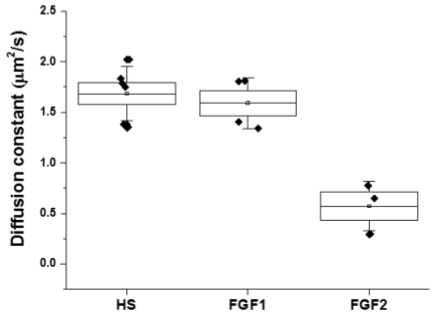


Mean difference (µm²/s)

| Factor | HS | FGF1 | FGF2 |
|---|---|---|---|
| HS | | -0.09 | **-1.11** |
| FGF1 | | | **-1.02** |
| FGF2 | | | |

Supplementary figure 5.2: Quantitative analysis of the effect of FGF1 and FGF2 on HS mobility.
Time-resolved profile analysis was used to extract the size (top) and diffusion constant (bottom) of the mobile fraction from FRAP data obtained before (HS) and after 30 min incubation with FGFs at 0.28 µM and rinsing with working buffer. A box plot of the standard error is presented with the mean of the values (black diamonds) marked by a line. The whiskers are indicate to the standard deviations. The mean comparisons tests (right panels) were carried out with a Fisher test at a level of significance of 5 %. The tables present the mean difference between factors; significant differences are highlighted in bold. The data presented is for a minimum of 3 independent measurements.

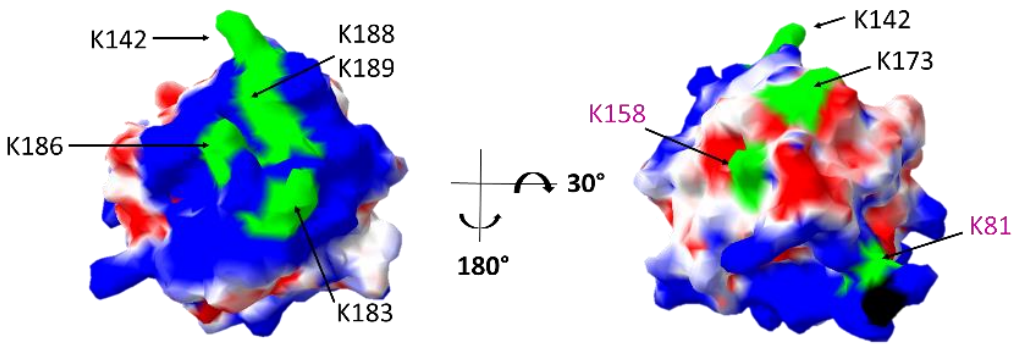


Supplementary figure 5.3: Surface electrostatic potential mapping and position of heparin binding lysines in FGF4.
Identified heparin binding lysines in HBS1 and HBS3 in FGF4 (1IJT) are labelled in green (56). The electrostatic mapping of partial charges [-1.8 (red), 0 (white) and +1.8 (blue)] was generated using the Poisson-Boltzmann algorithm in SPDBV. The N-terminal residue is labelled in black.

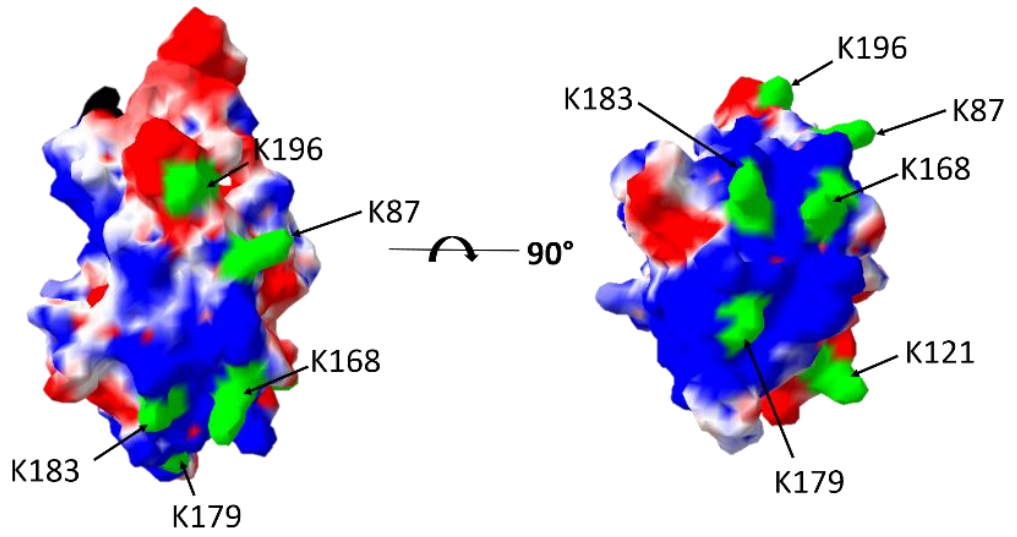


Supplementary figure 5.4: Surface electrostatic potential mapping and position of heparin binding lysines in FGF9.
Predicted heparin binding lysines in HBS1 of FGF9 (1IHK) are labelled in green (56). The electrostatic mapping of partial charges [-1.8 (red), 0(white) and +1.8 (blue)] was generated using the Poisson-Boltzmann algorithm in SPDBV. The N-terminal residue is labelled in black.

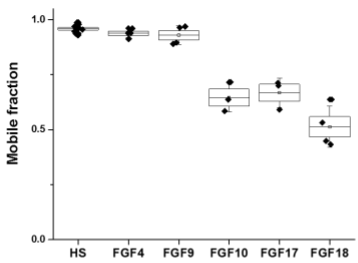


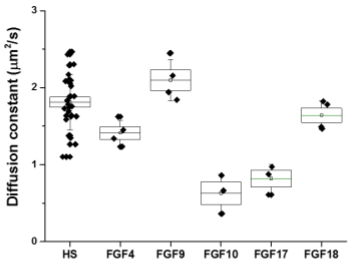


| Factor | HS | FGF1 | FGF2 | FGF4 | FGF9 | FGF10 | FGF17 | FGF18 |
|---|---|---|---|---|---|---|---|---|
| **HS** | | **-0.02** | **-0.52** | **-0.02** | **-0.03** | **-0.31** | **-0.29** | **-0.45** |
| **FGF1** | | | **-0.50** | 0.00 | -0.01 | **-0.29** | **-0.27** | **-0.42** |
| **FGF2** | | | | **0.49** | **0.49** | **0.20** | **0.22** | 0.07 |
| **FGF4** | | | | | -0.01 | **-0.29** | **-0.27** | **-0.42** |
| **FGF9** | | | | | | **-0.28** | **-0.26** | **-0.42** |
| **FGF10** | | | | | | | 0.02 | -0.13 |
| **FGF17** | | | | | | | | -0.15 |
| **FGF18** | | | | | | | | |

| Factor | HS | FGF1 | FGF2 | FGF4 | FGF9 | FGF10 | FGF17 | FGF18 |
|---|---|---|---|---|---|---|---|---|
| **HS** | | -0.09 | **-1.11** | **-0.40** | 0.29 | **-1.18** | **-0.99** | -0.17 |
| **FGF1** | | | **-1.08** | -0.18 | 0.51 | -0.96 | -0.77 | 0.05 |
| **FGF2** | | | | **0.90** | **1.59** | 0.12 | 0.31 | **1.13** |
| **FGF4** | | | | | 0.69 | -0.78 | -0.59 | 0.23 |
| **FGF9** | | | | | | **-1.47** | **-1.28** | **-0.46** |
| **FGF10** | | | | | | | 0.19 | **1.01** |
| **FGF17** | | | | | | | | **0.82** |
| **FGF18** | | | | | | | | |

Supplementary figure 5.5: Quantitative analysis of the effect of FGFs on HS mobility. Time-resolved profile analysis was used to extract the size (left) and diffusion constant (right) of the mobile fraction from FRAP data obtained before (HS) and after 30 min incubation with FGFs at 0.28 µM and rinsing with working buffer. The mean comparison tests (bottom panels) were carried out with a Fisher test at a level of significance of 5 %. The tables present the mean difference between factors; significant differences are highlighted in bold. The data presented is for a minimum of 3 independent measurements

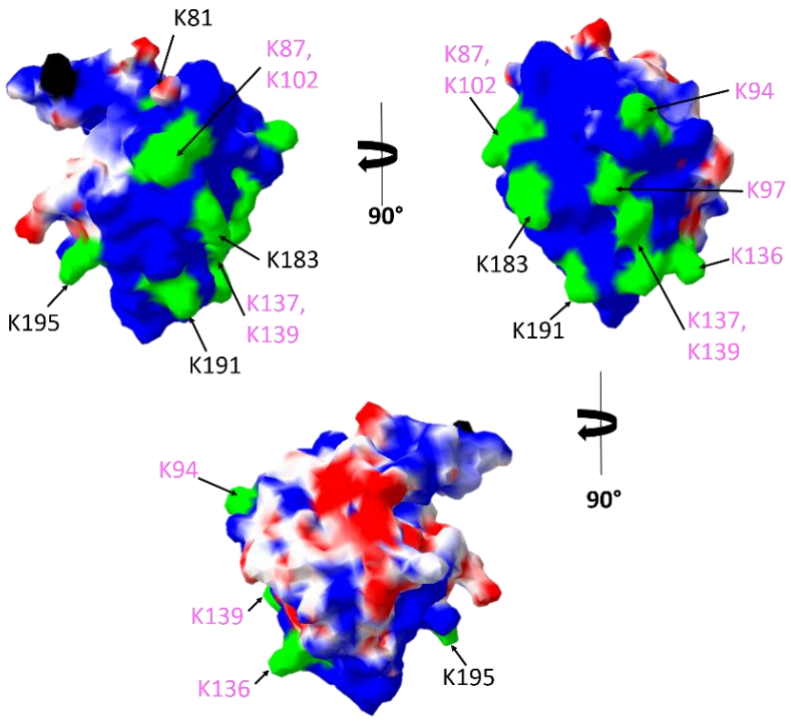


Supplementary figure 5.6: Surface electrostatic potential mapping and position of heparin binding lysines in FGF10.
Identified hepbinding lysines in HBS1 and HBS4 in FGF10 (1NUN) are labelled in green (56). The electrostatic mapping of partial charges [-1.8 (red), 0(white) and +1.8 (blue)] was generated using the Poisson-Boltzmann algorithm in SPDBV. The N-terminal residue is labelled in black.

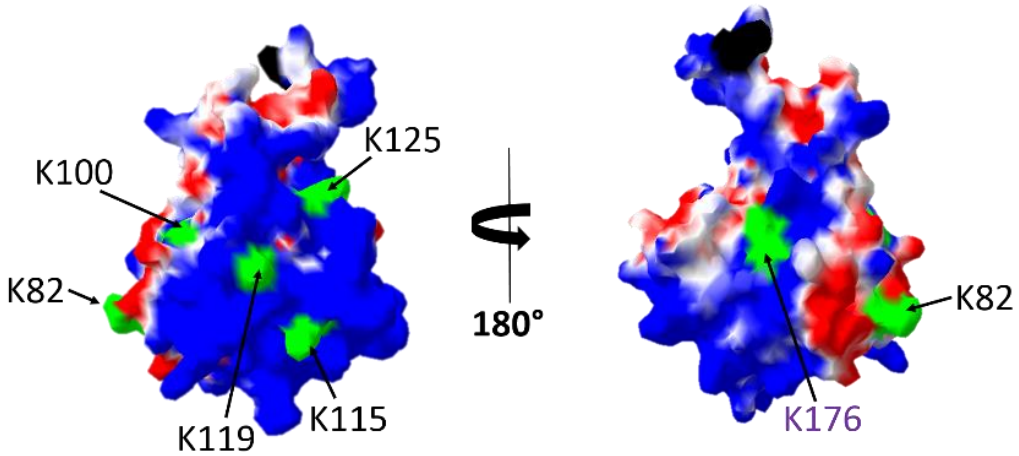


Supplementary figure 5.7: Surface electrostatic potential mapping and position of hepbinding lysines in FGF17.
Identified hepbinding lysines in HBS1 and HBS2 in FGF17 (2FDB) are labelled in green (56). The electrostatic mapping of partial charges [-1.8 (red), 0(white) and +1.8 (blue)] was generated using the Poisson-Boltzmann algorithm in SPDBV on the structure of FGF8 (2FDB). The N-terminal residue is labelled in black.

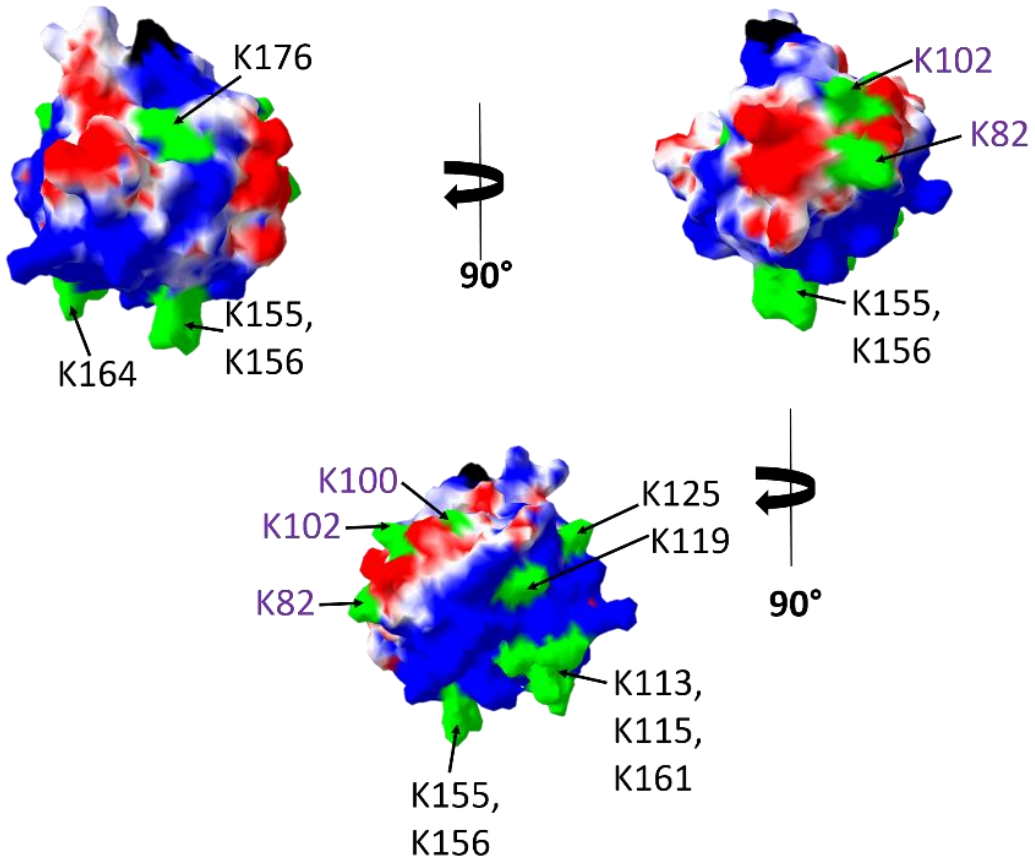


Supplementary figure 5.8: Surface electrostatic potential mapping and position of heparin binding lysines in FGF18.
Identified hepbinding lysines in HBS1 and HBS2 in FGF18 (4CJM) are labelled in green (56). The electrostatic mapping of partial charges [-1.8 (red), 0(white) and +1.8 (blue)] was generated using the Poisson-Boltzmann algorithm in SPDBV. The N-terminal residue is labelled in black.

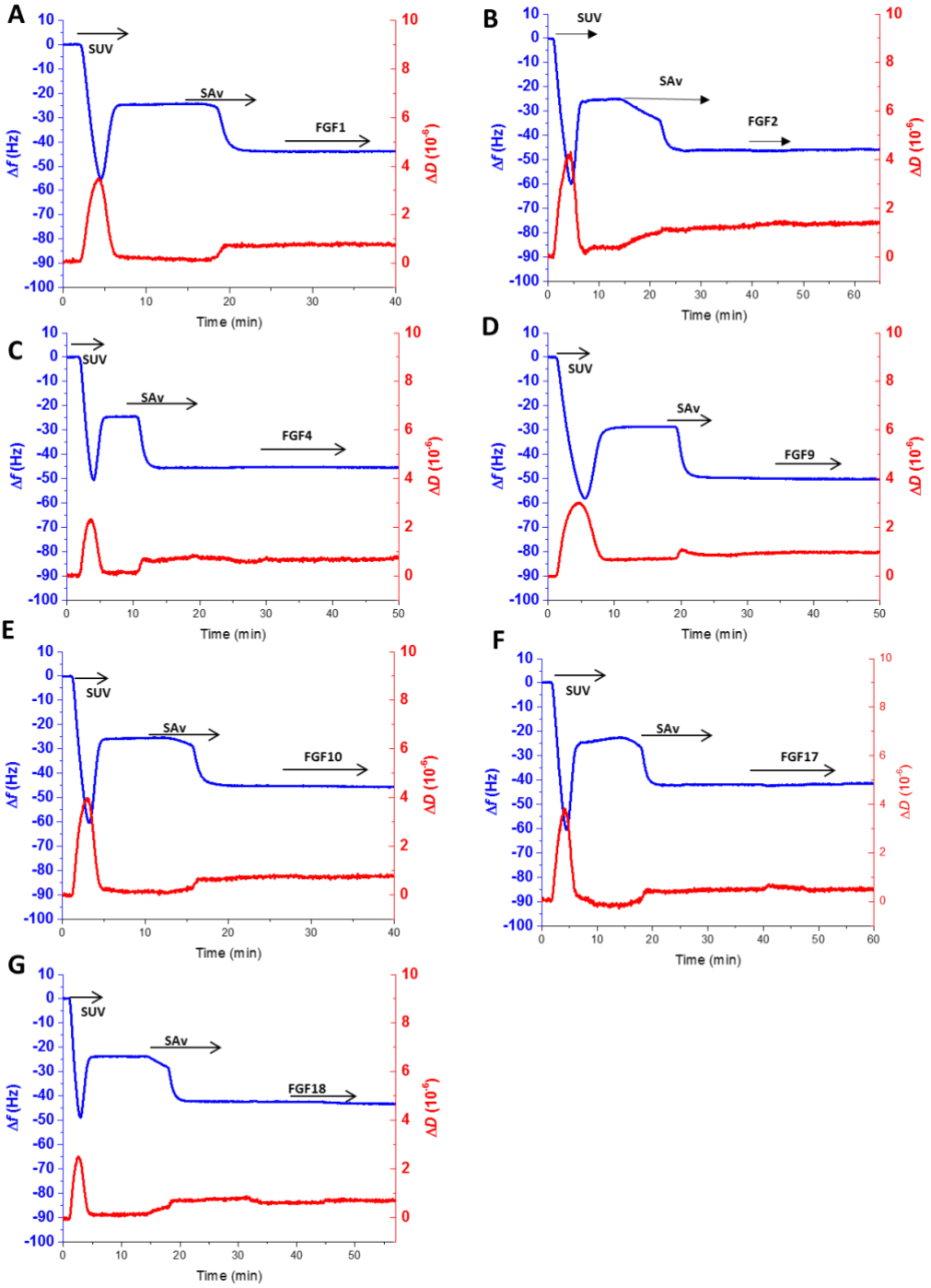


Supplementary figure 5.9: SAv-coated SLBs are inert to FGF binding as monitored by QCM-D. After the formation of the SLB and SAv layer as described in Figure 5.3, the FGFs were infused at 0.28 µM to test for non-specific interactions with the HS-free surface. The tested FGFs: FGF1 (A), FGF2 (B), FGF4 (C), FGF9 (D), FGF10 (E), FGF17 (F) and FGF18 (G) did not present any interaction with the system.

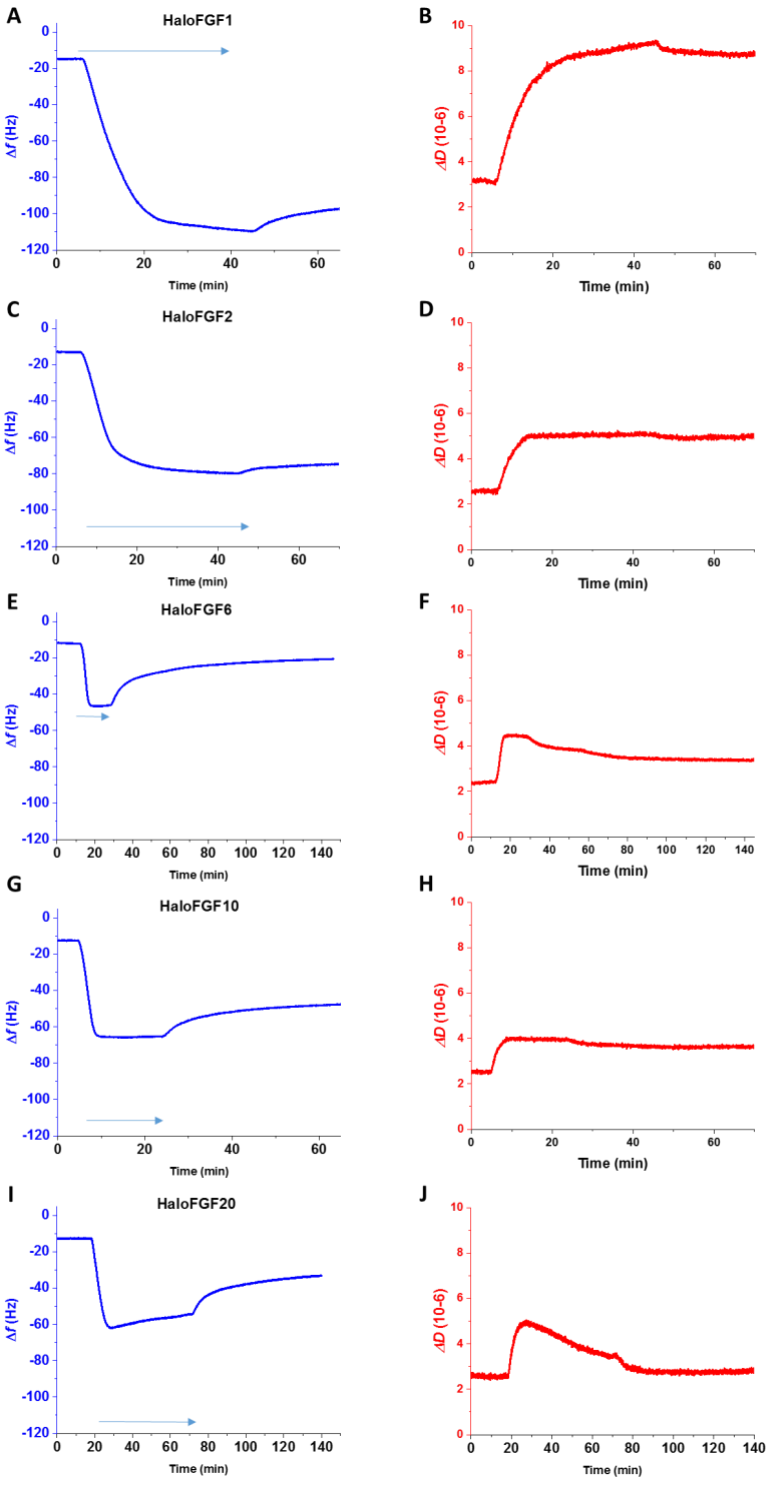


Supplementary figure 5.10: QCM-D monitoring of HaloFGF binding to mid-dense HS films. The frequency (panels A, C, E, G and I) and dissipation (panels B, D, F, Hand J) shifts presented are offset after the formation of the HS brush. HaloFGF1 (panels A and B), HaloFGF2 (panels C and D), HaloFGF6 (panels E and F), HaloFGF10 (panels G and H) and HaloFGF20 (panels I and J) were infused at 0.28 µM until maximum of binding (blue arrows indicate the duration of the incubation) before rinsing with working buffer. The rinsing step was carried out for a minimum of 20 minutes.

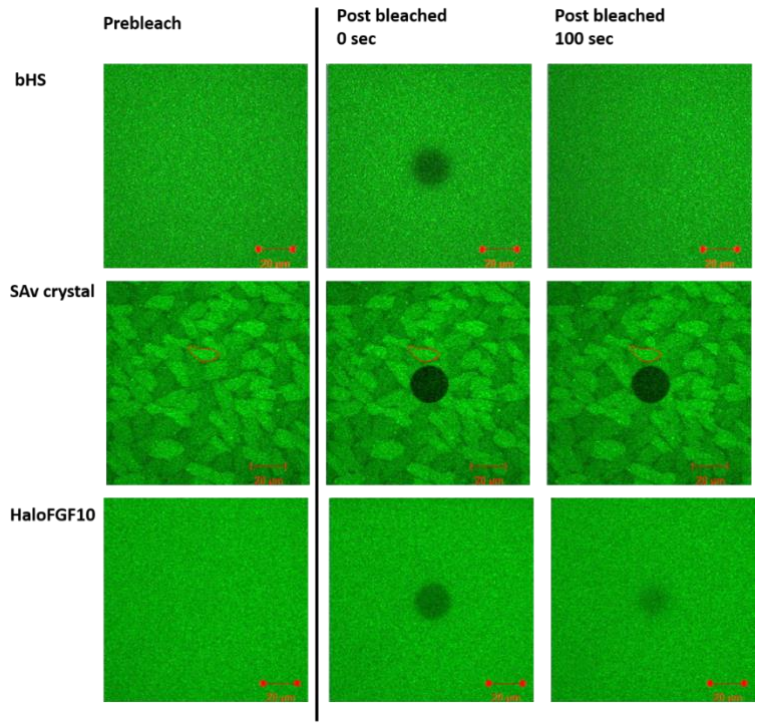


Supplementary figure 5.11: Illustration of FRAP of biomolecules in the ECM models.
HS. SUVs containing 99.5:0.5 mol:mol DOPC:DOPE-CAP-biotin were put in contact with a clean glass cover slip for 30 min at 50 µg.mL$^{-1}$. After rinsing, SAv-atto was incubated for 30 min at 20 µg.mL$^{-1}$. The surface was rinsed with working buffer and incubated with 5 µg.mL$^{-1}$ HS for 30 min. Soluble HS was rinsed off with working buffer prior to FRAP. The panel shows that the bHS brushes recovered the fluorescence in the bleached area by lateral mobility within 100 s. SAv crystal. SUVs containing 95:5 mol:mol DOPC:DOPE-CAP-biotin were put in contact with a clean glass cover slip for 30 min at 50 µg.mL$^{-1}$. After rinsing, SAv-atto was incubated for 30 min at 20 µg.mL$^{-1}$. The surface was rinsed with working buffer prior to FRAP. Domains of homogeneous fluorescence intensity can be observed that are stable over time and immobile (one domains is outlined in red). These most likely represent single two-dimensional crystals, with the fluorescence intensity varying between domains owing to their different orientation (fluorescence anisotropy). HaloFGF10. SUVs containing 95:5 mol:mol DOPC:DOPE-CAP-biotin were put in contact with a clean glass cover slip for 30 min at 50 µg.mL$^{-1}$. After rinsing, non-labelled SAv was incubated for 30 min at 20 µg/ml. The surface was rinsed with working buffer and incubated with 5 µg.mL$^{-1}$ of HS for 30 min, forming an immobile dense HS brush. After rinsing, HaloFGF10 was incubated for 30 minutes at 0.28 µM, rinsed with working buffer and FRAP images were recorded to track the mobility of the HaloFGF proteins.

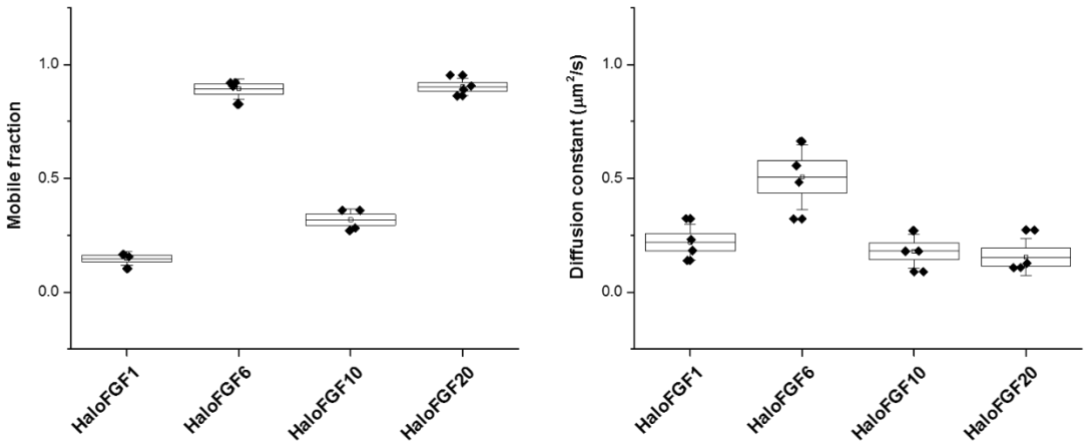


Supplementary figure 5.12: Quantitative analysis of HaloFGF mobility in HS films.
Time-resolved profile analysis was used to extract the size (left) and diffusion constant (right) of the mobile fraction from FRAP data obtained after 30 min incubation with FGFs at 0.28 µM and rinsing with working buffer. HAloFGF2 did not present a detectable mobile fraction.

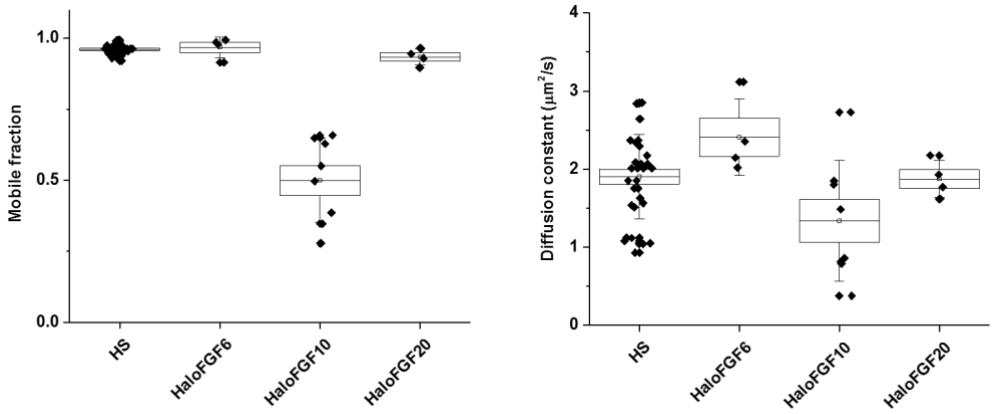


Supplementary figure 5.13: Quantitative analysis of the effect of HaloFGFs on HS mobility.
Time-resolved profile analysis was used to extract the size (left) and diffusion constant (right) of the mobile fraction from FRAP data obtained before (HS) and after 30 min incubation with HaloFGFs at 0.28 µM and rinsing with working buffer. The mean comparison tests (bottom panels) were carried out with a Fisher test at a level of significance of 5 %. The tables present the mean difference between factors; significant differences are highlighted in bold. The data presented is for a minimum of 3 independent measurements

## 5.3 A HBS3- mutant of FGF2 also rigidifies and immobilizes HS brushes

In section 5.2, we showed the differences and similarities between FGF1 and FGF2 and suggested that the HBS composition along with acidic borders regulates the immobilisation of HS brushes by FGFs. Here we compare an HBS3- mutant of FGF2 with its native counterpart to draw an understanding of the relative role of HBS3 in FGF2 interaction with HS. A cDNA encoding for a mutant of FGF2 with a silenced hepbinding site 3 (160K/A, 163K/A and 164R/A) (FGF2 HBS3-) (Life Technologies, Paisley, UK) with restriction sites for BamHI (New Englands Biolabs, Ipswich, USA) and NcoI (New Englands Biolabs) was amplified by polymerase chain reaction and inserted in the plasmid vector pET-M11 using the T4 DNA ligase (New Englands Biolabs) (57).

The binding of FGF2 HBS3- to HS in QCM-D triggered a drop in $\Delta f$ that stabilised to a maximum of binding (Figure 5.18). The final change in $\Delta f$, 38 Hz was higher than the one of FGF2, 32 Hz (section 5.2), though the $\Delta f$ (measure of surface coverage) in QCM-D encompasses not only the bound molecules but also the coupled solvent. Thus, the greater $\Delta f$, observed for FGF2 HBS3- may not reflect differences in the amount of bound protein. The rinsing step seemed to have the same effect on both brushes, partially desorbing the protein with a 16 Hz shift in $\Delta f$. The $\Delta D$ showed a transient increase quickly followed by a decrease, suggestive of a rearrangement of the film. The final $\Delta D$ was lower than that of the original brush, similarly to the level observed for native FGF2, suggesting the establishment of rigid structures.

The quantification of FGF2 HBS3- in HS brushes by SE showed that at maximum binding the amounts of FGF2 and FGF2 HBS3- bound to HS were equivalent with no significant difference. Thus, at maximum of binding the areal mass densities of 6.1 ± 0.7 and of 7.1 ± 1.0 pmol.cm$^{-2}$ for FGF2 and FGF2 HBS3-, respectively, were not significantly different. Assuming a molecular weight of 12 kDa for the HS chains (181) and its areal mass density of 1.1 pmol.cm$^{-2}$ (section 5.2), this yielded an average stoichiometry of 6 ± 1 FGF2 and FGF2 HBS3- molecules, per HS chain, respectively, at

maximal loading (Figure 5.19). After rinsing, the amount of FGF per brush decreased slightly to 4 ± 2 FGF2 and 4 ± 1 FGF2 HBS3- per HS chain, again the values for the mutant and the native FGF2 were not significantly different. Consequently, the greater reduction in $\Delta f$ observed for FGF2 HBS3- will reflect a difference in coupled solvent.

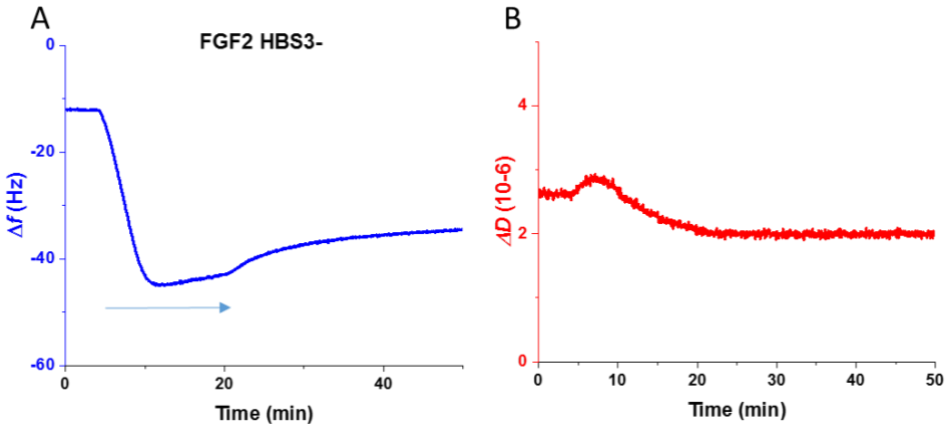


Figure 5.18: QCM-D monitoring of FGF2 HBS3- binding to a mid-dense HS brush.
The frequency (A) and dissipation (B) were offset after the formation of the HS brush (cf. Figure 5.3). FGF2 HBS3- was infused at 0.28 µM until equilibrium (blue arrows indicate the infusion time) before rinsing with working buffer.

In QCM-D (Figure 5.18), the level of $\Delta D/-\Delta f$ = 0.07 × $10^{-6}$ $Hz^{-1}$ at maximal coverage is comparable for FGF2 and FGF2 HBS3-, and a superposition of the parametric plots (Figure 5.20C) shows that the trends for rigidification on binding are similar for both the mutant and the native FGF2. Upon rinsing and release of the molecules both films did not recover softness while releasing some of the protein, suggesting that the established rigid film could release some FGF while staying stiffly crosslinked. However, during the dissociation the trends were different, as seen in the superimposed parametric plots (Figure 5.20), suggesting that the final structures of the films might differ.

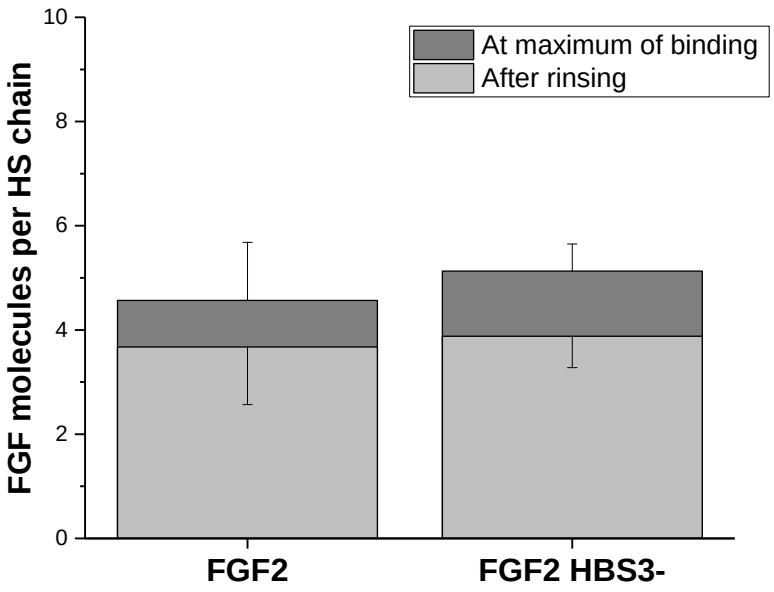


Figure 5.19: Stoichiometry of FGF2 and FGF2 HBS3- binding to HS.
Molar FGF surface densities were determined by SE at equilibrium after incubation at 0.28 µM (dark grey), and after rinsing with working buffer for at least 60 minutes (light grey), and compared to molar HS surface densities obtained in the same measurements. The data presented is for a minimum of 2 independent measurements, and mean values with standard deviations are presented. The data for FGF2 from was extracted from section 5.2.2.

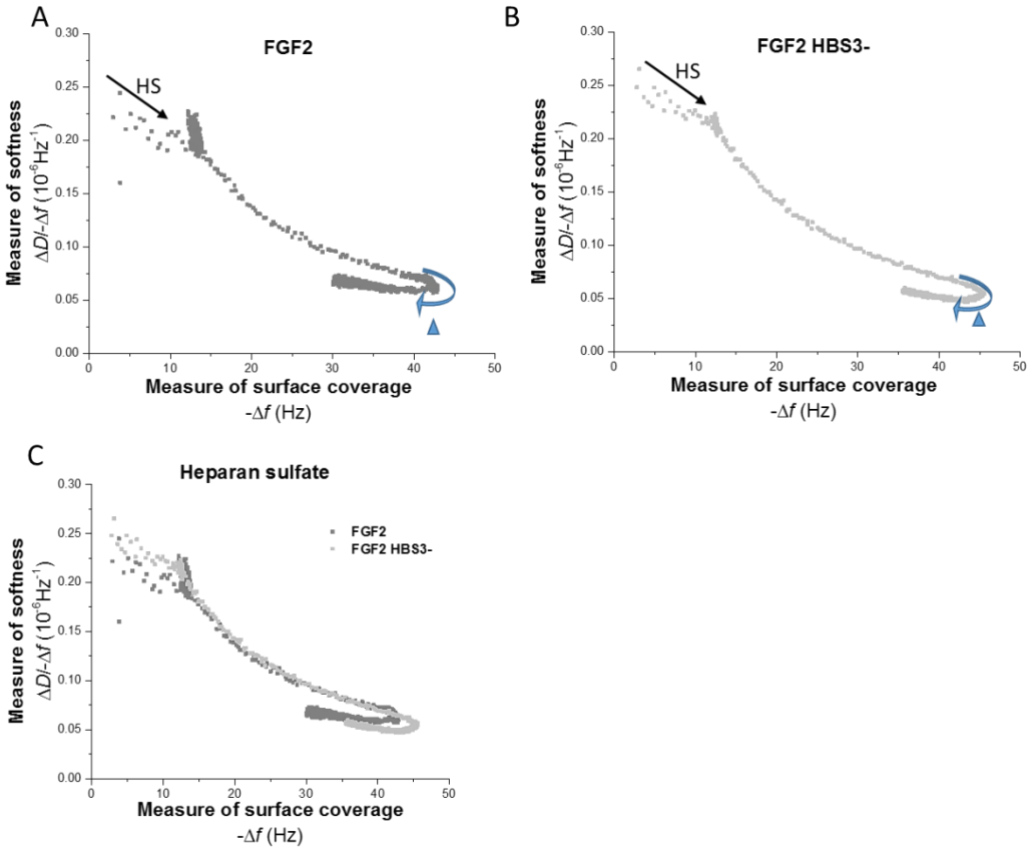


Figure 5.20: HBS3 mutant of FGF2 subfamily bind and rigidify HS brushes.

Parametric plots of $\Delta D/-\Delta f$ (a measure of softness) vs. $-\Delta f$ (a measure of surface coverage) for the HS film, first without (until $-\Delta f \approx 12$ Hz, process of HS film formation indicated with black arrow) and then with FGFs bound (data extracted from Figure 5.18 and section 5.2). HS brushes rigidify progressively upon FGF2 (A) and FGF2 HBS3- (B) binding. Upon rinsing (the start of rinsing is indicate with a blue arrow head), the FGFs desorbed following protein specific trends (blue arrows). Overlay of the parametric plots (C) show that all binding curves fall on top of each other, indicating that the proteins have very similar coverage-dependent effects on HS film morphology. Unbinding curves were also similar upon rinsing and protein release.

In FRAP measurements, we recorded the mobility of the SAv-anchored HS molecules. To this end, we exploit the inherently high lateral mobility of SAv when formed as mid-dense monolayers on SLBs. Figure 5.21 shows how the mean intensity of the bleached spot recovers over time for a film of bare HS (Figure 5.21A) and for HS films that were incubated with FGF2 and FGF2 HBS3- at 0.28 µM for 30 min and then rinsed with incubation buffer (Figure 5.21B-C). These plots provide a simple visual comparison of the recovery of fluorescence, and the mobility of the fluorescent SAv with bound HS chains. In addition, Figure 5.22 provides a quantitative analysis of the size and diffusion constant of the mobile fraction.

The quantitative analysis of the FRAP data characterised an HS brush as 97 ± 1% mobile with a diffusion constant of 1.7 ± 0.5 $\mu m^2.s^{-1}$ (Figure 5.22). FGF2 essentially immobilised the HS chains, and only little recovery was observed for 300s post bleaching (Figure 5.21B). In contrast, HS in the HS-FGF2 HBS3- films was much more mobile (Figure 5.21C). HS brushes with bound FGF2 HBS3- recovered up to 80% of the fluorescence in the bleached area. Accordingly, the mobile fraction of the bHS-FGF2 HBS3- brush was significantly higher than in the HS-FGF2 brush, but lower than in the bare HS brush (Figure 5.21 and Figure 5.22).

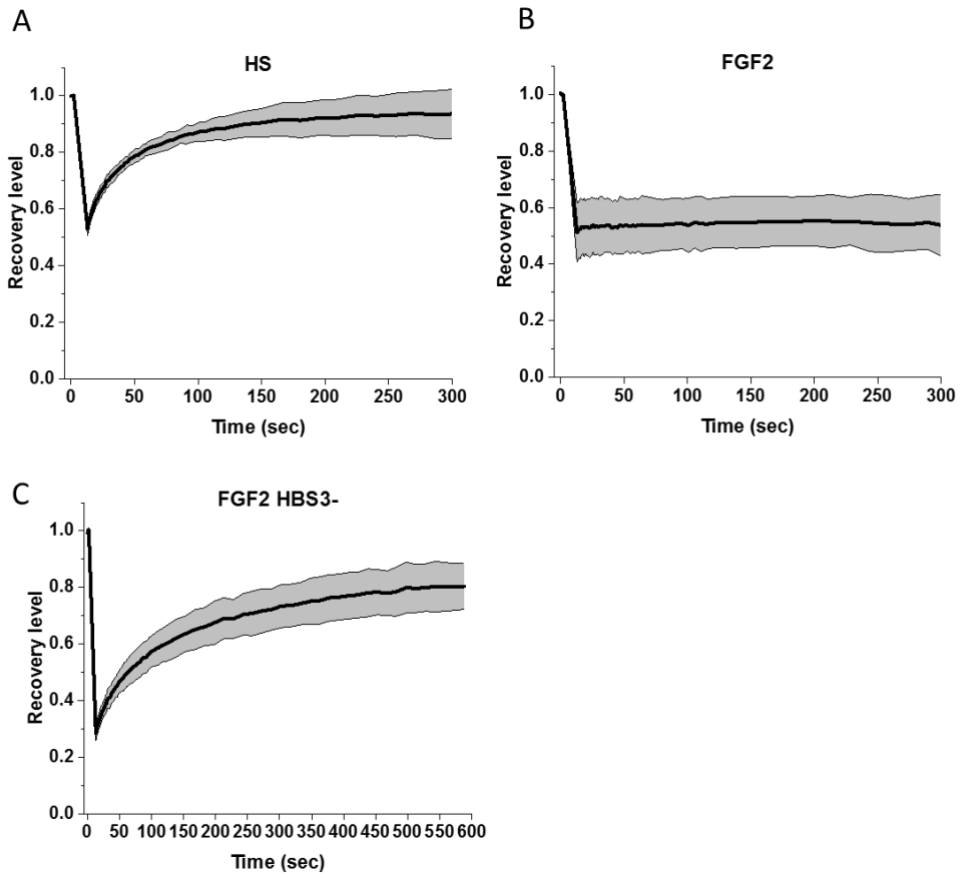


Figure 5.21: FGF2 and FGF2 HBS3- immobilise HS with different potencies.
FRAP curve of atto488-SAv supporting HS (A), HS-FGF2 (B, extracted from section 5.2and HS-FGF2 HBS3- (C) films. The black curve and the grey region around it are the mean and standard deviation, respectively, of 4 measurements obtained after rinsing with the working buffer.

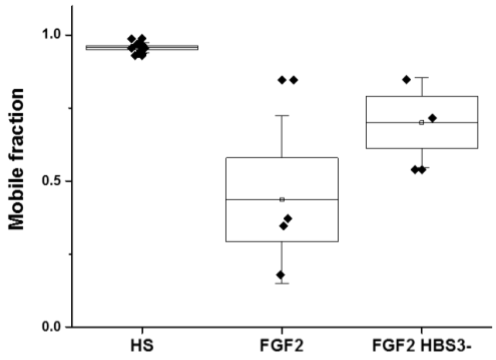


Mean difference

| Factor | HS | FGF2 | FGF2 HBS3- |
|---|---|---|---|
| HS | | -0.52 | -0.26 |
| FGF2 | | | 0.26 |
| FGF2 HBS3- | | | |

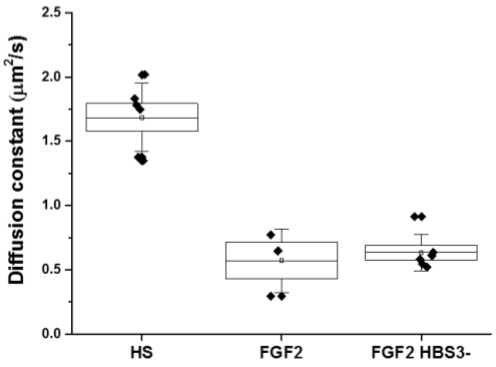


Mean difference (µm²/s)

| Factor | HS | FGF2 | FGF2 HBS3- |
|---|---|---|---|
| HS | | -1.11 | -1.05 |
| FGF2 | | | 0.06 |
| FGF2 HBS3- | | | |

Figure 5.22: Quantitative analysis of the effect of FGF2 and FGF2 HBS3- on HS mobility. Time-resolved profile analysis was used to extract the size (top) and diffusion constant (bottom) of the mobile fraction from FRAP data obtained before (HS) and after 30 min incubation with FGFs at 0.28 µM and rinsing with working buffer. A box plot of the standard error is presented with the mean of the values (black diamonds) marked by a line. The whiskers are indicate to the standard deviations. The mean comparisons tests (right panels) were carried out with a Fisher test at a level of significance of 5 %. The tables present the mean difference between factors; significant differences are highlighted in bold. The data presented is for a minimum of 3 independent measurements.

## 5.4 Discussion

The results in section 5.2 suggest that the HBS3 mutation did not affect the level of binding of the protein to the HS brush (Figure 5.20), but the generated film undoubtedly has a different structure and viscoelastic properties than the film formed by the native FGF2 and HS. The primary determinant for binding is HBS1, since this has an affinity that is over two orders of magnitude higher than the secondary HBSs (102, 189). So it is not surprising that the FGF2 HBS3- mutant binds to the same extent as the wild-type protein. However, it is clear that once bound, the presence or absence of HBS3 has an effect on the film's properties. In terms of affinity, once HBS1 is engaged with the polysaccharide, proximity will mean that the secondary HBSs are likely to bind strongly, which is consistent with the efficient

selective labelling of the lysines in these sites (Ori et al., 2009). The FGF2 HBS3-mutant crosslinks HS, but compared to FGF2, a substantial fraction of the HS chains are somewhat mobile. Thus, FGF2 HBS3 is less effective at crosslinking HS chains than FGF2, which suggests a role for this secondary binding site in determining this effect of the FGF on HS.

In terms of the relative importance of the different secondary HBSs in contributing to the crosslinking of HS by an FGF further mutants could not be analysed, since the FGF2 HBS2- and the double HBS2-/HBS3- mutants were not expressed as stable or soluble proteins, respectively. For an FGF to crosslink HS chains it would seem that it must have multiple HBSs and that these should be isolated from one another by an acidic border. It is also possible that HBS2 and HBS3 contribute differently. Thus, HBS2 is part of the core structure of the FGF, whereas HBS3 is at the N-terminus of this, lying at the start or in front of beta strand 1. HBS3 is consequently on the opposite face of the protein to HBS1 and so may have a greater contribution to crosslinking than HBS2. Such ideas will require an extensive set of mutant proteins (section 8.2).

In this chapter, the interactions of FGFs with HS have been measured. However, at least some FGFs interact with other sulfated GAGs. For example, FGF10 is demonstrated to bind CS and DS *in vitro* and also to CS/DS on cells (56, 185). Moreover, it has been established by others that the CS-E behaves for at least some proteins, notably, FGF2, similar to hepin terms of its ability to bind the protein and enable signalling through the FGFR (190). However, there have been very few quantitative analyses of the interactions of proteins, let alone FGFs, with sulfate GAGs other than HS/heparin. In addition, the backbone and sulfation pattern of the chondroitin based GAGs differs from heparin/HS (section 1.3.3). Thus, an analysis of the interactions of the FGFs used in this chapter with other GAGs would provide considerable insight into the potential roles that these different interactions might have.

# 6 Interaction of FGFs with brushes formed with different GAGs.

## 6.1 Introduction

In this chapter, I investigated the effect of FGFs on brushes made from a selection of sulfated GAGs other than HS. Specifically, I tested FGF1, FGF2, FGF2 HBS3-, FGF4, FGF9, FGF10, FGF17 and FGF18 with the GAGs: hep(Hep), chondroitin sulfate A (CS-A), chondroitin sulfate C (CS-C), chondroitin sulfate E (CS-E), and dermatan sulfate (DS), and with DS-derived oligosaccharides of 18 monosaccharide units (DS dp18). The GAG brushes were prepared for QCM-D, SE and FRAP assays as described in sections **Error! Reference source not found.** and **Error! Reference source not found.** and the results were analysed as described in sections **Error! Reference source not found.** and **Error! Reference source not found.**.

### 6.1.1 Origin, composition and structural characteristics of GAGs

The GAGs differ by their glycosidic linkage, disaccharide composition, and sulfation as briefly described in section 1.3.3.

*Highly sulfated GAGs, HS and Hep.* The HS polysaccharide used in (insert here reference to section 5) is relatively well characterized: it is from porcine intestinal mucosa, and the employed batch had an average molecular weight of 12 kDa, a polydispersity index of 1.6 and an average sulfation of 1.4 sulfates per disaccharide (124). Although we do not have the provenance of our hep batch, hep from various sources have been well characterised in the literature. The main disaccharide unit of porcine Hep is: 4-) L-IdoA,2S α (1-4) D-GlcNS,6S (1- (191-193), with an average of 2.75 sulfate groups per disaccharide (43).

*Chondroitin and dermatan sulfates*. The DS (dp18) oligosaccharide has an average size of 4.5 kDa and contains mostly IdoA (1-3) GalNAc,4S (88%) and also IdoA,2S (1-3) GalNAc,4S (7%). It was obtained by partial chondroitin ABC lyase digestion of shark dermatan sulfate (125). The other GAG polymers were less characterized. Based on assumed molecular weights of 13 kDa for Hep and 30 kDa for CS-A, the molecular weights of CS-C, CS-E and DS polysaccharides were estimated at 26 kDa, 26 kDa and

6.5 kDa, respectively, using size exclusion chromatography analysis (section 4.2.3). The CS-A (GlcA (1-3) GalNAc,4S) sample is from bovine trachea, the provenance of the CS-C (GlcA (1-3) GalNAc,6S) is not known, and CS-E (GlcA (1-3) GalNAc,4,6diS) was prepared by chemical modification of the CS-C as described previously (194). DS, IdoA (1-3) GalNAc-4S is from porcine intestinal mucosa. The disaccharide composition of our CS-A, CS-C, CS-E and DS was not analysed and it is likely that these are not pure but do also contain fractions of other CS or DS disaccharides. Indeed in the case of the bovine trachea CS-A, it appears that this is a mixture of non- (10%), 4- (52%) and 6- (39%) sulfated of GlcA (1-3) GalNAc disaccharides (195). Thus, it contains approximately 39% of CS-C disaccharides. All GAGs were biotinylated by oxime ligation at the reducing end (section 4.2.3, (123)).

Brushes of non-HS GAGs have not been produced previously so the first step was to characterise these. Following their assembly and characterisation, they were probed with different FGFs. The in solution preferences of the FGFs used here for different GAGs have been extensively characterised (56, 104). However, these preferences may change when the GAG chains are presented as a brush, so the analysis was not restricted to just FGFs that are considered to bind GAGs such as CS-A. Otherwise, as in chapters 5, the measurements were QCM-D, SE and FRAP.

### 6.1.2 Characterization of GAG brushes.

Prior to the infusion of FGFs, GAG brushes were formed on mid-dense SAv monolayers as described earlier (sections 4.2 and 5.2). The GAG binding was monitored by QCM-D and the GAG surface density was quantified by SE (**Error! R eference source not found.**). All GAG types were found to bind to the SAv monolayer: binding occurred at largely comparable rates, and all GAGs remained stably bound upon rinsing with working buffer (**Error! Reference source not found.**A). Moreover, the QCM-D frequency shifts (**Error! Reference source not found.**A) were associated with substantial increases in dissipation (**Error! Reference source not found.**B) indicating that relatively soft films are formed. All these responses are consistent with the specific attachment of the GAG chains via biotin at the reducing end, and indicate that GAG brushes formed as expected.

The parametric plot (Figure 6.1C) enables a comparison of the GAG film softness (parameterized as $\Delta D/-\Delta f$) as a function of surface coverage (parameterized as $-\Delta f$). It can be seen that all GAGs produce films of similar softness: Hep, CS-C, CS-E and DS (6.5 kDa) exhibit a softness that is virtually indistinguishable from HS, and CS-A and DS (dp18) are only slightly softer.

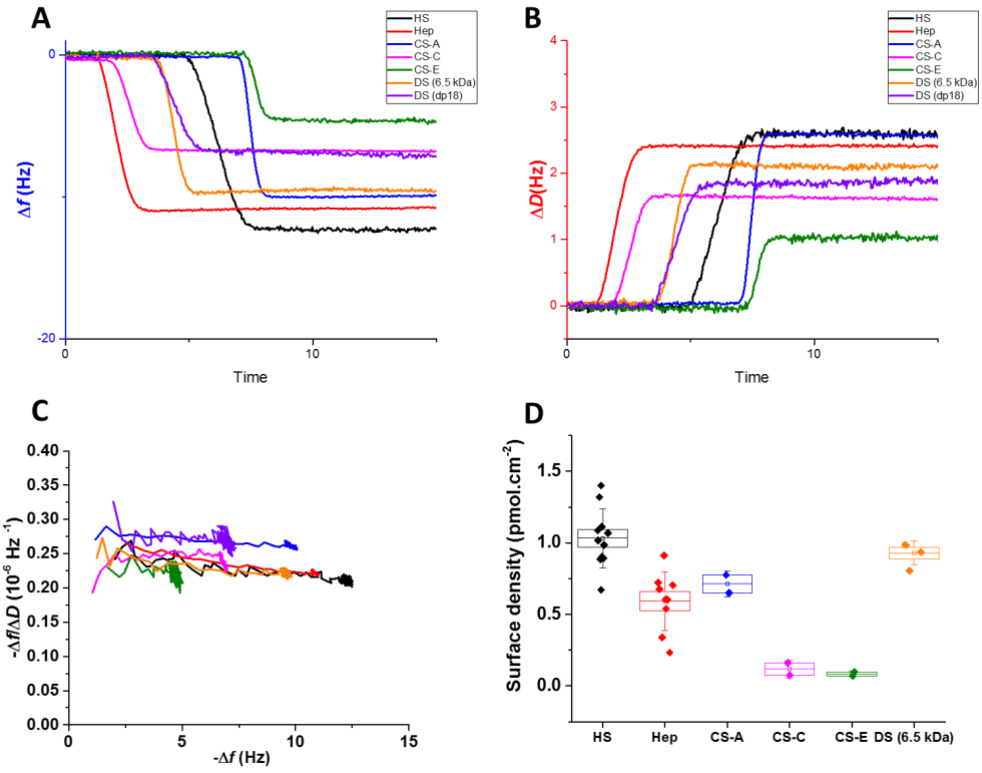


Figure 6.1: Characterisation of mid-dense GAG brushes.
The changes in $\Delta f$ (A) represent the evolution of mass adsorption at the surface of the sensor; $\Delta D$ (B) provides information about the mechanical properties of the film with an increase being associated with a softer film. The biotinylated GAGs were infused at 5 µg.mL$^{-1}$ on mid-dense SAv monolayers as described previously (sections 4.2 and 5.2). The time before infusion of each GAG was purposely varied to facilitate visibility of each data set. C. Parametric plot of the QCM-D data in (A) and (B). The binding of biotinylated Hep, HS, CS-C, CS-E and DS (6.5 kDa) followed the same trend while the ones of CS-A and DS (dp18) followed a slightly different one. D. Surface densities of mid-dense GAG polymer brushes as measured by SE (surface densities of DS (dp18) were not determined).

Figure 6.1D shows the GAG molar surface densities at saturation. These where calculated from the areal GAG mass densities, measured by SE, and the nominal GAG molecular weights. It is notable that the molar surface densities varied: they were between 0.5 and 1 pmol.cm$^{-2}$ for most GAGs, though CS-C and CS-E had exceptionally low surface densities of 0.11 ± 0.01 and 0.08 ± 0.02 pmol.cm$^{-2}$, respectively. At first

view, these variations are unexpected, because the SAv monolayers have a defined density of free biotin binding sites and with one biotin per GAG the molar GAG surface density should equal the density of binding sites. Specifically, for a SAv density of 1.7 pmol.cm$^{-2}$, the average residual valence has been estimated at 1.7 (137), giving a surface density of free biotin binding sites of 2.6 pmol.cm$^{-2}$. One explanation for the lower apparent surface densities is that the biotinylated hep, CS-A, CS-C, CS-E and DS supplied still had individual free biotin. This would compete for the SAv. At least for the CS-A, CS-C, CS-E and DS there may also be uncertainty as to their average molecular weight. If so, the overestimated molecular weights would lead to apparent reduction of the surface densities. Moreover, the size distribution based measurements of hydrodynamic radius will, when converted to molarity, be skewed towards smaller polymers. Thus, even for the same reactivity, there may be a bias towards smaller sizes in the reacted product simply because of differences in concentration of larger and smaller reactants. There is also some uncertainty about the average molecular weight of the GAG polymers (Heparin, CS-A, CS-C, CS-E and DS (6.5 kDa)) in the solution phase. Taken together, the above analysis provides evidence that brushes can be formed with all GAG types, but that the molar surface density (and the average molecular weight) of GAG polymers in the brush should be considered with caution (196). These considerations are also applicable to the HS brush (Chapter 5), as described previously, where the average molecular weight of this HS batch appears to be 5.2 ± 0.6 kDa when anchored by our method (section 4) instead of the 12 kDa measured in the solution phase (120).

## 6.2 Interaction of members of the FGF1 subfamily with sulfated GAGs

In this section, I describe and characterise the binding of the members of the FGF1 subfamily towards different GAG types and the consequent changes in the structure of the GAG brushes. In addition, the FGF2 HBS3- mutant was also used, to determine if the loss of the N-terminal secondary HBS, HBS3, had an impact on interactions with GAGs other than HS.

### 6.2.1 Binding of FGF1 and FGF2 to GAG brushes.

To assess the binding propensity and stioichiometry of the members of the FGF1 subfamily, the proteins were infused on GAG brushes in QCM-D to detect their interactions with the films and in SE to quantify the binding stoichiometry. Detailed plots of the QCM-D assays are presented in section 5 for HS, and in Supplementary figure 6.1 to Supplementary figure 6.3 for the other GAGs.

*FGF1.* In the conditions of the assays, FGF1 showed detectable binding to Hep, CS-E, DS (6.5 kDa) and DS (dp18), but none to CS-A or CS-C (Supplementary figure 6.1). Upon rinsing in working buffer, some FGF1 dissociated from heparin, but not from DS and the DS-derived dp18. In contrast, the FGF1 rapidly and fully dissociated from CS-E. The binding of FGF1 to the brushes generated a decreased (DS (dp18)) or increased (Hep, DS (6.5 kDa), CS-E) $\Delta D$ signal. The $\Delta D$ remained stable during the rinsing (Hep, DS) or returned to the bare brush level in the case of CS-E. The small and rapid changes in $\Delta f$ and $\Delta D$ (Supplementary figure 6.1) observed upon infusion of FGF1 on brushes of CS-A and of CS-C are likely to reflect changes in solvent. Thus, FGF1 bound to heparin, as expected, and DS, had a weak transient interaction with CS-E and did not interact with CS-A and CS-C.

*FGF2.* FGF2, on the other hand, bound to brushes of all the tested GAGs (Supplementary Figure 6.2). The change in $\Delta f$ was similar to that seen for HS brushes for brushes of hep but lower for brushes of CS-A, CS-C, and CS-E and very low for DS (Supplementary Figure 6.2). After rinsing there was little dissociation of FGF2 from the heparin, CS-A, CS-C, and CS-E brushes, whereas for DS the frequency shift returned to the level observed before the addition of FGF2, indicative of complete dissociation. The $\Delta D$ signals upon binding of FGF2 were significantly decreased (Hep) or increased (CS-A and CS-C), or unchanged (CS-E and DS). GAG brushes were also probed with FGF2 HBS3-, which has a mutated HBS3 (Sections 5) to determine whether this secondary binding site might affect interactions with GAGs other than HS (Supplementary figure 6.3). In these experiments, binding to CSC was not tested. FGF2 HBS3- bound hepto the same extent as HS, however it bound CS-E, DS (6.5 kDa) and DS (dp18) to a much lesser extent and failed to bind to brushes of CS-A (CS-C was not tested). After rinsing there was some dissociation of FGF2 HBS3- from hepand

proportionally more from CS-E, DS (6.5 kDa) and DS (dp18), suggesting that the interaction with the latter was quite transient. In the instances where FGF2 HBS3- bound the GAG brushes, the dissipation signal was the same as for FGF2: decreased (Hep) or unchanged (CS-E and DS).

Individually, FGF1, FGF2 and FGF2 HBS3- thus presented different binding towards the tested GAGs, as also shown by the range of frequency shifts upon their exposure to the brushes. Notable differences were: (1) FGF2, but not FGF1, bound to CS-A and CS-C brushes; (2) FGF2 binding to CS-E was stable, but FGF1 binding was transient and so rapidly reversible; and (3) mutation of the HBS3 in FGF2 prevented the binding to CS-A and markedly affected the interaction with CS-E.

The results for FGF1 concur with previous reports by others. In a study of genuine CS-E isolated form a natural source, no binding of FGF1 was observed (190), which is consistent with the transient interaction seen with the CS-E brush here, since after washing, all the FGF1 dissociates. Similarly, a weak interaction of FGF1 with DS and an absence of interaction with CS-A or CS-C and a weak interaction with DS have previously been reported (104). Somewhat puzzling is the greater interaction of FGF1 with the DS derived dp18 compared to DS itself. This may result from the partial digestion with chondroitinase ABC enriching binding sequences or to differences in grafting density of these DS species.

The FGF2 data are more puzzling. The interaction with CS-E was expected, since this has been previously reported and indeed CS-E has been shown to enable the formation of a signalling complex between FGF2 and the FGFR (190). The weak, transient interaction with DS is also consistent with previous data (56). However, the marked interaction with CS-A and CS-C has not previously been reported. Indeed, these galactosaminoglycans are considered to not bind FGF2 (56). The interaction of FGF2 with brushes of CS-A and CS-C are unlikely to be due to contaminating HS, since FGF1 failed to bind. They are also unlikely to be due to simple charge density of the brush and ion-exchange, because the interaction with brushes of DS were much weaker. One possibility is that presentation of CS-A and CS-C in a mid-dense brush allows movement of the SAv and so local reorganisation of the brush upon initial FGF2 binding. This may allow good binding sites, likely contributed by several chains

to form, though the same would be expected for DS, which contains iduronate residues, known to be important in the interaction of the HBS1 of FGF2 with hep and HS (55).

### 6.2.2 Rigidification of GAG brushes by members of the FGF1 subfamily

The parametric plots of the QCM-D data were used to analyse the effect of FGFs on GAG brush stiffness. These plots are in Supplementary Figs 6.1, 6.2 and 6.3 for FGF1, FGF2 and FGF2 HBS3-, respectively. Figure 6.2 combines these data for HS, Heparin, CS-E and DS (i.e. for all GAGs that showed binding of FGF1 and FGF2), for comparison between the two members of the FGF1 subfamily. In all instances where FGFs bound to the GAG brushes, a decrease in $\Delta D/-\Delta f$ was observed, denoting a stiffening of the GAG films.

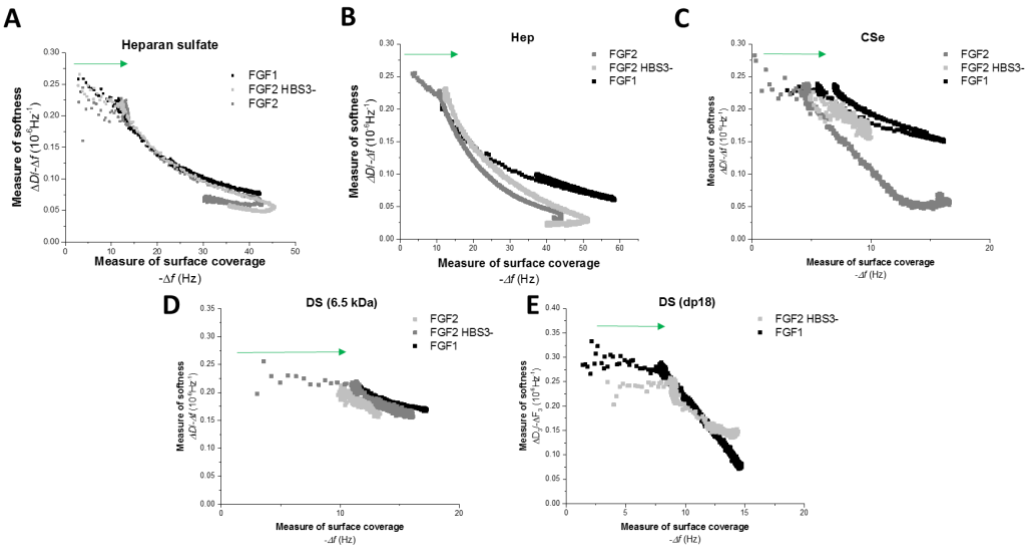


Figure 6.2: Comparative parametric plot analysis of the interaction of members of the FGF1 subfamily with GAG brushes.
Representative data is shown for the formation of mid-dense HS (A), Hep (B), CS-E (C), DS (6.5 kDa) (D) and DS (dp18) (E) brushes (green arrows), binding of FGFs at 0.28 µM until equilibrium, and subsequent rinsing with the buffer until stabilisation of the signal. Data for HS are taken from (insert here reference to chapter V). All other data were extracted from Supplementary Figures 6.1 to 6.3. Data of FGF2 binding to CS-A and CS-C are not shown here.

*Binding to HS and Hep brushes.* At a given frequency shift, FGF1 generated significantly softer Hep films than FGF2 (Figure 6.2B), indicating that the effect of the two FGFs on Hep brushes is distinct. This is in contrast to HS, where the effects of

FGF1 and FGF2 were indistinguishable (Figure 6.2A), as already discussed in detail in section 5. The difference between HS and Hep with regard to rigidification is notable given that their FGF binding to the two GAGs was quite similar. It may arise from the greater charge density of hep compared to HS and the acidic isoelectric point of FGF1, which, compared to FGF2, could result in a film where the constituents repel each other to a greater extent. In contrast, FGF2 and FGF2 HBS3- did not present any detectable difference in binding to heparin, and were very similar towards HS (section 5.2). Apparently, the mutation of HBS3 does affect neither the magnitude of binding nor the morphology of the FGF loaded hep or HS films.

*Binding to CS-E brushes.* There were substantial differences in film softness between FGF1 and FGF2 with CS-E: at comparable loading (i.e. frequency shifts), the binding of FGF1 generates a much softer structure than FGF2 (Figure 6.2C). Notably, the FGF2 HBS3- mutant also generated a softer CS-E film than wild type FGF2. These differences likely reflect that FGF1 and FGF2 HBS3- dissociated from the brush rapidly, indicative of a transient interaction. Moreover, they support a role for HBS3 in the interaction of FGF2 with CS-E brushes. FGF2 is the only FGF from this subfamily that has bound CS-A and CS-C. The binding rigidified the films in a rather smaller extent than HS, Hep or even CS-E (Supplementary figure 6.6). Indeed, the $\Delta D$ signals of FGF2 binding to CS-A and CS-C were increased, suggesting the formation of softer films when it was decreased for other GAGs.

*Binding to DS brushes.* FGF1, FGF2 and FGF2 HBS3- induced similar degrees of rigidification on DS (6.5 kDa) brushes (Figure 6.2D). This is despite the fact that FGF2 and FGF2 HBS3- appear to bind transiently to this brush, whereas at least a part of the bound FGF1 did not dissociate. The observed stiffening of the brush may then simply reflect the presence of proteins of very similar structure.

In binding to DS (dp18), FGF1 and FGF2 HBS3- presented different rigidification trends. FGF1 had a much higher propensity to stiffen DS (dp18) than FGF2 HBS3- (Figure 6.2E) .This again is likely to reflect the differences in the interactions of these two proteins with this particular brush. FGF1 remains bound after rinsing, whereas FGF2 HBS3- dissociates, as the interaction is transient.

### 6.2.3 Binding stoichiometries of the FGF1 subfamily.

To quantify the surface density of FGFs in GAG brushes, I performed complementary SE measurements for selected FGF-GAG interactions observed in QCM-D. : presents the binding stoichiometries, expressed in FGF molecules per GAG disaccharide. This presentation is preferable over the number of FGF molecules per GAG chain, because of the uncertain average molecular weight of the GAGs employed. Moreover, it enables quantitative comparison of the binding across GAGs, whilst a comparison of absolute amounts of FGF binding would be compounded by the fact that the areal GAG mass density varies substantially between GAGs.

From Figure 6.3 it can be seen that the highest binding stoichiometries at equilibrium are observed for FGF1 on HS and DS, and for FGF2 on HS, Hep and CS-C. In all these cases, approximately one FGF binds per 4 disaccharides, corresponding to a footprint of roughly 4 nm GAG chain per FGF, on average.

The disparities in binding stoichiometry towards HS for FGF1 *vs* FGF2 and FGF2 HBS3- were previously described in section 5: stoichiometries at equilibrium were comparable, but the rinsing step desorbed more FGF1 than FGF2 and FGF2 HBS3-, suggesting that the binding to FGF1 to HS is weaker than those FGF2 and FGF2 HBS3- ; notable is also the similarity in FGF2 and FGF2 HBS3- bindings on HS. The new data for FGF2 and FGF2 HBS3- on Hep brushes (Figure 6.3) shows binding stoichiometries that are comparable to HS, at equilibrium and also after rinsing. This is surprising, given that FGF2 is expected to bind preferably to the highly sulfated regions which are more frequent in Heparin.

FGF2 bound to CS-C with a similar stoichiometry as to HS and Heparin, but there was less FGF2 bound per disaccharide for brushes of CS-A, CS-E and DS. Whereas rinsing did not significantly alter the amount of FGF2 bound per disaccharide of HS, heparin, CS-E and DS, it did result in a very large reduction in binding for CS-C, such that the amount of FGF2 bound per disaccharide of these galactosaminoglycans after rinsing was equivalent (Figure 6.3).

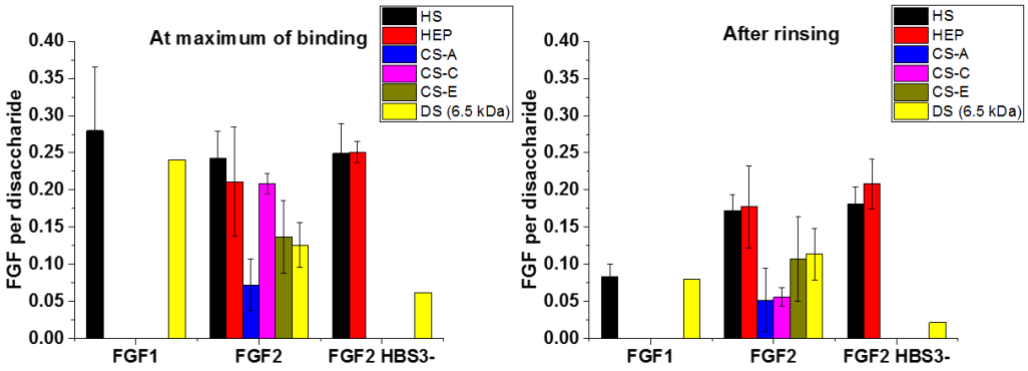


Figure 6.3: Stoichiometry of binding of members of the FGF1 subfamily to GAG brushes. The molar FGF surface densities were determined by SE, at equilibrium after incubation at 0.28 µM (A), and after rinsing with working buffer until stabilisation (B), and compared to the GAG surface densities obtained in the same measurements. Binding stoichiometries are expressed as FGF molecules per GAG disaccharide, and were calculated as $(m_{FGF}/M_{W,FGF})/(m_{GAG}/M_{W,GAG\ disaccharide})$ where $m_{FGF}$ and $m_{GAG}$ are the areal mass densities of FGF and GAG (determined by SE), $M_{W,FGF}$ is the molecular mass of the FGF, and the average molecular mass of the GAG disaccharide was assumed to be $M_{W,GAG\ disaccharide}$ = 0.5 kDa (180). Results are presented for FGF1 on HS and DS (6.5 kDa), for FGF2 on HS, Hep, CS-A, CS-C, CS-E and DS (6.5 kDa), and for FGF2 HBS3- on HS, Hep and DS (6.5 kDa). Error bars indicate minimal and maximal responses based on two independent measurements; where error bars are missing, a single measurement was performed. The equivalent FGF per GAG chains values are reported in Supplementary figure 6.4.

### 6.2.4 Cross-linking of GAG brushes by FGF1 and FGF2.

Rigidification of the films may result from the cross-linking of the GAG chains by the FGFs, and so the immobilisation of the chains (if cross-linking is stable), or from some other effect. Immobilisation occurs when the FGF has multiple HBSs and these interact with different GAG chains. It also depends on these interactions having a lifetime that is not similar to that of the measurement time of the FRAP experiments. These were discussed in detail in section 5. It should be noted that whereas the selective labelling of lysine side chains provides a direct insight into the kinetics of interaction of particular HBSs and individual lysines therein for hep and in all likelihood HS, this is by no means certain for other sulfated GAGs, as there are no equivalent data published. Therefore the mobility of GAG chains in the FGF-loaded GAG brushes was analysed by FRAP. Figure 6.4 shows FRAP traces for the different GAG brushes loaded with FGF1 vs FGF2, and Supplementary Figure 6.9 shows the corresponding quantitative analysis of the mobile fraction and its diffusion constant.

The trends of the fluorescence recovery curves in Figure 6.4B show that the binding of FGF2 but not FGF1 reduces the mobility of heparin. This observation is consistent with our previous observation that FGF2 but not FGF1 immobilised HS (Figure 6.4A and section 5.). Although the recovery in the FGF2-loaded Hep brush appeared to be slightly faster in the FRAP traces (compare Figure 6.4A vs. B), the mobility parameters did not reveal significant differences between Hep and HS (Supplementary Figure 6.9).

In stark contrast to Hep and HS, FGF2 did not affect the mobility of CS-A and CS-C chains: the FRAP traces (Figure 6.4C-D) and the mobility parameters were virtually indistinguishable with and without FGF2 loading (Supplementary Figure 6.8 and Supplementary Figure 6.9). This demonstrates that FGF2 does not have the ability to cross-link CS-A and CS-C stably. Moreover, the increase in $\Delta D$ upon FGF2 binding to CS-A and CS-C brushes (Supplementary Figure 6.2), and related to this the relatively small decrease in $\Delta D/-\Delta f$ (Supplementary Figure 6.7), show that FGF2 rigidifies CS-A and CS-C brushes to a much lesser extent than Hep and HS brushes. Collectively, these data suggest that the propensity of FGF2 to cross-link CS-A and CS-C, even transiently, is low.

Neither FGF1 nor FGF2 reduced the mobility of CS-E, as seen in the FRAP assays curves (Figure 6.4E and Supplementary Figure 6.9) and from the mobility parameters which were equivalent to the bare CS-E brush (Supplementary Figure 6.9).

In regard to DS (6.5 kDa), we observed differential behaviour of FGF1 and FGF2. Whilst FGF1 did not significantly immobilise the brush, FGF2 did. The mobile fraction and diffusion constant of the FGF2-DS (6.5 kDa) were lower than the ones of the bare brushes, clearly showing the presence of an immobilised fraction of GAGs in the FGF2-loaded brush (Supplementary Figure 6.9).

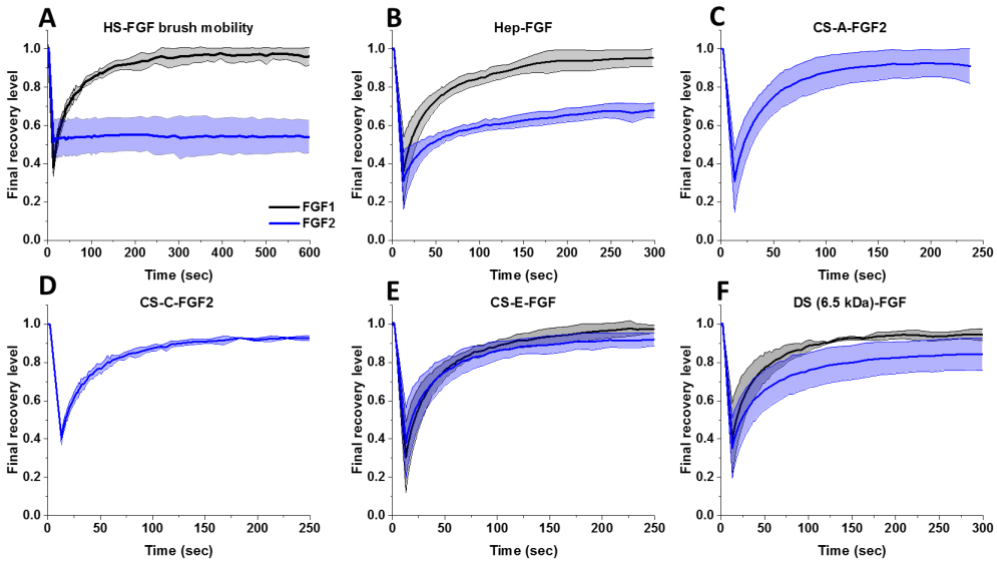


Figure 6.4: Mobility of GAG chains in GAG brushes with FGF1 or FGF2.
FRAP curves of atto488-SAv supported GAG brushes with FGF1 and/or FGF2. Prior to the measurement, mid-dense GAG brushes were incubated for 30 min with 0.28 µM of FGF1 or FGF2, and rinsed 10 times with working buffer (insert here reference to method section). FGF1 did not bind CS-A and CS-C brushes (cf. Supplementary Fig. A-1), and thus FRAP measurements were not performed. The black (FGF1) and blue (FGF2) curves are the means and their standard deviation of 4 independent measurements. Reference curves for the mobility of GAGs in virgin GAG brushes (without FGFs) are shown in Supplementary Fig. A-8, and results of the quantitative analysis of FRAP data are shown in Supplementary Fig. A-9.

In highly sulfated GAGs (HS and Hep), FGF2 generated cross-linked/immobile fractions, 100% in HS and 55% in Hep. However, FGF2 did not crosslink chains in brushes formed from galactosaminoglycans. This includes CS-E, which is an uncontroversial binding partner of FGF2 (190). It is interesting that a greater level of cross-linking was observed for HS than for heparin. Heparin, which has more GlcNS residues has less flexibility than HS around the glycosidic bond, due to transient H-bonds between the N-sulfate and the neighbouring uronic acid's C3 hydroxyl (197), but more flexibility around the uronic acid due to a greater IdoA content. These data suggest that crosslinking may depend in part on the flexibility of the glycosidic bond.

## 6.3 Interactions of FGF4, FGF9, FGF10, FGF17 and FGF18 with GAG brushes.

In this section, interactions of FGF4 (HBS1 and HBS3), FGF9 (HBS1), FGF10 (HBS1 and HBS4), FGF17 (HBS1 and HBS3) and FGF18 (HBS1 and HBS3) with GAG brushes were studied in QCM-D (Supplementary Figure 6.10 to Supplementary figure 6.19).

### 6.3.1 Binding of FGFs to GAG brushes

FGF4 bound to Hep, CS-E and DS (dp18), generating decreases in Δ*f*. Upon rinsing, these slightly desorbed from the brushes but the major part of the bound protein remained. The decreases in Δ*f* were associated with decreases in Δ*D*, indicating FGF4 bound only weakly to CS-A, CS-C and DS (6.5 kDa), the Δ*f* of binding was minor and rapid desorption occurred upon binding. FGF4 has a binding preference for N-sulfated and 2-sulfated disaccharides over 6-sulfated ones (56).

FGF9 binding to HS, Hep and CS-E was slow and continuous, and did not reach equilibrium over the timescale of the measurement. The bound FGF9 was not released upon binding, suggesting strong interactions with the GAGs. FGF9 also bound DS (dp18) and (6.5 kDa) brushes though in these cases equilibrium was attained and the chemokines was released upon rinsing (Supplementary figure 6.12), indicating weak interactions. FGF9 did not bind CS-A. FGF9 is a dimer and each monomer contains one canonical HBS1. The dimer offers a long alignment of these two HBS1 (198) that thus require enough sulfated stretches on GAG chains to be stably bound. Furthermore, the restricted availability of HBSs to this elongated double HBS1 renders the binding of FGF9 specific to the sulfated patterns that are accessible in the GAG chains. In the GAG brushes, FGF9 did not bind to a chain that is mostly made of monosulfated disaccharides with glucuronic residues (CS-A), bound weakly to chains that are mainly composed of monosulfated disaccharides with iduronic residues (DS) and continuously bound to chains that contained disaccharides with at least 2 sulfations on their disaccharide units (CS-E, Hep and HS). This would suggest that the degree sulfation is a key driver of FGF9 binding, or alternatively, that the 6-sulfation is a condition to FGF9 binding on GAG chains.

### 6.3.2 Rigidification of GAG brushes by FGFs

As in previous sections, the parametric plot of QCM-D data was used to assess the changes in GAG brush softness (*ΔD*/*-Δf*) upon FGF uptake (*-Δf*). The GAG brushes have softness parameters between 0.20 and 0.32 $10^{-6}$.$Hz^{-1}$ before the introduction of the FGF. FGFs caused different rigidification of the brushes as observed by the variety of rigidification trends and final measure of softness (Figure 6.5).

The magnitude in the decrease of $\Delta D/-\Delta f$ with $-\Delta f$ (that is, the slope of the curves) close to the onset of protein binding provides a measure for the intrinsic propensity of the FGFs to rigidify GAG brushes. The comparative analysis in Figure 6.7 shows clear trends. The magnitude of the slope for FGF9-loaded GAG brushes is the smallest. This is readily seen on Hep, HS and CS-E were FGF9 binding was substantial. From the slopes of the curves for Hep, HS ad CS-E, it can also be seen that FGF4 has the second weakest propensity to rigidify GAG films. Among the remaining FGFS - FGF10, FGF17 and FGF18 - the propensities to rigidify CS-D and DS (6.5 kDa) are comparable, and this is also the case for FGF10 and FGF18 with CS-A where no data for FGF17 is available. On Hep, FGF18 would appear to have a slightly higher propensity to rigidify than FGF10 and FGF17, whereas the trend is opposite for HS. It is though not clear if these differences are significant, and it may well be that FGF10, FGF17 and FGF18 have identical rigidification propensities for any of the GAGs.

It should be noted that the effective film rigidity induced by binding of a given FGF depends on the intrinsic propensity to rigidify (measured by slope in the parametric plot) and on the amount of protein bound to the film (measured by $-\Delta f$). Thus, for example, FGF18 rigidified DS (6.5 kDa) much more ($\Delta D/-\Delta f = 0.01 \times 10^{-6}.\mathrm{Hz}^{-1}$) than FGF17 ($\Delta D/-\Delta f = 0.13 \times 10^{-6}.\mathrm{Hz}^{-1}$) did because even though both proteins have the same intrinsic propensity to rigidify, FGF 18 binds in much larger amounts.

Taken together, it can be seen that the trends in the propensity to rigidify that were established for HS in Chapter 5, are recapitulated for all other GAGs tested. Moreover, these trends also correlate well with the ability of the FGFs to immobilize HS chains. That is, FGF9 and FGF4 with a low propensity to rigidify essentially do not affect the lateral mobility of HS, whereas FGF10, FGF17 and FGF18 with a similarly high propensity to rigidify all reduce HS mobility substantially (see Supplementary Figure 5.5 in Chapter 5).

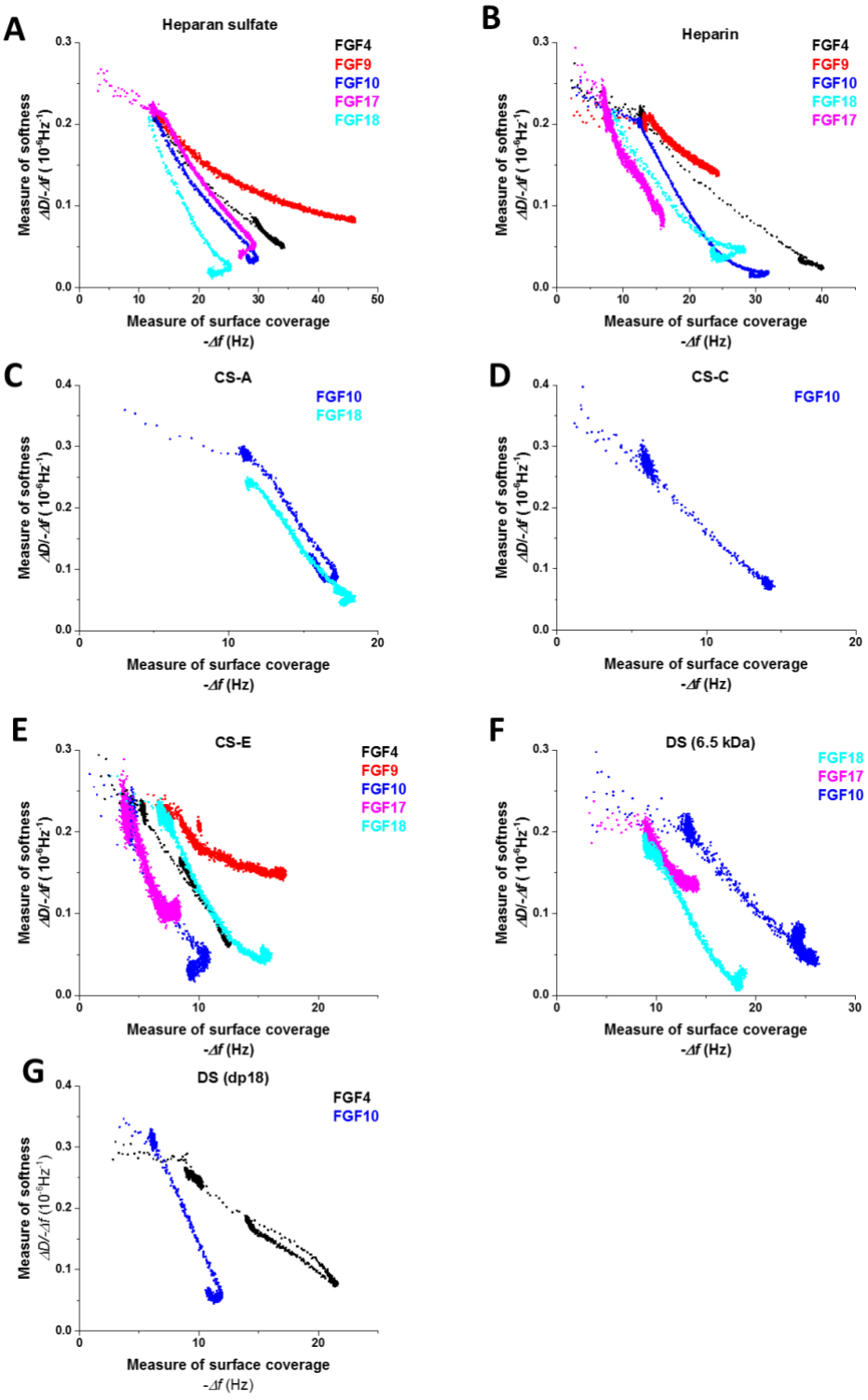


Figure 6.5: Parametric plot analysis of FGFs interaction with GAG brushes.
Mid-dense Heparan sulfate (A), Hep(B), CS-A (C), CS-C (D), CS-E (E), DS (6.5 kDa, F) and DS (dp18, G) brushes were formed (green arrows) and exposed to 0.28 µM FGF4 (black), FGF9 (red), FGF10 (blue), FGF17 (magenta) or FGF18 (cyan) in QCM-D until equilibrium. The brushes were then rinsed with the buffer until stabilisation of the signal.

FGF10 bound to brushes of all tested GAGs. The binding reached various equilibrium values in $\Delta f$ and no or little unbinding was observed upon rinsing (Supplementary figure 6.14).

The binding of FGF17 to Hep, CS-E and DS (6.5 kDa) was slow and did not reach equilibrium, and the rinsing step did not remove the bound protein (Supplementary figure 6.16). This is in contrast to HS (section 5), where binding equilibrium was reached, where the magnitude of the frequency shift was larger, and where the protein was partially released upon rinsing. CS-A, CS-C and DS (dp18) were not tested with FGF17.

FGF18 bound all tested GAG brushes (HS, Hep, CS-A, CS-E and DS (6.5 kDa)) to equilibrium. The magnitude of binding was relatively low in CS-A, CS-E and DS (6.5 kDa) though there was no unbinding upon rinsing in these cases (Supplementary figure 6.18). In the cases of HS and Hep, the magnitude of $\Delta f$ was noticeably higher, yet the rising step partially desorbed the FGF18. However, the remaining bound FGF18 was still significantly higher than in the CS-A, CS-E and Ds (6.5 kDa) brushes.

### 6.3.3 Stoichiometries of FGF binding to GAGs

Using SE, I measured the binding stoichiometry for FGF4, FGF10, FGF17 and FGF18 to Hep, and in addition for FGF9, FGF17 and FGF18 on DS (6.5 kDa). The results, and in addition the data previously obtained for HS (see Chapter 5) are reported in Figure 6.6.

FGF4 bound hep to a higher stoichiometry than HS at maximum of binding, but the rinsing step reduced it to a level equivalent to the final stoichiometry for HS (Figure 6.6). This was consistent with QCM-D data where, at maximum of binding the measure of surface coverage was higher for hep than for HS.

As observed in QCM-D, the binding of FGF9 to DS (6.5 kDa) was very low and the rinsing step completely desorbed the protein. This characteristic was confirmed in SE quantification of FGF9 on a DS (6.5 kDa) brush. The stoichiometry at the maximum of binding was very low and the bound FGF9 undetectable after rinsing (Figure 6.6). FGF10 was shown to bind hep brushes in larger amount than HS in SE, although the

QCM-D data suggested that they were equivalent. Here, the SE data is prevalent as it measures the absolute surface density, without trapped solvent of biomolecules on the surface. The binding stoichiometry of FGF17 for HS and hep were equivalent before at the maximum of binding as measured in the SE quantification of their surface densities. At the maximum of binding, we measured $6 \pm 1$ and 5 FGF17 per HS and Hep chain respectively (Figure 6.6). Upon rinsing, FGF17 partially desorbed from both HS and Hep brush. The stoichiometry of binding to DS (6.5) was relatively low compared to HS and Hep. However, the bound FGF17 was not released from the brush during the rinsing step. The amount of FGF18 bound were variable across the GAG brushes as measured by SE. FGF18 bound hep in the largest amount, significantly higher than to HS and to DS (6.5 kDa). The binding to CS-A and CS-E was evaluated in QCM-D only and the *Δf*, measures of surface coverage showed relatively low amount of FGF18 compared to HS and Hep but similar to DS (6.5 kDa).

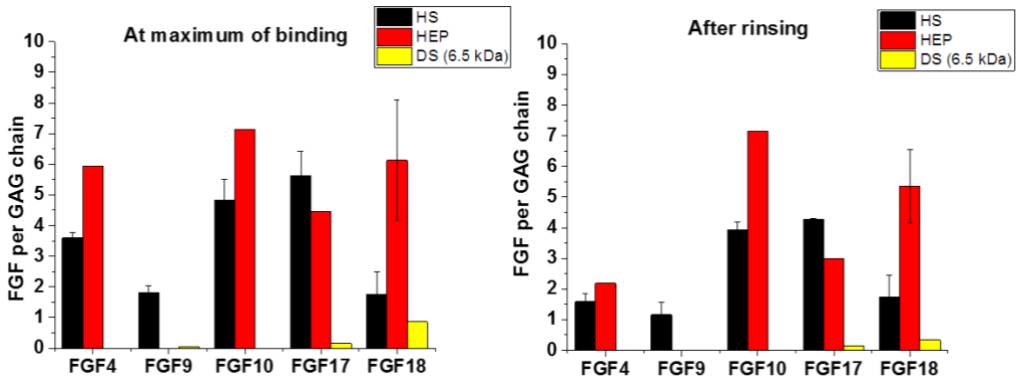


Figure 6.6: Stoichiometric quantification of FGF bound to GAG brushes.
FGF were incubated at 0.28 µM on HS (FGF4, FGF9, FGF10, FGF17 and FGF18), Hep (FGF4, FGF10, FGF17 and FGF18) and DS (FGF9, FGF17 and FGF18). The molar FGF surface densities were determined by SE equilibrium after incubation at 0.28 µM, and after rinsing with working buffer until stabilisation, and compared to molar GAG (HS, Heparin, DS (6.5 kDa)) surface densities (**Error! Reference source not found.**) obtained in the same measurements. T he data presented is for 1 or 2 independent measurements. The binding stoichiometires for HS were previously reported in (section 5.2).

## 6.4 Discussion

In this section, we have measured the interactions of FGFs with different GAGs. There are considerable data on some of these interactions acquired using other techniques, particularly for FGF1 and FGF2 (56, 104, 190).

In the here presented assay, all FGFs bound to hep brushes in equivalent or higher amount than on HS brushes. This is consistent with the higher degree of sulfation in Hep than in HS and the expected preferential binding of FGFs to sulfated regions. For this purpose FGF1, FGF2, FGF2 HBS3-, FGF4, FGF9, FGF10, FGF17 and FGF18 were purified in-house using hep affinity chromatography and their binding affinity and thermos-stabilisation by hep oligosaccharides were studied (56, 103, 104, 190) and concurred with our results where all FGFs bound to HS and Hep (chapter 5 and sections 6.1 to 6.3).

In the same prospect, interactions of CS-A and CS-C with FGF10, FGF17 (56) and FGF18 (104), and of CS-E with FGF2 (190) had been previously reported. Interactions of DS with FGF1 (104), FGF4, FGF10 and FGF17 (56) and FGF18 (104) have also been described. Some FGF did not interact with the GAG brushes they were probed with. In particular, there was no detectable interaction between FGF4 and CS-A and CS-C, and a very weak and transient interaction between FGF4 and CS-E. Our data support the weak or absent interactions between FGF4 and CS described previously (56). The lacking interactions between FGF1 and CS-E (190), between CS-C and CS-A and FGF1 and FGF9, and between FGF2 and DS (56) were also reproduced here in the QCM-D measurements. Li et al (56) also reported that FGF2 did not bind CS but we could detect stable interaction with CS-A, CS-C and CS-E brushes and suggested that this may be the result of the latter being anchored as brushes on a surface.

The mid-dense GAG brushes used here differ substantially from the solution and surface analyses used by others previously. In solution the GAG chains are dilute and possess 3 degrees of translational freedom, like the FGF ligand, whereas in past surface analyses, the GAG chains are immobilised on the sensor surface. In contrast, on a mid-dense brush, the GAG chains are anchored, but have two degrees of translational freedom, in x and y. A consequence is that FGF binding can alter the

organisation of the brush, which could in turn alter the likelihood of interaction with further FGF molecules and/or alter the probability of dissociation from the brush. The data are somewhat sparse, in that further experiments are required to repeat some measurements and some measurements were not done. Nonetheless, there are some intriguing conclusions that can be drawn, though some may at this stage be tentative.

# Supplementary information

**Binding of FGFs to GAG brushes – GAG type specificity of binding, brush rigidification and GAG mobility.**

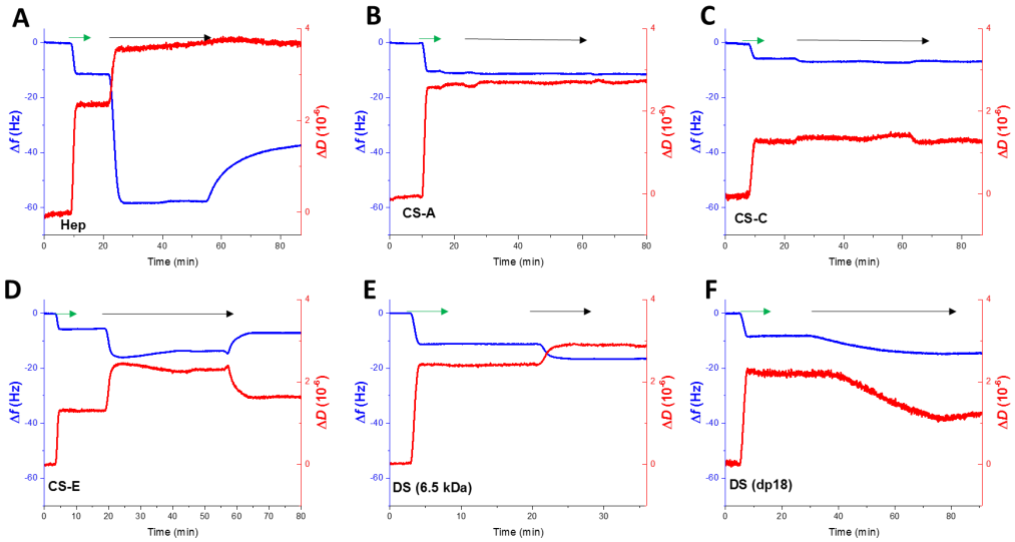


Supplementary figure 6.1: QCM-D monitoring of FGF1 interaction with mid-dense GAG brushes.
SUV, SAv and GAGs (Hep, CS-A, CS-C, CS-E, DS (6.5 kDa) and DS (dp18); green arrows) were infused at 50, 20 and 5 µg/ml, respectively. Every step was followed by a minimum of 5 min infusion of incubation buffer at 20 µl/min, and FGF1 was infused at 0.28 µM at a 10 µl/min flow rate (black arrow).

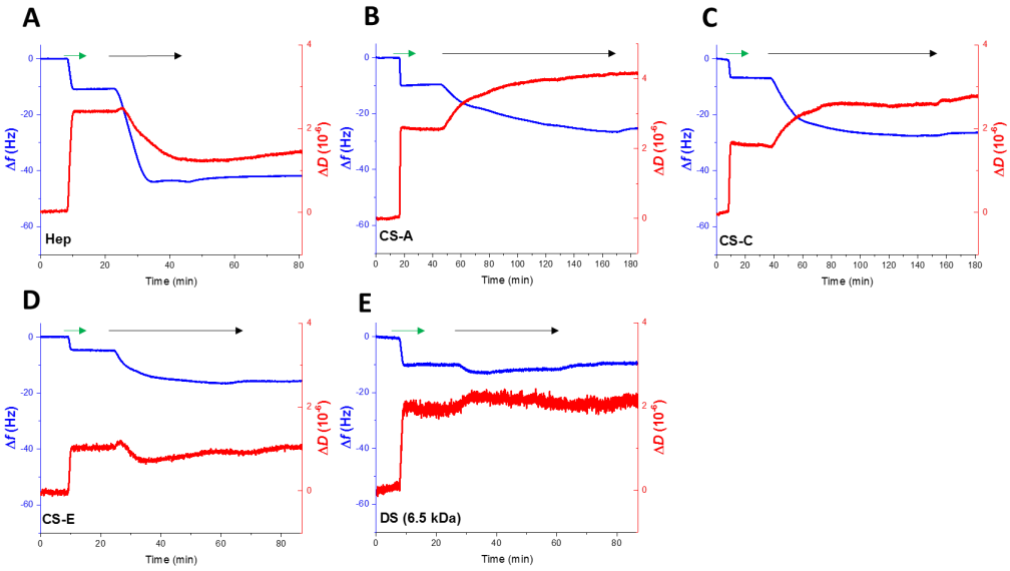


Supplementary Figure 6.2: QCM-D monitoring of FGF2 interaction with mid-dense GAG brushes.
Measurements were performed, and data are presented, analogous to Supplementary Figure A-1. FGF2 binds stably to Hep, CS-A, CS-c, CS-E and DS (6.5 kDa).

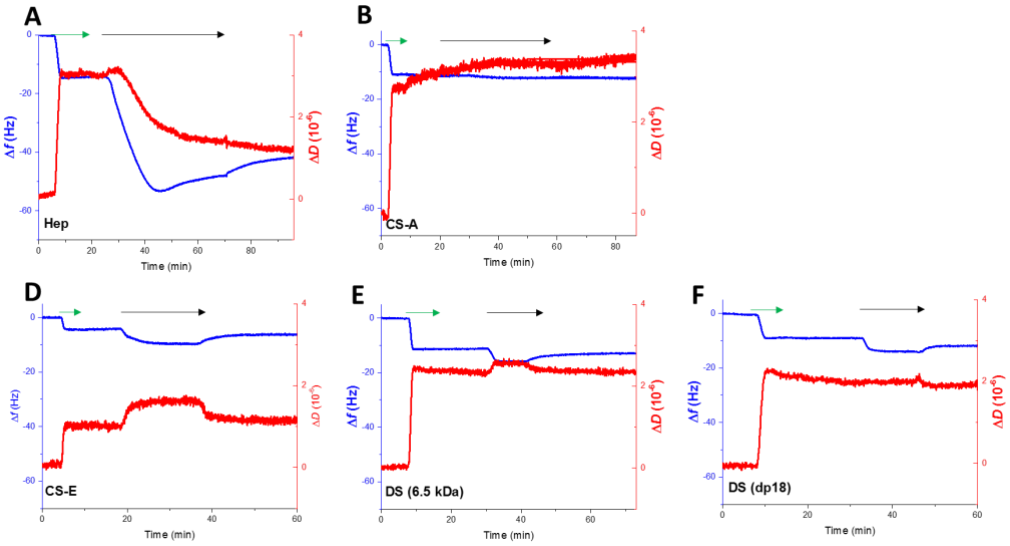


Supplementary figure 6.3: QCM-D monitoring of FGF2 HBS3- interaction with mid-dense GAG brushes.
Measurements were performed, and data are presented, analogous to Supplementary Figure A-1. FGF2 HBS3- binds to Hep, CS-A, CS-E, DS (6.5 kDa) and DS (dp18). We did not test the binding to CS-C.

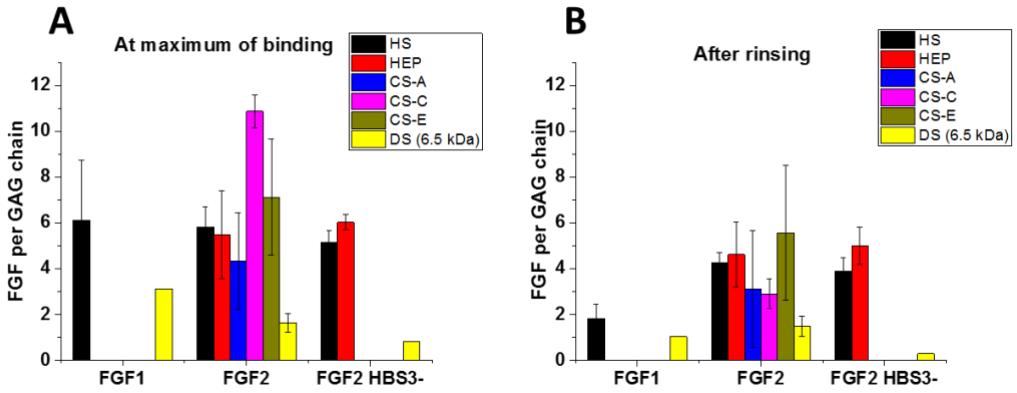


Supplementary figure 6.4: Stoichiometry of binding of members of the FGF1 subfamily to GAG brushes.
The molar FGF surface densities were determined by SE, at equilibrium after incubation at 0.28 µM (A), and after rinsing with working buffer until stabilisation (B), and compared to the molar surface densities of the GAGs (HS, Heparin, CS-A, CS-C, CS-E and DS (6.5 kDa), obtained in the same measurements. Results presented for experiment of FGF1 (on HS and DS (6.5 kDa)), FGF2 (on HS, Heparin, CS-A, CS-C, CS-E and DS (6.5 kDa)) and FGF2 HBS3- (on HS, Hep and DS (6.5 kDa)). Error bars indicate minimal and maximal responses based on two independent measurements; where error bars are missing, a single measurement was performed.

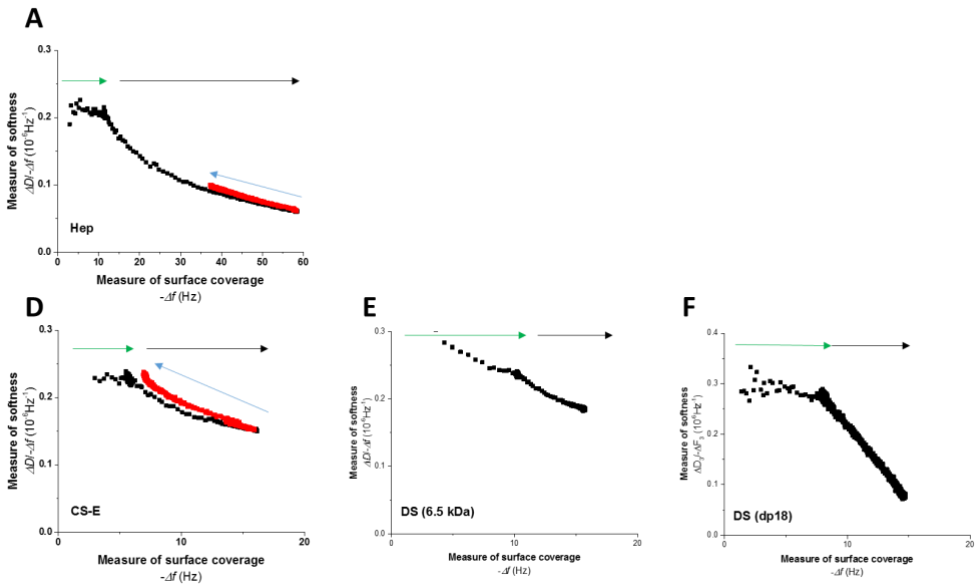


Supplementary Figure 6.5: Parametric plot analysis of FGF1 interaction with mid-dense GAG brushes.
Representative data is shown for formation of mid-dense Hep (A), CS-E (D), DS (6.5 kDa) (E) and DS (dp18) (F) brushes (green arrows) and binding of FGF1 at 0.28 µM FGF1 until equilibrium (black arrow), and subsequent rinsing with the buffer until stabilisation of the signal (blue arrow; not shown for DS as binding was fully stable in this case). Data were extracted from QCM-D experiments presented in Supplementary figure 6.1; data for CS-A and CS-B are not shown, as FGF1 did not bind to these GAGs.

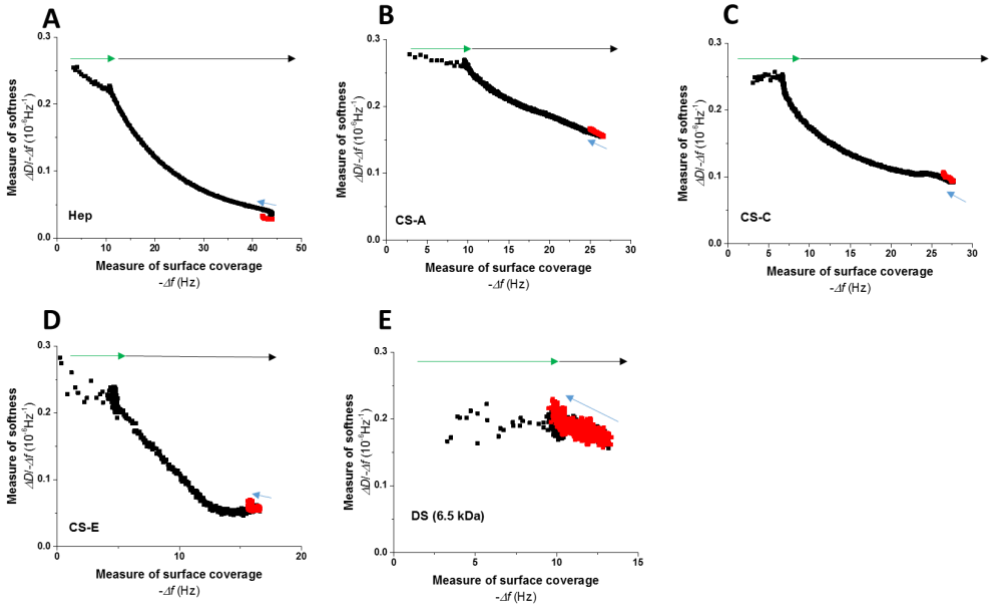


Supplementary figure 6.6: Parametric plot analysis of FGF2 interaction with mid-dense GAG brushes.
Plots are presented analogous to Supplementary Figure 6.5, and data were extracted from data presented in Supplementary Figure 6.2.

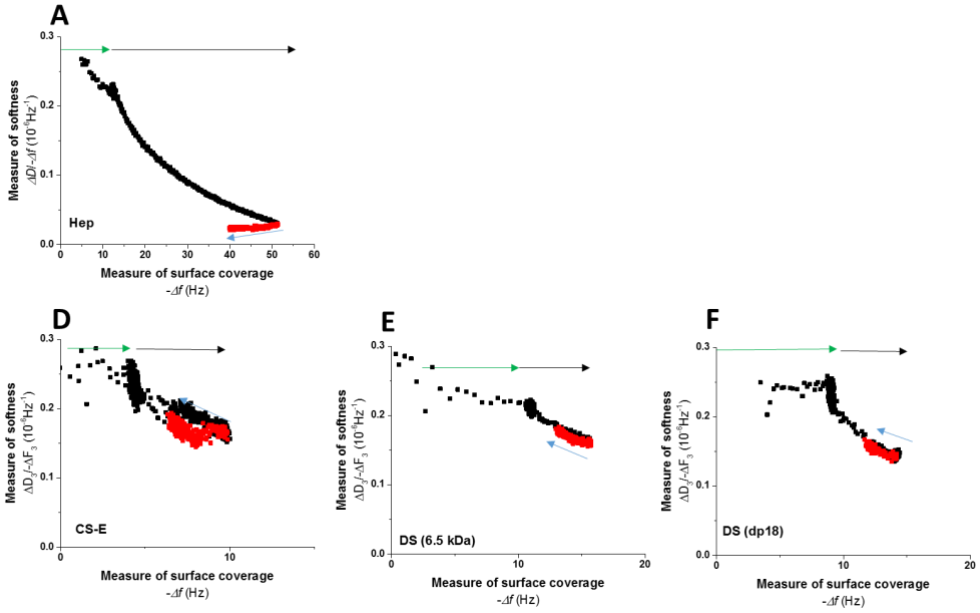


Supplementary figure 6.7: Parametric plot analysis of FGF2 HBS3- interaction with mid-dense GAG brushes.
Plots are presented analogous to Supplementary Figure 6.5, and data were extracted from data presented in Supplementary Fig. B-3; data for CS-A are not shown as FGF2 HBS3- did not bind to this GAG.

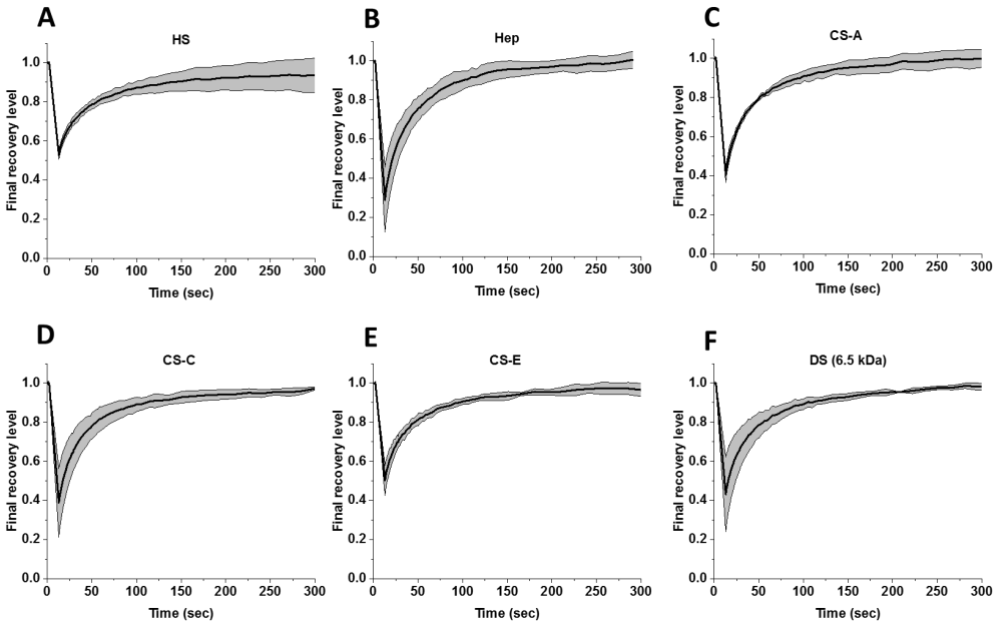


Supplementary Figure 6.8: Fluorescence recovery curves of mid-dense GAG brushes.
FRAP curves of atto488-SAv supported GAG brushes prepared as described in section 4.6.4). The black curve and the grey area are the means and their standard deviations based on 4 measurements, obtained after GAG brush formation. Briefly, SUVs containing 99.5:0.5 mol:mol DOPC:DOPE-CAP-biotin were put in contact with a clean glass cover slip for 30 min at 50 µg.mL$^{-1}$. After rinsing, SAv-atto was incubated for 30 min at 20 µg.mL$^{-1}$. The surface was rinsed with working buffer and incubated with 5 µg.mL$^{-1}$ biotinylated GAGs for 30 min. Soluble GAGs were rinsed off with working buffer prior to FRAP (section 4.6.1).

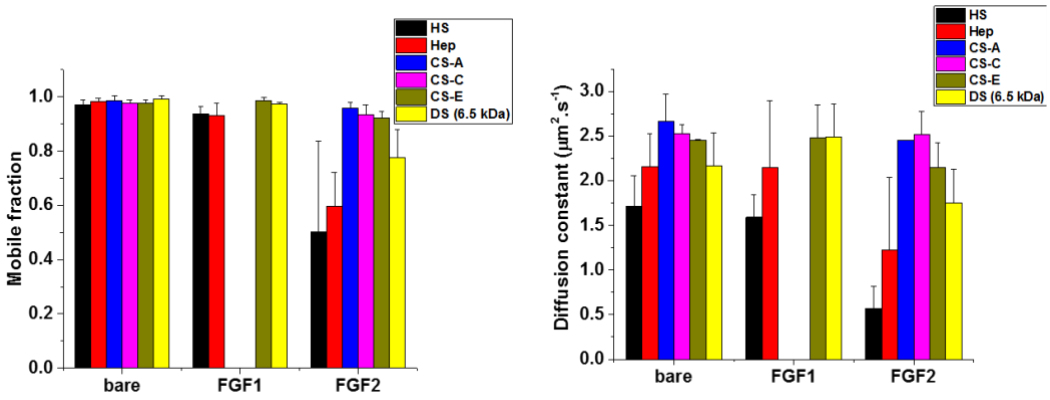


Supplementary Figure 6.9: Mobility parameters of bare GAG brushes, and GAG brushes with bound FGF1 and FGF2.
Mobile fraction (A) and its diffusion constant (B) were obtained from 4 independent measurements of FRAP on atto488-SAv supported GAG brushes. Data for bare GAG brushes were obtained after rinsing with working buffer; data for GAG brushes with FGFs were obtained after 30 min incubation with 0.28 µM FGF1 or FGF2. The soluble FGF1 and FGF2 were rinsed off prior to the measurements. FRAP measurements were not performed for CS-A and CS-C brushes with FGF1 as FGF1 did not bind to these GAGs (see Supplementary Fig. 6.1).

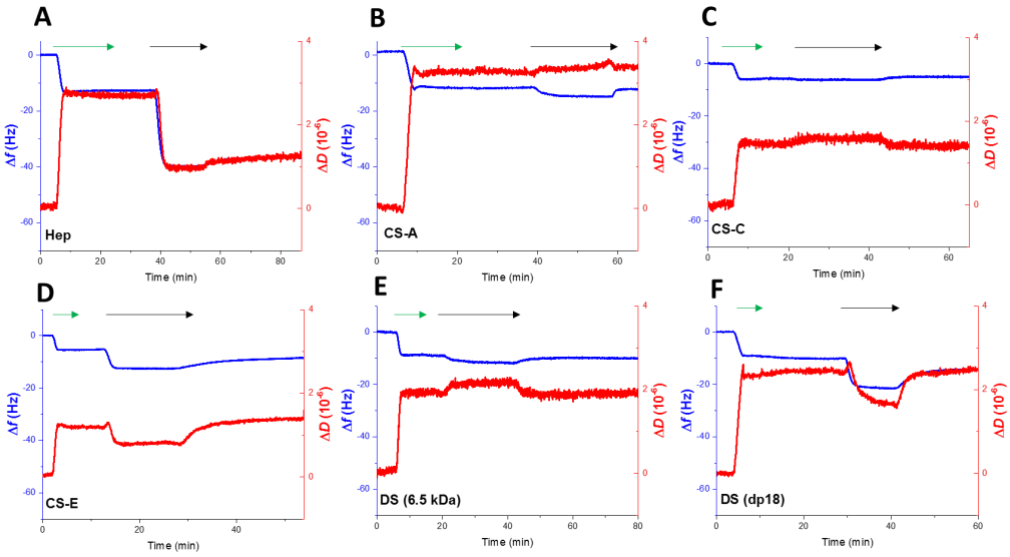


Supplementary Figure 6.10: QCM-D monitoring of FGF4 interaction with GAG brushes. Measurements were performed, and data are presented, analogous to Supplementary Figure 6.1. FGF4 binds to Hep, CS-A, CS-E, DS (6.5 kDa) and DS (dp18).

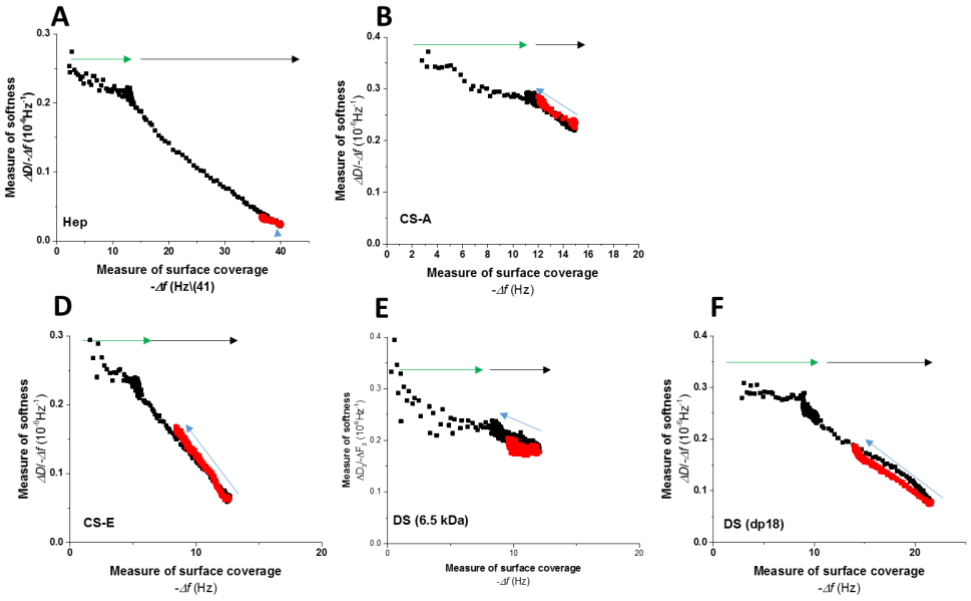


Supplementary figure 6.11: Parametric plot analysis of FGF4 interaction with GAG brushes. Plots are presented analogous to Supplementary Figure 6.5, and data were taken from Supplementary Fig. B-10; data for CS-C are not shown as FGF4 did not bind to this GAG.

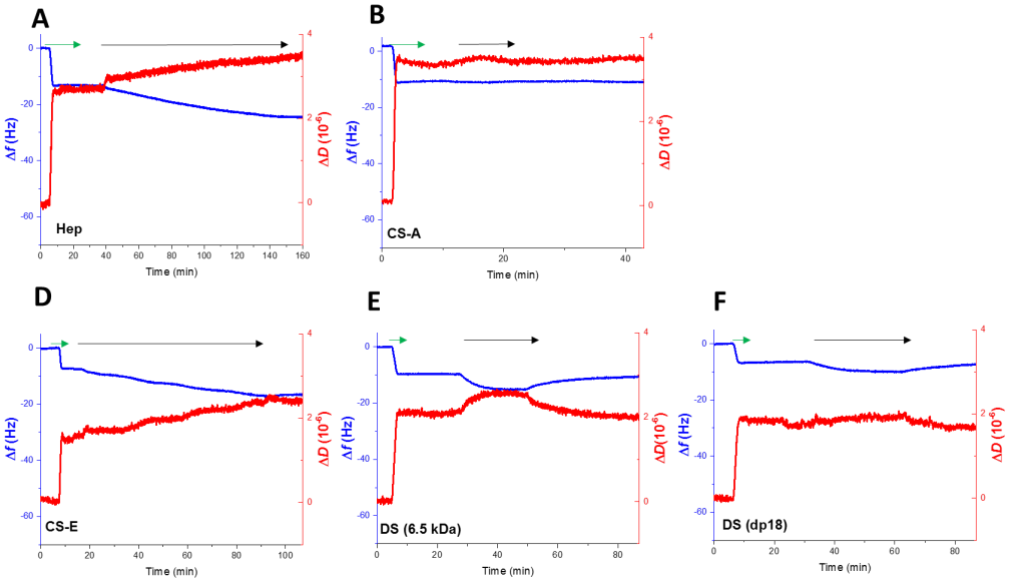


Supplementary figure 6.12: QCMD monitoring of FGF9 interaction with GAG.
SUV, SAv and GAGs (green arrow) were all infused at 50, 20 and 5 µg/ml respectively and a 20 µl/min flow rate during 5 min prior to protein infusion. Every step was followed by a minimum of 5 min infusion of incubation buffer at 20 µl/min and FGF9 was infused at 0.28 µM at a 10 µl/min flow rate (black arrow). The real-time monitoring of FGF9 binding to Heparin, CS-A, CS-E, DS (6.5 kDa) and DS (dp18) show a stable binding of the protein.

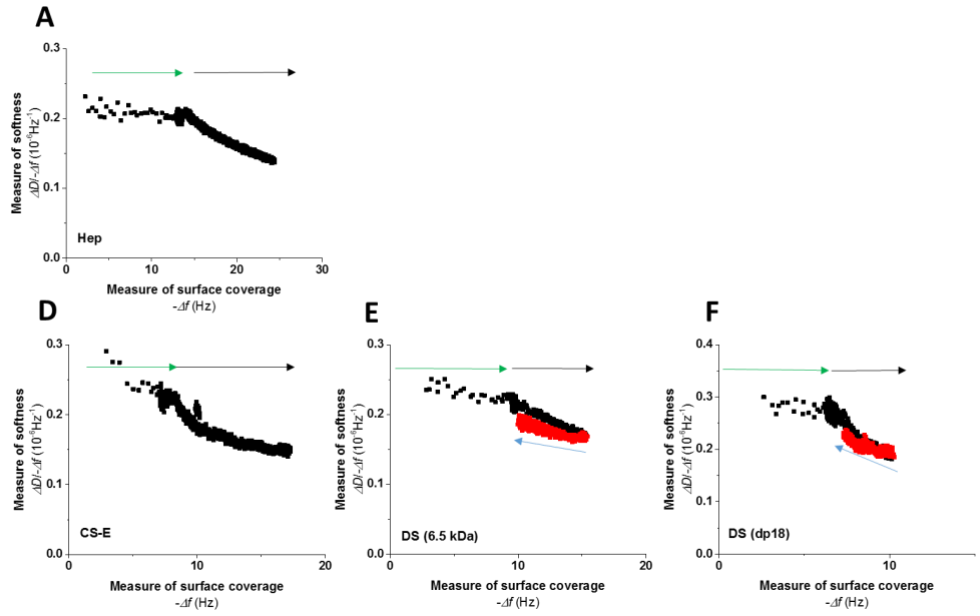


Supplementary figure 6.13: Parametric plot analysis of FGF9 interaction with GAGs.
Mid-dense Hep (A), CS-E (D), DS 6.5 kDa (E) and DS dp18 (F) brushes were formed (green arrow) and exposed to 0.28 µM FGF9 in QCM-D until equilibrium (black arrow). The brushes were then rinsed with the buffer until stabilisation of the signal (blue arrow).

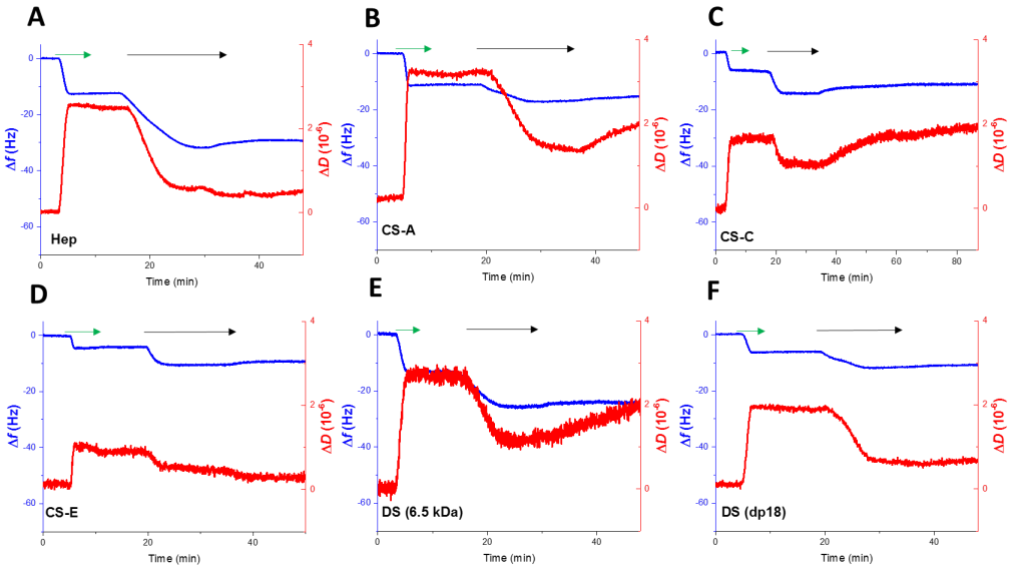


Supplementary figure 6.14: QCMD monitoring of FGF10 interaction with GAG.
SUV, SAv and GAGs (green arrow) were all infused at 50, 20 and 5 µg/ml respectively and a 20 µl/min flow rate during 5 min prior to protein infusion. Every step was followed by a minimum of 5 min infusion of incubation buffer at 20 µl/min and FGF10 was infused at 0.28 µM at a 10 µl/min flow rate (black arrow). The real-time monitoring of FGF10 binding to Heparin, CS-A, CS-C, CS-E, DS (6.5 kDa) and DS (dp18) show a stable binding of the protein.

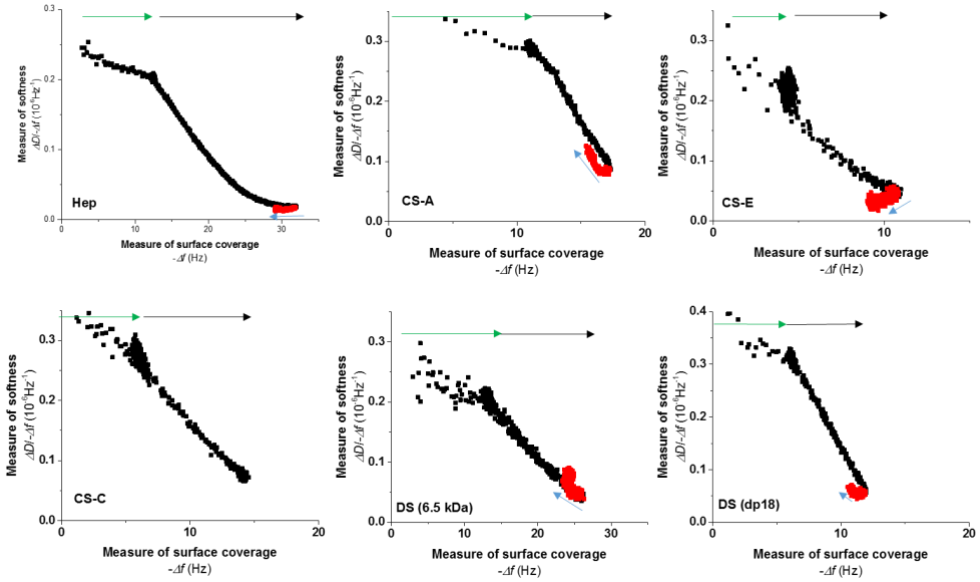


Supplementary figure 6.15: Parametric plot analysis of FGF10 interaction with GAGs.
Mid-dense Hep (A), CS-A (B), CS-E (C), CS-C (D), DS 6.5 kDa (E) and DS dp18 (F) brushes were formed (green arrow) and exposed to 0.28 µM FGF10 in QCM-D until equilibrium (black arrow). The brushes were then rinsed with the buffer until stabilisation of the signal (blue arrow).

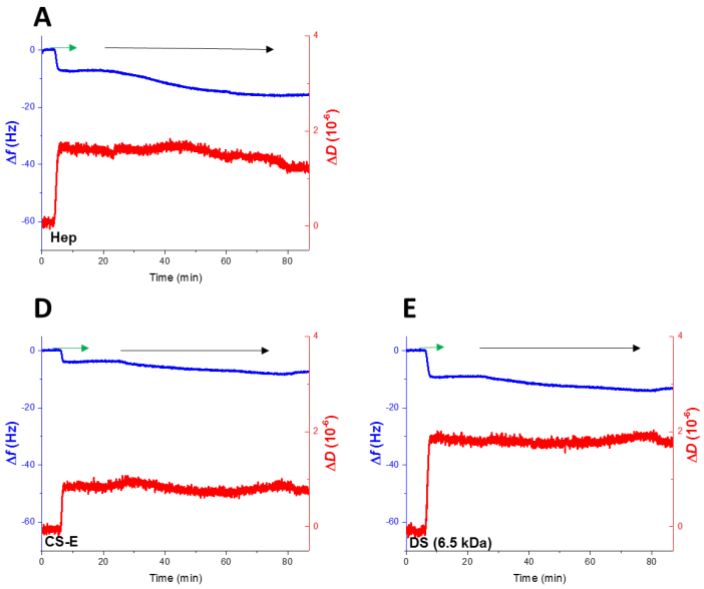


Supplementary figure 6.16: QCMD monitoring of FGF17 interaction with GAG.
SUV, SAv and GAGs (green arrow) were all infused at 50, 20 and 5 µg/ml respectively and a 20 µl/min flow rate during 5 min prior to protein infusion. Every step was followed by a minimum of 5 min infusion of incubation buffer at 20 µl/min and FGF17 was infused at 0.28 µM at a 10 µl/min flow rate (black arrow). The real-time monitoring of FGF17 binding to Hep (A), CS-E (D), and DS (6.5 kDa, E) show a stable binding of the protein.

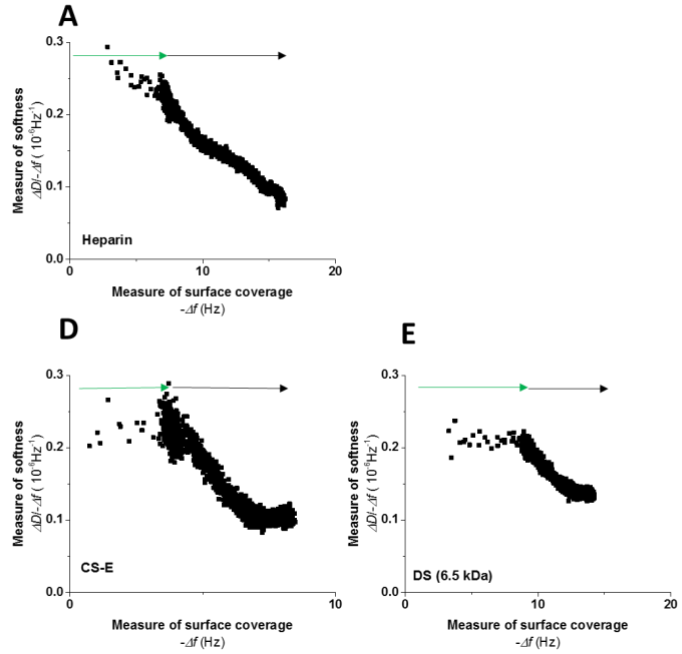


Supplementary figure 6.17: Parametric plot analysis of FGF17 interaction with GAGs.
Mid-dense Hep (left), CS-E (middle) and DS 6.5 kDa (right) brushes were formed (green arrow) and exposed to 0.28 µM FGF17 in QCM-D until equilibrium (black arrow). The brushes were then rinsed with the buffer until stabilisation of the signal (blue arrow).

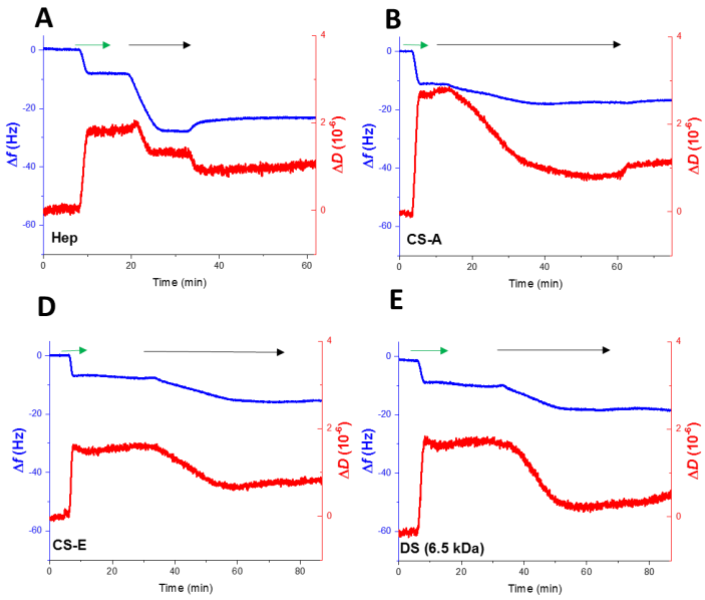


Supplementary figure 6.18: QCMD monitoring of FGF18 interaction with GAG.
SUV, SAv and GAGs (green arrow) were all infused at 50, 20 and 5 µg/ml respectively and a 20 µl/min flow rate during 5 min prior to protein infusion. Every step was followed by a minimum of 5 min infusion of incubation buffer at 20 µl/min and FGF18 was infused at 0.28 µM at a 10 µl/min flow rate (black arrow). The real-time monitoring of FGF18 binding to Heparin, CS-A, CS-E and DS (6.5 kDa) show a stable binding of the protein.

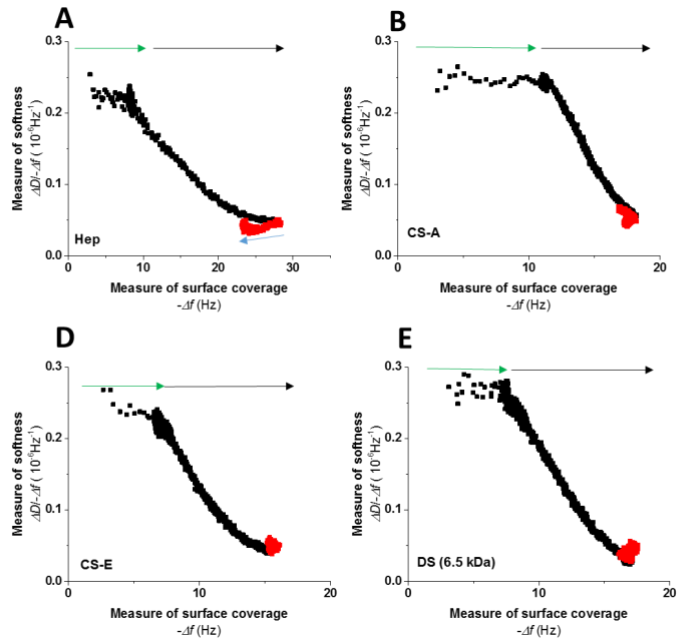


Supplementary figure 6.19: Parametric plot analysis of FGF18 interaction with GAGs.
Mid-dense Hep(A), CS-A (B), CS-E (D) and DS 6.5 kDa (E) brushes were formed (green arrow) and exposed to 0.28 µM FGF18 in QCM-D until equilibrium (black arrow). The brushes were then rinsed with the buffer until stabilisation of the signal (blue arrow).

# 7 Mobility of FGFs in pericellular matrices

## 7.1 Introduction

In chapters 5 and 6, I analysed the molecular interactions of FGFs with GAG brushes and evaluated their binding, ability to cross-link the GAG chains and their mobility in instances where a halotagged version of the FGF was available. In this chapter preliminary data are presented on the binding and mobility of fluorescently labelled halotagged FGFs in the pericellular matrix of keratinocytes. Previously, similar work has been done in a rat mammary fibroblast cell (185) and in the same cells at the single molecule level (187). However, it is not known if the pericellular matrix of an epithelial cell presents similar FGF binding properties. While the HS on the fibroblasts and the keratinocytes are expected to differ, these differences may be reduced, unaffected or magnified by the differences in endogenous HS binding proteins occupying a subset of binding sites in the polysaccharide and modifying at least some of the neighbouring sites. The basic controls of autofluorescence and fluorescence due to non-specific binding of the TMR dye and of TMR-labelled halotag were performed. Fluorescent images were then acquired following incubation with TMR-labelled HaloFGFs. As care was taken to avoid saturation, the fluorescence could be quantified to provide a measure of the binding of the different HaloFGFs. The mobility of FGFs in the pericellular matrix of HaCaT cells was then measured using FRAP.

## 7.2 HaloFGFs bind to the pericellular matrix of keratinocytes.

### 7.2.1 Binding propensity and repartition.

The level of autofluorescence in HaCaT cells and the level of fluorescence due to non-specific binding of the TMR dye and of TMR-Halotag were first determined. TMR dye and TMR-Halotag protein were incubated with fixed HaCaT cells for 30 mins and then cells were rinsed in PBS prior to imaging (4.6.3). There was no detectable fluorescence (Figure 7.1), indicating that non-specific binding would not contribute to any signal observed with a TMR-HaloFGF.

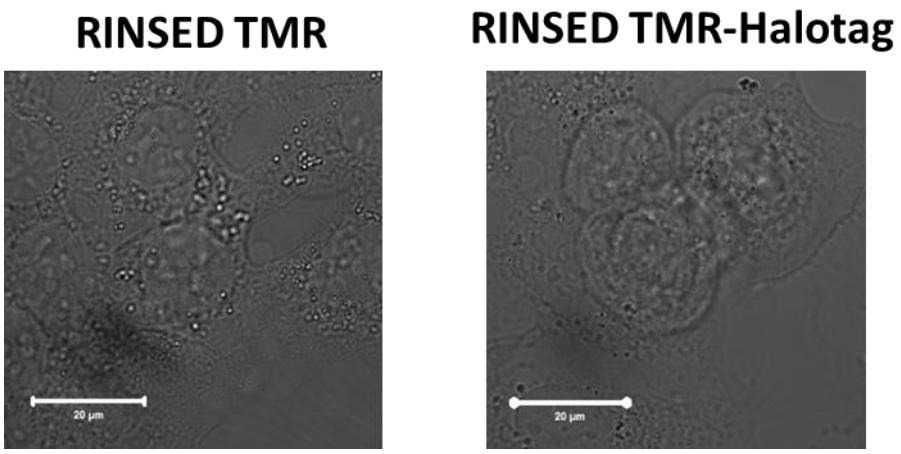


Figure 7.1: Non-specific binding control of TMR and TMR-Halotag on HaCaT cells.
Overlaid images of bright field and confocal fluorescence of fixed HaCaT cells. The cells were incubated for 30 minutes with 2 nM TMR (left) or TMR-Halotag (right) and rinsed with PBS before imaging. The cells were visible with no apparent fluorescent dye (TMR) or protein (TMR-Halotag).

The fluorescence of HaloFGF1 and HaloFGF2 was preferentially associated to lateral surfaces/edges of the cells, as shown by the elevated fluorescence on this area (Figure 7.2). In contrast, the fluorescence after incubation of the cells with HaloFGF6 was diffuse across the cell, yet also quite granular in appearance, indicating uneven association of the FGF6 with different parts of the pericellular matrix. The HaloFGF7, HaloFGF10 and HaloFGF17 fluorescence was diffuse across the cell and more homogeneous. HaloFGF18 fluorescence was somewhat granular, but less so than that of HaloFGF6, whereas FGF20 fluorescence was very heterogeneous (Figure 7.2). In some cases, e.g., HaloFGF20, fluorescence was punctate, resembling the size of an endosome or similar type of vesicle, but as the cells were fixed, it is unlikely that the FGFs associate with intracellular vesicles. Although z-stacks of images were not acquired, the focal plane in each case was similar, since the nucleus is apparent in each image. This suggests that the structures in HS that bind these FGFs on the lateral and the basal or apical surfaces of the cells may differ. While in the absence of z-stacks, it is not certain that the FGFs did not in some cases bind intracellular structures, it should be noted that there is no nuclear fluorescence. At least FGF1 and FGF2 bind strongly to nucleic acids (199, 200) (201) and it is likely that this is true for all FGFs, due to the similarity between the sugar-sulfate of HS and the sugar-phosphate of nucleic acids.

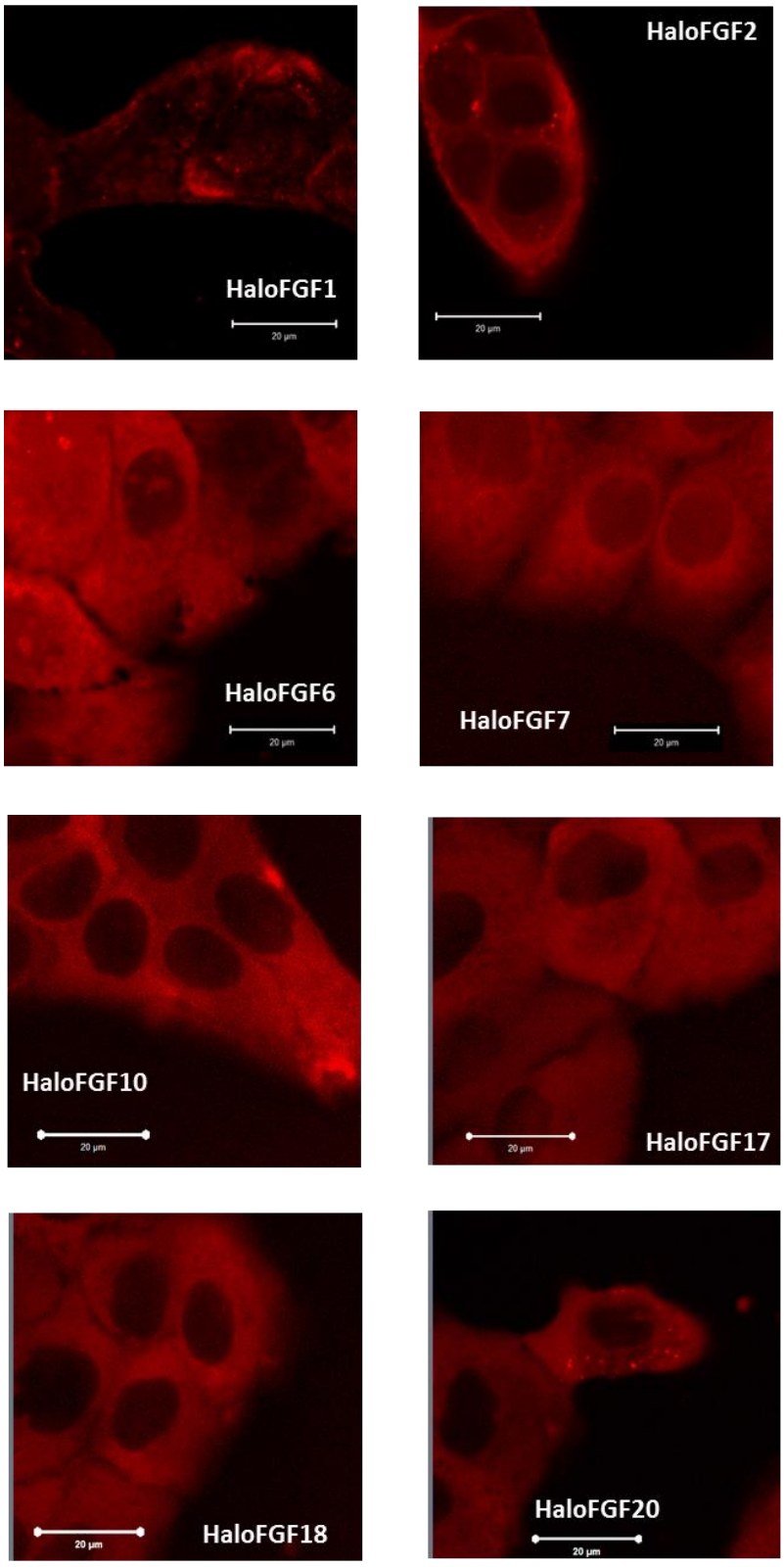


Figure 7.2: Fluorescent labelling the pericellular matrix of HaCaT cells with HaloFGFs.
The fixed cells were incubated with 2 nM TMR-HaloFGFs for 30 minutes at 37°C and rinsed 10 times with PBS. Images of the cells were taken in the same conditions (described in 4.6.3) for all FGFs using the LSM 780 microscope and processed with the Fiji software.

Thus, this suggests that all the fluorescence is extracellular, in accord with the absence of a cell permeabilisation step during fixation and previous results (185, 187).

The fluorescence intensities were extracted using Fiji® (Figure 7.3). The fluorescence intensities of HaloFGF1 (41 ± 8 A.U. $\mu m^{-2}$) and HaloFGF2 (38 ± 15 A.U. $\mu m^{-2}$) were the lowest and were equivalent to one another. Other HaloFGFs (HaloFGF6, HaloFGF10, HaloFGF18 and HaloFGF20) had a fluorescence intensity similar or higher than those of HaloFGF1 and HaloFGF2 (Supplementary figure 7.1). HaloFGF7 and HaloFGF17 has the highest fluorescence intensities at 77 ± 10 and 68 ± 10 A.U. $\mu m^{-2}$, respectively (Figure 7.3).

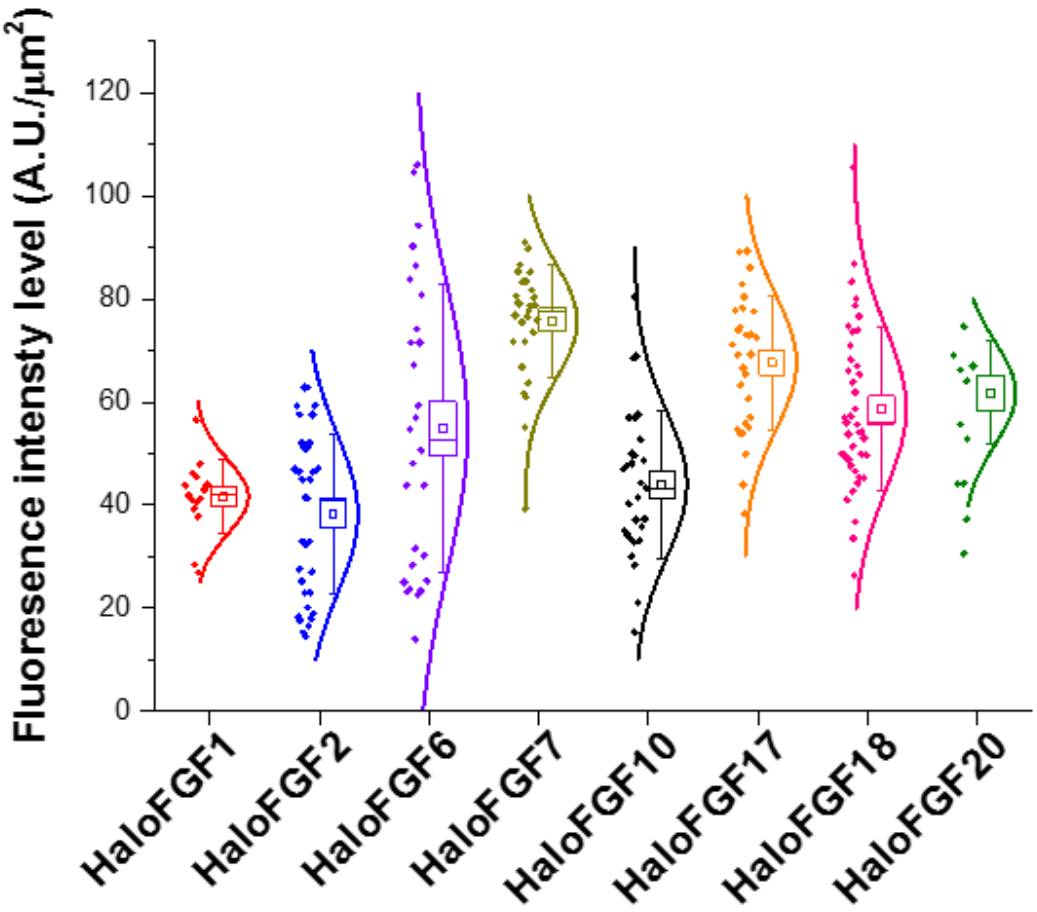


Figure 7.3: Average binding intensities of HaloFGFs to the pericellular matrix of HACaT. 500 µL fluorescently labelled HaloFGFs (2 nM) were incubated with fixed HaCaT cells for 30 min. The unbound fluorescent HaloFGFs were rinsed off and the fluorescence intensities per cell were measured using Fiji® (section 4). Each data point corresponds to the average fluorescence intensity across one cell. The means (square), the standard errors (box), the median (line) and the standard deviations (whiskers) are represented and the individual data points are also shown, as is their distribution.

However, these are values averaged across an entire cell, so the very heterogeneous distribution of some of the HaloFGFs, *e.g*, HaloFGF1, HaloFGF2 and Halo-FGF20 associated fluorescence means that their binding sites in pericellular matrix are far from evenly distributed.

### 7.2.2 HaloFGF mobility in native pericellular matrices

To measure the mobility of the HaloFGFs in the pericellular matrix of HaCaT keratinocytes, their binding is assumed to be stable, in that they are not expected to dissociate from the pericellular matrix and diffuse into the bulk culture medium. This stability was observed in the HS brushes after rinsing (section 5.2) and in fibroblasts previously (185, 187). The time scale of the FRAP experiments on a single dish of cells varied between one to two hours, so the assumption is reasonable, but yet not verified since we have not measured the fluorescence changes over time, unlike in fibroblasts (185). Images of FRAP assays are presented in Supplementary figure 7.3 and 6.4 and the recovery curves in Figure 7.4.

Following photobleaching, the fluorescence of HaloFGF1 recovered gradually, but never attained a maximal level (Figure 7.4A). After 300 s, the HaloFGF1 had recovered to 29 ± 12 % of the initial level whilst a plateau was not reached. The fluorescence of HaloFGF2 recovered to 19 ± 9 % of the initial level, which was not significantly different from HaloFGF1 in this respect. In contrast to HaloFGF1, the recovery of HaloFGF2 reached a plateau before the end of the assay. This suggests that the fluorescence recovery of HaloFGF2 is the result of a small (19 ± 9%) mobile fraction, whereas the remaining part of HaloFGF2 is essentially immobile. In contrast, the slow gradual recovery of fluorescence of HaloFGF1 indicates that a much greater level of recovery would be observed at longer times. Consequently, although the recovery level would seem equal after 300 s (Supplementary figure 7.2), the mobile fraction of HaloFGF1 is likely to be much more substantial than that of HaloFGF2. The mobility of HaloFGF6 (FGF4 subfamily) was low and reached a plateau of recovery of 14 ± 17% (Figure 7.4C and Supplementary figure 7.2). Thus, HaloFGF6 was similar to HaloFGF2, in that the majority of the protein appeared to be immobile.

HaloFGF7 and HaloFGF10 possessed distinct motilities even though they belong to the same FGF subfamily (FGF7). The recovery of fluorescence of HaloFGF7 had a very fast element: images acquired immediately after photobleaching already showed a considerable amount of recovery (Figure 7.4D and Supplementary figure 7.2), and within less than 1 min a recovery of 88 ± 12% was reached. In contrast, the fluorescence of HaloFGF10 recovered slowly, and reached only 27 ± 12% after 300 s. In the case of the two members of the FGF8 subfamily, HaloFGF17 and HaloFGF18, their fluorescence recovery was more similar (Figure 7.4F and G, and Supplementary figure 7.2). Thus, HaloFGF18 was completely immobile and HaloFGF17 contained only a small mobile fraction (18 ± 11%). HaloFGF20 (FGF9 subfamily) exhibited a gradual recovery of fluorescence and reached 41 ± 9% recovery but not a plateau after 300 s, indicating that the mobile fraction is rather large.

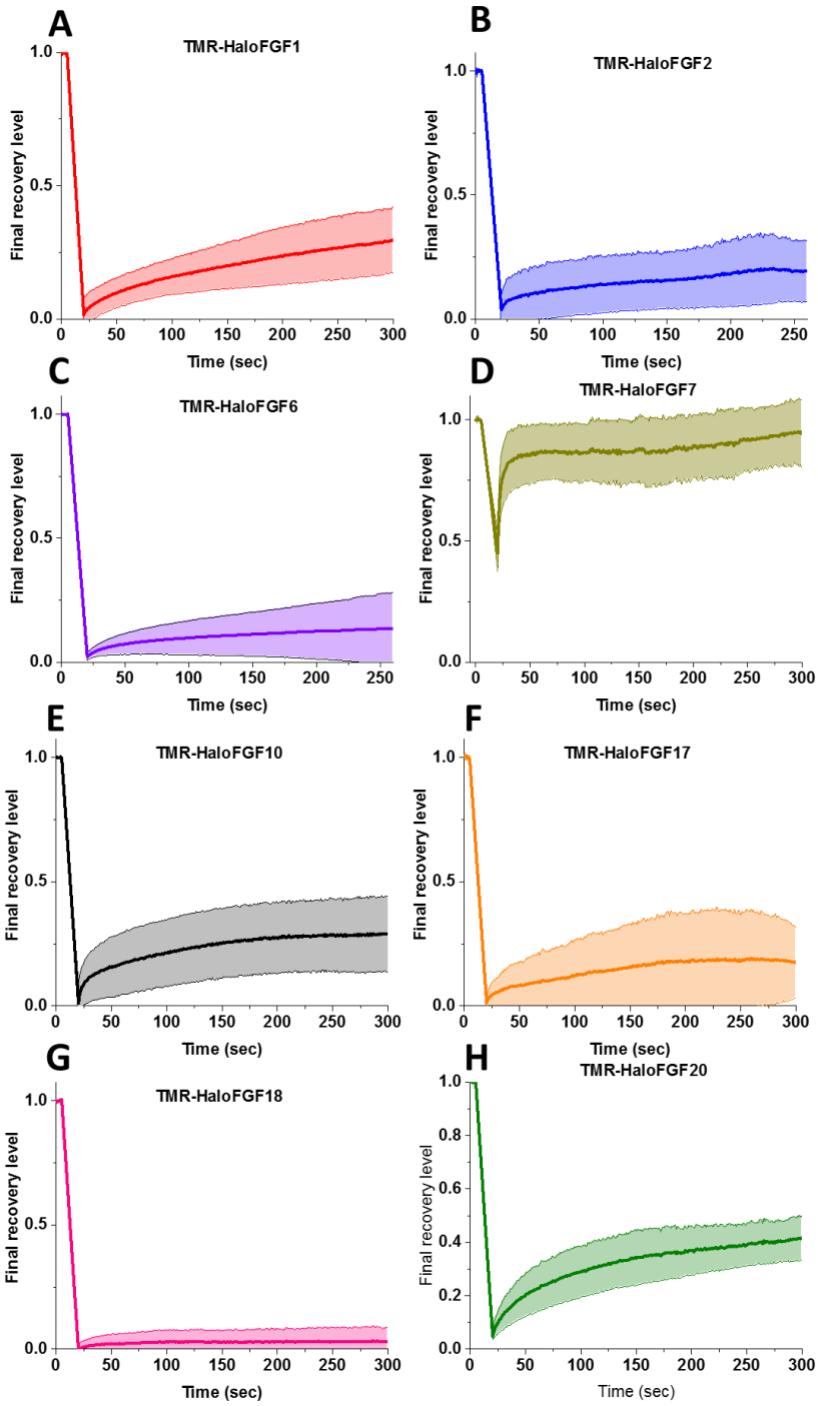


Figure 7.4: Fluorescence recovery of HaloFGFs following photobleaching in the pericellular matrix of HaCaT cells.

TMR565 labelled HaloFGFs were incubated with cells and, following washing with PBS, FRAP measurements were performed. All HaloFGFs were added at 2 nM and the number of measurements is indicated in parenthesis. A: HaloFGF1 (13), B: HaloFGF2 (12), C: HaloFGF6 (12), D: HaloFGF7 (10), E: HaloFGF10 (8), F: HaloFGF17 (10), G: HaloFGF18 (8) and H: HaloFGF20 (3). Recovery levels were extracted from the fluorescence data, as described in section 4.6.3. The thick curves and the light regions around them are the means and standard deviations, respectively, of 3 to 13 measurements.

## 7.3 Comparison of FGF mobility in HS brushes and pericellular matrices

The measurement of the binding and mobility of FGFs in the pericellular matrix of fixed HaCaT cells provides an important complement to the work on GAG brushes. The work in this and the previous chapters can be compared to previously published data on the characterisation of the structural basis of protein-GAG interactions and the mobility of FGFs in pericellular matrix.

In terms of comparing the pericellular matrix of HaCaT keratinocytes and the GAG brushes, it is interesting that despite the latter being a highly simplified model of pericellular matrix, some of the FGFs behave similarly in both. Thus, HaloFGF2 was immobile in HS brushes and has a very limited mobility on HaCaT, illustrated by the superimposition of the recovery curves (Figure 7.5A). HaloFGF1 (Figure 7.5B) and HaloFGF10 (Figure 7.5D) also had very similar motilities in the HS brush and in the pericellular matrix of HaCaT cells. However, in the case of HaloFGF6 and HaloFGF20, these proteins had a substantially reduced mobility in the pericellular matrix of HaCaT cells compared to HS brushes (Figure 7.5C and D). These differences may be due to the FGF6 and FGF20 binding structures in the HS produced by the HaCaT cells, which could specifically reduce the mobility of these FGFs. Such structures might be due to biosynthesis of HS and/or to the effect of the endogenous HaCaT cell HS binding proteins on the structure of HS chains. A role here for core proteins cannot be excluded. Different HSPG core proteins have been shown to carry HS chains with distinct protein binding structures. Thus, HS chains that preferentially engage FGF6 and FGF20 may be on particular core proteins that localise to a subdomain of the pericellular matrix that prevent protein movement. There is limited evidence for this, since the fluorescence of the FGFs is not uniform, and that of HaloFGF20 is particularly punctate in places, though such subdomains could easily be below the limit of diffraction of an optical microscope. In addition, without controls for specificity, such as digestion of HS with heparinases, or CS with chondroitinase ABC, it cannot be excluded that HaloFGF6 and HaloFGF20 also engage protein partners, which may cause their immobility (185).

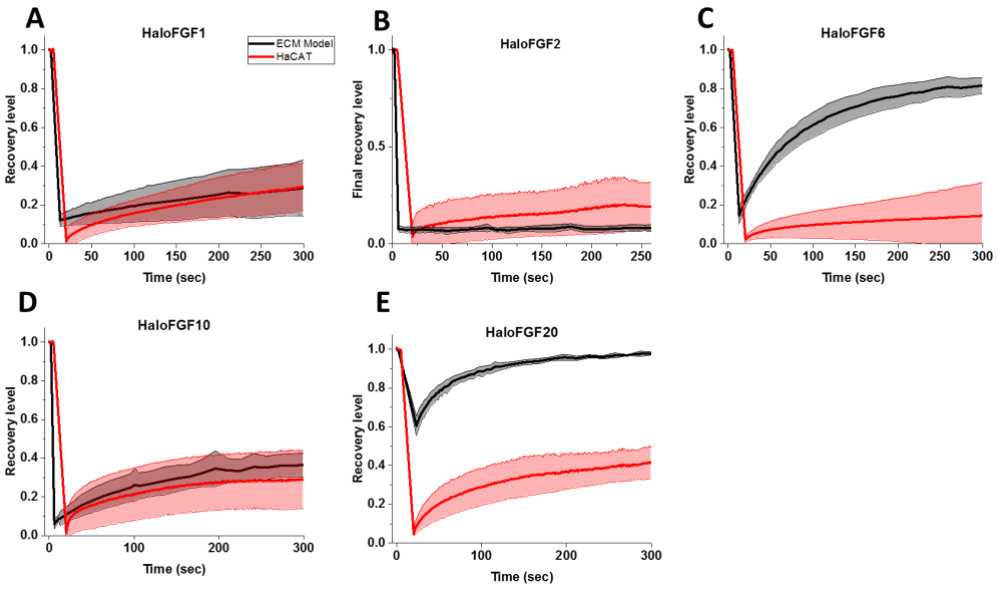


Figure 7.5: Comparison of mobility of HaloFGFs in HS brushes and native pericellular matrices.

FRAP curve of fluorescently labelled HaloFGFs; A: HaloFGF1, HaloFGF2, HaloFGF6, HaloFGF10 and HaloFGF20 in dense HS brushes (as previously reported in section 5.2, black) and pericellular matrix of HaCaT (as previously reported in Figure 7.4, red). Recovery levels were extracted from the fluorescence data as described in section 4. The thick curves and the light regions around them are the means and standard deviations, respectively, of a minimum of 4 independent measurements obtained after rinsing with the working buffer.

## 7.4 Discussion

In this chapter, the halo-tagged FGFs were used as a tool to track FGFs in the pericellular matrix of fixed HaCaT keratinocytes. In work described in chapters 5 and 6, I showed that HaloFGFs possessed sufficiently similar binding properties to a GAG brush that they could be used as proxy to track the mobility of FGFs. This validates previously published work using HaloFGFs and FRAP to measure their mobility in the pericellular matrix of fibroblasts (177, 185). There are interesting differences in both the binding and mobility of the HaloFGFs in keratinocytes and fibroblasts.

One difference is the binding of HaloFGF20 to HaCaT pericellular matrix, as this FGF failed to bind to fibroblast pericellular matrix (185), yet bound to both the GAG brushes and the pericellular matrix of HaCaT cells. FGF20 is a dimer (202) and has been found to require long oligosaccharides for optimal binding (56). This requirement was the explanation for the lack of interaction with fibroblast pericellular matrix. Thus it would seem that in HaCaT pericellular matrix there may be relatively frequent unoccupied long sulfated tracts (contiguous NAS and S domains) that enable FGF20 binding.

In terms of mobility, only FGF6 was similar between fibroblast and keratinocyte pericellular matrix. Thus, FGF1 and FGF2 both had substantial mobile fractions in fibroblast pericellular matrix (185), but not in that of keratinocytes. In contrast, FGF10 was immobile in the pericellular matrix of fibroblasts (185), but at least partially mobile in the one of keratinocytes (Figure 7.4). This presumably relates to the sulfation pattern of the GAGs (FGF10 binds HS and CS/DS) produced by the two cell types. FGF10 has been previously suggested to be immobile in extracellular matrix, since it was found to require the activity of heparanase to exert its growth and morphogenetic activities in salivary gland development (203). This is consistent with the immobility of the HaloFGF10 in fibroblast pericellular matrix. In vivo, FGF10 is the product of mesenchymal fibroblasts, but its target is the neighbouring epithelium, whose cells produce FGFR2b. It would be interesting to test a range of fibroblasts and epithelial cells to see whether FGF10 is immobile on the source cells (the fibroblasts), but mobile in the pericellular matrix of the target epithelial cells. There are no comparator data for FGF17 and FGF18 in the literature.

## Supplementary figures

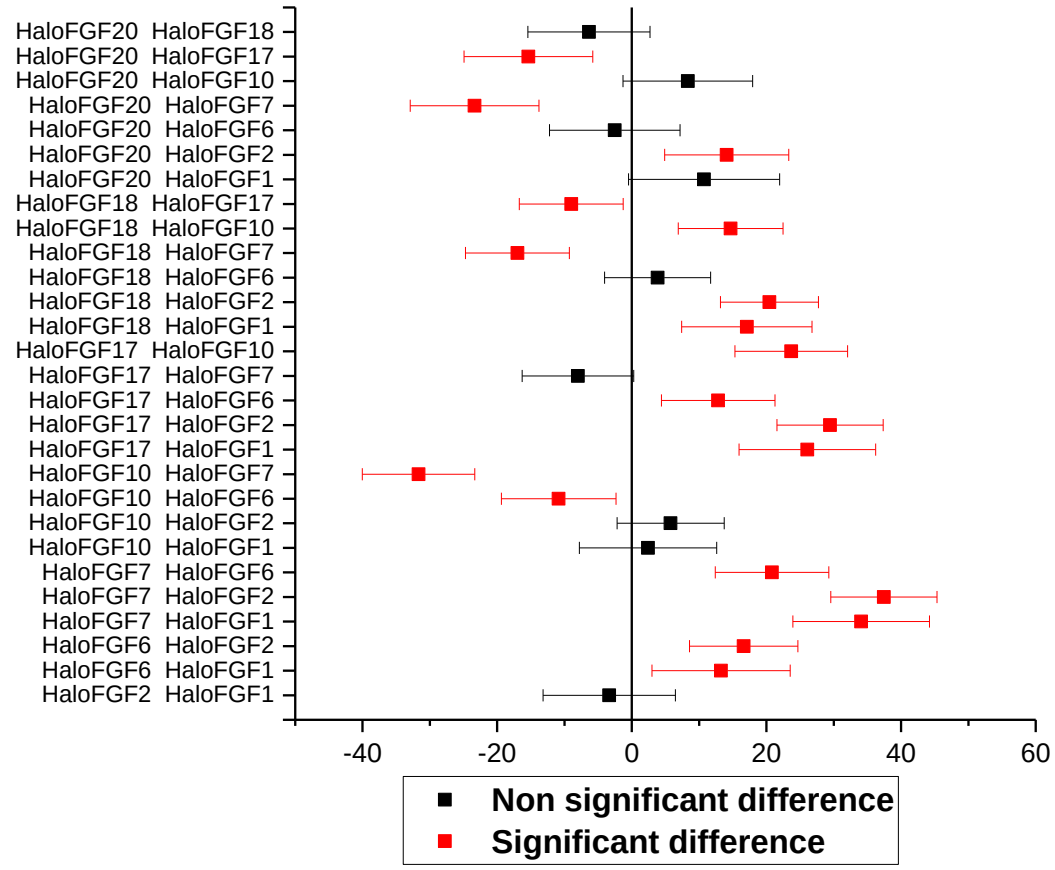


Supplementary figure 7.1: mean comparison of HaloFGF binding intensities.
The fixed cells were incubated with 2 nM TMR-HaloFGFs for 30 minutes at 37°C and rinsed 10 times with PBS. Images of the cells were taken using the LSM 780 microscope and processed with the Fiji® software. The data were reported in Figure 7.3 and a mean comparison Fisher statistical test was carried out at the significance level of 5%.

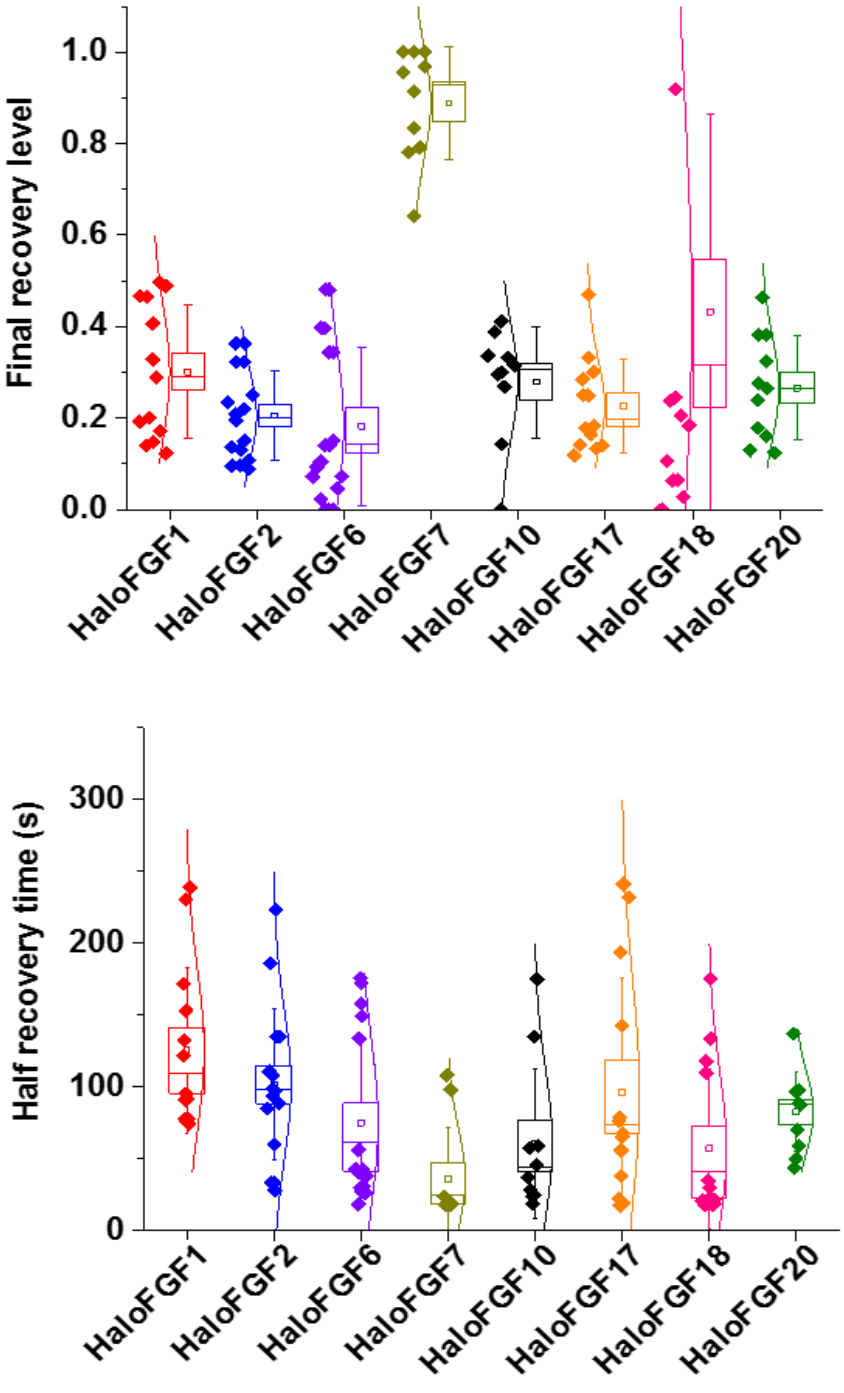


Supplementary figure 7.2: Mobility parameters of HaloFGFs in the pericellular matrix of HaCaT.

Half recovery times and final recovery levels of FRAP on TMR labelled HaloFGFs in the pericellular matrix of HaCaT. The fixed cells were incubated for 30 min at 37°C with 2 nM TMR-HaloFGF and rinsed with the working buffer before the measurements. Final recovery level is the recovered intensity at the end of the experiment (300 s) and calculated as described earlier in section4.6.4. The half-recovery time is the time at which 50% of that level is reached. The data is presented as a box of its standard error with the mean represented as a square. The whiskers represent the standard deviation and the line shows the median of the data.

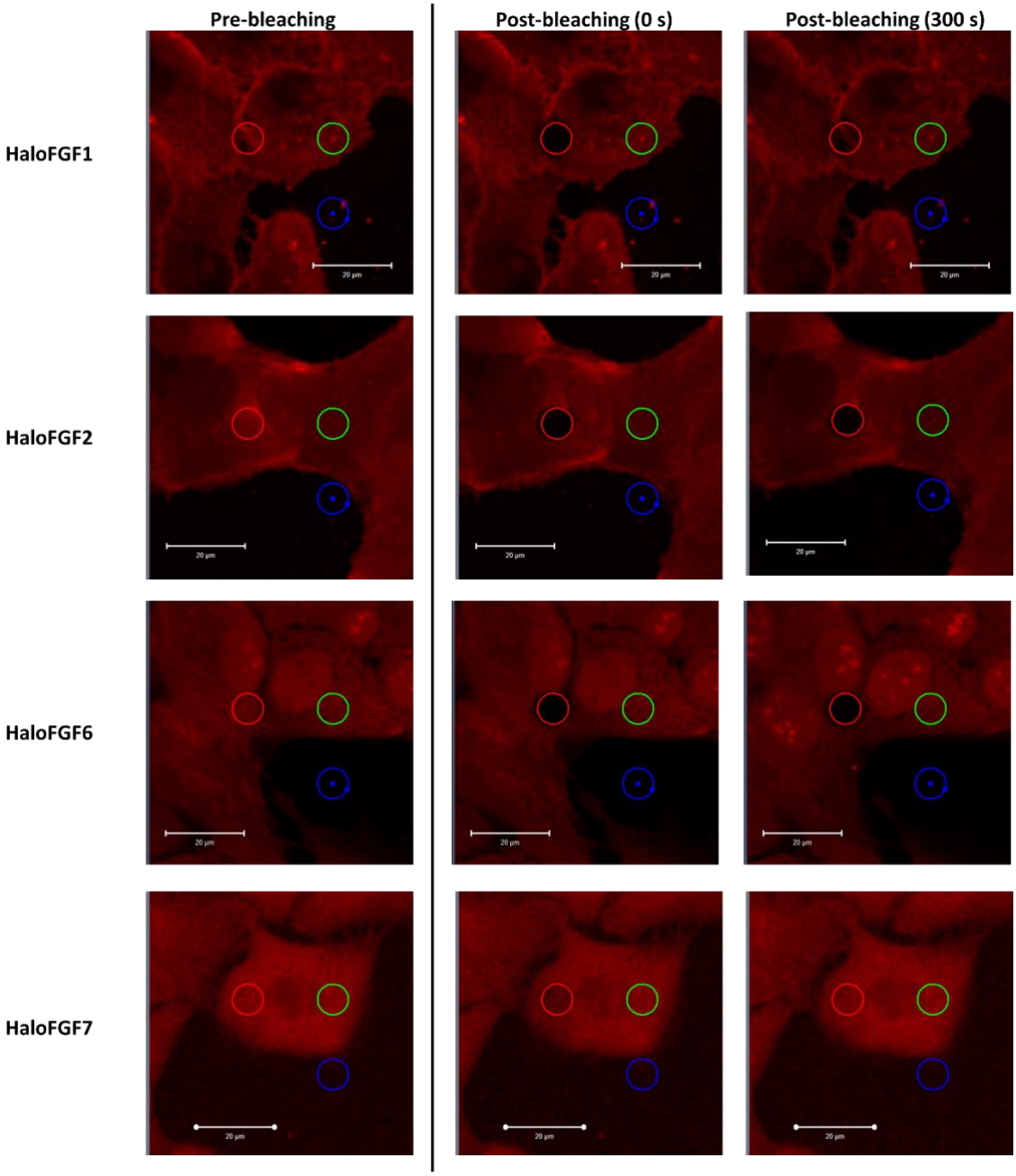


Supplementary figure 7.3: FRAP images of HaloFGFs on HaCaT cells.
The fixed cells were incubated with 2 nM TMR-HaloFGFs for 30 minutes at 37°C and rinsed 10 times with PBS. Images of the cells were taken using the LSM 780 microscope and processed with the Zen software. The fluorescence intensities were recorded in the bleached (red), the background (blue) and the reference (green) as described earlier (section 4.6.3).

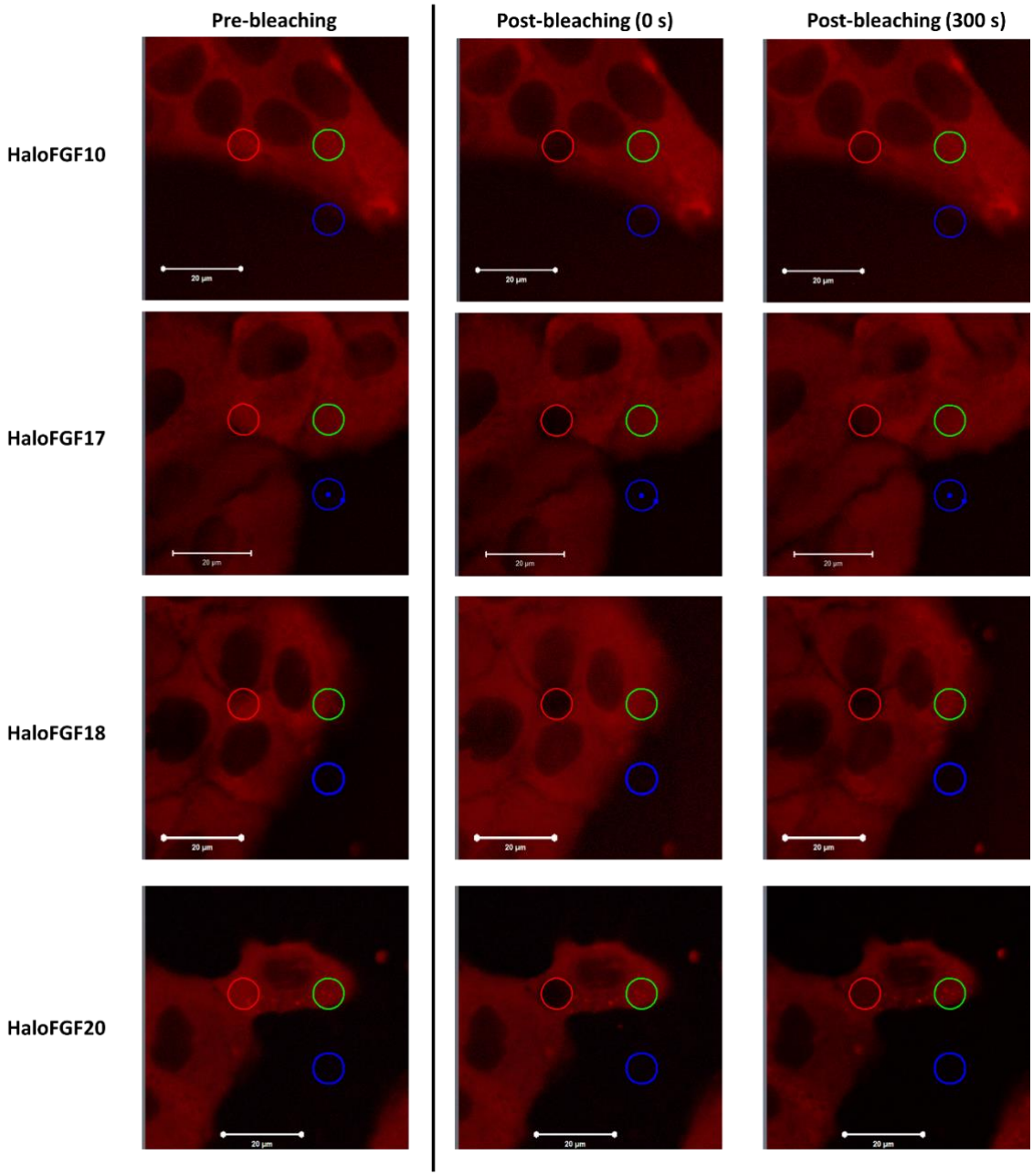


Supplementary figure 7.4: FRAP images of HaloFGFs on HaCaT cells.
The fixed cells were incubated with 2 nM TMR-HaloFGFs for 30 minutes at 37°C and rinsed 10 times with PBS. Images of the cells were taken using the LSM 780 microscope and processed with the Zen® software. The fluorescence intensities were recorded in the bleached (red), the background (blue) and the reference (green) as described earlier. The scale shows a length of 20 µm.

# 8 Discussion and further work

## 8.1 General discussion

Literature and proteomic data have identified more than 435 human hep binding proteins (47, 48). Though their physiological partner is more often than not HS or another sulfated GAG, they have been termed 'heparin-binding' as this is the GAG-binding property that has been established *in vitro*. The paracrine FGFs (section 1.4) represent a group of evolutionarily related heparin-binding proteins, with the two members of the FGF1 subfamily, FGF1 and FGF2 the most studied in this and other respects (Section 1.4.1). For 11 of the paracrine FGFs, the interaction with model GAGs is reasonably well established in terms of the binding sites on the protein recognized by hep and the size and the sulfation pattern in hep necessary for binding (56, 103, 104, 114). It is also now established that some paracrine FGFs can also interact with GAGs other than hep and HS (56, 104). One aspect of FGF function controlled by the interaction with GAGS is their transport in the extracellular matrix and between tissue compartments. This was discovered when FGF2 bound to extracellular matrix, was found to remain trapped there, rather than being released into the bulk cell culture medium. Nevertheless, the matrix bound FGF2 was able to stimulate endothelial cells, leading to a first hypothesis that FGF2 could be stored in extracellular matrix and from there activate its receptors on the cell surface (25). FGF2 was indeed observed in the extracellular matrix of tissues (204) and, at least during the development of the mammary gland, the binding capacity of HS was related to tissue growth. Subsequently the transport of FGF2 in extracellular matrix of different cell types was measured directly (205-207). An intriguing idea to emerge was that the domain structure of HS might allow relatively rapid movement of bound proteins. This was proposed to occur through a sliding mechanism, with the proteins 'hopping' over the NA domains and binding/sliding along NS-NAS units (208). These and other observations led to the idea that binding of growth factors to HS may contribute to the formation of gradients.

More recently direct measurements have been made. Thus, Duchesne *et al* tracked single FGF2 molecules in the pericellular matrix of fibroblasts. They demonstrated

that FGF2 is not transported by free diffusion, but rather has different types of movements involving binding to HS, ranging from confined motion though short displacements to long and directed ones (187). It was suggested that these types of movements are determined by the distribution, availability and selectivity of effector binding sites/patterns on the ECM GAGs. Later work using FRAP of HaloTag FGFs in the pericellular matrix of the same fibroblasts was consistent with the single molecule study.

Our understanding of protein-HS interactions is largely based on *in vitro* structure and biophysical characterization, measurement of cell activity in systems engineered to be deficient in HS and the analysis of the distribution of the proteins in cells and tissues. There is thus a major gap, since the former uses highly defined molecules usually in solution and never organised into a matrix-like structure, while the latter involve the full complexity of the extracellular matrix. Consequently, in this thesis supramolecular assemblies of GAG chains, in the form of a brush, have been used. This has allowed an exploration of new aspects of protein-GAG interactions, namely the ability of a GAG-binding protein to alter the supramolecular structure of the brush. This has been done in the context of paracrine FGFs and HS (chapter 5), and other sulfated GAGs (chapter 6). Finally, the same FGFs were used in experiments on HaCaT pericellular matrix (chapter 7).

In chapter 5, the data acquired did not fit a hypothesis established from a previous analysis of just FGF2 and FGF9. Thus, although the presence of multiple HBSs remains a requirement for an FGF to crosslink HS chains, it was not sufficient. This led to the development of a hypothesis incorporating both multiple HBSs and their isolation from one another by acidic borders as an explanation that was consistent with the data. All hep binding proteins identified to date (47, 48) must contain at least one HBS. In addition to the FGFs, some others are known to possess multiple HBSs, for example, the matrix proteins fibronectin (209) and collagens (210).

The analysis of movement of the FGFs in the GAG brushes provides direct evidence for a sliding/hopping mechanism to contribute to FGF mobility. This interpretation is only possible because of the experiments done by others that labelled the lysine side chains involved in hep binding. This work involves a first protection step, where

side chains of non-binding lysine side chains are blocked with N-hydroxysuccinimide acetate. This reaction is fast and employs a very large molar excess of N-hydroxysuccinimide acetate, to guard against false positives (103). As the time of reaction is similar to that of FRAP, the presence of biotinylated lysines in an HBS, that are not identified as acetylated demonstrates that the lysine's ionic or hydrogen bond with the polysaccharide is not broken and replaced by an interaction with water. At least not for significant lengths of time. In the cases where an FGF moves, because a dense brush is used in these experiments, where the underlying SAv forms 2-D crystalline domains, movement has to be due to the FGF and not the HS chain/SAv unit. Thus, these experiments are consistent with a sliding/hopping mechanism for FGF movement, but not with cycles of substantial dissociation prior to re-association. It is interesting to note observations made on DNA and DNA binding proteins. DNA possesses a largely regular sugar-phosphate backbone ('largely regular' owing to different forms of DNA and kinks). Some of these experiments have demonstrated *in vitro* that DNA binding proteins could slide along a nucleic acid and indeed even move to a neighbouring strand without ever dissociating (188). This is not simply an *in vitro* curiosity, this has been illustrated by single molecular analysis of the *lac* repressor in *E. coli* (211). Key to the mechanism whereby the lac repressor protein 'finds' its binding site on the bacterial chromosome is sliding along DNA, which is balanced by periods of dissociated and re-binding; together these provide for a very efficient 'search' mechanism to enable the small number of *lac* repressors (1-2/cell) to perform their function of inhibiting transcription from the *lac* operon. The underlying chemistry of the DNA-binding protein binding to the DNA backbone is the same as FGFs binding to GAGs, although the DNA strands are longer and have a homogenous ion charge repartition, whereas GAG chains do not. It was reasonable to propose sliding/hopping as a mechanism for the movement of hep binding proteins (208). The data in this thesis, coupled to that on the labelling of lysine side chains in HBSs strongly suggest that such a mechanism occurs at least in the context of a GAG brush.

The present data suggest that FGS that are monovalent or multivalent but without an acidic border behave similarly: they do not cross-link HS chains and are mobile in

an HS brush. Bivalent FGFs without acidic borders isolating the HBSs from one another as is the case for FGF4 and FGF6 (used as HaloFGF6), would slide/hop in a similar way to monovalent FGFs. FGFs with two or more HBSs separated with acidic borders, cross-linked HS brushes and were either immobile or exhibited a mix of a mobile fraction and an immobile one. Thus there appears to also be a relationship between the ability of an FGF to cross-link HS chains and its mobility in an HS brush.

In chapter 6, I have probed the various GAG (HS, Hep, CS and DS) chains with the FGFs (FGF1, FGF2, FGF2 HBS3-, FGF4, FGF9, FGF10, FGF17 and FGF18) and evaluated the viscoelastic properties and in some instances the mobility of theses FGF-GAG films. I here highlighted interesting observations in viscoelastic and dynamic properties of FGF-GAG films based on their submolecular features. The sugar backbone of HS/Hep offer more versatility in sulfate disposition along the chains than CS/DS. This led to a clear preference for FGF to bind HS/Hep (all tested FGFs did) when only a few bind to CS/DS. The binding propensity and stoichiometry were higher for HS and Hep than for other GAGs and many failed to bind (FGF1, FGF2 HBS3-, FGF9) or bound very little (FGF4, FGF17) to CS/DS. Furthermore, the cross-linking of HS (1.4 sulfates per disaccharide) and Hep (2.7 sulfates per disaccharide), but not CS-E (2 sulfate per disaccharide) by FGF2 showed that this is, not a consequence of "low" sulfate groups in CS/DS, but rather a matter of pattern and disposition. It also leads to to cross-linking of HS/Hep but not of CS/DS as depicted by FGF2 and FGF1.

The measurement of the mobility of FGFs in keratinocyte pericellular matrix is described in chapter 7. This provides an insight into the extent to which hypotheses generated from the work on brushes may apply *in vivo*. As the cells were fixed, it is expected that the pericellular matrix components are also fixed – there is an extensive discussion of this point in Duchesne et al., 2012. The fixative does not affect FGF binding, since it is a primary amine reactive reagent, and so will not modify N-acetyl or N-sulfate groups. It is well established that matrices from different cell types and tissues have distinct binding capacities for different heparin-binding proteins. This is central to the idea that the regulation of HS biosynthesis is central to the regulation of a cell's and a tissue's response to heparin-binding effectors. The present data demonstrate that the mobility and the transport of FGFs, and so presumably

hep binding proteins in general, can be differentially regulated by cells varying the menu of sulfated GAG structures they incorporate into their extracellular matrix. The data also demonstrate that movement of FGFs differs in the pericellular matrix of different cell types: fibroblast (Sun et al) and keratinocyte. Though there is no information on this, since cells are known to produce HS with different structures during development (159), as well as in ageing (212). Thus, an important conclusion is that the diffusion and gradients of FGFs, and in all likelihood other hep binding proteins are determined by the structure of HS (and to a lesser extent CS/DS species) produced by cells. A corollary is that because cells and tissues regulate the biosynthesis of their HS dynamically in response to environmental cues, this may concomitantly regulate diffusion of heparin-binding proteins. Another likely means to regulate binding and diffusion of proteins in matrix is the profile of endogenous hep binding proteins. These, at the very least will occupy a good many binding sites on HS chains. Binding may also alter the 3-dimensional structure of the chain. Both should impact on binding and diffusion of an exogenous hep binding protein.

## 8.2 Further work

Two FGFs from each subfamily and a panel of 6 different GAGs were investigated. However, there are a number of combinations of FGF-GAG for which some data are missing, more repeats and further enzyme digestion controls for specificity are required. Finally, one mutant, FGF2 HBS3- was tested in this thesis. The generation of further mutants, which would involve not just HBSs, but also acidic borders would provide direct evidence for the architecture(s) required for crosslinking HS chains. An understanding of the reason underlying the observation of an interaction of FGF2 with CS-A and CS-C here, but not by others is also important, as this establishes the limits of particular measurement systems, e.g., solution vs brush. As discussed in Chapter 6, should the interaction observed here be due to the presentation of the CS-A and CS-C in a brush, this may have implications for scarring and attempts to wounded tissues, particularly in the context of spinal cord injuries, where dense networks of CS chains may act rather like the brush. In addition, it would be particularly interesting to test the hypothesis regarding the structural features

required for HS chain crosslinking with proteins fibronectin, laminin and selected collagens, e.g., collagen I and collagen IV.

The analysis of the interaction of matrix proteins would then lead to the assembly of a more complex brush. This would have the HS chain as now, but then incorporate matrix proteins. The ability to control precisely assembly would enable testing of the ideas above on the effects of endogenous hep binding proteins on the binding and diffusion of exogenously added FGFs.

The work in this thesis provides the impetus to test rigorously a hopping/sliding mechanism for FGF movement. The parallel development in the research Group of chemistry to label arginine residues in hep binding sites will provide a complete picture of the side chains that are involved in binding to hep and that are not exposed to solvent. However, a weakness of the selective labelling of lysines and now arginines is that hitherto it has only been achieved using hep affinity chromatography supports. This means that the applicability of the results to HS or another GAG is uncertain. However, very recently, a member of the research group has successfully extended the methodology to soluble GAGs and applied it, in solution, to not just to FGF-hep interactions, but also to those with CS and DS. A more direct test of sliding would be to conduct force spectroscopy using AFM. A recent paper demonstrates that this is feasible (213). However, the method of immobilising the FGF (adsorption) and in particular the HS chain (conjugated via internal free carboxylic acids) precluded the possibility of detecting sliding. In contrast, using HaloFGFs and oxime ligation at the reducing end of the polysaccharide would enable such measurements. While these would not provide insight directly to what occurs in an actual extracellular matrix, the quantification of sliding *in* vitro would strengthen this as a candidate mechanism for FGF diffusion *in vivo*. Moreover, *in situ* selective labelling of FGFs in an extracellular matrix (rather than on a hep affinity column) would determine whether lysines and arginine residues involved in GAG binding are protected from solvent, as is the case on a hep affinity column. Measurement of the movement of such an FGF then closes the case for the sliding/hopping mechanism.

# 9 References


1. Kumar NM, Gilula NB. The Gap Junction Communication Channel. Cell. 1996;84(3):381-8.
2. Macri L, Silverstein D, Clark RAF. Growth factor binding to the pericellular matrix and its importance in tissue engineering. Advanced Drug Delivery Reviews. 2007;59(13):1366-81.
3. Fantl WJ, Johnson DE, Williams LT. Signalling by receptor tyrosine kinases. Annual review of biochemistry. 1993;62:453-81.
4. Bandyopadhyay A, Tsuji K, Cox K, Harfe BD, Rosen V, Tabin CJ. Genetic analysis of the roles of BMP2, BMP4, and BMP7 in limb patterning and skeletogenesis. PLoS genetics. 2006;2(12):e216.
5. Armelin HA. Pituitary extracts and steroid hormones in the control of 3T3 cell growth. Proc Natl Acad Sci U S A. 1973;70(9):2702-6.
6. Gospodarowicz D. Localisation of a fgf and its effect alone and with hydrocortisone on 3t3 cells growth. Nature. 1974;249:123-7.
7. Leddy HA, Christensen SE, Guilak F. Microscale Diffusion Properties of the Cartilage Pericellular Matrix Measured Using 3D Scanning Microphotolysis. Journal of Biomechanical Engineering. 2008;130(6):061002--8.
8. Bosman FT, Stamenkovic I. Functional structure and composition of the extracellular matrix. J Pathol. 2003;200(4):423-8.
9. Gelse K, Poschl E, Aigner T. Collagens--structure, function, and biosynthesis. Adv Drug Deliv Rev. 2003;55(12):1531-46.
10. Epstein EH, Jr., Munderloh NH. Human skin collagen. Presence of type I and type III at all levels of the dermis. J Biol Chem. 1978;253(5):1336-7.
11. Kern B, Shen J, Starbuck M, Karsenty G. Cbfa1 contributes to the osteoblast-specific expression of type I collagen genes. J Biol Chem. 2001;276(10):7101-7.
12. Kuo HJ, Maslen CL, Keene DR, Glanville RW. Type VI collagen anchors endothelial basement membranes by interacting with type IV collagen. J Biol Chem. 1997;272(42):26522-9.
13. Lössl P, Kölbel K, Tänzler D, Nannemann D, Ihling CH, Keller MV, et al. Analysis of Nidogen-1/Laminin γ1 Interaction by Cross-Linking, Mass Spectrometry, and Computational Modeling Reveals Multiple Binding Modes. PLoS ONE. 2014;9(11):e112886.
14. Manhardt CT, Punch PR, Dougher CWL, Lau JTY. Extrinsic sialylation is dynamically regulated by systemic triggers in vivo. J Biol Chem. 2017;292(33):13514-20.
15. Gross J, Lapiere CM. Collagenolytic activity in amphibian tissues: a tissue culture assay. Proc Natl Acad Sci U S A. 1962;48:1014-22.
16. Eisen AZ, Jeffrey JJ, Gross J. Human skin collagenase, isolation and mechanism of attack on the collagen molecule. Biochimica et Biophysica Acta (BBA) - Enzymology. 1968;151(3):637-45.
17. Wang Q, Uhlirova M, Bohmann D. Spatial Restriction of FGF Signaling by a Matrix Metalloprotease Controls Branching Morphogenesis. Developmental Cell. 2010;18(1):157-64.
18. Wiseman BS, Sternlicht MD, Lund LR, Alexander CM, Mott J, Bissell MJ, et al. Site-specific inductive and inhibitory activities of MMP-2 and MMP-3 orchestrate mammary gland branching morphogenesis. The Journal of Cell Biology. 2003;162(6):1123.
19. Pilcher BK, Dumin JA, Sudbeck BD, Krane SM, Welgus HG, Parks WC. The activity of collagenase-1 is required for keratinocyte migration on a type I collagen matrix. J Cell Biol. 1997;137(6):1445-57.
20. Gaffney J, Solomonov I, Zehorai E, Sagi I. Multilevel regulation of matrix metalloproteinases in tissue homeostasis indicates their molecular specificity in vivo. Matrix Biology. 2015;44–46:191-9.

21. McGuire JK, Li Q, Parks WC. Matrilysin (Matrix Metalloproteinase-7) Mediates E-Cadherin Ectodomain Shedding in Injured Lung Epithelium. The American Journal of Pathology. 2003;162(6):1831-43.
22. Caley MP, Martins VLC, O'Toole EA. Metalloproteinases and Wound Healing. Advances in Wound Care. 2015;4(4):225-34.
23. Baird A, Ling N. Fibroblast growth factors are present in the extracellular matrix produced by endothelial cells in vitro: implications for a role of heparinase-like enzymes in the neovascular response. Biochem Biophys Res Commun. 1987;142(2):428-35.
24. Whitelock JM, Murdoch AD, Iozzo RV, Underwood PA. The degradation of human endothelial cell-derived perlecan and release of bound basic fibroblast growth factor by stromelysin, collagenase, plasmin, and heparanases. J Biol Chem. 1996;271(17):10079-86.
25. Bashkin P, Doctrow S, Klagsbrun M, Svahn CM, Folkman J, Vlodavsky I. Basic fibroblast growth factor binds to subendothelial extracellular matrix and is released by heparitinase and heparin-like molecules. Biochemistry. 1989;28(4):1737-43.
26. Li Q, Park PW, Wilson CL, Parks WC. Matrilysin shedding of syndecan-1 regulates chemokine mobilization and transepithelial efflux of neutrophils in acute lung injury. Cell. 2002;111(5):635-46.
27. Ruhrberg C, Gerhardt H, Golding M, Watson R, Ioannidou S, Fujisawa H, et al. Spatially restricted patterning cues provided by heparin-binding VEGF-A control blood vessel branching morphogenesis. Genes Dev. 2002;16(20):2684-98.
28. Schulz T, Schumacher U, Prehm P. Hyaluronan export by the ABC transporter MRP5 and its modulation by intracellular cGMP. J Biol Chem. 2007;282(29):20999-1004.
29. Zhang L, David G, Esko JD. Repetitive Ser-Gly sequences enhance heparan sulfate assembly in proteoglycans. J Biol Chem. 1995;270(45):27127-35.
30. Kreuger J, Kjellen L. Heparan sulfate biosynthesis: regulation and variability. The journal of histochemistry and cytochemistry : official journal of the Histochemistry Society. 2012;60(12):898-907.
31. Kitagawa H, Shimakawa H, Sugahara K. The tumor suppressor EXT-like gene EXTL2 encodes an alpha1, 4-N-acetylhexosaminyltransferase that transfers N-acetylgalactosamine and N-acetylglucosamine to the common glycosaminoglycan-protein linkage region. The key enzyme for the chain initiation of heparan sulfate. J Biol Chem. 1999;274(20):13933-7.
32. Sugahara K, Kitagawa H. Recent advances in the study of the biosynthesis and functions of sulfated glycosaminoglycans. Current opinion in structural biology. 2000;10(5):518-27.
33. Sugahara K, Kitagawa H. Heparin and heparan sulfate biosynthesis. IUBMB life. 2002;54(4):163-75.
34. McCormick C, Duncan G, Goutsos KT, Tufaro F. The putative tumor suppressors EXT1 and EXT2 form a stable complex that accumulates in the Golgi apparatus and catalyzes the synthesis of heparan sulfate. Proc Natl Acad Sci U S A. 2000;97(2):668-73.
35. Dou W, Xu Y, Pagadala V, Pedersen LC, Liu J. Role of Deacetylase Activity of N-Deacetylase/N-Sulfotransferase 1 in Forming N-Sulfated Domain in Heparan Sulfate. J Biol Chem. 2015;290(33):20427-37.
36. Aikawa J, Grobe K, Tsujimoto M, Esko JD. Multiple isozymes of heparan sulfate/heparin GlcNAc N-deacetylase/GlcN N-sulfotransferase. Structure and activity of the fourth member, NDST4. J Biol Chem. 2001;276(8):5876-82.
37. van den Born J, Pikas DS, Pisa BJ, Eriksson I, Kjellen L, Berden JH. Antibody-based assay for N-deacetylase activity of heparan sulfate/heparin N-deacetylase/N-sulfotransferase (NDST): novel characteristics of NDST-1 and -2. Glycobiology. 2003;13(1):1-10.

38. Campbell P, Hannesson HH, Sandback D, Roden L, Lindahl U, Li JP. Biosynthesis of heparin/heparan sulfate. Purification of the D-glucuronyl C-5 epimerase from bovine liver. J Biol Chem. 1994;269(43):26953-8.
39. Yates EA, Santini F, Guerrini M, Naggi A, Torri G, Casu B. 1H and 13C NMR spectral assignments of the major sequences of twelve systematically modified heparin derivatives. Carbohydrate Research. 1996;294(Supplement C):15-27.
40. Rudd TR, Yates EA. A highly efficient tree structure for the biosynthesis of heparan sulfate accounts for the commonly observed disaccharides and suggests a mechanism for domain synthesis. Mol Biosyst. 2012;8(5):1499-506.
41. Murphy KJ, Merry CL, Lyon M, Thompson JE, Roberts IS, Gallagher JT. A new model for the domain structure of heparan sulfate based on the novel specificity of K5 lyase. J Biol Chem. 2004;279(26):27239-45.
42. Lindahl U, Kusche-Gullberg M, Kjellen L. Regulated diversity of heparan sulfate. J Biol Chem. 1998;273(39):24979-82.
43. Toida T, Yoshida H, Toyoda H, Koshiishi I, Imanari T, Hileman RE, et al. Structural differences and the presence of unsubstituted amino groups in heparan sulphates from different tissues and species. The Biochemical journal. 1997;322 ( Pt 2):499-506.
44. Gallagher JT, Walker A. Molecular distinctions between heparan sulphate and heparin. Analysis of sulphation patterns indicates that heparan sulphate and heparin are separate families of N-sulphated polysaccharides. The Biochemical journal. 1985;230(3):665-74.
45. Dickson CD, R.; Dixon, M.; Peters, G. Structure and fonction of the int2 oncogene. Progress in Growth Factor Research. 1989;1:123-32.
46. Pacheco B, Malmstrom A, Maccarana M. Two dermatan sulfate epimerases form iduronic acid domains in dermatan sulfate. J Biol Chem. 2009;284(15):9788-95.
47. Ori A, Wilkinson MC, Fernig DG. A systems biology approach for the investigation of the heparin/heparan sulfate interactome. J Biol Chem. 2011;286(22):19892-904.
48. Ori A, Wilkinson MC, Fernig DG. The heparanome and regulation of cell function: structures, functions and challenges. Front Biosci. 2008;13:4309-38.
49. Mulloy B, Forster MJ. Conformation and dynamics of heparin and heparan sulfate. Glycobiology. 2000;10(11):1147-56.
50. Sanderson PN, Huckerby TN, Nieduszynski IA. Conformational equilibria of alpha-L-iduronate residues in disaccharides derived from heparin. The Biochemical journal. 1987;243(1):175-81.
51. Hricovini M. Solution Structure of Heparin Pentasaccharide: NMR and DFT Analysis. J Phys Chem B. 2015;119(38):12397-409.
52. Rudd TR, Yates EA, Hricovini M. Spectroscopic and theoretical approaches for the determination of heparin saccharide structure and the study of protein-glycosaminoglycan complexes in solution. Curr Med Chem. 2009;16(35):4750-66.
53. Rudd TR, Guimond SE, Skidmore MA, Duchesne L, Guerrini M, Torri G, et al. Influence of substitution pattern and cation binding on conformation and activity in heparin derivatives. Glycobiology. 2007;17(9):983-93.
54. Casu B, Petitou M, Provasoli M, Sinaÿ P. Conformational flexibility: a new concept for explaining binding and biological properties of iduronic acid-containing glycosaminoglycans. Trends in Biochemical Sciences.13(6):221-5.
55. Faham S, Hileman RE, Fromm JR, Linhardt RJ, Rees DC. Heparin structure and interactions with basic fibroblast growth factor. Science. 1996;271(5252):1116-20.
56. Li Y, Sun C, Yates EA, Jiang C, Wilkinson MC, Fernig DG. Heparin binding preference and structures in the fibroblast growth factor family parallel their evolutionary diversification. Open Biol. 2016;6(3).

57. Li Y. Specificities of the interaction of fibroblast growth factor and heparan sulfate. [Doctor of Philosophy thesis]: University of Liverpool; 2015.
58. Rudd TR, Uniewicz KA, Ori A, Guimond SE, Skidmore MA, Gaudesi D, et al. Comparable stabilisation, structural changes and activities can be induced in FGF by a variety of HS and non-GAG analogues: implications for sequence-activity relationships. Org Biomol Chem. 2010;8(23):5390-7.
59. Guimond S, Maccarana M, Olwin BB, Lindahl U, Rapraeger AC. Activating and inhibitory heparin sequences for FGF-2 (basic FGF). Distinct requirements for FGF-1, FGF-2, and FGF-4. J Biol Chem. 1993;268(32):23906-14.
60. Casu B, Naggi A, Torri G. Heparin-derived heparan sulfate mimics that modulate inflammation and cancer. Matrix biology : journal of the International Society for Matrix Biology. 2010;29(6):442-52.
61. Lin X, Perrimon N. Dally cooperates with Drosophila Frizzled 2 to transduce Wingless signalling. Nature. 1999;400(6741):281-4.
62. Garcia-Garcia MJ, Anderson KV. Essential role of glycosaminoglycans in Fgf signaling during mouse gastrulation. Cell. 2003;114(6):727-37.
63. Yan D, Lin X. Shaping morphogen gradients by proteoglycans. Cold Spring Harb Perspect Biol. 2009;1(3):a002493.
64. Cadigan KM, Fish MP, Rulifson EJ, Nusse R. Wingless repression of Drosophila frizzled 2 expression shapes the Wingless morphogen gradient in the wing. Cell. 1998;93(5):767-77.
65. Torroja C, Gorfinkiel N, Guerrero I. Patched controls the Hedgehog gradient by endocytosis in a dynamin-dependent manner, but this internalization does not play a major role in signal transduction. Development. 2004;131(10):2395-408.
66. Belenkaya TY, Han C, Yan D, Opoka RJ, Khodoun M, Liu H, et al. Drosophila Dpp morphogen movement is independent of dynamin-mediated endocytosis but regulated by the glypican members of heparan sulfate proteoglycans. Cell. 2004;119(2):231-44.
67. Marjoram L, Wright C. Rapid differential transport of Nodal and Lefty on sulfated proteoglycan-rich extracellular matrix regulates left-right asymmetry in Xenopus. Development. 2011;138(3):475-85.
68. Duchesne A, Tessera E, Dedovic K, Engert V, Pruessner JC. Effects of panel sex composition on the physiological stress responses to psychosocial stress in healthy young men and women. Biol Psychol. 2012;89(1):99-106.
69. Marics I, Adelaide J, Raybaud F, Mattei MG, Coulier F, Planche J, et al. Characterization of the HST-related FGF.6 gene, a new member of the fibroblast growth factor gene family. Oncogene. 1989;4(3):335-40.
70. Fernig DG, Gallagher JT. Fibroblast growth factors and their receptors: An information network controlling tissue growth, morphogenesis and repair. Progress in Growth Factor Research. 1994;5(4):353-77.
71. Gospodorawicz DaM, J. Effect of a Fibroblast Growth Factor, Insulin, Dexamethasone, and Serumon the Morphology of BALB/c 3T3 Cells. Proc Natl Acad Sci U S A. 1974;71(12):4648-52.
72. Gospodarowicz DW, J.; Moran, J. Presence in brain of a mitogenic agent promoting proliferation of myoblasts in low density culture. . Nature. 1975;256:216-9.
73. Oulion S, Bertrand S, Belgacem MR, Le Petillon Y, Escriva H. Sequencing and analysis of the Mediterranean amphioxus (Branchiostoma lanceolatum) transcriptome. PLoS One. 2012;7(5):e36554.
74. Oulion S, Bertrand S, Escriva H. Evolution of the FGF Gene Family. Int J Evol Biol. 2012;2012:298147.
75. Dickson CP, G. Potential oncongene product related to growth factors. Nature. 1987;326:833.

76. Yoshida TS, H.; Miyagawa, K.; Sugimura, T.; Terada, M. Characterisation of HST1 gene and its product. ANNALS NEW YORK ACADEMY OF SCIENCES. 1989:27-37.
77. Goldfarb M, Bates B, Drucker B, Hardin J, Haub O. Expression and possible functions of the FGF-5 gene. Annals of the New York Academy of Sciences. 1991;638:38-52.
78. Zhan X, Bates B, Hu XG, Goldfarb M. The human FGF-5 oncogene encodes a novel protein related to fibroblast growth factors. Molecular and cellular biology. 1988;8(8):3487-95.
79. Coulier F, Ollendorff V, Marics I, Rosnet O, Batoz M, Planche J, et al. The FGF6 gene within the FGF multigene family. Annals of the New York Academy of Sciences. 1991;638:53-61.
80. Aaronson SA, Bottaro DP, Miki T, Ron D, Finch PW, Fleming TP, et al. Keratinocyte growth factor. A fibroblast growth factor family member with unusual target cell specificity. Annals of the New York Academy of Sciences. 1991;638:62-77.
81. Finch PW, Rubin JS, Miki T, Ron D, Aaronson SA. Human KGF is FGF-related with properties of a paracrine effector of epithelial cell growth. Science. 1989;245(4919):752-5.
82. Tanaka A, Miyamoto K, Minamino N, Takeda M, Sato B, Matsuo H, et al. Cloning and characterization of an androgen-induced growth factor essential for the androgen-dependent growth of mouse mammary carcinoma cells. Proc Natl Acad Sci U S A. 1992;89(19):8928-32.
83. Miyamoto M, Naruo K, Seko C, Matsumoto S, Kondo T, Kurokawa T. Molecular cloning of a novel cytokine cDNA encoding the ninth member of the fibroblast growth factor family, which has a unique secretion property. Molecular and cellular biology. 1993;13(7):4251-9.
84. Yamasaki M, Miyake A, Tagashira S, Itoh N. Structure and expression of the rat mRNA encoding a novel member of the fibroblast growth factor family. J Biol Chem. 1996;271(27):15918-21.
85. Smallwood PM, Munoz-Sanjuan I, Tong P, Macke JP, Hendry SH, Gilbert DJ, et al. Fibroblast growth factor (FGF) homologous factors: new members of the FGF family implicated in nervous system development. Proc Natl Acad Sci U S A. 1996;93(18):9850-7.
86. Hoshikawa M, Ohbayashi N, Yonamine A, Konishi M, Ozaki K, Fukui S, et al. Structure and expression of a novel fibroblast growth factor, FGF-17, preferentially expressed in the embryonic brain. Biochem Biophys Res Commun. 1998;244(1):187-91.
87. Miyake A, Konishi M, Martin FH, Hernday NA, Ozaki K, Yamamoto S, et al. Structure and expression of a novel member, FGF-16, on the fibroblast growth factor family. Biochem Biophys Res Commun. 1998;243(1):148-52.
88. Nishimura T, Nakatake Y, Konishi M, Itoh N. Identification of a novel FGF, FGF-21, preferentially expressed in the liver. Biochimica et biophysica acta. 2000;1492(1):203-6.
89. Ohbayashi N, Hoshikawa M, Kimura S, Yamasaki M, Fukui S, Itoh N. Structure and expression of the mRNA encoding a novel fibroblast growth factor, FGF-18. J Biol Chem. 1998;273(29):18161-4.
90. Ohmachi S, Watanabe Y, Mikami T, Kusu N, Ibi T, Akaike A, et al. FGF-20, a novel neurotrophic factor, preferentially expressed in the substantia nigra pars compacta of rat brain. Biochem Biophys Res Commun. 2000;277(2):355-60.
91. Nishimura T, Utsunomiya Y, Hoshikawa M, Ohuchi H, Itoh N. Structure and expression of a novel human FGF, FGF-19, expressed in the fetal brain. Biochimica et biophysica acta. 1999;1444(1):148-51.
92. Nakatake Y, Hoshikawa M, Asaki T, Kassai Y, Itoh N. Identification of a novel fibroblast growth factor, FGF-22, preferentially expressed in the inner root sheath of the hair follicle. Biochimica et biophysica acta. 2001;1517(3):460-3.

93. Yamashita T, Yoshioka M, Itoh N. Identification of a novel fibroblast growth factor, FGF-23, preferentially expressed in the ventrolateral thalamic nucleus of the brain. Biochem Biophys Res Commun. 2000;277(2):494-8.
94. Perwad F, Zhang MY, Tenenhouse HS, Portale AA. Fibroblast growth factor 23 impairs phosphorus and vitamin D metabolism in vivo and suppresses 25-hydroxyvitamin D-1alpha-hydroxylase expression in vitro. Am J Physiol Renal Physiol. 2007;293(5):F1577-83.
95. Laestander C, Engstrom W. Role of fibroblast growth factors in elicitation of cell responses. Cell Prolif. 2014;47(1):3-11.
96. Olsen SK, Garbi M, Zampieri N, Eliseenkova AV, Ornitz DM, Goldfarb M, et al. Fibroblast growth factor (FGF) homologous factors share structural but not functional homology with FGFs. J Biol Chem. 2003;278(36):34226-36.
97. Murzin AG, Lesk AM, Chothia C. β-Trefoil fold. Journal of Molecular Biology. 1992;223(2):531-43.
98. Schlessinger J, Plotnikov AN, Ibrahimi OA, Eliseenkova AV, Yeh BK, Yayon A, et al. Crystal structure of a ternary FGF-FGFR-heparin complex reveals a dual role for heparin in FGFR binding and dimerization. Mol Cell. 2000;6(3):743-50.
99. Bellosta P, Iwahori A, Plotnikov AN, Eliseenkova AV, Basilico C, Mohammadi M. Identification of receptor and heparin binding sites in fibroblast growth factor 4 by structure-based mutagenesis. Molecular and cellular biology. 2001;21(17):5946-57.
100. Pellegrini L, Burke DF, von Delft F, Mulloy B, Blundell TL. Crystal structure of fibroblast growth factor receptor ectodomain bound to ligand and heparin. Nature. 2000;407(6807):1029-34.
101. Baird A, Schubert D, Ling N, Guillemin R. Receptor- and heparin-binding domains of basic fibroblast growth factor. Proc Natl Acad Sci U S A. 1988;85(7):2324-8.
102. Kinsella L, Chen HL, Smith JA, Rudland PS, Fernig DG. Interactions of putative heparin-binding domains of basic fibroblast growth factor and its receptor, FGFR-1, with heparin using synthetic peptides. Glycoconj J. 1998;15(4):419-22.
103. Ori A, Free P, Courty J, Wilkinson MC, Fernig DG. Identification of heparin-binding sites in proteins by selective labeling. Mol Cell Proteomics. 2009;8(10):2256-65.
104. Xu R, Ori A, Rudd TR, Uniewicz KA, Ahmed YA, Guimond SE, et al. Diversification of the structural determinants of fibroblast growth factor-heparin interactions: implications for binding specificity. J Biol Chem. 2012;287(47):40061-73.
105. Nguyen TKN, Raman K, Trana VM, Kuberan B. Investigating the mechanism of the assembly of FGF1-binding heparan sulfate motifs. FEBS letters. 2011;585(17):2698-702.
106. Safaiyan F, Lindahl U, Salmivirta M. Structural Diversity of N-Sulfated Heparan Sulfate Domains: Distinct Modes of Glucuronyl C5 Epimerization, Iduronic Acid 2-O-Sulfation, and Glucosamine 6-O-Sulfation. Biochemistry. 2000;39(35):10823-30.
107. Sugaya N, Habuchi H, Nagai N, Ashikari-Hada S, Kimata K. 6-O-sulfation of heparan sulfate differentially regulates various fibroblast growth factor-dependent signalings in culture. J Biol Chem. 2008;283(16):10366-76.
108. Naimy H, Buczek-Thomas JA, Nugent MA, Leymarie N, Zaia J. Highly sulfated nonreducing end-derived heparan sulfate domains bind fibroblast growth factor-2 with high affinity and are enriched in biologically active fractions. J Biol Chem. 2011;286(22):19311-9.
109. Turnbull JE, Fernig DG, Ke Y, Wilkinson MC, Gallagher JT. Identification of the basic fibroblast growth factor binding sequence in fibroblast heparan sulfate. J Biol Chem. 1992;267(15):10337-41.
110. Lundin L, Larsson H, Kreuger J, Kanda S, Lindahl U, Salmivirta M, et al. Selectively desulfated heparin inhibits fibroblast growth factor-induced mitogenicity and angiogenesis. J Biol Chem. 2000;275(32):24653-60.

111. Wang S, Ai X, Freeman SD, Pownall ME, Lu Q, Kessler DS, et al. QSulf1, a heparan sulfate 6-O-endosulfatase, inhibits fibroblast growth factor signaling in mesoderm induction and angiogenesis. Proc Natl Acad Sci U S A. 2004;101(14):4833-8.
112. Jastrebova N, Vanwildemeersch M, Lindahl U, Spillmann D. Heparan sulfate domain organization and sulfation modulate FGF-induced cell signaling. J Biol Chem. 2010;285(35):26842-51.
113. Schultz V, Suflita M, Liu X, Zhang X, Yu Y, Li L, et al. Heparan Sulfate Domains Required for Fibroblast Growth Factor 1 and 2 Signaling through Fibroblast Growth Factor Receptor 1c. J Biol Chem. 2017;292(6):2495-509.
114. Uniewicz KA, Ori A, Xu R, Ahmed Y, Wilkinson MC, Fernig DG, et al. Differential scanning fluorimetry measurement of protein stability changes upon binding to glycosaminoglycans: a screening test for binding specificity. Anal Chem. 2010;82(9):3796-802.
115. Xu R, Rudd TR, Hughes AJ, Siligardi G, Fernig DG, Yates EA. Analysis of the fibroblast growth factor receptor (FGFR) signalling network with heparin as coreceptor: evidence for the expansion of the core FGFR signalling network. FEBS J. 2013;280(10):2260-70.
116. Babik S, Samsonov SA, Pisabarro MT. Computational drill down on FGF1-heparin interactions through methodological evaluation. Glycoconjugate Journal. 2017;34(3):427-40.
117. Steiner T. The Hydrogen Bond in the Solid State. Angewandte Chemie International Edition. 2002;41(1):48-76.
118. Del Bene JE, Frisch MJ, Pople JA. Molecular orbital study of the complexes (AHn)2H+ formed from ammonia, water, hydrogen fluoride, phosphine, hydrogen sulfide, and hydrogen chloride. The Journal of Physical Chemistry. 1985;89(17):3669-74.
119. Blanksby SJ, Ellison GB. Bond dissociation energies of organic molecules. Acc Chem Res. 2003;36(4):255-63.
120. Migliorini E, Thakar D, Sadir R, Pleiner T, Baleux F, Lortat-Jacob H, et al. Well-defined biomimetic surfaces to characterize glycosaminoglycan-mediated interactions on the molecular, supramolecular and cellular levels. Biomaterials. 2014;35(32):8903-15.
121. Sun C, Li Y, Taylor SE, Mao X, Wilkinson MC, Fernig DG. HaloTag is an effective expression and solubilisation fusion partner for a range of fibroblast growth factors. PeerJ. 2015;3:e1060.
122. Richter R, Mukhopadhyay A, Brisson A. Pathways of Lipid Vesicle Deposition on Solid Surfaces: A Combined QCM-D and AFM Study. Biophysical Journal. 2003;85(5):3035-47.
123. Thakar D, Migliorini E, Coche-Guerente L, Sadir R, Lortat-Jacob H, Boturyn D, et al. A quartz crystal microbalance method to study the terminal functionalization of glycosaminoglycans. Chem Commun (Camb). 2014;50(96):15148-51.
124. Jasnin M, van Eijck L, Koza MM, Peters J, Laguri C, Lortat-Jacob H, et al. Dynamics of heparan sulfate explored by neutron scattering. Phys Chem Chem Phys. 2010;12(14):3360-2.
125. Iduron. [Available from: http://iduron.co.uk/product/dermatan-sulphate-oligosaccharides.
126. Mason WP, McSkimin HJ. Measurement of Shear Elasticity and Viscosity of Liquids by Means of Ultrasonic Shear Waves. The Journal of the Acoustical Society of America. 1949;21(1):58-.
127. Sittel K, Rouse PEJ, Bailey ED. Method for Determining the Viscoelastic Properties of Dilute Polymer Solutions at Audio-Frequencies. Journal of Applied Physics. 1954;25(10):1312-20.
128. Rodahl M, Hook F, Kasemo B. QCM Operation in Liquids: An Explanation of Measured Variations in Frequency and Q Factor with Liquid Conductivity. Anal Chem. 1996;68(13):2219-27.

129. Rodahl M, Hook F, Fredriksson C, Keller CA, Krozer A, Brzezinski P, et al. Simultaneous frequency and dissipation factor QCM measurements of biomolecular adsorption and cell adhesion. Faraday Discuss. 1997(107):229-46.
130. Reviakine I, Johannsmann D, Richter RP. Hearing what you cannot see and visualizing what you hear: interpreting quartz crystal microbalance data from solvated interfaces. Anal Chem. 2011;83(23):8838-48.
131. Tsortos A, Papadakis G, Gizeli E. Shear acoustic wave biosensor for detecting DNA intrinsic viscosity and conformation: a study with QCM-D. Biosens Bioelectron. 2008;24(4):842-7.
132. Richter RP, Rodenhausen KB, Eisele NB, Schubert M. Coupling Spectroscopic Ellipsometry and Quartz Crystal Microbalance to Study Organic Films at the Solid-Liquid Interface. In: Hinrichs K, Eichhorn K-J, editors. Ellipsometry of Functional Organic Surfaces and Films. Berlin, Heidelberg: Springer Berlin Heidelberg; 2014. p. 223-48.
133. Gonçalves D, Irene EA. Fundamentals and applications of spectroscopic ellipsometry. Química Nova. 2002;25:794-800.
134. Humlíček J. 1 - Polarized Light and Ellipsometry A2 - Tompkins, Harland G. In: Irene EA, editor. Handbook of Ellipsometry. Norwich, NY: William Andrew Publishing; 2005. p. 3-91.
135. Woollam JA, Snyder PG. Fundamentals and applications of variable angle spectroscopic ellipsometry. Materials Science and Engineering: B. 1990;5(2):279-83.
136. De Feijter JA, Benjamins J, Veer FA. Ellipsometry as a tool to study the adsorption behavior of synthetic and biopolymers at the air–water interface. Biopolymers. 1978;17(7):1759-72.
137. Dubacheva GV, Araya-Callis C, Geert Volbeda A, Fairhead M, Codee J, Howarth M, et al. Controlling Multivalent Binding through Surface Chemistry: Model Study on Streptavidin. J Am Chem Soc. 2017;139(11):4157-67.
138. Daimon M, Masumura A. Measurement of the refractive index of distilled water from the near-infrared region to the ultraviolet region. Appl Opt. 2007;46(18):3811-20.
139. Müller M. Vibrational Spectroscopic and Optical Methods. In: Stamm M, editor. Polymer Surfaces and Interfaces: Characterization, Modification and Applications. Berlin, Heidelberg: Springer Berlin Heidelberg; 2008. p. 47-70.
140. Pavlov G, Finet S, Tatarenko K, Korneeva E, Ebel C. Conformation of heparin studied with macromolecular hydrodynamic methods and X-ray scattering. Eur Biophys J. 2003;32(5):437-49.
141. Tumolo T, Angnes L, Baptista MS. Determination of the refractive index increment (dn/dc) of molecule and macromolecule solutions by surface plasmon resonance. Anal Biochem. 2004;333(2):273-9.
142. Zhao H, Brown Patrick H, Schuck P. On the Distribution of Protein Refractive Index Increments. Biophysical Journal. 2011;100(9):2309-17.
143. Bingen P, Wang G, Steinmetz NF, Rodahl M, Richter RP. Solvation effects in the quartz crystal microbalance with dissipation monitoring response to biomolecular adsorption. A phenomenological approach. Anal Chem. 2008;80(23):8880-90.
144. Reimhult E, Larsson C, Kasemo B, Höök F. Simultaneous Surface Plasmon Resonance and Quartz Crystal Microbalance with Dissipation Monitoring Measurements of Biomolecular Adsorption Events Involving Structural Transformations and Variations in Coupled Water. Analytical Chemistry. 2004;76(24):7211-20.
145. Salamon Z, Tollin G. Optical Anisotropy in Lipid Bilayer Membranes: Coupled Plasmon-Waveguide Resonance Measurements of Molecular Orientation, Polarizability, and Shape. Biophysical Journal. 2001;80(3):1557-67.
146. Sheppard CJ, Kompfner R. Resonant scanning optical microscope. Appl Opt. 1978;17(18):2879-82.

147. Kuhnle J. Lipid assemblies on nanostructured surfaces. Diploma thesis, Faculty of Physics and Astronomy, University of Heidelberg. 2007.
148. Migliorini E, Thakar D, Kuhnle J, Sadir R, Dyer DP, Li Y, et al. Cytokines and growth factors cross-link heparan sulfate. Open Biol. 2015;5(8).
149. Reviakine I, Brisson A. Streptavidin 2D Crystals on Supported Phospholipid Bilayers: Toward Constructing Anchored Phospholipid Bilayers. Langmuir. 2001;17(26):8293-9.
150. Ratanabanangkoon P, Gast AP. Effect of Ionic Strength on Two-Dimensional Streptavidin Crystallization. Langmuir. 2003;19(5):1794-801.
151. Boukamp P, Petrussevska RT, Breitkreutz D, Hornung J, Markham A, Fusenig NE. Normal keratinization in a spontaneously immortalized aneuploid human keratinocyte cell line. The Journal of Cell Biology. 1988;106(3):761-71.
152. Wrenshall LE, Platt JL, Stevens ET, Wight TN, Miller JD. Propagation and control of T cell responses by heparan sulfate-bound IL-2. Journal of immunology (Baltimore, Md : 1950). 2003;170(11):5470-4.
153. Wang L, Fuster M, Sriramarao P, Esko JD. Endothelial heparan sulfate deficiency impairs L-selectin- and chemokine-mediated neutrophil trafficking during inflammatory responses. Nature immunology. 2005;6(9):902-10.
154. Kimelman D, Kirschner M. Synergistic induction of mesoderm by FGF and TGF-beta and the identification of an mRNA coding for FGF in the early Xenopus embryo. Cell. 1987;51(5):869-77.
155. Dyer DP, Salanga CL, Johns SC, Valdambrini E, Fuster MM, Milner CM, et al. The Anti-inflammatory Protein TSG-6 Regulates Chemokine Function by Inhibiting Chemokine/Glycosaminoglycan Interactions. J Biol Chem. 2016;291(24):12627-40.
156. Kuschert GS, Coulin F, Power CA, Proudfoot AE, Hubbard RE, Hoogewerf AJ, et al. Glycosaminoglycans interact selectively with chemokines and modulate receptor binding and cellular responses. Biochemistry. 1999;38(39):12959-68.
157. Lord MS, Cheng B, Farrugia BL, McCarthy S, Whitelock JM. Platelet Factor 4 Binds to Vascular Proteoglycans and Controls Both Growth Factor Activities and Platelet Activation. J Biol Chem. 2017;292(10):4054-63.
158. Chuang CY, Lord MS, Melrose J, Rees MD, Knox SM, Freeman C, et al. Heparan sulfate dependent signaling of fibroblast growth factor (FGF) 18 by chondrocyte-derived perlecan. Biochemistry. 2010;49(26):5524-32.
159. Thompson SM, Connell MG, van Kuppevelt TH, Xu R, Turnbull JE, Losty PD, et al. Structure and epitope distribution of heparan sulfate is disrupted in experimental lung hypoplasia: a glycobiological epigenetic cause for malformation? BMC Dev Biol. 2011;11:38.
160. Theodoraki A, Hu Y, Poopalasundaram S, Oosterhof A, Guimond SE, Disterer P, et al. Distinct patterns of heparan sulphate in pancreatic islets suggest novel roles in paracrine islet regulation. Mol Cell Endocrinol. 2015;399:296-310.
161. Liu Z, Lavine KJ, Hung IH, Ornitz DM. FGF18 is required for early chondrocyte proliferation, hypertrophy and vascular invasion of the growth plate. Developmental Biology. 2007;302(1):80-91.
162. Theodoraki A, Hu Y, Poopalasundaram S, Oosterhof A, Guimond SE, Disterer P, et al. Distinct patterns of heparan sulphate in pancreatic islets suggest novel roles in paracrine islet regulation. Molecular and Cellular Endocrinology. 2015;399:296-310.
163. Rudland PS, Platt-Higgins AM, Wilkinson MC, Fernig DG. Immunocytochemical identification of basic fibroblast growth factor in the developing rat mammary gland: variations in location are dependent on glandular structure and differentiation. The journal of histochemistry and cytochemistry : official journal of the Histochemistry Society. 1993;41(6):887-98.
164. Allen BL, Filla MS, Rapraeger AC. Role of heparan sulfate as a tissue-specific regulator of FGF-4 and FGF receptor recognition. The Journal of Cell Biology. 2001;155(5):845.

165. Rudd TR, Preston MD, Yates EA. The nature of the conserved basic amino acid sequences found among 437 heparin binding proteins determined by network analysis. Mol Biosyst. 2017;13(5):852-65.
166. Zhang C, Li Y, Wu Y, Wang L, Wang X, Du J. Interleukin-6/signal transducer and activator of transcription 3 (STAT3) pathway is essential for macrophage infiltration and myoblast proliferation during muscle regeneration. J Biol Chem. 2013;288(3):1489-99.
167. Escobar Galvis ML, Jia J, Zhang X, Jastrebova N, Spillmann D, Gottfridsson E, et al. Transgenic or tumor-induced expression of heparanase upregulates sulfation of heparan sulfate. Nature chemical biology. 2007;3(12):773-8.
168. Koenig A, Norgard-Sumnicht K, Linhardt R, Varki A. Differential interactions of heparin and heparan sulfate glycosaminoglycans with the selectins. Implications for the use of unfractionated and low molecular weight heparins as therapeutic agents. Journal of Clinical Investigation. 1998;101(4):877-89.
169. Maccarana M, Casu B, Lindahl U. Minimal sequence in heparin/heparan sulfate required for binding of basic fibroblast growth factor. J Biol Chem. 1994;269(5):3903.
170. Jemth P, Kreuger J, Kusche-Gullberg M, Sturiale L, Gimenez-Gallego G, Lindahl U. Biosynthetic oligosaccharide libraries for identification of protein-binding heparan sulfate motifs. Exploring the structural diversity by screening for fibroblast growth factor (FGF)1 and FGF2 binding. J Biol Chem. 2002;277(34):30567-73.
171. Vanpouille C, Deligny A, Delehedde M, Denys A, Melchior A, Lienard X, et al. The heparin/heparan sulfate sequence that interacts with cyclophilin B contains a 3-O-sulfated N-unsubstituted glucosamine residue. J Biol Chem. 2007;282(33):24416-29.
172. Faham S, Linhardt RJ, Rees DC. Diversity does make a difference: fibroblast growth factor-heparin interactions. Current opinion in structural biology. 1998;8(5):578-86.
173. Najjam S, Mulloy B, Theze J, Gordon M, Gibbs R, Rider CC. Further characterization of the binding of human recombinant interleukin 2 to heparin and identification of putative binding sites. Glycobiology. 1998;8(5):509-16.
174. Poluri KM, Joseph PRB, Sawant KV, Rajarathnam K. Molecular Basis of Glycosaminoglycan Heparin Binding to the Chemokine CXCL1 Dimer. The Journal of Biological Chemistry. 2013;288(35):25143-53.
175. Zhang X, Ibrahimi OA, Olsen SK, Umemori H, Mohammadi M, Ornitz DM. Receptor specificity of the fibroblast growth factor family. The complete mammalian FGF family. J Biol Chem. 2006;281(23):15694-700.
176. Ornitz DM, Xu J, Colvin JS, McEwen DG, MacArthur CA, Coulier F, et al. Receptor specificity of the fibroblast growth factor family. J Biol Chem. 1996;271(25):15292-7.
177. Sun C. Control of binding and movement of fibroblast growth factors by heparan sulfate in extracellular matrix. [Doctor of Philosophy thesis]: University of Liverpool; 2015.
178. Eisele NB, Frey S, Piehler J, Gorlich D, Richter RP. Ultrathin nucleoporin phenylalanine-glycine repeat films and their interaction with nuclear transport receptors. EMBO reports. 2010;11(5):366-72.
179. J. K. Lipid assemblies on nanostructured surfaces. Diploma thesis, Faculty of Physics and Astronomy, University of Heidelberg. 2007.
180. Zhang Z, Xie J, Liu H, Liu J, Linhardt RJ. Quantification of heparan sulfate disaccharides using ion-pairing reversed-phase microflow high-performance liquid chromatography with electrospray ionization trap mass spectrometry. Anal Chem. 2009;81(11):4349-55.
181. Mulloy B, Gee C, Wheeler SF, Wait R, Gray E, Barrowcliffe TW. Molecular weight measurements of low molecular weight heparins by gel permeation chromatography. Thromb Haemost. 1997;77(4):668-74.
182. Esko JD, Lindahl U. Molecular diversity of heparan sulfate. The Journal of clinical investigation. 2001;108(2):169-73.

183. Rosenberg RD, Shworak NW, Liu J, Schwartz JJ, Zhang L. Heparan sulfate proteoglycans of the cardiovascular system. Specific structures emerge but how is synthesis regulated? The Journal of clinical investigation. 1997;100(11 Suppl):S67-75.
184. Shukla D, Liu J, Blaiklock P, Shworak NW, Bai X, Esko JD, et al. A novel role for 3-O-sulfated heparan sulfate in herpes simplex virus 1 entry. Cell. 1999;99(1):13-22.
185. Sun C, Marcello M, Li Y, Mason D, Levy R, Fernig DG. Selectivity in glycosaminoglycan binding dictates the distribution and diffusion of fibroblast growth factors in the pericellular matrix. Open Biol. 2016;6(3).
186. Johannsmann D, Reviakine I, Richter RP. Dissipation in films of adsorbed nanospheres studied by quartz crystal microbalance (QCM). Anal Chem. 2009;81(19):8167-76.
187. Duchesne L, Octeau V, Bearon RN, Beckett A, Prior IA, Lounis B, et al. Transport of fibroblast growth factor 2 in the pericellular matrix is controlled by the spatial distribution of its binding sites in heparan sulfate. PLoS biology. 2012;10(7):e1001361.
188. Halford SE, Marko JF. How do site-specific DNA-binding proteins find their targets? Nucleic Acids Research. 2004;32(10):3040-52.
189. Thompson LD, Pantoliano MW, Springer BA. Energetic characterization of the basic fibroblast growth factor-heparin interaction: identification of the heparin binding domain. Biochemistry. 1994;33(13):3831-40.
190. Deepa SS, Umehara Y, Higashiyama S, Itoh N, Sugahara K. Specific molecular interactions of oversulfated chondroitin sulfate E with various heparin-binding growth factors. Implications as a physiological binding partner in the brain and other tissues. J Biol Chem. 2002;277(46):43707-16.
191. Perlin AS, Mackie DM, Dietrich CP. Evidence for a (1→4)-linked 4-O-(α-L-idopyranosyluronic acid 2-sulfate)-(2-deoxy-2-sulfoamino-D-glucopyranosyl 6-sulfate) sequence in heparin. Carbohydrate Research. 1971;18(2):185-94.
192. Linhardt RJ, Wang HM, Loganathan D, Lamb DJ, Mallis LM. Analysis of glycosaminoglycan-derived oligosaccharides using fast-atom-bombardment mass-spectrometry. Carbohydr Res. 1992;225(1):137-45.
193. Pervin A, Gallo C, Jandik KA, Han XJ, Linhardt RJ. Preparation and structural characterization of large heparin-derived oligosaccharides. Glycobiology. 1995;5(1):83-95.
194. Ryan E, Shen D, Wang X. Structural studies reveal an important role for the pleiotrophin C-terminus in mediating interactions with chondroitin sulfate. FEBS J. 2016;283(8):1488-503.
195. Muthusamy A, Achur RN, Valiyaveettil M, Madhunapantula SV, Kakizaki I, Bhavanandan VP, et al. Structural characterization of the bovine tracheal chondroitin sulfate chains and binding of Plasmodium falciparum-infected erythrocytes. Glycobiology. 2004;14(7):635-45.
196. Hermens WT, Benes M, Richter R, Speijer H. Effects of flow on solute exchange between fluids and supported biosurfaces. Biotechnol Appl Biochem. 2004;39(Pt 3):277-84.
197. Hughes A, Meneghetti M, Huang TY, Hung SC, Elli S, Guerrini M, et al. Investigating the relationship between temperature, conformation and calcium binding in heparin model oligosaccharides. Carbohydr Res. 2017;438:58-64.
198. Hecht HJ, Adar R, Hofmann B, Bogin O, Weich H, Yayon A. Structure of fibroblast growth factor 9 shows a symmetric dimer with unique receptor- and heparin-binding interfaces. Acta Crystallographica Section D. 2001;57(3):378-84.
199. Presta M, Gualandris A, Urbinati C, Rusnati M, Coltrini D, Isacchi A, et al. Subcellular localization and biological activity of M(r) 18,000 basic fibroblast growth factor: site-directed mutagenesis of a putative nuclear translocation sequence. Growth Factors. 1993;9(4):269-78.

200. Amalric F, Baldin V, Bosc-Bierne I, Bugler B, Couderc B, Guyader M, et al. Nuclear translocation of basic fibroblast growth factor. Annals of the New York Academy of Sciences. 1991;638:127-38.
201. Wiedlocha A, Sorensen V. Signaling, internalization, and intracellular activity of fibroblast growth factor. Curr Top Microbiol Immunol. 2004;286:45-79.
202. Kalinina J, Byron SA, Makarenkova HP, Olsen SK, Eliseenkova AV, Larochelle WJ, et al. Homodimerization controls the fibroblast growth factor 9 subfamily's receptor binding and heparan sulfate-dependent diffusion in the extracellular matrix. Molecular and cellular biology. 2009;29(17):4663-78.
203. Patel VN, Rebustini IT, Hoffman MP. Salivary gland branching morphogenesis. Differentiation. 2006;74(7):349-64.
204. Gonzalez AM, Buscaglia M, Ong M, Baird A. Distribution of basic fibroblast growth factor in the 18-day rat fetus: localization in the basement membranes of diverse tissues. J Cell Biol. 1990;110(3):753-65.
205. Dowd CJ, Cooney CL, Nugent MA. Heparan sulfate mediates bFGF transport through basement membrane by diffusion with rapid reversible binding. J Biol Chem. 1999;274(8):5236-44.
206. Izvolsky KI, Shoykhet D, Yang Y, Yu Q, Nugent MA, Cardoso WV. Heparan sulfate-FGF10 interactions during lung morphogenesis. Dev Biol. 2003;258(1):185-200.
207. Chu CL, Buczek-Thomas JA, Nugent MA. Heparan sulphate proteoglycans modulate fibroblast growth factor-2 binding through a lipid raft-mediated mechanism. The Biochemical journal. 2004;379(Pt 2):331-41.
208. Zhou S, Lo WC, Suhalim JL, Digman MA, Gratton E, Nie Q, et al. Free extracellular diffusion creates the Dpp morphogen gradient of the Drosophila wing disc. Curr Biol. 2012;22(8):668-75.
209. Yamada KM, Kennedy DW, Kimata K, Pratt RM. Characterization of fibronectin interactions with glycosaminoglycans and identification of active proteolytic fragments. J Biol Chem. 1980;255(13):6055-63.
210. San Antonio JD, Lander AD, Karnovsky MJ, Slayter HS. Mapping the heparin-binding sites on type I collagen monomers and fibrils. J Cell Biol. 1994;125(5):1179-88.
211. Elf J, Li G-W, Xie XS. Probing Transcription Factor Dynamics at the Single-Molecule Level in a Living Cell. Science. 2007;316(5828):1191.
212. Kinnunen T, Raulo E, Nolo R, Maccarana M, Lindahl U, Rauvala H. Neurite outgrowth in brain neurons induced by heparin-binding growth-associated molecule (HB-GAM) depends on the specific interaction of HB-GAM with heparan sulfate at the cell surface. J Biol Chem. 1996;271(4):2243-8.
213. Sevim S, Ozer S, Jones G, Wurzel J, Feng L, Fakhraee A, et al. Nanomechanics on FGF-2 and Heparin Reveal Slip Bond Characteristics with pH Dependency. ACS Biomaterials Science & Engineering. 2017;3(6):1000-7.